applied sciences

Novel Approaches for Structural Health Monitoring II

Edited by
Cecilia Surace

Printed Edition of the Special Issue Published in *Applied Sciences*

www.mdpi.com/journal/applsci

MDPI

Novel Approaches for Structural Health Monitoring II

Novel Approaches for Structural Health Monitoring II

Editor

Cecilia Surace

MDPI • Basel • Beijing • Wuhan • Barcelona • Belgrade • Manchester • Tokyo • Cluj • Tianjin

Editor
Cecilia Surace
Politecnico di Torino
Italy

Editorial Office
MDPI
St. Alban-Anlage 66
4052 Basel, Switzerland

This is a reprint of articles from the Special Issue published online in the open access journal *Applied Sciences* (ISSN 2076-3417) (available at: https://www.mdpi.com/journal/applsci/special_issues/Structural_Health_Monitoring_II).

For citation purposes, cite each article independently as indicated on the article page online and as indicated below:

LastName, A.A.; LastName, B.B.; LastName, C.C. Article Title. *Journal Name* **Year**, *Volume Number*, Page Range.

ISBN 978-3-0365-7542-1 (Hbk)
ISBN 978-3-0365-7543-8 (PDF)

Cover image courtesy of Elizabeth Caroline Storer

© 2023 by the authors. Articles in this book are Open Access and distributed under the Creative Commons Attribution (CC BY) license, which allows users to download, copy and build upon published articles, as long as the author and publisher are properly credited, which ensures maximum dissemination and a wider impact of our publications.
The book as a whole is distributed by MDPI under the terms and conditions of the Creative Commons license CC BY-NC-ND.

Contents

About the Editor . . . . . **vii**

Cecilia Surace
Editorial for the Special Issue on Novel Approaches for Structural Health Monitoring II
Reprinted from: *Appl. Sci.* **2023**, *13*, 5027, doi:10.3390/app13085027 . . . . . **1**

Franco Concli, Ludovico Pierri and Claudio Sbarufatti
A Model-Based SHM Strategy for Gears—Development of a Hybrid FEM-Analytical Approach to Investigate the Effects of Surface Fatigue on the Vibrational Spectra of a Back-to-Back Test Rig
Reprinted from: *Appl. Sci.* **2021**, *11*, 2026, doi:10.3390/app11052026 . . . . . **5**

Janardhan Padiyar M., Luca Zanotti Fragonara, Ivan Petrunin, Joao Raposo, Antonios Tsourdos, Iain Gray, Spyridoyla Farmaki, et al.
Fast, Accurate, and Reliable Detection of Damage in Aircraft Composites by Advanced Synergistic Infrared Thermography and Phased Array Techniques
Reprinted from: *Appl. Sci.* **2021**, *11*, 2778, doi:10.3390/app11062778 . . . . . **27**

Chang-Sheng Lin and Yi-Xiu Wu
Response-Only Parametric Estimation of Structural Systems Using a Modified Stochastic Subspace Identification Technique
Reprinted from: *Appl. Sci.* **2021**, *11*, 11751, doi:10.3390/app112411751 . . . . . **43**

Marco Civera and Cecilia Surace
An Application of Instantaneous Spectral Entropy for the Condition Monitoring of Wind Turbines
Reprinted from: *Appl. Sci.* **2022**, *12*, 1059, doi:10.3390/app12031059 . . . . . **63**

Giulia Delo, Marco Civera, Erica Lenticchia, Gaetano Miraglia, Cecilia Surace and Rosario Ceravolo
Interferometric Satellite Data in Structural Health Monitoring: An Application to the Effects of the Construction of a Subway Line in the Urban Area of Rome
Reprinted from: *Appl. Sci.* **2022**, *12*, 1658, doi:10.3390/app12031658 . . . . . **83**

Rosario Ceravolo, Erica Lenticchia, Gaetano Miraglia, Valerio Oliva and Linda Scussolini
Modal Identification of Structures with Interacting Diaphragms
Reprinted from: *Appl. Sci.* **2022**, *12*, 4030, doi:10.3390/app12084030 . . . . . **105**

Cristian Tufisi, Catalin V. Rusu, Nicoleta Gillich, Marius Vasile Pop, Codruta Oana Hamat, Christian Sacarea and Gilbert-Rainer Gillich
Determining the Severity of Open and Closed Cracks Using the Strain Energy Loss and the Hill-Climbing Method
Reprinted from: *Appl. Sci.* **2022**, *12*, 7231, doi:10.3390/app12147231 . . . . . **121**

Sinem Tola, Joaquim Tinoco, José C. Matos and Eugene Obrien
Scour Detection with Monitoring Methods and Machine Learning Algorithms—A Critical Review
Reprinted from: *Appl. Sci.* **2023**, *13*, 1661, doi:10.3390/app13031661 . . . . . **139**

About the Editor

Cecilia Surace

Prof. Dr. Cecilia Surace has been an associate professor of structural mechanics at Politecnico di Torino, Turin, Italy, since 2014. She is also a member of the committee for doctoral students in aerospace engineering and head of the laboratory of bio-inspired nanomechanics in the Department of Structural, Building, and Geotechnical Engineering. Furthermore, she has been active in the fields of structural dynamics and structural health monitoring since the early 1990s, with more than 100 publications on these topics.

applied sciences

MDPI

Editorial

Editorial for the Special Issue on Novel Approaches for Structural Health Monitoring II

Cecilia Surace

Department of Structural, Geotechnical and Building Engineering, Politecnico di Torino, 10129 Turin, Italy; cecilia.surace@polito.it

The emphasis of this Special Issue is on showcasing the most recent advancements in the field of Structural Health Monitoring (SHM), accounting for all its applications in mechanical systems and civil structures or infrastructures. The eight papers presented here represent relevant contributions in their specific aspects.

In the work of Concli, Pierri and Sbarufatti [1], transmission maintenance for the condition monitoring of gearboxes was addressed. Specifically, the researchers considered a back-to-back test rig consisting of two parallel axes gearboxes connected by means of two shafts in a closed mechanical loop. They also focused on surface damage (namely, pitting), numerically simulating several types and severities of damage. The proposed Machine Learning (ML) approach, based on a multilayer perceptron, is able to perform damage detection, localization and quantification. The training phase of the Artificial Neural Network (ANN) was performed resorting to signal examples generated by a hybrid analytical–numerical model.

Janardhan Padiyar et al. [2] presented a synergistic non-destructive method for the automated inspections of aircraft composite structures. Specifically, a sensor fusion procedure was outlined, combining two image-based non-destructive evaluation (NDE) techniques: phased-array ultrasonic testing and infrared thermography. The approach was experimentally validated on an aircraft-grade painted composite material skin panel with stringers. Importantly, the miniaturized sensor systems tested and validated here were intended to be integrated in a vortex-robotic platform inspector, in the framework of the Horizon-2020 'CompInnova' project.

The work of Lin and Wu [3] concerned the well-known Stochastic Subspace Identification (SSI) technique, widely used for the output-only system identification of a target structure or mechanical system from ambient vibration testing. This falls into the field of Operational Modal Analysis (OMA). Importantly, two main variants of the SSI algorithm exist: the covariance-driven SSI (SSI-COV) and the data-driven SSI (SSI-DATA). In brief, the second option (SSI-DATA) operates directly on measured output response data with no further processing. Conversely, SSI-COV utilizes the covariance functions for the purpose of modal parameter estimation; these need to be estimated in advance from raw output time histories. In this context, the authors introduced a procedure to solve the system matrix in SSI-COV in conjunction with SSI-DATA, allowing modal estimation to be well implemented.

Civera and Surace [4] discussed an application of Instantaneous Spectral Entropy (ISE) for the real-time condition monitoring of a faulty three-stage gearbox. In particular, the case study came from a 2.5 MW Nordex N100 wind turbine located in Northern Sweden. The proposed algorithm employs the instantaneous formulation of Shannon Spectral Entropy (SSE), which was proven to be damage-sensitive in previous studies on masonry buildings and steel pipelines, in combination with Continuous Wavelet Transform (CWT). The Generalized Morse Wavelet (GMW) was proposed as the best choice for the CWT mother wavelet. A sensitivity analysis was performed on the two GMW parameters

Citation: Surace, C. Editorial for the Special Issue on Novel Approaches for Structural Health Monitoring II. *Appl. Sci.* **2023**, *13*, 5027. https://doi.org/10.3390/app13085027

Received: 1 April 2023
Accepted: 4 April 2023
Published: 17 April 2023

Copyright: © 2023 by the author. Licensee MDPI, Basel, Switzerland. This article is an open access article distributed under the terms and conditions of the Creative Commons Attribution (CC BY) license (https://creativecommons.org/licenses/by/4.0/).

(symmetry γ and compactness β), suggesting the use of $3 \leq \gamma \leq 4$ and $20 \leq \beta \leq 40$ to increase fault detectability.

The work of Delo et al. [5] explored a remote sensing approach to SHM, based on interferometric data and focusing on representation techniques that can be adopted to highlight their advantages for the field. In the paper, the authors analyzed Line-of-Sight displacement records from the urban area of Rome (Italy). They analyzed an area subject to the construction of a new subway line. These data were exploited to create a velocity map to highlight the possible subsidence phenomenon induced by excavations. Then, entropy–energy representations were applied to single buildings and building complexes. Finally, the authors concluded that future developments and the continuous increase in the quality of satellite data may allow for the practical application of such information for SHM, leading to a low-cost automated process for the study of large urban areas.

Ceravolo et al. [6] proposed a methodology to approach the identification of interconnected diaphragmatic structures using a simplified analytical model (i.e., spring–masses model). The simplified model is exploited to aid the identification of a significant case study, represented by the Pavilion V, designed by Riccardo Morandi as a hypogeum hall in the Turin Exhibition Center composed of three interconnected blocks with joints. Not only does the presence of these joints result in modal complexity but also in very high sensitivity of the stiffness parameters, especially when the joints are fully effective. This complexity also affects the design of the experimental setups, which are often unable to capture the whole-body dynamics. As the main result, light was shed on the contribution of the stiffness of the joints to the global dynamic behavior of structures composed of interacting diaphragms and, in particular, on the effectiveness of the joints of Pavilion V.

Tufisi et al. [7] evaluated the damage severity of cantilever beams by means of an optimization algorithm known as Stochastic Hill Climbing (SHC). This is applied to the deflections of fixed-free structural elements with both open and closed cracks at different locations. The algorithm, which was implemented in a Python application named PySHC, was validated via an experimental test. It was found to be capable of estimating the location and depth of the crack with minimal error (respectively, 1.1% and 0.3 mm).

Tola et al. [8] presented a critical review of bridge monitoring methods and ML algorithms for scour detection. This is an extremely relevant topic, as foundation scour is one of the first causes of total or partial bridge collapse. Furthermore, its effects are mainly located underwater and are, thus, not detectable from visual inspection only. They also depend on underground soil conditions that are even more difficult to investigate from above ground. The authors present and detail the techniques and the main outcomes of 36 studies, divided into two broad categories: conventional-monitoring-based studies and advanced Machine-Learning-based studies to detect scour.

In conclusion, this Special Issue collected high-quality contributions on various SHM applications in applied sciences, and it also provided a solid state-of-the-art reference in this research area.

Acknowledgments: This Special Issue collected the efforts of all the authors, reviewers, and members of the *Applied Sciences* Editorial Office. We would like to thank all the professional contributions to this publication. The Special Issue benefited from the coordination efforts and support from Marco Civera.

Conflicts of Interest: The authors declare no conflict of interest.

References

1. Concli, F.; Pierri, L.; Sbarufatti, C. A Model-Based SHM Strategy for Gears—Development of a Hybrid FEM-Analytical Approach to Investigate the Effects of Surface Fatigue on the Vibrational Spectra of a Back-to-Back Test Rig. *Appl. Sci.* **2021**, *11*, 2026. [CrossRef]
2. Janardhan Padiyar, M.; Fragonara, L.Z.; Petrunin, I.; Raposo, J.; Tsourdos, A.; Gray, I.; Farmaki, S.; Exarchos, D.; Matikas, T.E.; Dassios, K.G. Fast, Accurate, and Reliable Detection of Damage in Aircraft Composites by Advanced Synergistic Infrared Thermography and Phased Array Techniques. *Appl. Sci.* **2021**, *11*, 2778. [CrossRef]
3. Lin, C.S.; Wu, Y.X. Response-Only Parametric Estimation of Structural Systems Using a Modified Stochastic Subspace Identification Technique. *Appl. Sci.* **2021**, *11*, 11751. [CrossRef]

4. Civera, M.; Surace, C. An Application of Instantaneous Spectral Entropy for the Condition Monitoring of Wind Turbines. *Appl. Sci.* **2022**, *12*, 1059. [CrossRef]
5. Delo, G.; Civera, M.; Lenticchia, E.; Miraglia, G.; Surace, C.; Ceravolo, R. Interferometric Satellite Data in Structural Health Monitoring: An Application to the Effects of the Construction of a Subway Line in the Urban Area of Rome. *Appl. Sci.* **2022**, *12*, 1658. [CrossRef]
6. Ceravolo, R.; Lenticchia, E.; Miraglia, G.; Oliva, V.; Scussolini, L. Modal Identification of Structures with Interacting Diaphragms. *Appl. Sci.* **2022**, *12*, 4030. [CrossRef]
7. Tufisi, C.; Rusu, C.V.; Gillich, N.; Pop, M.V.; Hamat, C.O.; Sacarea, C.; Gillich, G.R. Determining the Severity of Open and Closed Cracks Using the Strain Energy Loss and the Hill-Climbing Method. *Appl. Sci.* **2022**, *12*, 7231. [CrossRef]
8. Tola, S.; Tinoco, J.; Matos, J.C.; Obrien, E. Scour Detection with Monitoring Methods and Machine Learning Algorithms—A Critical Review. *Appl. Sci.* **2023**, *13*, 1661. [CrossRef]

Disclaimer/Publisher's Note: The statements, opinions and data contained in all publications are solely those of the individual author(s) and contributor(s) and not of MDPI and/or the editor(s). MDPI and/or the editor(s) disclaim responsibility for any injury to people or property resulting from any ideas, methods, instructions or products referred to in the content.

applied sciences

MDPI

Article

A Model-Based SHM Strategy for Gears—Development of a Hybrid FEM-Analytical Approach to Investigate the Effects of Surface Fatigue on the Vibrational Spectra of a Back-to-Back Test Rig

Franco Concli [1,*], Ludovico Pierri [2] and Claudio Sbarufatti [2]

[1] Free University of Bolzano/Bozen, Faculty of Science and Technology, Piazza Università 1, 39100 Bolzano, Italy
[2] Department of Mechanical Engineering, Politecnico di Milano, via la Masa 1, 20157 Milano, Italy; ludovico.pierri@polimi.it (L.P.); claudio.sbarufatti@polimi.it (C.S.)
* Correspondence: franco.concli@unibz.it; Tel.: +39-0471-017748

Abstract: Transmissions are extensively employed in mechanical gearboxes when power conversion is required. Being able to provide specific maintenance is a crucial factor for both economics and reliability. However, although periodic transmission maintenance increases the systems' longevity, it cannot prevent or predict sporadic major failures. In this context, structural health monitoring (SHM) represents a possible solution. Identifying variations of a specific measurable signal and correlating them with the type of damage or its location and severity may help assess the component condition and establish the need for maintenance operation. However, the collection of sufficient experimental examples for damage identification may be not convenient for big gearboxes, for which destructive experiments are too expensive, thus paving the way to model-based approaches, based on a numerical estimation of damage-related features. In this work, an SHM approach was developed based on signals from numerical simulations. To validate the approach with experimental measurements, a back-to-back test rig was used as a reference. Several types and severities of damages were simulated with an innovative hybrid analytical–numerical approach that allowed a significant reduction of the computational effort. The vibrational spectra that characterized the different damage conditions were processed through artificial neural networks (ANN) trained with numerical data and used to predict the presence, location, and severity of the damage.

Keywords: gears; SHM; FEM; pitting; surface fatigue

Citation: Concli, F.; Pierri, L.; Sbarufatti, C. A Model-Based SHM Strategy for Gears—Development of a Hybrid FEM-Analytical Approach to Investigate the Effects of Surface Fatigue on the Vibrational Spectra of a Back-to-Back Test Rig. *Appl. Sci.* **2021**, *11*, 2026. https://doi.org/10.3390/app11052026

Academic Editor: Cecilia Surace

Received: 9 February 2021
Accepted: 22 February 2021
Published: 25 February 2021

Publisher's Note: MDPI stays neutral with regard to jurisdictional claims in published maps and institutional affiliations.

Copyright: © 2021 by the authors. Licensee MDPI, Basel, Switzerland. This article is an open access article distributed under the terms and conditions of the Creative Commons Attribution (CC BY) license (https://creativecommons.org/licenses/by/4.0/).

1. Introduction

Many industrial components are subjected to cumulative damages associated with cyclic loadings. In a damage-tolerant scenario, each mechanical component needs to retain its residual health, safety, and functionality as long as possible to avoid extra maintenance, which is expensive, difficult to perform, or even impossible, as it often requires extensive knowledge of potential damage evolution. Most mechanical systems are currently monitored during both scheduled and unscheduled maintenance by means of nondestructive inspection technologies (NDIs); however, in recent years, the problem of real-time monitoring of mechanically stressed components has become a critical research topic.

Condition-monitoring techniques are of multiple natures, as described by Salameh et al. [1] The most intuitive is vibration analysis, which works with machinery vibration, and in which faulted elements promote different vibration spectra from healthy ones. Several authors have proposed experimental-based works dealing with vibration measurements. Zhao et al. [2] studied the effects of damages on gears and bearings. Cao et al. [3] studied the effects of damages with noncontact techniques. Kien et al. [4] studied

the effects of the presence of tooth root cracks on plastic gears by means of neural networks [4]. Ümütlü et al. studied the surface-fatigue damages on worm gears [5]. Huang et al. proposed a computational-based approach [6] instead. A similar work based on cyclostationary analysis was presented by Mauricio et al. [7] and by Sun et al. [8].

Acoustic-emission monitoring is an extension of vibration analysis. Although it suffers from background noise, which often yields useless results, it is simple and cost-effective. Lubricant analysis is one of the most challenging methods, as it requires oil sampling and further chemical analysis. It does not operate in real time; due to this characteristic, it may detects faults when it is often too late to intervene with maintenance. Sensible sensors are often added to have this type of condition monitoring done online (in real time), but most of the time these sensors are expensive and need rigorous inspection. For applications in which the transmission is attached to an electrical generator, the analysis of the absorbed power signal's fluctuations gives information about the presence of a defect, but not about its location in the transmission. Qu et al. [9] employed piezoelectric sensors and optical fibers to detect dynamic strain at specific points on gears with various type of defects. In this study, it was also stated that strain analysis has to be preferred to vibration analysis, because the latter suffers from errors due to the wave's propagation paths, hence a more direct contact between the faulty part and the sensor is preferred. Indeed, while vibration analyses are often not capable of detecting incipient damages due to noises, they are the easiest to set up. The advantages of transmission health monitoring shift the ideology of maintenance from "check at fixed intervals" to "always check and repair at the same time." By acting at the right time, major failures, which can cause breakdowns and hence downtimes, could be avoided, guaranteeing the expected working life. This translates to minimum and efficient spending for maintenance, which lowers the overall economical effort of keeping machinery running. This is particularly true for big/complex systems such as wind-turbine gearboxes, which on one hand are very complex and expensive, while the other hand are often placed in areas that are difficult to access.

While SHM is useful especially for very complex systems, for such configurations an experimentally based training of the SHM algorithm allows the inclusion of realistic sources of uncertainty retrieved in the field, but it is constrained by the huge costs of the prototypes, especially as the experimental replication of all the potential damages and faults is inconceivable. Thus, model-based approaches can be exploited, in which data from analytical and numerical models can be used as preliminary information for SHM system training and optimization; however, they require that the model be fast enough to allow for multiple simulations of the system in different conditions of interest, including both environmental influences and different damage configurations. In this scenario, a recent method for relatively fast modeling of transmissions [10] and prediction of vibration-based signal features that relies on a hybrid analytical–numerical approach is used in this study. It combines a traditional finite element method (FEM) to simulate the system deformations with an analytical Hertzian solution of the contact between gears or rolling elements. In this way, it allows the numerical simulation of very complex systems without geometrical simplifications, with a good accuracy and with a reasonable computational effort. With this approach, many different vibrational spectra can be generated for a healthy condition and with the presence of different sources of damage. The same hybrid approach has been tested on planetary transmissions of wind-turbine gearboxes by the NREL (National Renewable Energy Laboratory—USA), in which the entire multistage transmission was modeled and promisingly validated with a test rig owned by the NREL [11].

After generating a database of simulated signals in healthy and faulted conditions, made realistic by adding noise extracted from real sensor data, damage identification was performed in this study based on machine-learning algorithms, particularly artificial neural networks (ANNs). Specific ANNs, in the form of multilayer perceptrons (MLPs) have been trained to detect, localize, and quantify pitting damage over the transmission's gear teeth, verifying the performance of the model-based strategy for the global damage

identification hierarchical structure defined by Rytter [12], thus paving the way toward future implementation of prognostic algorithms for predictive maintenance.

The paper is structured as follows: The modelling approach is presented in the next section, with focus on the application scenario, with details of the hybrid model in both the healthy and damaged conditions, and examples of validated simulated signals. The results of damage identification algorithms for detection, localization, and assessment are provided in a separate section. A conclusion section completes the paper.

2. Modeling Methods

2.1. The Hybrid Modeling Approach

The present modeling strategy used a hybrid numerical–analytical approach. This was developed to simulate entire geared transmissions with a reduced computational effort. The mechanical components of the system, such as gears, bearings (including the rolling elements), shafts, housing, etc., could be modeled without the need of geometrical simplifications, ensuring a much higher accuracy of the results. The approach exploited a traditional finite element (FE) solver to model the macroscopic deformations of the components and the Hertzian theory to predict the pressures in the contacts (i.e., gear teeth, rolling elements, races in bearings, etc.) for which a traditional FE method requires an immense mesh refinement.

The points at which the individual contacting surfaces were closest to each other before the application of the load were computed first [13]. After that, the surface's normals were identified, and the size of the contact zone was estimated. A computational grid was laid out around each principal contact point (Figure 1) and projected on both body surfaces. The computed contact pressures were not very sensitive to the size of the grid.

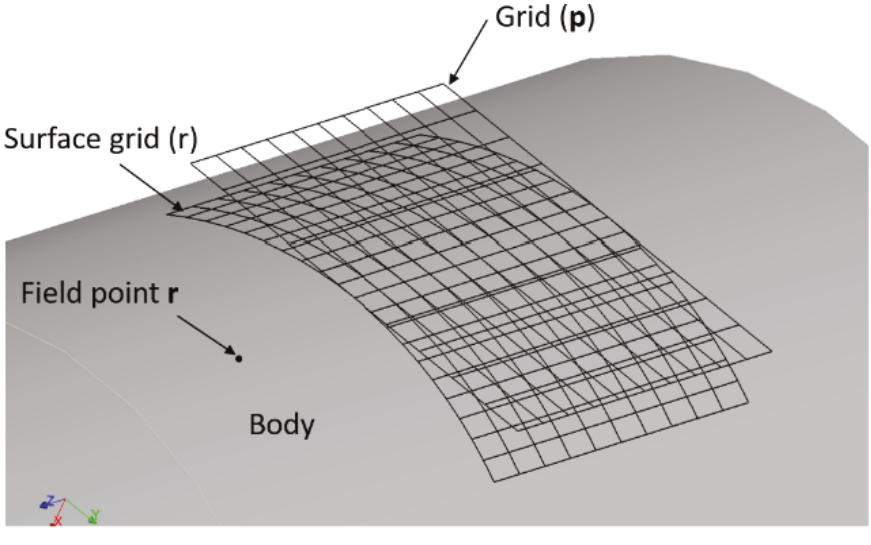

Figure 1. The contacting surface and the computational grid.

The displacement $u(\mathbf{r}_{ij}; \mathbf{r})$ of a field point $\mathbf{r}$ due to a load at the surface grid point $\mathbf{r}_{ij}$ can be expressed as:

$$u(\mathbf{r}_{ij}; \mathbf{r}) = [u(\mathbf{r}_{ij}; \mathbf{r}) - u(\mathbf{r}_{ij}; \mathbf{q})] + u(\mathbf{r}_{ij}; \mathbf{q}) \quad (1)$$

where **q** is a point inside the solid body, sufficiently far from the surface (Figure 2). The term [u($\mathbf{r}_{ij}$; **r**) and u($\mathbf{r}_{ij}$; q)] was evaluated using the surface integral approach, and u($\mathbf{r}_{ij}$; **q**), was obtained from FE.

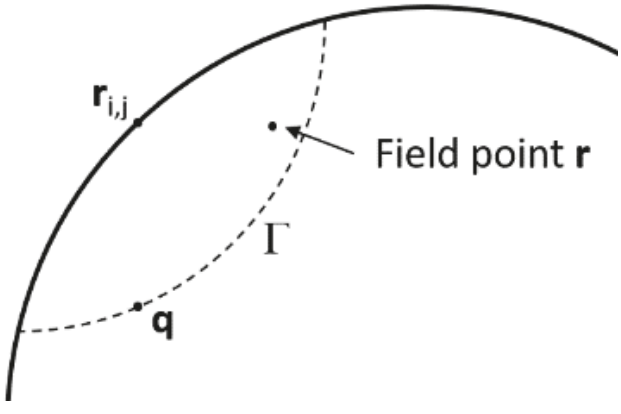

Figure 2. The matching interface Γ.

The term between square brackets represents the deflection of **r** with respect to the point **q**. This relative component can be better estimated using the Bousinesq half space solution (Prueter et al. 2011) rather than using the FE results. The deformation of the body will, in fact, not significantly affect this term. On the other hand, if **q** is far enough from the surface, the term u($\mathbf{r}_{ij}$; **q**) is not significantly affected by local stresses at the surface. u(r_{ij}; **q**) is better estimated from the FE model of the solid body. The location of **q** is called the "matching" point. In order to match the surface integral and FE solution, a set of points Γ can be used instead of a single point q (Figure 2) [14]. Additional details are given in (Parker et al. 2000).

2.2. Application Scenario

2.2.1. The Back-to-Back Test Rig

To be able to validate the presented approach, a back-to-back test rig was used as reference (Figure 3). It consisted of 2 parallel axes gearboxes connected by means of two shafts in a closed mechanical loop. The slave- (better called service-) and test-gearboxes had the same gear ratio (17/18) but a different number of teeth (34/36 and 17/18 respectively). The slave reduction had helical gears, while the gears of the test one were spur. A rotating hydraulic actuator was used to preload the system. An e-motor connected to the main shaft supplied the power that was dissipated in terms of losses during operation.

While this approach has already proven to be very computationally efficient, by substituting the bearings with equivalent springs, the stiffness of which was calculated with separate simulations, the computational effort could be further reduced, and plenty of simulations could be performed in a reasonable amount of time. In fact, in the past the authors have modeled the same configuration by means of traditional FE software. The time required for the solution of a single time step on 115GFLOPS hardware was about 30 h. With the present approach, the simulation of the same gearbox performed, in the same amount of time and on the same hardware, about 700 time-steps. The substitution of the bearings with equivalent springs (Figure 4) further doubled the number of time-steps that could be computed in the same amount of time.

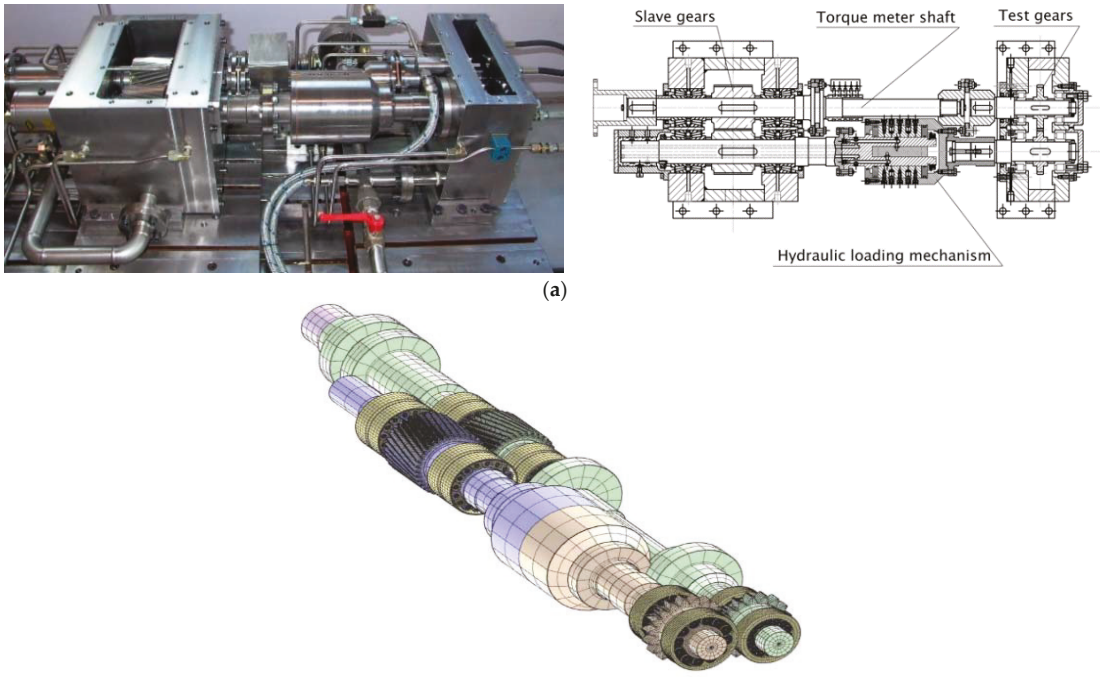

Figure 3. (**a**) Layout of the back-to-back system; (**b**) numerical model.

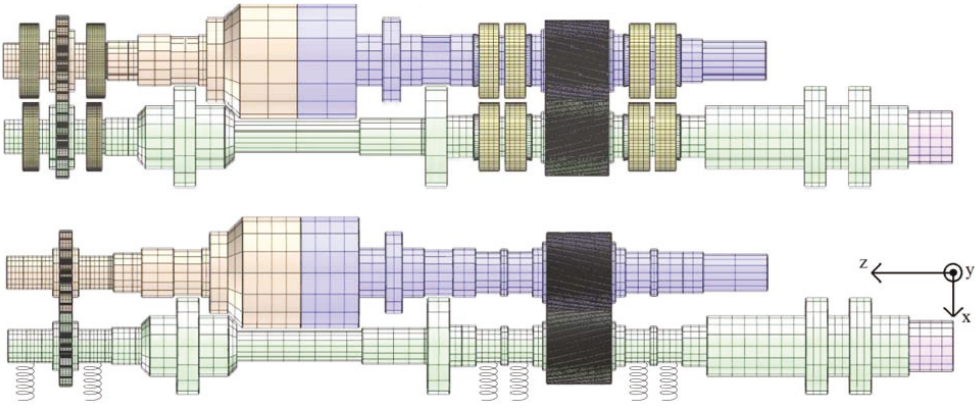

Figure 4. Simplification of the model.

The stiffness of a bearing is a function of the applied load. Considering an applied load of 300 Nm on the long shaft, the stiffnesses of the ball bearings of the test gearbox (left in Figure 4), resulted in 0.77 kN/m (left bearing) and 0.86 kN/m (right bearing). For the 4 supports of the longer shaft of the slave gearbox, the stiffness results, starting from the right side, were 2.46 kN/m, 0.82 kN/m, 1.71 kN/m, and 0.03 kN/m; while the 4 bearings of the shortest shaft showed values of 0.01 kN/m, 2.22 kN/m, 1.11 kN/m, and 3.39 kN/m. The different values of stiffness that similar bearings showed when mounted on different shafts and/or on different axial positions, was related to how the total load transmitted by

the mating gears was shared among the supports. This effect was more evident for the slave gearbox, in which the helical gears also promoted an axial loading with opposite directions on the two shafts. While one of two adjacent bearings was always higher-loaded and, consequently, its stiffness was higher, from the extracted values it can be clearly observed that, while in the longer shaft, the force flowed from the gears mainly to the left end of the shaft, in the shorter shaft, it was transmitted to the housing mainly by means of the right bearings. By inverting the rotational speed, for instance, the stiffness values changed.

Considering that the dynamic analysis is aimed at extracting the displacements (and after a double integration also the vibrations) of the model at a certain regime, the time discretization (sampling) must be selected accurately. On one hand, the time discretization should be enough dense to avoid aliasing phenomena, while on the other hand, it should be kept as large as possible to limit the computational effort.

The factors that affect the time-step to be selected are the rotational speed, the number of teeth, the number of meshing pairs, the number of harmonics to be considered, and the desired number of time-steps for each meshing period. The latter strongly defines the resolution of the analysis. To determine the sampling time, the gear-meshing frequencies (GMFs) of the two pairs must be calculated:

$$GMF = \frac{z_{min} \cdot n_{min}}{2\pi} \quad (2)$$

where z is the number of teeth and n is the rotational speed. For the 2 gearboxes of the back-to-back test rig, the 2 GMFs resulted, for a 3000 rpm rotational speed of the e-motor, in frequencies of 850 and 1700 Hz. To have a time resolution capable to model the first 5 harmonics of the highest meshing frequency, a time step of 0.000117 s was selected. Moreover, in order to simulate the engagement between two gear teeth in at least 9 different positions (the meshing stiffness is a function of the position of the contact along the tooth's flank), the final time step for the simulation was chosen to be 0.000013 s. A total of 3600 time steps were simulated, corresponding to 30 meshing periods. Most of these were subjected to the transient start-up and were excluded from the analysis, which focuses on the steady-state condition only.

2.2.2. Experimental Validation

To validate the results of this hybrid approach, some experimental measurements were performed on the real back-to-back test rig. The two gear-meshing frequencies—850 Hz (meshing frequency of the test gears) and 1700 Hz (meshing frequency of the slave gears)—were clearly visible in the measurements (Figure 5). Other peaks corresponding to 2550 Hz, 3400 Hz, 4250 Hz etc. were the harmonics of the GMFs. The agreement between the predicted and measured frequencies was good; the amplitudes differed, but it must be considered that the damping factors introduced in the model were not calibrated—the goal was to predict the frequencies only.

The lowest frequency was an eigenfrequency of the system. The numerical value results were higher since the inertia of the e-motor was neglected.

2.3. Modeling of Damages—Surface Fatigue (Pitting)

One of the most important damages that occurs in gears and that has a progressive evolution that can be monitored by means of SHM is surface fatigue; namely, pitting. This phenomenon is generated in the contact regions where the Hertzian pressure distribution generates very high shear stresses just under the surface. These local shear-stress peaks can, especially in presence of microdefects or subsuperficial inclusions, promote the nucleation of microcracks. These, with repeated loading cycles, propagate up to the surface, causing the detachment of small portions of material, called pits (Figure 6).

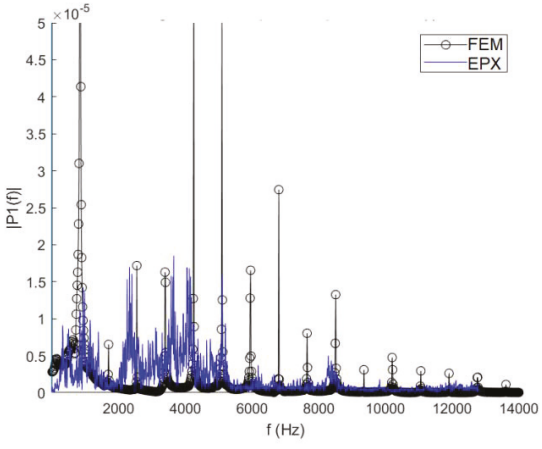

FEM [Hz]	EXP [Hz]	Δ
678	580	14,5%
851	850	0,1%
1702	1700	0,1%
2553	2550	0,1%
3404	3400	0,1%
4225	4250	-0,6%
5106	5100	0,1%
5945	5950	-0,1%
6796	6800	-0,1%
…	…	…

Figure 5. Comparison between the numerical and experimental data for the back-to-back test rig (housing).

Figure 6. Example of pitting.

While the initial stage leads to vibrations and noise only, with the progression of the damage, more and more pits are generated. The coalescence of multiple pits leads to the formation of big cavities on the surface. This phenomenon, once initiated, is accelerated by the presence of the lubricant that, during the contact, is pumped inside the cracks, promoting their propagation. The presence of cavities on the surfaces is in turn responsible for a nonhomogeneous distribution of the contact pressures on the surfaces (because, in correspondence with the pits, the surfaces are not in contact). Consequently, highly loaded areas generate promotion of an acceleration of the damage evolution. Finally, when the damage reaches a certain value, a complete failure of the system is also possible.

In the present work, the presence of damage on the surface was modeled by selecting the position (radial and tangential coordinates S and T) on the teeth flank (Figure 7), the main diameters of the pits (intended as an ellipse), and their depths.

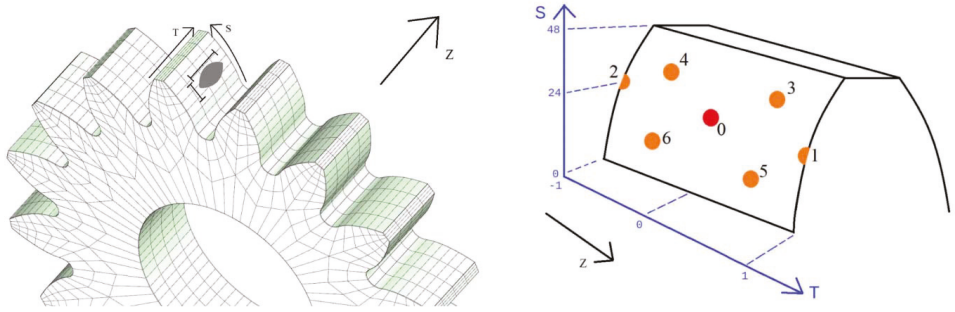

(**a**) (**b**)

Figure 7. (**a**) Representation of a pit on the face of a tooth; (**b**) position indexes. S is the radial reference axis and T is the axial one.

Table 1 reports the different conditions that were simulated. In addition to the healthy condition, 7 damages (PitX) were chosen. Their dimensions varied, as shown in Table 1. Moreover, these 7 damage severities were modeled in different positions on the flank (position indexes shown in Table 1). A total of 40 transient simulations were performed.

Table 1. Simulated pit parameters, positions indexes, and simulations performed.

Code	Radial Dimension [mm]	Axial Dimension [mm]	Depth [mm]	Position Index	Radial Position [mm]	Axial Position [mm]
Healthy	0	0	0	0	24	0
PitA	1	2	0.5	1	24	1
PitB	2	5	1	2	24	−1
PitC	2.5	7	1	3	36	0.5
PitD	3	8	2	4	36	−0.5
PitE	3.5	9	2	5	12	0.5
PitF	5	10	1	6	12	−0.5
PitG	20	14	3			

Position Index (PI)	PitA	PitB	PitC	PitD	PitE	PitF	PitG
0	✓	✓	✓	✓	✓	✓	✓
1	x	x	x	x	x	✓	✓
2	x	x	x	x	x	✓	✓
3	✓	✓	✓	✓	✓	✓	✓
4	✓	✓	✓	✓	✓	✓	✓
5	✓	✓	✓	✓	✓	✓	✓
6	✓	✓	✓	✓	✓	✓	✓

Figure 8 clearly shows the effect of the presence of a pit on the pressure distribution in the contact. While the stresses were zero due to the missing contact in correspondence with the damage, in the surrounding region, stress peaks were generated.

While the vibrational spectrum already had a characteristic frequency related to the GMF (which is also the main source of excitation), the presence of a pit on a single tooth promoted the excitation of an additional frequency (1/n), where n is the rotational speed (Figure 9). The vibrational spectra were obtained with a double derivative of the displacement data obtained from the simulations.

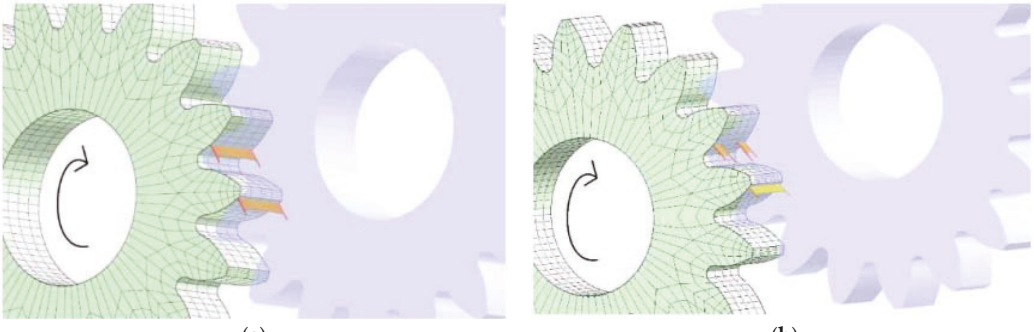

(**a**) (**b**)

Figure 8. Pressure profile on the meshing gears of the testing gearbox: (**a**) nonpitted spur gears; (**b**) pitted (PitF) spur gears.

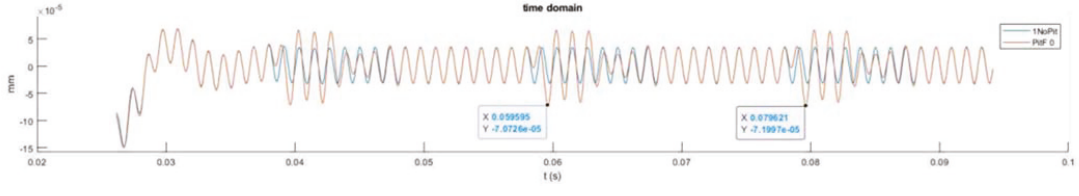

Figure 9. Comparison of the vibrational spectra on one bearing between the healthy transmission and the damaged one (time domain).

The abovementioned effect can be better visualized in the frequency domain. Therefore, the vibrational spectra in terms of accelerations were converted via fast Fourier transformations (FFTs) (Figure 10).

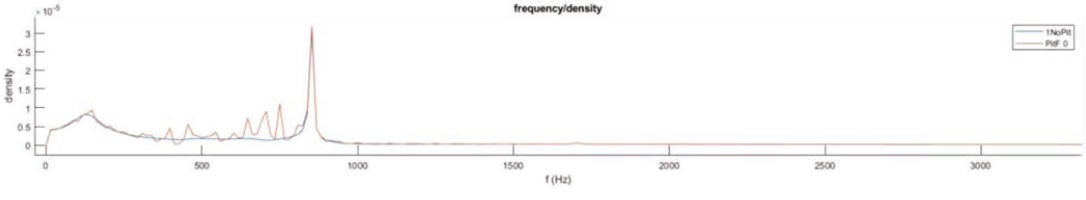

Figure 10. Comparison of the vibrational spectra on one bearing between the healthy transmission and the damaged one (frequency domain).

2.4. Spectral Analysis

As Figures 9 and 10 show, the spectra of the damaged conditions differed from the spectra of the healthy one, mainly in the excitation of new frequencies below the GMF. In order to better visualize this effect, Figure 11 shows the differential spectra of the damaged gearbox (damaged minus healthy) for different pitting severities (A to F). The increase of the vibration amplitude at certain frequencies with the increasing level of damage was evident.

On the other hand, Figure 12 shows the spectra predicted for damage level D and different positions on the flank (PI 3, 4, 5, and 6).

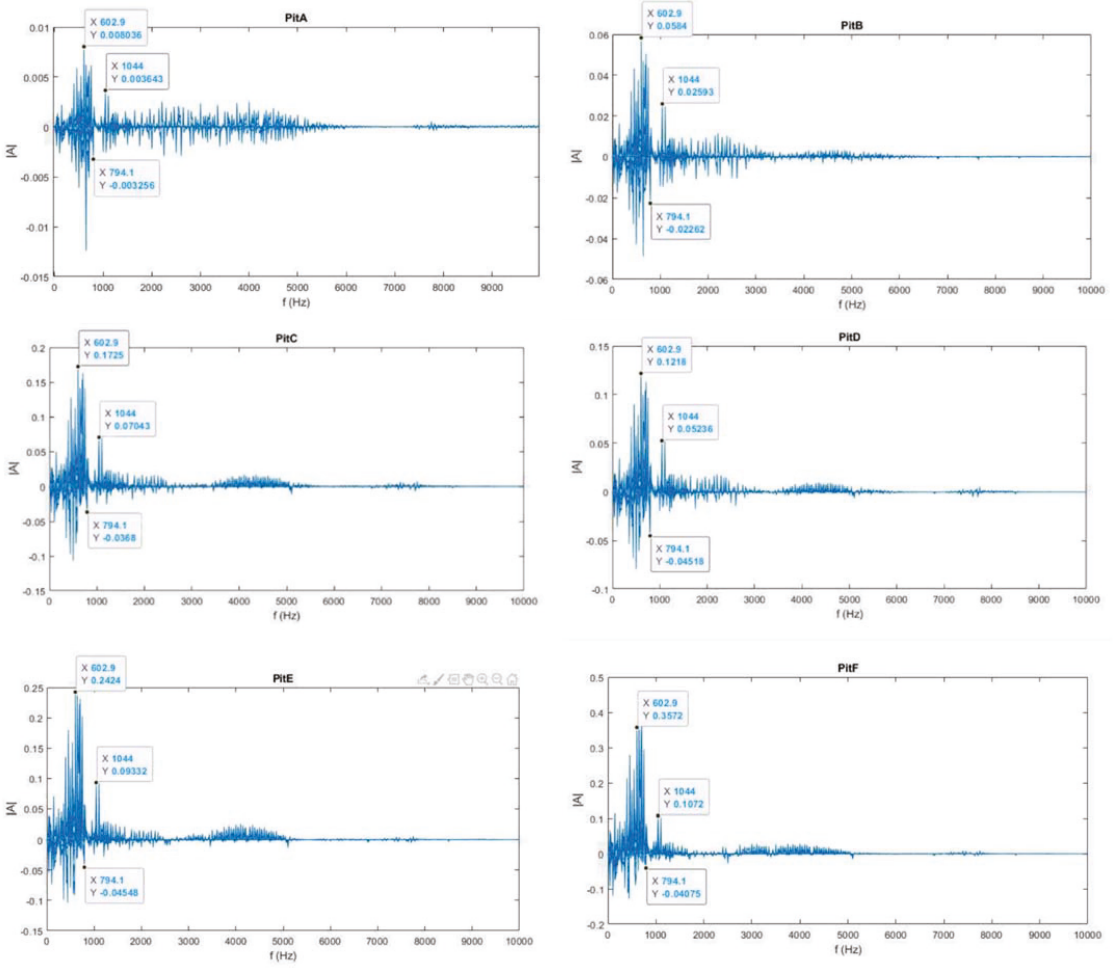

Figure 11. Differential spectra for different damage levels.

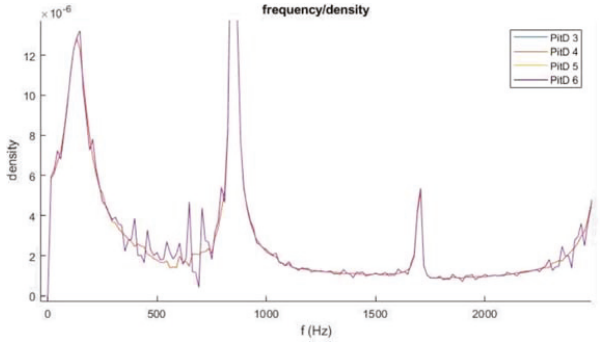

Figure 12. Spectra for damage level D and different positions on the flank.

Positions 3 (having coordinates S = 36 and T = 0.5) and 4 (S = 36, T = −0.5) had the same radial coordinate (S = 36) but different axial coordinates (they lay on opposite sides of the flank). The two spectra were very similar and overlapped, as shown in Figure 12. The same could be observed for the spectra of positions 5 (S = 12, T = 0.5) and 6 (S = 12, T = −0.5). Therefore, it can be concluded that the data were not significantly affected by the axial position.

On the contrary, positions 4 (S = 36, T = −0.5) and 6 (S = 12, T = −0.5) differed in the radial coordinate only. The impact of the radial position was visible in the spectra (Figure 12). The same effect could be observed between position 3 (S = 36, T = 0.5) and 5 (S = 12, T = 0.5).

Moreover, the smaller pit with code A did not produce meaningful differential spectra. In other words, the impact of such small pits on the vibration could not be captured by the numerical model.

3. Basics for Implementation of the Machine-Learning Algorithm

A machine-learning (ML) approach based on artificial neural networks (ANNs) was used in this study for damage identification, and to solve the inverse problem of correlating some input features extracted from the observed signals with some damage parameters, including (i) a binary variable for damage detection, (ii) damage coordinates for localization, and (iii) damage extent for its assessment. In particular, the ANN used here was the Multilayer perceptron (MLP), consisting of a collection of connected nodes; namely, the input layer nodes, the hidden layer nodes, and the output nodes. In this work, the input nodes collected the input vector x, including the frequency pattern of the FFT of the vibration signal, one hidden layer is used for computation, and the output vector y included either a binary variable (for damage detection) or continuous variables for damage localization and quantification.

The general structure for the MLP is schematized in Figure 13. Each node i was connected to each node j in the preceding and the following layers through a connection of weights. Signals passed through each node as follows: in layer k (hidden layer), a weighted sum was performed at each node i of all the signals from the preceding layer, giving the excitation of the node; this was then passed through a nonlinear activation function f to emerge as the output node to the next layer; the activation function f in this case was restricted to $f(x) = tanh(x)$. One node of the network, the bias node b, was special in that it was connected to all other nodes in the hidden and output layers; the output of the bias node was held fixed throughout to allow constant offsets in the excitations of each node. The response of node i is reported in Equation (3):

$$x_i^k = f\left(z_i^k\right) = f\left(\sum_j w_{ij}^k * x_j^{k-1} + b_j^{k-1}\right) \quad (3)$$

Finally, after combination of the outputs from each node in the hidden layer, the output-unit activation function generated the output values x_1^O. Here, a sigmoidal activation function was used for damage detection, which was posed as a classification problem, and a linear activation function was considered for damage localization and quantification, which were posed as a regression problem in this work.

The first stage of using a network to model an input–output system is to establish the appropriate values for the connection weights and biases. This is the training (or learning) phase. The type of training adopted here was a form of supervised learning and made use of a set of network inputs for which the desired network outputs were known. Note that in this specific application, the examples used for training were generated based on the simulation previously described. At each training step, a set of inputs was passed forward through the network, yielding trial outputs that could be compared with the desired outputs. If the comparison error was considered small enough, the weights were not adjusted. If, however, a significant error was obtained, the error was passed backwards

through the net and a training algorithm used the error to adjust the connection weights. The networks used for this study were designed and trained using MATLAB code.

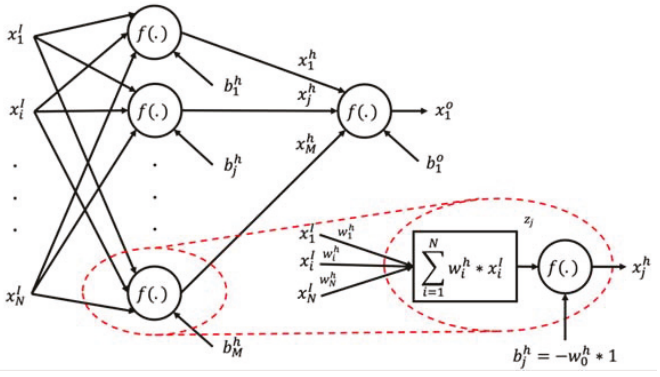

Figure 13. MLP structure.

However, to guarantee a sufficient capability of the algorithm trained on some examples to generalize well on new experimental signals was a non-trivial task. A procedure suitable for the optimization of the ANN structure and the evaluation of its performances in terms of damage diagnosis was used, including cross-validation techniques with an early-stopping criterion [15], thus avoiding data overfitting, even in presence of a limited number of examples. For cross-validation, the available dataset was split into three subsets; namely, for training, validation, and testing of the ANN structure, with proportions of 70%, 15%, and 15%, respectively, with the latter allowing us to verify the ANN prediction performance on new data.

3.1. Reduction of Input-Space Dimension

In a model-based scenario, one might want to reduce the number of simulations to a minimum, especially if multiple damage parameters are considered, as the computational burden might hamper the feasibility of the SHM system design. However, there would normally be issues of generalization if a training set that is too small is adopted. For example, the current wisdom in the ANN field demands that there usually be 10 training patterns per weight [15], although this requirement can be relaxed if some technique for ANN regularization is used, as in this study. In a vibration-based SHM, if the entire frequency pattern in the FFT is passed as input to the ANN, this will sensibly grow the input space dimension, thus the ANN parameters to be tuned and, as a consequence, the number of required examples for training. Thus, one might be interested in reducing the input-space dimension, which can be accomplished through principal component analysis (PCA), one of the most commonly used feature-extraction techniques. It was chosen because it is easy and fast to compute, and it retains maximal information among all linear projections [16]. Due to the widespread knowledge of the method, only its application will be described hereafter.

The PCA allows for dimensionality reduction by using the covariance matrix of the dataset to rotate the reference system and to obtain a more efficient data description. An example is presented in Figure 14, where a rotation of the reference system from (X, Y) to (X_1, Y_1) allows describing the dataset by using the new variable X_1 only, thus reducing the dataset dimensionality from 2 to 1.

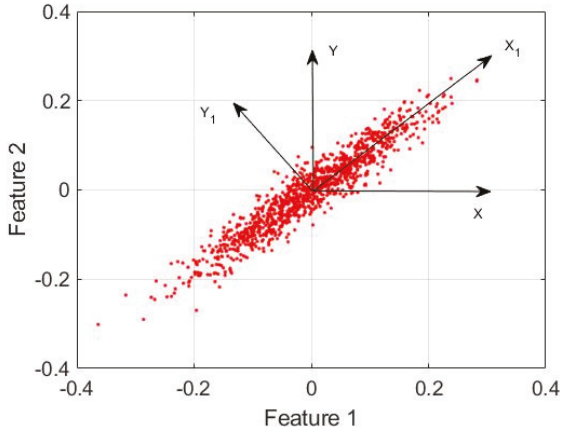

Figure 14. Example of PCA in $\mathbb{R}^2$.

In general, after calculating the covariance matrix of the input dataset, its eigenvectors are the principal components (PC), and their associated eigenvalues λ_i are an index of the amount of variance retained by any *i*th component. It is usual to list the PCs in descending order of eigenvalues, so that the first PC corresponds to the largest variance of any linear combination of the original variables. A useful heuristic method to reduce input space dimension is to plot singular values to see if there is a point at which the values level off, or to select the first M components so that a fraction of the total variance will be retained [16], calculated as follows:

$$\frac{\sum_{i=1}^{M} \lambda_i}{\sum_{i=1}^{d} \lambda_i} \tag{4}$$

where d and M are the original and the reduced-input space dimensions, respectively. In particular, the new input matrix is obtained by multiplication of the original input matrix by the matrix containing the first M eigenvectors.

3.2. Noise Modeling

A crucial aspect to be considered while training either a machine-learning classifier or regressor is to guarantee sufficient algorithm generalization, meaning a good performance on new data never seen during training. In this respect, one drawback of model-based training is the lack of noise and disturbances typical of real operative scenarios. It can be shown that an ANN trained with a noise-free signal will perform poorly when requested to classify a new sample acquired in noisy conditions, especially if no control against overfitting is taken. Thus, in addition to other regularization techniques such as cross-validation and early stopping, which limit the overfitting, superposition of noise during training is seen as a further means to improve generalization [15]. For this reason, the training dataset was modified by adding the effect of noise on the FFT of the vibration signals.

To superpose the effects of noise on the numerical FFT, an acquisition from the previously presented bench test was used (Figure 15a), specifically extracting the FFT peaks from 10 kHz to 13 kHz. The probability distribution function (PDF) of the peak amplitudes in the considered frequency range is presented in Figure 15b, where its approximation through a log-normal distribution is highlighted, with parameters reported in Table 2. The training dataset was thus artificially modified by adding a value sampled from the noise PDF to each FFT feature and for each sample, assuming the noise level was approximated as constant in the whole frequency range [0–13 kHz]. An example of FFT with added noise is presented in Figure 16.

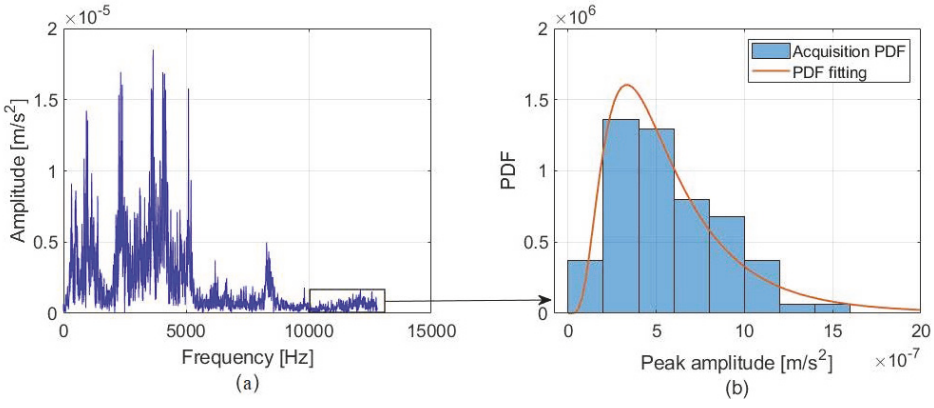

Figure 15. (**a**) FFT of vibration signal measured on the test bench and (**b**) PDF of the peaks in the range of 10–13 kHz.

Table 2. Lognormal distribution parameters.

Parameter Name	Parameter Value	Units
μ_{log}	−14.5345	$\left[\log\left(\frac{m}{s^2}\right)\right]$
σ^2_{log}	0.6171	$\left[\log\left(\frac{m}{s^2}\right)\right]^2$

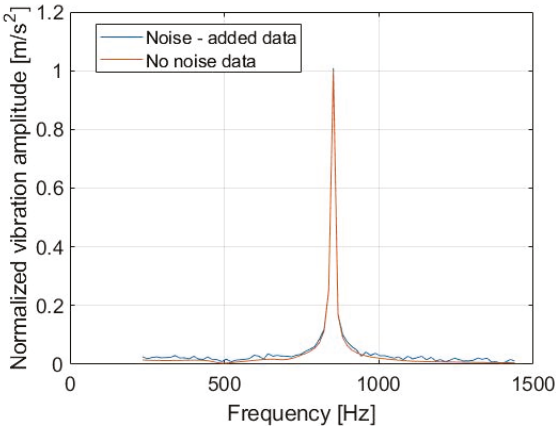

Figure 16. Example of noise-free signal and noise-added signal.

3.3. Damage-Identification Results

The procedure for ANN design and testing results are presented in this section. As shown in Figure 17, the damage identification inverse problem was subdivided into a three-step hierarchical structure, calling three separate ANNs to perform damage detection, localization, and quantification. The first ANN was used to classify whether damage was present or not; if damage was detected, two additional ANN regressors assessed the radial position and extent of the damage.

During training, the ANNs used the FFT of the vibration signal simulated by the FEM as an input. The training set was composed of signals affected by pit damages that varied in terms of their radial position and extent, with the latter expressed in terms of a normalized equivalent pitted area, as reported in Table 3. Specifically, the input was limited

by the FFT in the frequency range of 235 Hz to 1440 Hz. A PCA routine was implemented before the classification and regression ANNs to project their input space in order to reduce the input-space dimensionality and, consequently, the number of ANN parameters to be optimized.

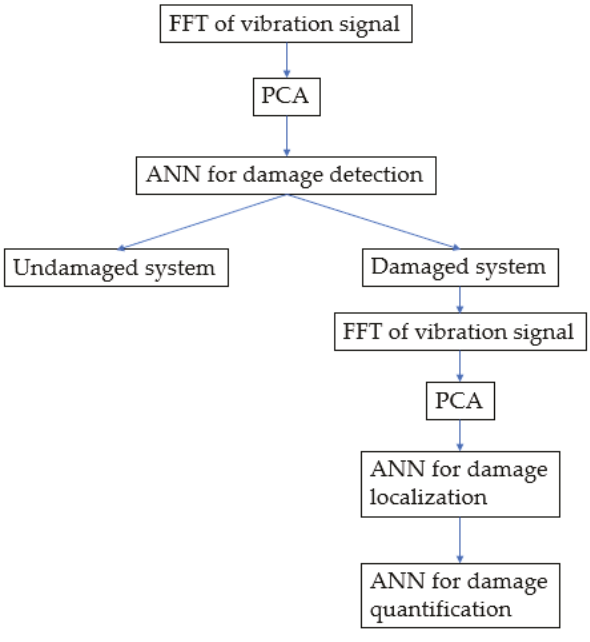

Figure 17. SHM architecture.

Table 3. Training dataset composition.

	Range of Values	Units of Measure
Damage radial position	[12 24 36]	mm
Damage entity	[0 0.2 0.35 0.48 0.63 1]	Equivalent pitted area

3.3.1. Damage Detection

The dataset organized in Table 4 was used for training the detection ANN; it was composed of 560 observation samples, including 81 features each. The FFT in the dataset were affected by damages that varied in terms of position and dimension. Note that 280 examples of the same undamaged condition were sampled from the noise PDF in order to produce a balanced database.

The PCA was applied to reduce the input-space dimensionality, thus allowing a more efficient ANN training. In Figure 18, the variance associated with each principal component of the detection dataset is presented, in which it is possible to see, by considering only the first 10 principal components, that it was possible to consider 99% of the total variance included in the dataset. As an example, six FFTs observed in presence of different damage extents were compared with their PCA reconstructions in Figure 19, specifically including just 10 out of 81 principal components. It is clear that a negligible error was made when considering the reduced input space when including the first 10 principal components only.

Table 4. Training-set composition for damage detection.

# Observations	Equivalent Pitted Area	Classification
280	0	Undamaged
56	0.2	Damaged
56	0.35	Damaged
56	0.48	Damaged
56	0.63	Damaged
56	1	Damaged

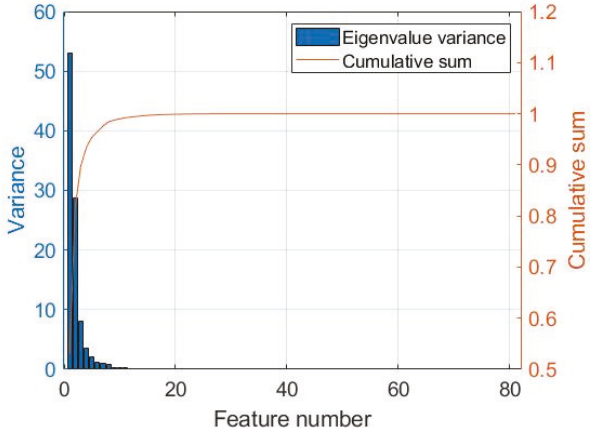

Figure 18. Variance associated with each feature after PCA on the detection dataset and cumulative sum.

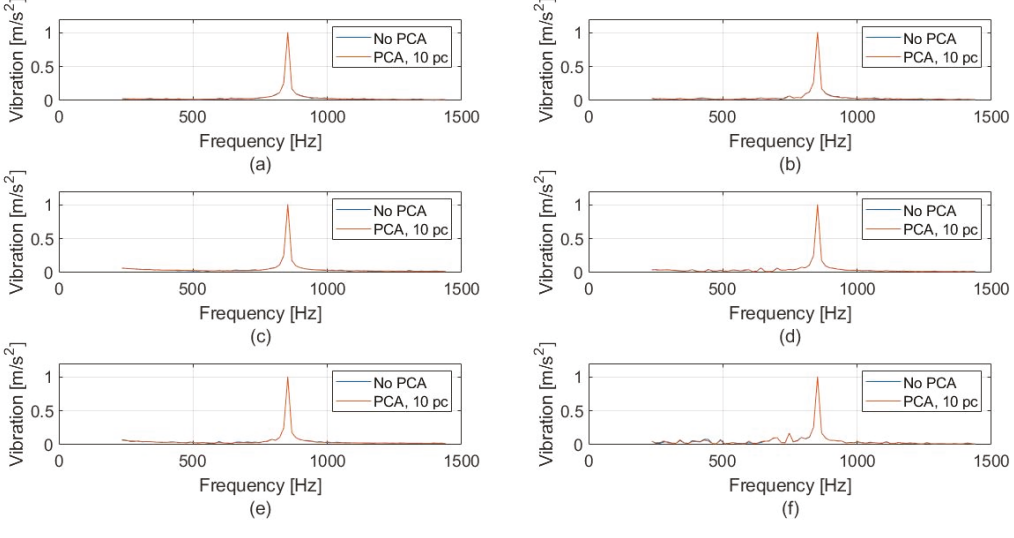

Figure 19. A comparison among the original FFT and the reconstructed FFT with 10 principal components: (**a**) Undamaged, (**b**) damage = 0.2, (**c**) damage = 0.35, (**d**) damage = 0.48, (**e**) damage = 0.63, (**f**) damage = 1.

The classification ANN architecture included 10 input nodes, one binary output node, and 20 hidden nodes, with the latter defined based on trial-and-error procedure; however, as a compromise was made between training accuracy and generalization performance on test data never seen during training, to avoid overfitting. The ANN performances were synthetized with confusion matrices as shown in Figure 20, in which the similar performances in the training, validation, and test sets suggest the ANN possessed a high generalization capability, and no overfitting error occurred. Overall, less than 10% of misclassified examples were obtained.

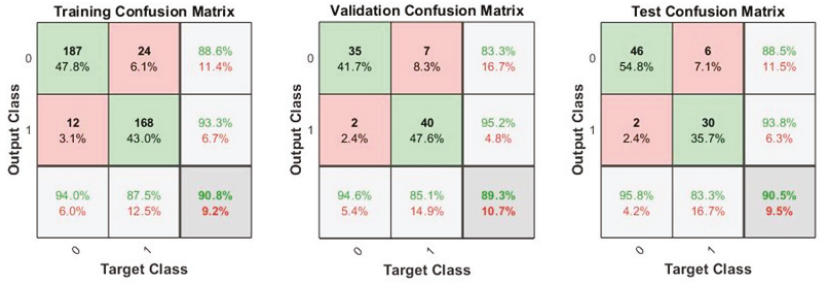

Figure 20. Detection ANN performances. Results are provided for the training, validation, and test subsets.

Since the detection performance was tested in the presence of damages of increasing extent, thus with different influences on the simulated signal, it was interesting to verify the detection performance (in terms of the number of misclassified samples) as a function of the damage dimension. It is clear from Table 5 that the probability for missed detection reasonably increased for smaller damages, while the detection performance improved with increasing damage entity.

Table 5. Detailed detection ANN performance.

Equivalent Pitted Area	# Errors	Type
0	16/280	False alarm
0.2	20/56	Missed detection
0.35	13/56	Missed detection
0.48	4/56	Missed detection
0.63	0/56	Missed detection
1	0/56	Missed detection

3.3.2. Damage Localization

The dataset in Table 6 was used for localization ANN training; it was composed of 276 observation samples, including 81 features each. Also in this context, the PCA could be used to reduce the dataset dimensionality. It can be noticed in Figure 21 that more than 95% of the information within the signals was captured by considering the first 20 principal components of the dataset only.

Table 6. Training-set composition for damage localization.

# Observations	Damage Radial Position	Units of Measure
92	12	mm
92	24	mm
92	36	mm

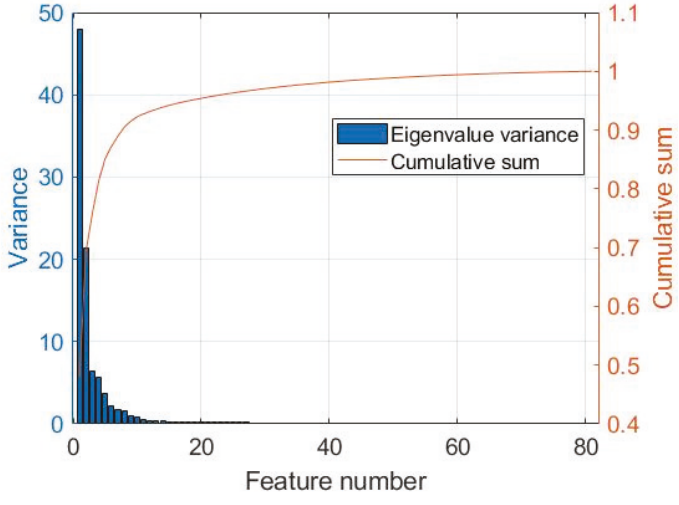

Figure 21. Variance associated with each feature after PCA on the localization dataset.

Thus, the first 20 principal components of the dataset were used to train the regression ANN for damage localization. The network architecture included 20 input nodes, one output node describing the radial position of the damage as a continuous variable, and 10 hidden nodes, again defined in a way to avoid overfitting. The ANN performances are presented in Figure 22, in which the training, validation, and test regression plots are shown. As the increasing trend was correctly captured by the ANN in all the subsets, it was possible to conclude that the algorithm could generalize on new data, and no overfitting occurred. It is worth noticing that the entire dataset was processed by the algorithm in Figure 22a–c, including small damages with reduced sensitivity.

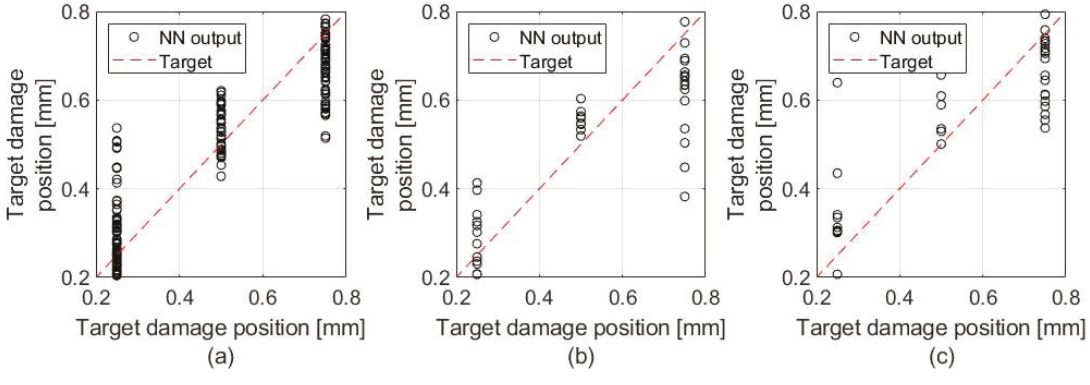

Figure 22. Localization ANN performances for the (**a**) training, (**b**) validation, and (**c**) test subsets (entire database).

3.3.3. Damage Quantification

The same database used for localization was considered for damage quantification, specifically organized as in Table 7, in view of data regression as a function of the damage extent. For this reason, the same conclusions could be drawn on the application of PCA, resulting in a reduction of the input space from $\mathbb{R}^{81}$ to $\mathbb{R}^{20}$. The regression ANN architecture included 21 input nodes, one output node describing the equivalent pitted area as a continuous variable, and 10 hidden nodes, again defined in a way to avoid overfitting.

Focusing on the input layer, it included the first 20 PCA of the FFT calculated from the signal database, and one additional node collecting the damage location estimated by the previous diagnostic layer.

Table 7. Training-set composition for damage quantification.

# Observations	Equivalent Pitted Area
55	0.2
55	0.35
55	0.48
55	0.63
55	1

The ANN performances are presented in Figure 23. Specifically, Figure 23a–c show the training, validation, and test regression plots, while the correct damage location was passed as input to the network, verifying the correct data synthesis during algorithm training. However, while using the algorithm in a realistic scenario, one might argue that an erratic location can be provided as input to the algorithm, based on the performance of the localization ANN. For this reason, the quantification ANN was also tested while receiving as input the position estimation in Figure 22c, affected by errors, and results are shown in Figure 23d for the test subset only. When comparing Figure 23d with the corresponding Figure 23c, a reduction in algorithm precision was noticed, although the ANN could capture the trend with marked accuracy, demonstrating its potential for application in a realistic scenario.

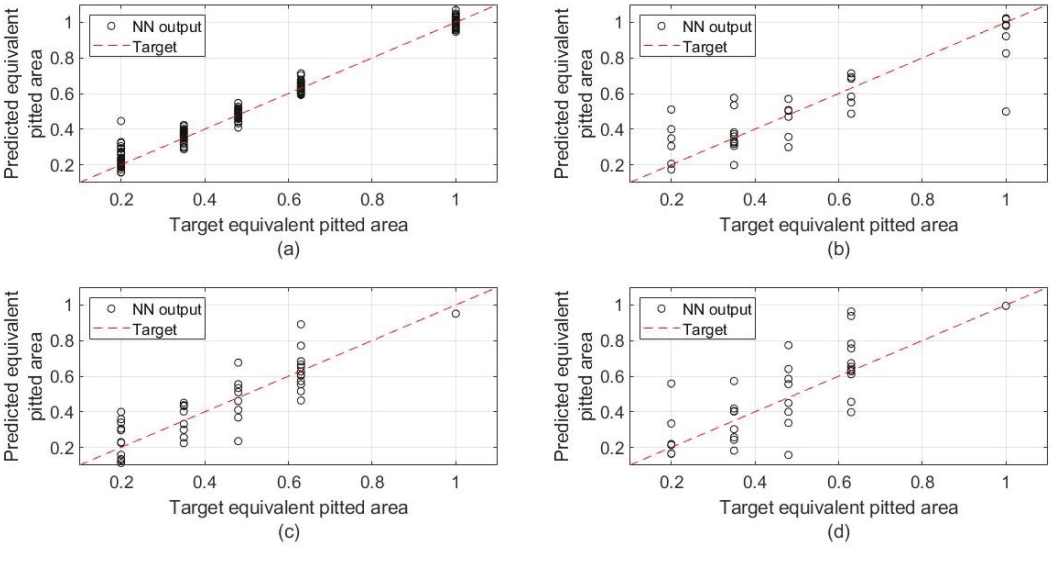

Figure 23. Quantification ANN performances: (**a**) training, (**b**) validation, (**c**) test with the correct damage location as input, and (**d**) test with the estimated damage location as input.

4. Conclusions

A model-based approach to condition monitoring of gearbox transmissions was presented in this study, leveraging on a hybrid analytical–numerical model for the generation of signal examples to be used for algorithm training. The approach was applied to a

back-to-back test rig, and experimental data in normal conditions were used to validate the baseline model and to extract realistic noise components to be superposed on numerically simulated signals. After a feature-extraction module used principal component analysis to project data in a more compact space dimension, these were passed as input to a hierarchical structure of artificial neural networks. A classification ANN was used for detection of pitting damage positioned on the teeth flank, intuitively manifesting better performances when signals in the presence of larger damages were processed. After damage was detected, two regression ANNs were used to correlate the variations of the signal FFT with the radial position of the damage and its severity. Specifically, it was found that an improved performance of the damage assessment algorithm was obtained while the information about damage position, estimated by the localization ANN, was passed to the network through an additional input node.

The algorithm performances were assessed at each level of the damage-identification hierarchy, and demonstrated to be extremely satisfactory, given the limited amount of simulations used to construct the training database, even in the presence of a realistic noise corrupting the ideal simulated data. Augmented accuracy and precision of the algorithm output was expected by increasing the density of the damage entity and position grids. However, considering the aim of this paper was to show the consistency of the approach, the adopted number of simulations was considered sufficient at this stage. Although the methodology described herein remains valid for any test configuration, it must be specified that the results obtained throughout this project were consistent and valid only for this bench test, since the digital model was coherent only with it, while a new database must be created for each examined scenario.

A final note must be made regarding the future developments of the project. It could be expanded by adding different damages to the simulation database; for example, including fatigue damage at the root of different teeth, or analyzing the effect of multiple simultaneous damages. However, while the combinations are endless, a perfectly tuned condition-monitoring system could be built only by investing a great amount of computational effort.

Author Contributions: F.C. followed the development of the rig, performed the experimental tests and the FEM analyses, and wrote the paper; C.S. and L.P. post-processed the results via ANN and wrote the paper. All authors have read and agreed to the published version of the manuscript.

Funding: This work is based on the project RTD 2018—SMOG, Structural health monitoring of mechanical gearboxes, funded by the Free University of Bozen-Bolzano (PI: Franco Concli) and supported by Politecnico di Milano. This work also was supported by the Open Access Publishing Fund of the Free University of Bozen-Bolzano.

Data Availability Statement: The datasets used and/or analyzed during the current study are available from the corresponding author on reasonable request.

Conflicts of Interest: The authors declare that they have no competing interests.

Abbreviations

ANN	Artificial Neural Network
FE	Finite Element
FFT	Fast Fourier Transform
GMF	Gear-Meshing Frequency
ML	Machine Learning
MLP	Multilayer Perceptron
PCA	Principal Component Analysis
PDF	Probability Distribution Function
SHM	Structural Health Monitoring

Nomenclature

q	point inside the solid body
r	field point
$\mathbf{r}_{ij}$	surface grid point
S	radial reference axis
T	axial reference axis
$u(\mathbf{r}_{ij}; \mathbf{r})$	displacement of a field point **r** due to a load at the surface
Γ	set of points

References

1. Salameh, J.P.; Cauet, S.; Etien, E. Gearbox condition monitoring in wind turbines: A review. *Mech. Syst. Signal Process.* **2018**, *111*, 251–264. [CrossRef]
2. Zhao, D.; Cheng, W.; Gao, R.X. Generalized Vold-Kalman Filtering for Nonstationary Compound Faults Feature Extraction of Bearing and Gear. *IEEE Trans. Instrum. Meas.* **2020**, *69*, 401–410. [CrossRef]
3. Cao, X.; Rembe, C. Non-contact damage detection under operational conditions with multipoint laservibrometry. *Sensors* **2020**, *20*, 732. [CrossRef] [PubMed]
4. Kien, B.H. Effect of image size on performance of a plastic gear crack detection system based convolutional neural networks: An experimental study. *Proceed. SPIE Int. Soc. Optic. Eng.* **2020**, *11381*.
5. Ümütlü, R.C.; Hizarci, B.; Ozturk, H.; Kiral, Z. Classification of pitting fault levels in a worm gearbox using vibration visualization and ANN. *Sadhana Acad. Proc. Eng. Sci.* **2020**, *45*, 1–13. [CrossRef]
6. Huang, D.; Hong, L.; Liu, C. Computational technique to free vibration response in a multi-degree of freedom parametric system. *Mech. Syst. Signal Process.* **2020**, *142*, 106777. [CrossRef]
7. Mauricio, A.; Zhou, L.; Mba, D.; Gryllias, K. Vibration based condition monitoring of helicopter gearboxes based on cyclostationary analysis. *J. Eng. Gas Turbines Power* **2019**, *142*, 031010. [CrossRef]
8. Sun, R.; Song, C.; Zhu, C. Computational study of pitting defect influence on mesh stiffness for straight beveloid gear. *Eng. Fail. Anal.* **2021**, *119*, 104971. [CrossRef]
9. Qiu, Y.; Hong, L.; Jiang, X. Experimental study of dynamic strain for gear tooth using fiber Bragg gratings and piezoelectric strain sensors. *Proc. Inst. Mech. Eng. Part C J. Mech. Eng. Sci.* **2017**, *232*, 3992–4003. [CrossRef]
10. Concli, F. Dynamic Modelling Of Gears: An Innovative Hybrid Fem-Analytical Approach. In *WIT Transactions on Engineering Sciences*; Wit Press: Southampton, UK, 2020.
11. Cheng, P.; Wan, D.; Hu, C. Unsteady aerodynamic simulations of floating offshore wind turbines with overset grid technology. In Proceedings of the 26th International Ocean and Polar Engineering Conference, Rhodes, Greece, 26 June–1 July 2016; Wang, A.M., Chung, J.S., KTMM, Eds.; pp. 391–398.
12. Rytter, A. Vibrational Based Inspection of Civil Engineering Structures. Ph.D. Thesis, Aalborg University, Aalborg, Denmark, 1993.
13. Vijayakar, S.M.; Busby, H.R.; Houser, D.R. Linearization of multibody frictional contact problems. *Comput. Struct.* **1988**, *29*, 569–576. [CrossRef]
14. Vijayakar, S. A combined surface integral and finite element solution for a three-dimensional contact problem. *Int. J. Numer. Methods Eng.* **1991**, *31*, 525–545. [CrossRef]
15. Bishop, C.M. *Neural Network for Pattern Recognition*; Oxford University Press: New York, NY, USA, 1995.
16. Nabney, I.T. *NETLAB Algorithms for Pattern Recognition*; Springer: London, UK, 2019.

applied sciences

MDPI

Article

Fast, Accurate, and Reliable Detection of Damage in Aircraft Composites by Advanced Synergistic Infrared Thermography and Phased Array Techniques

Janardhan Padiyar M. [1,*], Luca Zanotti Fragonara [1,*], Ivan Petrunin [1], Joao Raposo [1], Antonios Tsourdos [1], Iain Gray [1], Spyridoyla Farmaki [2], Dimitrios Exarchos [2], Theodore E. Matikas [2] and Konstantinos G. Dassios [2,3,*]

[1] School of Aerospace, Transport and Manufacturing, Cranfield University, Cranfield MK43 0AL, UK; i.petrunin@cranfield.ac.uk (I.P.); j.raposo@cranfield.ac.uk (J.R.); a.tsourdos@cranfield.ac.uk (A.T.); i.gray@cranfield.ac.uk (I.G.)
[2] Department of Materials Science & Engineering, University of Ioannina, 45110 Ioannina, Greece; s.farmaki@uoi.gr (S.F.); d.exarchos@uoi.gr (D.E.); matikas@otenet.gr (T.E.M.)
[3] Department of Chemical Engineering, University of Patras, 26504 Patras, Greece
* Correspondence: m.padiyar@cranfield.ac.uk (J.P.M.); l.zanottifragonara@cranfield.ac.uk (L.Z.F.); kdassios@uoi.gr (K.G.D.)

Featured Application: The synergistic non-destructive method has been developed in the framework of automated inspections of aircraft composite structures.

Abstract: This paper presents an advanced methodology for the detection of damage in aircraft composite materials based on the sensor fusion of two image-based non-destructive evaluation techniques. Both of the techniques, phased-array ultrasonics and infra-red thermography, are benchmarked on an aircraft-grade painted composite material skin panel with stringers. The sensors systems for carrying out the inspections have been developed and miniaturized for being integrated on a vortex-robotic platform inspector, in the framework of a larger research initiative, the Horizon-2020 'CompInnova' project.

Keywords: aircraft composites inspection; NDT; phased array ultrasonic testing; automated inspection; IRT; infrared thermography

Citation: Padiyar M., J.; Zanotti Fragonara, L.; Petrunin, I.; Raposo, J.; Tsourdos, A.; Gray, I.; Farmaki, S.; Exarchos, D.; Matikas, T.E.; Dassios, K.G. Fast, Accurate, and Reliable Detection of Damage in Aircraft Composites by Advanced Synergistic Infrared Thermography and Phased Array Techniques. *Appl. Sci.* **2021**, *11*, 2778. https://doi.org/10.3390/app11062778

Academic Editor: Ana Paula Betencourt Martins Amaro

Received: 21 December 2020
Accepted: 5 February 2021
Published: 19 March 2021

Publisher's Note: MDPI stays neutral with regard to jurisdictional claims in published maps and institutional affiliations.

Copyright: © 2021 by the authors. Licensee MDPI, Basel, Switzerland. This article is an open access article distributed under the terms and conditions of the Creative Commons Attribution (CC BY) license (https://creativecommons.org/licenses/by/4.0/).

1. Introduction

New-generation wide-body civilian aircrafts, such as Dreamliner Boeing 787 and Airbus A350 series, are manufactured from Carbon Fiber Reinforced Polymers (CFRPs) composites at a much higher percentage than compared to narrow-body aircrafts; relevant outer parts include their wing skins and fuselage skins. During aircraft service, thin-walled fuselage and wing skin surfaces are primarily prone to impact damages throughout their lifetime [1]. Impact damages can be caused by different threats, like human-induced defects, such as paint shop-prone tool drop, runway debris, ground hail, in-flight hail, and bird impacts. Impact damages are classified as Barely Visible Impact Damage (BVID) and Visible Impact Damage (VID), which may or may not cause full penetrations. Even though BVID's cause considerable sub-surface damage, the identification of their location is particularly challenging under typical lighting conditions while using conventional manual visual Non-Destructive Testing (NDT) [2]. Nondestructive testing (NDT) methods are currently the most efficient means of aircraft inspection for identifying superficial, or otherwise undetectable by conventional visual inspection, damages and flaws [3]. Damage detection in aircraft is primarily linked to human lives and secondarily to equipment protection; hence, it must be efficient and reliable to the maximum degree possible in eliminating fatal consequences on the structure that can cause massive human life loss. To that end, an extreme effort is continuously invested towards the improvement of

aircraft inspection worthiness and the development of reliable, automated, and synergistic techniques for capturing barely visible damage on aircraft. Currently, manual point-to-point inspection using conventional ultrasonic transducer and line-by-line Phased Array (PA) wheel probe [4] are used as a fundamental quantitative method, as per schedule-based maintenance for in-service inspections of composite skin surfaces. Such inspections are tactical and categorized in A-, C-, and D- checks, depending on the level of detail with respect to the aircraft age, hours in service, and the number of landing/take-off cycles. D-checks are the most thorough, involving a series of extremely detailed inspections of the fuselage skin and wing skin surfaces, requiring a minimum defect detectability of 6×6 mm, and carried out approximately every six years. For an aircraft, like an Airbus A320-200, a D-check can last up to six weeks and cost up to $1.8 million [5]. The automation of in-service NDT inspections can lead to reduced cost, by an increase in the availability of aircraft [6]. Consequently, there is both research and industrial interest in reducing the time and cost of aircraft maintenance, especially during C and D-checks maintenance, which involves detailed NDT inspection. The automation of slower point-to-point ultrasonic inspection has received considerable attention in the oil and gas sectors, for tank and pipe inspection; a substantial number of mature solutions based on magnetic adhesion mobile robots have been suggested. There are only a few automated solutions for in-service inspection of aircraft using conventional ultrasonic transducers, like the MAUS-V system based on Cartesian scanners and flexible tracks with suction pads as adhesion [7–9]. Moreover, the application of these scanners is limited by the length of the scanner arms and it needs to be moved and fixed sequentially to cover a large area, thus increasing the time that is required for inspection.

When compared to the point-to-point inspection method, full-field inspection NDT methods, such as infrared thermography (IRT) and shearography, have the inherent advantage of being non-contact and can scan large areas for defects in composites without the need for couplant agents. In recent years, full-field non-contact IRT has proved to be effective in detecting impact damages in aircraft CFRP composites, while new thermographic methodologies are constantly being improved at both the hardware level and post-processing stages to offer improved defect characterization [10–15]. IRT is rapid, contactless, and accurate, and it allows for automation for minimal operator involvement, hence offering the potential for minimization of human error. It operates on the principle of the thermo-mechanical coupling under the thermoelastic effect, wherein a change in the stress field in the material is related to a change in temperature [16]. Hence, collection and analysis, by passive IRT, of thermal energy dissipated from material under stress, provides information of its internal mechanical state [17]. For stress-free materials with pre-existing internal damages, such as the case of fuselage and wing skin of grounded aircraft undergoing inspection, active thermography is used in order to identify damage by capturing and analyzing the thermal energy dissipated from the surface while it is being thermally excited by an external thermal energy source. Independent of the technique used (active or passive IRT), the severer the damage in the material, the more intense the thermographic fingerprint of the damaged area, which appears on a thermogram as warmer or brighter color than pristine/unaffected areas. IRT is particularly applicable to composite materials, which are currently trending to replace more than 50% of the metallic aircraft fuselage and wing parts [18,19]. The technique has been highly successful in assessing the delamination damage typical of impact incidents that are found in aircraft-grade composites [20,21]. Most importantly, the technique is extremely versatile, as it can operate as stand-alone or complementary to other inspection methods [22,23]. The impact damage detectability of IRT depends on the thickness of the material, shape, dimensions, type of damage, and camera hardware sensitivity [24]. Although few previous studies have investigated combined the IRT and PA methods to characterize impact damages in CFRP composites [25–28], measurements in such studies have been performed with heavy equipment, which is unsuitable for deployment in the field and robotic applications or

related to different engineering domains [29]. Moreover, automated in-service inspection of aircraft using combined PA and IRT methods have received little attention.

The limitations in available IRT techniques restricted their ability to perform fast and, at the same time, reliable quantitative inspections [30]. The recent development of an advanced variant of IRT, termed Pulsed Phase-informed Lock-in Thermography (PPI-LT), lifted this limitation [20]. As a two-step approach, PPI-LT relies on the fast initial assessment of defect presence, by pulsed-phase thermography (PPT) and the subsequent quantitative investigation of the area by lock-in thermography (LT). However, although PPI-LT can be particularly rapid and effective in imaging a wide material area (depending on sensor resolution and the instantaneous field of view-IFOV) from afar in a single acquisition and detecting the presence of defects therein, it is not equally powerful in the accurate quantitative assessment of the defects' full geometrical and dilatational characteristics, under rapid wide-area mode. In other words, although rapid IRT could be used to scan a whole aircraft fuselage for damage in a cost-effective manner, the collected data would not contain sufficient defect sizing and depth profiling information for a reliable repair. Phased Array, on the other hand, is a slower and extremely accurate technique requiring contact-full and coupling; it is particularly powerful in achieving high-resolution three-dimensional (3D) geometrical assessment of superficial and subsurface defects. Although it would not cost-effectively scan a whole aircraft, it could provide extremely detailed information on size, shape, and depth profiling of a defect at a known fixed location.

The present paper reports the development of a novel synergistic strategy for the fast, accurate, and reliable detection, with full geometrical representation of damage in aircraft composites, by the sequential application of PPI-LT and PA. The strategy is suitable for automated inspection of impact damage in composite aircrafts and it consists of two sequential inspection steps: firstly, the entire composite structure of the aircraft is rapidly inspected with a newly-developed state-of-the-art, compact, and powerful IRT module operating under PPI-LT mode with custom control and analysis software (presented in [20]) mounted on a Vortex Robotic (VR)) platform to detect, identify, and mark all of the impact damage locations. In the next step, a newly developed PA module that explained in subsequent section is mounted on the VR platform and high-resolution scanning pursues on locations identified by IRT as a suspect of damage presence, for full dilatational and dimensional characterization of damage. The wheeled robot based on a negative pressure-based actuation method using EDF motors was developed for climbing and traversing over the surface of aircraft [31,32] with an NDT module as a payload. The strategy lifts the current trade-off between speed and reliability of aircraft inspection by utilizing IRT as a fast initial indicator of damage presence, over which thorough inspection by PA may ensue. Hence, by taking advantage of the wide non-contact area and reliability of thermal imaging, it is no more required to scan the complete structure by detailed and time-consuming PA inspection, but only damage-suspect areas. This maximizes the efficiency of the inspection while proving to be highly cost-effective. The strategy and individual VRP-mountable synergistic modules form part of a revolutionary fully automated NDT inspection solution offering an unprecedented reduction of aircraft inspection time and cost and increase of defect detection reliability in commercial aircraft, in the context of an ongoing Future and Emerging Technologies (FET) European Commission Horizon 2020 research project [33,34].

2. Material and Methods

2.1. Description of Materials and Specimens

The benchmarking of the synergistic PLI-LT/PA strategy was performed on aircraft-grade composite of different scales: initially on composite coupons of material UD pre-preg IMS-977-2 having layup of [45/−45/90/0/90/0/90/−45/45] and $[45/-45/90/0/90/0/90/-45/45]_{2s}$ and two flat laminates, and subsequently one curved laminate of same material as coupons and [45/−45/90/0/90/0/90/−45/45] layup. All of the laminates carried artificially BVID inflicted using a gas gun; the coupons carried BVID of variable dimensions due to the varying of the impact energies in an impact drop tower.

A stringer stiffened composite panel representative of the aircraft structure with dimensions of 1250 x 865.5 mm^2 was prepared by stacking carbon-fiber prepreg DeltaTech T800S-150-DT120-35 with the symmetric [45/−45/90/0/90/0/90/−45/45] sequence; T-shape stringer stacking followed a [45/−45/90/0/90/−45/45] sequence was also manufactured. The schematic of Figure 1 presents the skin with attached stringer geometry, dimensions, and layup sequence. A copper-mesh layer was integrated in the stacking sequence to account for the lighting-strike protection system typical of commercial and military aircraft. The mesh, DEXMET 2Cu6-100FA, an expanded film of copper of a thickness of 0.051 mm and a cavity area of 76%, Long Way Measurement (LWM) of 2.54 mm, was the second ply in the laminate and it resided just below the top GFRP ply, at an approximate depth of 0.18 mm. Autoclave co-curing at 120 °C and 6 bars of pressure for 90 min., of the skin with attached stringers pursued, as per prepreg manufacturer specifications. Finally, the external surface of the panel was finished using the same aircraft-grade paint as the coupons. Three barely visible impact damages, termed D1, D2, and D3, were inflicted equally in number locations on the panel while using a gas gun; the schematic of Figure 1b shows their exact positions. D1 was inflicted on the skin region between stringers, D2 on a skin region just above a stringer foot bond area, and D3 on a skin region just above a stringer. Neither damages produced observable surface dents on the skin. Figure 1c shows a view of the panel's rear face with stringers. Thermographic and ultrasonic inspection was performed with the IRT and PA modules that were mounted on prototype VR platforms to perform automated operation on this panel.

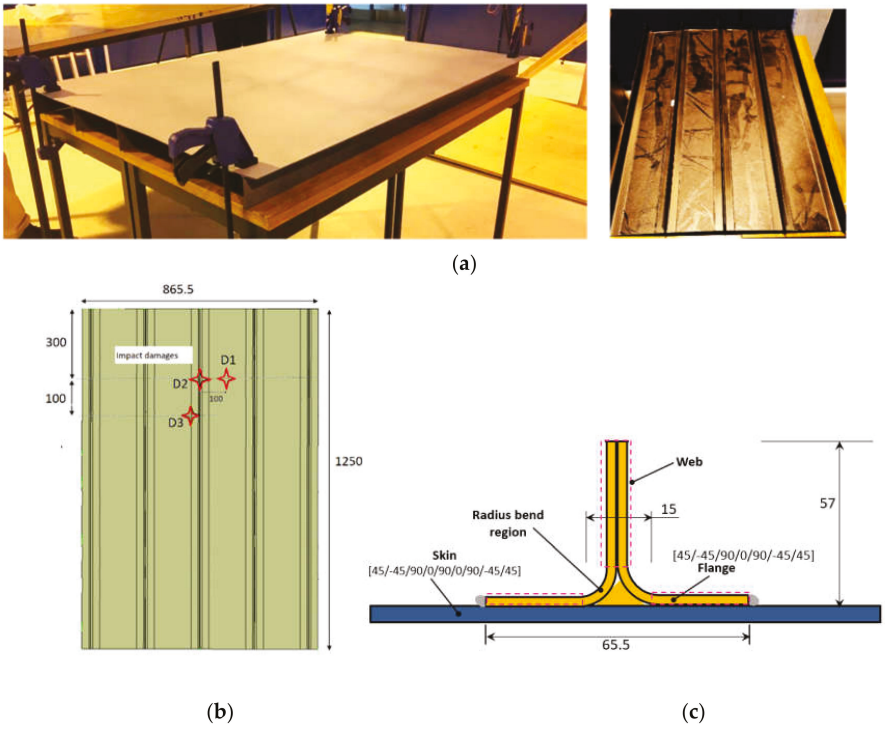

Figure 1. Stiffened composite flat panel (**a**) finished external surface clamped for infrared thermography/Phased Array (IRT/PA) inspection and panel rear face (**b**) schematic of barely visible impact damages (BVID) locations on the panel front face (**c**) T-stringer configuration.

2.2. Experimental Setup Details—IRT

A state-of-the-art IRT module was developed and presented previously to account for extreme compactness and lightweight required for automated inspection on a VR platform [20]. In brief, the module consisted of two main parts: a microbolometer shutterless longwave infrared (LWIR) sensor, the spectral response of 7–14 μm, made of resistive amorphous silicon in aluminum housing that was equipped with a lens with a ratio of F/1.25, a focal length of 16.7 mm, wide field of view of 37.5°, and manual focus end piece, and a 300 W halogen lamp excitation source housed in a bell-shaped reflector with IR-filtering eyepiece to block IR reflections from hitting back to the sensor. The sensor offered advanced technical specifications, including thermal sensitivity (noise equivalent temperature difference, NETD) of less than 50 mK, resolution of 640 × 480 pixel, time-to-image of less than 1 s, and a frame capture rate adjustable between 9 Hz and 120 Hz.

The module was assembled by mounting the sensor and source on an autoclave-cured carbon fiber reinforced polymer (CFRP) plate. Figure 2a presents the module face, while Figure 2b demonstrates it mounted on the VR platform. The lens protruded from the plate by 20 mm while the lamp position in the reflector was recessed by 30 mm from the plate. The dimensions of the sensor and the complete module were 30 × 30 × 45 mm^3 and 200 × 150 × 100 mm^3, respectively. The optimization of the module height (distance of plate from the surface under examination) was performed under the condition of IFOV maximization while maintaining full thermographic information from the surface. The IFOV should be maximum for the corresponding scanned area to be as wide as possible, which minimizes the acquisition timescale requirement for the whole aircraft structure. Based on this, a module height of 400 mm from the surface provided a optimal field of view of 320 × 240 mm^2. Indicatively, a much smaller field-of-view of 200 × 150 mm^2 was measured at a module eight of 250 mm. Most importantly, the respective weights of sensor and complete module, 70 g and 407 g, are indicative of the compactness and maneuverability offered, which makes them ideal for the targeted field application and mounting method. Prior to the start of IRT inspection, the lens end piece was focused on the surface under examination and a sensor calibration procedure, where the following involved exposure of the sensor to uniformly hot and cold surfaces, in sequence. During the initial phase of PPI-LT, the lock-in frequency was selected after the identification of the thermogram associated with the maximum contrast among those that were collected at various frequencies. In the second step, the surface within the field of view was analyzed in detail by locking thermography at the selected frequency.

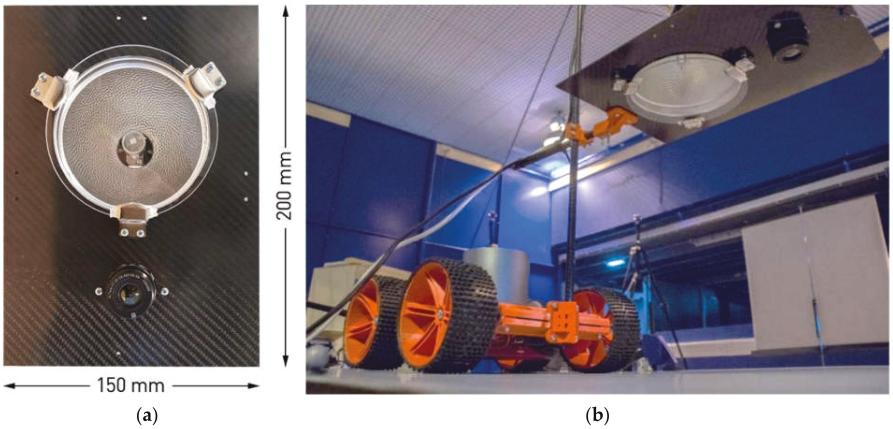

Figure 2. IRT module (**a**) dimensions and arrangement and (**b**) mounted on the prototype Vortex Robot Platform developed by Luleå University of Technology [31,32] for automated aircraft skin inspection of BVID by Pulsed Phase-informed Lock-in Thermography (PPI-LT).

A dedicated Graphical User Interface (GUI) was developed to allow for sensor control, thermogram acquisition, analysis, and communication with the VR platforms. The software offered functions for adjusting capture frame rate, calibrating, commencing, and ending PPI-LT, displaying live thermographic information, recording, analyzing, and post-processing thermograms, automatically detecting defects by pattern recognition, performing non-uniformity corrections of the IR sensor, thermogram analysis and post-processing, and many others. All of the thermograms were analyzed in the phase domain.

2.3. Experimental Setup and PA Module

2.3.1. PA Module Development

In general, the ultrasonic NDT module for automated scanning of a curved structure consists of a suitable ultrasonic transducer, with an efficient wedge to transfer ultrasonic wave from the transducer into the specimen material, a positioning fixture with a different degree of freedom suitable for either flat and curved surface, an encoder for capturing position data, highly efficient couplant distribution system and control system for interfacing between the scanner, and the data acquisition hardware for data storage and scanning control. Because of the technical requirements of the vortex robot design [31,32], the NDT module payload was limited 1 kg along with a restriction of relying on any free-flowing water or a local immersion coupling techniques in proximity of the robot to avoid potential sparking of the EDF motor or electronics damage. These requirements invalidate the use of different types of local immersion based wedges, including membrane based wedges. Based on these requirements, and a suitable PA module was designed and developed, as discussed in the following subsections.

PA Transducer

A linear array 10 MHz 64 element transducer with −6 dB level bandwidth between 7.8 and 11 MHz was used for the inspection. The fusleage skin thickness is between 1 to 3 mm. Inspection with a higher frequency transducer gives a higher axial resolution in the thickness direction of the material being inspected, but the corresponding signal to noise ratio is lower, due to higher structural noise and higher sensitivity to the surface when compared to a lower frequency transducer [21].

Wedge

An ultrasonic inspection typically requires the use of free-flowing water, a film of water, local immersion, or ultrasonic gel as a coupling medium between the transducer and surface under inspection. The restriction of existing methods of couplant usage by VR platform requirements was addressed by developing a new wedge of elastomer material that is similar to a wheel probe roller material [4], which has low attenuation, low acoustic impedance, and lower couplant requirements. The wedge thickness was optimized for a 10 MHz PA transducer that is based on ultrasonic beam characteristics, near-field length, and attenuation in the elastomer material. The elastomer wedge and transducer are enclosed in a light-weight nylon holder for the PA transducer-wedge assembly, as shown in Figure 3. A miniature encoder for capturing positional data is also clamped to the nylon holder.

Mist Couplant Delivery

During automated phased array inspection, the prerequisite requirement for reliable ultrasonic data collection is to ensure that the wedge is in contact with the surface along with uniform couplant distribution on the surface. The spray of water is a sufficient form of couplant for the elastomer wedge on a flat surface. However, the fuselage of the aircraft is curved, smooth, and painted, which results in any sprayed water droplets to coalesce and drip down the surface. It was seen experimentally that fine mist of water instead of spray using a appropriate nozzle ensures uniform distribution of mist on the surface under any orientation during inspection. A self-priming micro-diaphragm pump was used to

generate a fine mist of water using a nozzle with an orifice of 0.1 mm instead of spray during the inspection. The pump outlet was controlled by a flow control valve through a TEE connector to reduce the flow rate and provide a 50 PSI constant pressure water for generating a fine mist. The other end of TEE was connected to a hose to recirculate the extra water back to the water reservoir. It was observed that fine mist adheres to the painted surface, irrespective of the surface's orientation. The mist is uniformly distributed with less than 2 mL of water consumed, for a scan area of the size of a coupon 150 × 100 mm, thus minimizing the amount of couplant water near the VR.

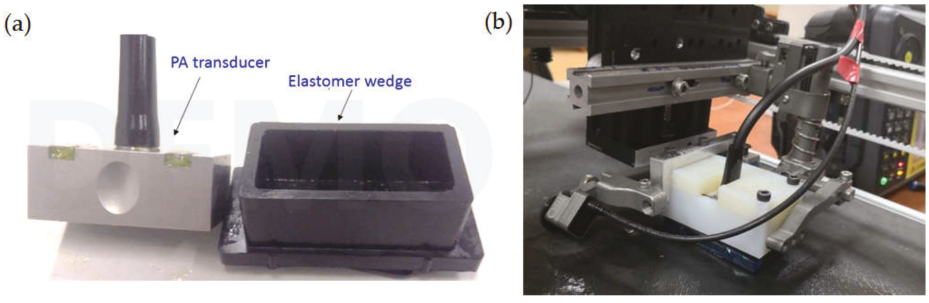

Figure 3. The PA module components (**a**) PA transducer and bespoke low attenuation elastomer wedge (**b**) customized spring-loaded positioning-fixture carrying the PA transducer and wedge in light weight Nylon enclosure and screw-clamped encoder.

Positioning Device

For maximum signal amplitude during the reception, the PA transducer-wedge assembly must maintain both normal incidence to the surface and constant contact between the wedge and inspected surface, throughout the scan in all orientations (vertical, horizontal, and inverted). This requirement is achieved by the customization of a spring-loaded positioning fixture with three degrees of freedom (one vertical and two rotations) suitable for flat and curved surfaces. This gimbaled probe holder also ensures adherence in the case of the inspection of curved surfaces (e.g., aircraft fuselage).

2.3.2. PA Inspection Procedure

The experimental inspection procedure consisted of an initial benchmarking of NDT characterization of low-velocity impact damages on composite coupons of two different thicknesses and laminates. The PA hardware consisted of a multi-channel pulse-receiver Sonatest (16:64) VEO+ series with simultaneous emission and reception along each channel and 16 active channels. This pulse-receiver is operated under a normal incidence pulse-echo configuration to excite the 10 MHz 64 element linear array PA transducer with a square pulse of a maximum permissible voltage of 70 V with eight active apertures. Prior to PA scanning, the hardware is pre-loaded with a specific PA configuration file, having information regarding material velocity, time-gain compensation, and scanning parameters. The receiver gain and range are set, as per the thickness of the component under inspection. These scans were performed by mounting the PA module on a simple X-Y-Z manipulator.

2.3.3. PA Inspection Data Post-Processing

During measurements, full waveform ultrasonic data were recorded and stored at 125 MHz sampling frequency. The proprietary raw data file format of PA data was converted to neutral Comma Separated Values (CSV) format and an initial auto error-check was carried out for any missing A-scans in the data, due to an error in the encoder movement during scanning. Impact damage affects both the amplitude of ultrasonic reflections and their time of arrival from the damaged region. The Time-of-Flight (ToF) C-scan was

generated with an ad hoc software suite in order to show the lateral extent of the impact damage. Before generating the C-scan image, each A-scans requires signal amplification, known as time-gain compensation, time-domain alignment of the A-scans, followed by ToF extraction of the first maximum peak after the front surface echo. Hilbert transform was used to find the maximum echo after the dead-zone, and maximum echo is time-tracked for the damage-depth information based on a specified threshold in each A-scan [35]. Furthermore, time-domain alignment of all A-scans is initially essential to account for delays in the arrival of the ultrasonic reflection from the top surface of the specimen due to composite surface flatness variations. This correction avoids C-scans images with false positives depth scale. It was observed that the time-domain alignment of all A-scans during post-processing is better than the digital floating-gate manually set in the PA hardware to track the front surface echo during data acquisition. The ImageJ software measures the damage area from the processed C-scan images.

3. Results and Discussion

3.1. Results of Manual IRT and PA Inspection on Coupons and Laminates

The synergistic PPI-LT/PA strategy minimizes the timescale that is required for reliable aircraft inspection by the preferential application of PA inspection, for thorough damage characterization, only to areas previously identified with damage presence by rapid wide-area IRT. Under this concept, PPI-LT and PA were used in succession to fast scan the composite and indicate areas that require further PA inspection. Figures 4–6 report pairs of successive results of IRT-identified and PA-quantified damaged areas on 9- and 18-layer composite coupons and laminates, respectively, for different levels of impact energy. All of the thermograms (figures on the left-hand side) are in the phase domain and they include relevant length and phase scale bars; the bars in the first thermogram of each subset are common for the rest, in the same subset. The C-scan image's horizontal scale represents the scan-axis, along which the C-scans were recorded with a resolution of 1 mm. The vertical scale represents the index resolution of 0.6 mm, which is also the pitch between the PA transducer elements. The grayscale color bar that is shown in the C-scan images represents ToF of the maximum peak echo of the received signal from the material's entire thickness except the dead-zone. The inverse 'gray' color-pallet with custom color-bar facilitates straightforward damage discrimination using an image processing routine in 'ImageJ' software. The calculated damage area provides a close estimation of the extent of the damage. Figure 4 compares the infrared thermograms and PA images from nine-layer composite coupons impacted with energies of 2.5 J (a), 4 J (b), 8 J (c), and 12 J (d). IRT and by PA also capture damage in composite coupons of 18-layers in Figure 5, for impact energies of 8 J (a), 12 J (b), and 20 J (c). In Figure 6, thermographic and subsequent PA investigation is presented for composite laminates that are impacted with different energies.

By observation of the thermographic results that are presented in Figures 4–6, it is concluded that damage is captured with exceptional precision by the developed PPI-LT approach and sensor in all types of specimens. It is interesting to note that the technique not only assesses the presence of damage, but it can represent its main geometrical features, such as shape and orientation, as documented by the high contrast area corresponding to damage in -45° laminas in the thermograms. In certain cases, such as Figure 5b,c, the barely visible dent produced at the site of impaction is also visible (dark circular mark at the damage center). The increasing extent of damage with increasing impact energy is efficiently assessed by IRT. Hence, it entails that the developed PPI-LT approach and sensor can not only identify damage presence, but can also provide its basic dilatational characteristics.

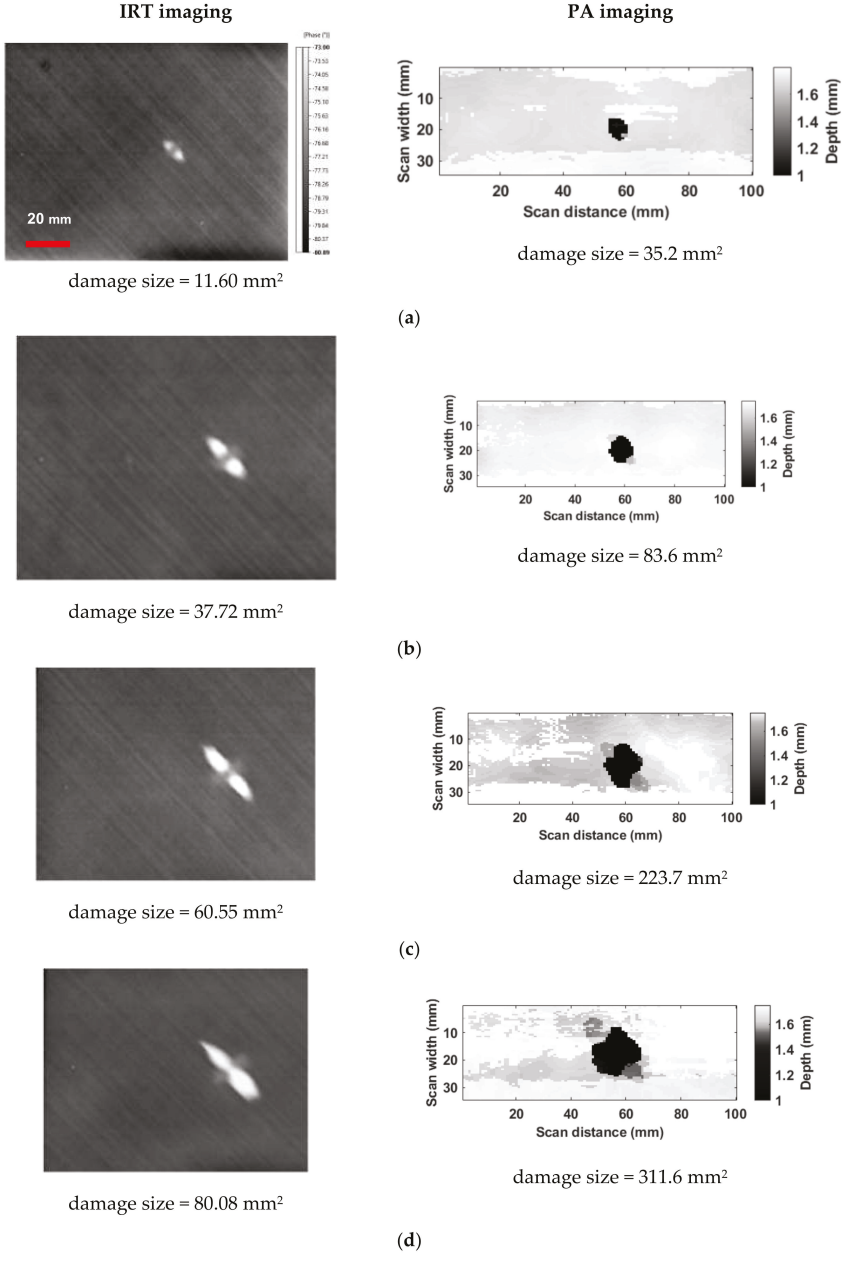

Figure 4. Detection of damage by rapid PPI-LT (thermograms, left column) and subsequent high-resolution characterization by PA imaging (right column) for nine-layer coupons with different impacted energies: (**a**) 2.5 J, (**b**) 4 J, (**c**) 8 J, and (**d**) 12 J.

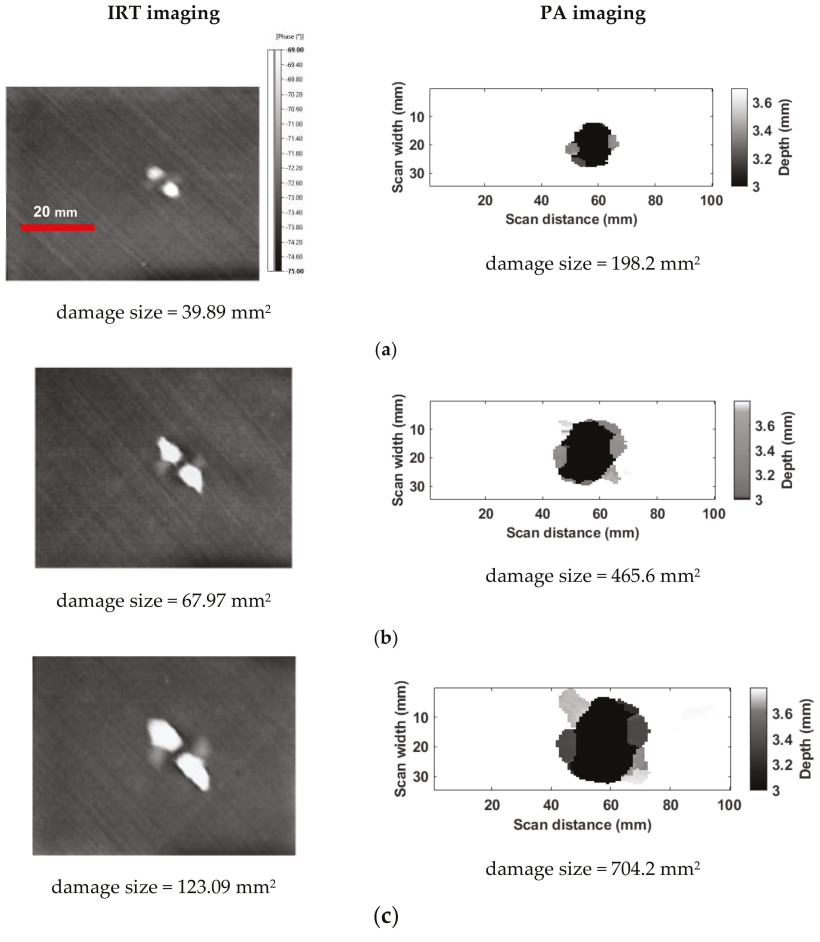

Figure 5. Detection of damage by rapid PPI-LT (thermograms, left column) and subsequent high-resolution characterization by PA imaging (right column) for 18-layers coupons with different impact energies: (**a**) 8 J, (**b**) 12 J, and (**c**) 20 J.

Observing PA C-scan images of impact damages that are presented in Figures 4–6, the following general observations can be derived: the impact damage size increases with impact energy, and damage tends to propagate along the 45° to fiber direction. In all coupons, the impact damage shows large sub-surface damage, with little or no external indication of the impact. Hence, it is vital to carry out detailed NDT inspections on the composite aircraft's external surface during heavy maintenance. In all coupons and laminates, IRT imaging shows the good detectability of damage, but the damage area is consistently smaller in size when compared to C-scan. This is because, under the rapid mode requirement of the target application, IRT is used as a fast initial indicator of damage presence; hence, PPI-LT does not offer the resolution that is required for performing full damage analysis. On the other hand, low-speed selective PA on IRT-identified areas only offers the added high-resolution feature that is required for this. In higher thickness coupons, IR thermograms exhibit lower sensitivity on impact damage, even though PA detects large sub-surface damage. These results indicate the importance of impact damage detection and the need for 100% inspection. However, adopting the proposed inspection strategy, 100% detailed inspection of the whole structure using thorough, but also time-consuming, PA can

be avoided. This is also brought forward by comparison of the timescales that are required for the full acquisition of a specified surface area, by the two techniques. While PPI-LT is imaging, the whole 320 × 240 mm^2 area under the optimal IFOV is done in approximately 60 s, the corresponding timescale requirement for full PA acquisition of the same surface must be carried out using the unidirectional raster scan approach of about ten line-scans taking about 4 min. with added complexity of VR forward and backward locomotion. This observation highlights the added value of the synergistic approach towards the rapid, but, at the same time, accurate, damage detection in aircraft composites.

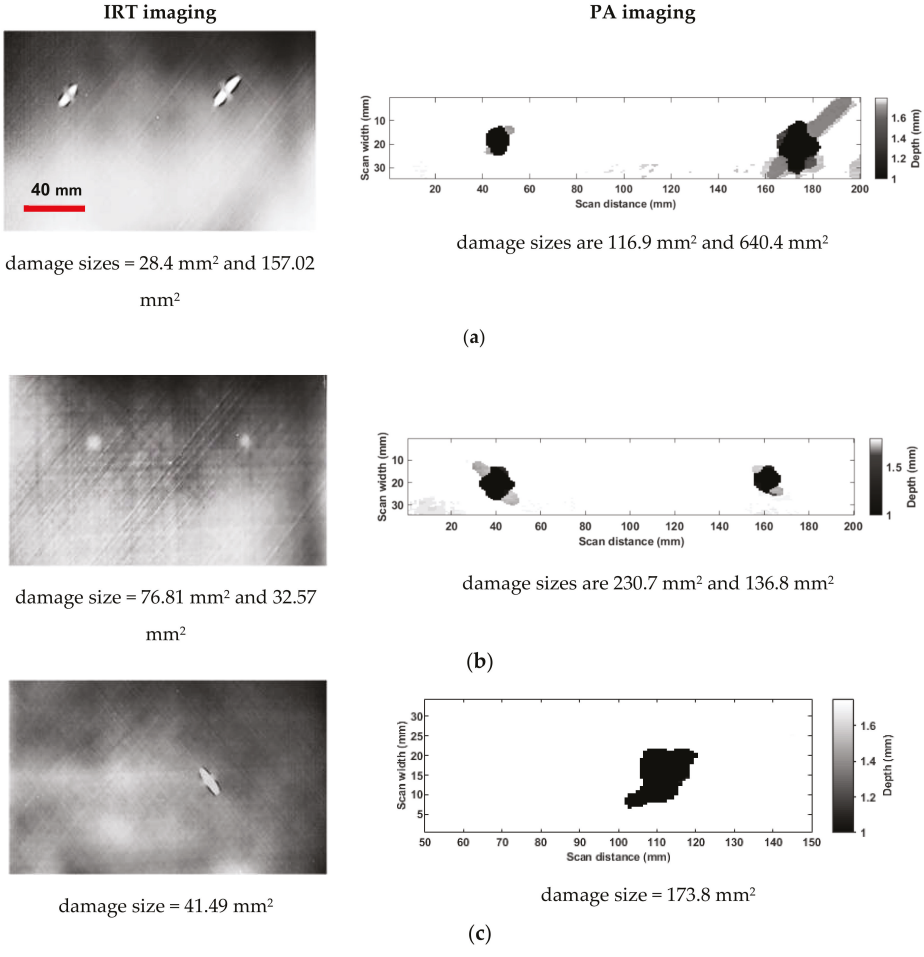

Figure 6. Detection of damage by rapid PPI-LT (thermograms, left column) and subsequent high-resolution characterization by PA imaging (right column) on flat laminates (9 layers) with estimated impact energies (**a**) 4.5 J (**b**) 5.5 J and a curved laminate with estimated impact (**c**) 4.5 J.

3.2. Automated IRT and PA Inspection on Stiffened Panel

The stiffened panel was initially scanned by PPI-LT for rapid wide-area identification of damage location, after which PA inspection was pursued. This primmer task was undertaken with the IRT module that was integrated on the VRP, as seen in Figure 2b as a lab-scale demonstration of the envisioned fully automated NDT solution for rapid

and reliable damage inspection in aircraft. The thermographic assessment of damage locations is presented in the left-hand side part of Figure 7. Therein, all three impact damages of the stiffened panel are observed to have been positively identified by the PPI-LT technique. Moreover, the extent of damage appears to be greater in the skin region D1, in the absence of back face stiffening, and smaller in the stiffened area, D3. It is interesting to note that the thermographic signal that was acquired from the stiffened panel did not appear to be deteriorated, when compared to previous findings, as a consequence of the presence, 0.2 mm below the surface, of the copper mesh lighting-protection lamina. Such behavior can be rationalized by the consideration of the small LWM dimension of the mesh with respect to the scanned area, which may lead to a uniformly higher background thermographic signal throughout the specimen, practically masked within the phase scale of thermographs containing high-contrast damage areas. The damaged locations that were identified by IRT were subsequently processed by PA.

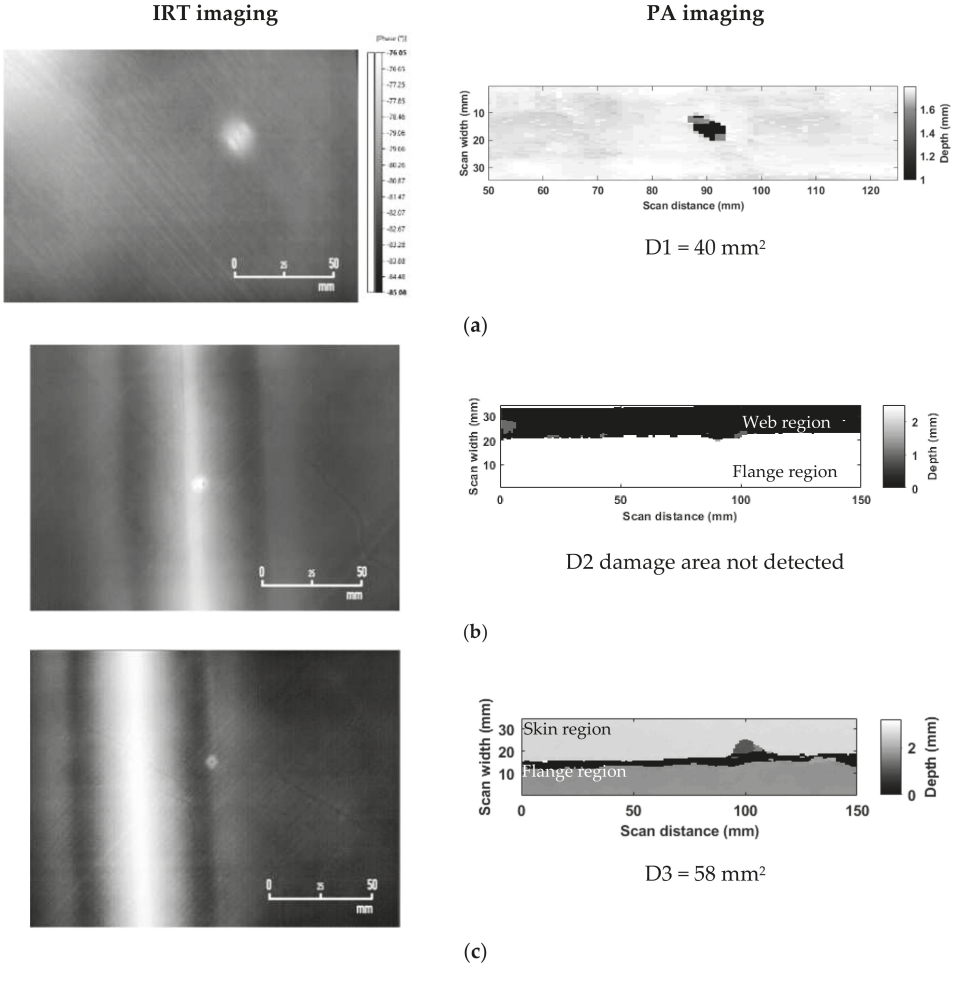

Figure 7. Comparison of IRT and PA imaging for the impact damages (D1, D2, and D3) on the stiffened panel collected using the IRT and PA module on the robot. (**a**) Skin region (**b**) web (T junction) region and (**c**) boundary of the skin-flange region.

Hence, in the next step, the PA module was integrated on to the vortex robot for automated scanning of the stiffened panel. Initially, the PA hardware was pre-loaded with a configuration file with all of the PA inspection parameters, as mentioned earlier; subsequently, PA hardware control was handed over to the robot. The robot interfaces with PA hardware through a custom-developed communication controller to control the PA data acquisition, storage, and water-pump operation for delivering water mist as couplant at the foot of the transducer. The robot then moves to the designated target area on the stiffened panel, around the damages (D1, D2, and D3), and it sequentially performs separate PA line scans. Each line-scans are of fixed 150 mm length and a width of 34.5 mm. The right-hand side graphs of Figure 7 represent the results of the assessment of impact damages on the stiffened panel performed by the PA module mounted on the VRP. The impact damage 'D1' on the skin region is well detected, as shown in Figure 5a. However, damage 'D2' exactly on the web region is not detected, but the damage 'D3' is partially detected. as shown in Figure 7. The thickness of the skin and flange region in the stiffened panel is 1.6 mm and 2.1 mm Figure 5b, c, respectively. At the T-junction region formed by the intersection of both the flanges, there is no backwall reflection of the ultrasonic waves due to the geometric curvature and web width, and, hence, the small damage 'D2' imaging was not successful. Furthermore, it was observed that, on the back-face of the panel, at the transition region between the skin and flange of the stringer, there is an accumulation of excess resin and, hence, at this region there is no reflection of the ultrasonic waves for a short width of 3–5 mm. Because to this reason, the damage 'D3' is partially masked, as shown in Figure 5c.

It is important to highlight that, provided the surface under examination is IRT/PA-active and of adequate surface smoothness, as in the case of large number of composite engineering surfaces, no other parameter of the proposed strategy appears to impose significant limitations on the type and nature of surfaces that can be inspected. This unfolds an exciting potential for the expansion of this strategy to automated inspection of other types of surfaces and industrial applications, such as defect detection in wind turbine blades and composite storage tanks. To that end, the imaging results of the present study indicate that the synergistic NDT approach and developed modules are suitable for automated inspection on a VRP. However, further considerations need to be addressed that require additional experimental investigations in order to prove the suitability of the modules for inspection on the curved stiffened composite structure that is representative of the fuselage skin of aircraft and other surfaces.

4. Conclusions

A synergistic strategy that was based on infrared thermography and phased array was presented for the rapid and, at the same time, accurate and reliable detection of damage in aircraft composites. Therein, a newly developed powerful IRT variant, termed PPI-LT, was adopted for the initial rapid, wide-area scanning of the structure for the identification and localization of damages. A thorough dilatational characterization of damages is pursued by the preferential application of an advanced PA inspection approach, only to areas previously identified as damage suspected by IRT. The synergistic strategy minimizes the timescale that is required for reliable aircraft inspection, as it eliminates the requirements of scanning the complete structure by detailed and time-consuming PA inspection. This lifts the current trade-off between speed and reliability of aircraft inspection and unravels the unprecedented potential for reduction of airplane accidents and inspection timescales, while, at the same time, maximizing the airworthiness and cost-effectiveness of tactical inspections, such as C-checks and D-checks. The strategy also offers highly reliable damage data for improved aircraft performance and effective repair. Most importantly, both of the inspection techniques were developed for field measurements, with custom state-of-the-art lightweight modules mountable on vortex robot platforms for fully automated NDT inspection of aircraft in the context of a Future and Emerging Technologies (FET) Horizon 2020 research project (Compinnova).

The strategy was successfully benchmarked across full-spec aircraft composite coupons, on selected case-study laminates with typical damages and repaired sections on a real aircraft composite panel with artificially induced barely visible impact damages (BVID). The panel was equipped with standard counter-lighting strike copper-mesh lamina and stiffening stringers on the back-face. The specimens and panels were finished in aircraft-grade paint. All of the impact-inflicted damages were successfully captured by IRT and further characterized by PA ultrasonic. The smallest defect identified by the resolution-limiting step of the approach, fast initial PPI-LT, was of the order of 35.2 mm^2 and met current FFA specifications for minimum defect detectability in tactical C- and D-checks.

It is important to highlight that, provided a smooth and IRT/PA-active surface, no other part of the proposed strategy imposes significant limitations on the type and nature of the inspected surfaces, which unfolds the potential for expansion to other types of engineering and industrial applications.

Author Contributions: Conceptualization, J.P.M., L.Z.F., I.P., K.G.D.; methodology, J.P.M., S.F., D.E.; software, I.P., L.Z.F., D.E.; validation, J.P.M., S.F., D.E.; formal analysis, J.P.M., S.F.; resources, A.T., I.G., T.E.M., K.G.D.; data curation, S.F., D.E.; writing—original draft preparation, J.P.M., K.G.D.; writing—review and editing, J.P.M., L.Z.F., K.G.D.; supervision, J.P.M, I.P., L.Z.F. project administration, J.R., I.G., K.G.D.; funding acquisition, I.G., T.E.M., K.G.D. and A.T. All authors have read and agreed to the published version of the manuscript.

Funding: This research was fully funded by the European Union's H2020 Framework Program, call FET-OPEN under REA grant agreement number 665238: CompInnova. http://compinnova.net/.

Institutional Review Board Statement: Not applicable.

Informed Consent Statement: Not applicable.

Acknowledgments: We would like to thank Spyridon Psarras and George Sotiriadis from the research team of V. Kostopoulos, Laboratory of Applied Mechanics and Vibrations, University of Patras, Greece for manufacturing composite coupons and laminates and Jose Carregado of Optimal Structural Solutions, Portugal for processing and providing the stiffened composite panel. We would also like to thank the wider CompInnova consortium for the support in carrying out this research.

Conflicts of Interest: The authors declare no conflict of interest.

References

1. Wenk, L.; Bockenheimer, C. Structure health monitoring. *Airbus Tech. Mag.* **2014**, *54*, 23–29.
2. Morteau, E.; Faivre, V. Damage tolerant composite fuselage sizing. *Airbus Tech. Mag.* **2011**, *48*, 15–19.
3. Avdelidis, N.P.; Hawtin, B.C.; Almond, D.P. Transient thermography in the assessment of defects of aircraft composites. *Ndt E Int.* **2003**, *36*, 433–439. [CrossRef]
4. Freemantle, R.J.; Hankinson, N.; Brotherhood, C.J. Rapid phased array ultrasonic imaging of large area composite aerospace structures. *Insight—Non-Destr. Test. Cond. Monit.* **2005**, *47*, 129–132. [CrossRef]
5. Ackert, S.P. Evaluation & Insights of Commercial Aircraft Maintenance Programs. Available online: http://www.aircraftmonitor.com/research-reports.html (accessed on 18 February 2021).
6. Fernandez, R.F.; Keller, K.; Robins, J. Design of a system for Aircraft Fuselage Inspection. In Proceedings of the 2016 IEEE Systems and Information Engineering Design Symposium (SIEDS), Charlottesville, VA, USA, 29–29 April 2016; IEEE: Piscataway, NJ, USA, 2016; pp. 283–288.
7. Katnam, K.B.; Da Silva, L.F.M.; Young, T.M. Bonded repair of composite aircraft structures: A review of scientific challenges and opportunities. *Prog. Aerosp. Sci.* **2013**, *61*, 26–42. [CrossRef]
8. Dragan, K.; Synaszko, P. In-Service Flaw Detection and Quantification in the Composite Structures of Aircraft. *Fatigue Aircr. Struct.* **2009**, *2009*, 37–41. [CrossRef]
9. TecFlex Scanner. Available online: http://www.tecscan.ca/products/manual-scanners/tecflex-scanner/ (accessed on 18 February 2021).
10. Liang, T.; Ren, W.; Tian, G.Y.; Elradi, M.; Gao, Y. Low energy impact damage detection in CFRP using eddy current pulsed thermography. *Compos. Struct.* **2016**, *143*, 352–361. [CrossRef]
11. Meola, C.; Boccardi, S.; Carlomagno, G.M.; Boffa, N.D.; Ricci, F.; Simeoli, G.; Russo, P. Impact damaging of composites through online monitoring and non-destructive evaluation with infrared thermography. *Ndt E Int.* **2017**, *85*, 34–42. [CrossRef]
12. Katunin, A.; Dragan, K.; Dziendzikowski, M. Damage identification in aircraft composite structures: A case study using various non-destructive testing techniques. *Compos. Struct.* **2015**, *127*, 1–9. [CrossRef]

13. Bates, D.; Smith, G.; Lu, D.; Hewitt, J. Rapid thermal non-destructive testing of aircraft components. *Compos. Part. B Eng.* **2000**, *31*, 175–185. [CrossRef]
14. Meola, C.; Carlomagno, G.M.; Squillace, A.; Vitiello, A. Non-destructive evaluation of aerospace materials with lock-in thermography. *Eng. Fail. Anal.* **2006**, *13*, 380–388. [CrossRef]
15. Wu, D.; Salerno, A.; Malter, U.; Aoki, R.; Kochendorfer, R.; Kachele, P.K.; Woithe, K.; Pfister, K.; Busse, G. Inspection of aircraft structural components using lock-in thermography. In Proceedings of the 1996 International Conference on Quantitative InfraRed Thermography; QIRT Council, Stuttgart, Germany, 2–5 September 1996.
16. Myriounis, D.P.; Kordatos, E.Z.; Hasan, S.T.; Matikas, T.E. Crack-Tip Stress Field and Fatigue Crack Growth Monitoring Using Infrared Lock-In Thermography in A359/SiCp Composites. *Strain* **2011**, *47*, e619–e627. [CrossRef]
17. Chrysochoos, A.; Dupre, J.C. An infrared set-up for continuum thermomechanics. In Proceedings of the 1992 International Conference on Quantitative InfraRed Thermography; QIRT Council, Paris, France, 7–9 July 1992.
18. Ciampa, F.; Mahmoodi, P.; Pinto, F.; Meo, M. Recent Advances in Active Infrared Thermography for Non-Destructive Testing of Aerospace Components. *Sensors* **2018**, *18*, 609. [CrossRef]
19. Hellard, G. Composites in Airbus—A Long Story of Innovations and Experiences. In Proceedings of the Global Investment Forum, Geneva, Switzerland, 2–3 June 2016; pp. 1–26.
20. Farmaki, S.; Exarchos, D.A.; Tragazikis, I.K.; Matikas, T.E.; Dassios, K.G. A Novel Infrared Thermography Sensing Approach for Rapid, Quantitative Assessment of Damage in Aircraft Composites. *Sensors* **2020**, *20*, 4113. [CrossRef]
21. Meola, C.; Boccardi, S.; Carlomagno, G.M. A quantitative approach to retrieve delamination extension from thermal images recorded during impact tests. *Ndt E Int.* **2018**, *100*, 142–152. [CrossRef]
22. Kordatos, E.Z.; Exarchos, D.A.; Stavrakos, C.; Moropoulou, A.; Matikas, T.E. Infrared thermographic inspection of murals and characterization of degradation in historic monuments. *Constr. Build. Mater.* **2013**, *48*, 1261–1265. [CrossRef]
23. Meola, C.; Boccardi, S.; Carlomagno, G.M.; Boffa, N.D.; Monaco, E.; Ricci, F. Nondestructive evaluation of carbon fibre reinforced composites with infrared thermography and ultrasonics. *Compos. Struct.* **2015**, *134*, 845–853. [CrossRef]
24. Schmutzler, H.; Alder, M.; Kosmann, N.; Wittich, H.; Schulte, K. Degradation monitoring of impact damaged carbon fibre reinforced polymers under fatigue loading with pulse phase thermography. *Compos. Part. B Eng.* **2014**, *59*, 221–229. [CrossRef]
25. Gaudenzi, P.; Bernabei, M.; Dati, E.; De Angelis, G.; Marrone, M.; Lampani, L. On the evaluation of impact damage on composite materials by comparing different NDI techniques. *Compos. Struct.* **2014**, *118*, 257–266. [CrossRef]
26. Dionysopoulos, D.; Fierro, G.-P.M.; Meo, M.; Ciampa, F. Imaging of barely visible impact damage on a composite panel using nonlinear wave modulation thermography. *Ndt E Int.* **2018**, *95*, 9–16. [CrossRef]
27. Quattrocchi, A.; Freni, F.; Montanini, R. Comparison between air-coupled ultrasonic testing and active thermography for defect identification in composite materials. *Nondestruct. Test. Eval.* **2021**, *36*, 97–112. [CrossRef]
28. Duan, Y.; Zhang, H.; Maldague, X.P.V.; Ibarra-Castanedo, C.; Servais, P.; Genest, M.; Sfarra, S.; Meng, J. Reliability assessment of pulsed thermography and ultrasonic testing for impact damage of CFRP panels. *Ndt E Int.* **2019**, *102*, 77–83. [CrossRef]
29. Quattrocchi, A.; Freni, F.; Montanini, R. Air-coupled ultrasonic testing to estimate internal defects in composite panels used for boats and luxury yachts. *Int. J. Interact. Des. Manuf.* **2020**, *14*, 35–41. [CrossRef]
30. Deane, S.; Avdelidis, N.P.; Ibarra-Castanedo, C.; Zhang, H.; Nezhad, H.Y.; Williamson, A.A.; Mackley, T.; Maldague, X.; Tsourdos, A.; Nooralishahi, P. Comparison of Cooled and Uncooled IR Sensors by Means of Signal-to-Noise Ratio for NDT Diagnostics of Aerospace Grade Composites. *Sensors* **2020**, *20*, 3381. [CrossRef]
31. Andrikopoulos, G.; Nikolakopoulos, G. Vortex Actuation via Electric Ducted Fans: An Experimental Study. *J. Intell. Robot. Syst.* **2019**, *95*, 955–973. [CrossRef]
32. Andrikopoulos, G.; Papadimitriou, A.; Brusell, A.; Nikolakopoulos, G. On Model-based adhesion control of a vortex climbing robot. In Proceedings of the 2019 IEEE/RSJ International Conference on Intelligent Robots and Systems (IROS), The Venetian Macau, Macau, China, 3–8 November 2019; IEEE: Piscataway, NJ, USA.
33. Gray, I.; Padiyar, M.J.; Petrunin, I.; Raposo, J.; Zanotti Fragonara, L.; Kostopoulos, V.; Loutas, T.; Psarras, S.; Sotiriadis, G.; Tzitzilonis, V.; et al. A novel approach for the autonomous inspection and repair of aircraft composite structures. In Proceedings of the 18th European Conference on Composite Materials (ECCM), Athens, Greece, 25–28 June 2018; pp. 24–28.
34. CompInnova. CompInnova: An Advanced Methodology for the Inspection and Quantification of Damage on Aerospace Composites and Metals using an Innovative Approach. Available online: http://compinnova.net/.
35. Mohammadkhani, R.; Zanotti Fragonara, L.; Padiyar, M.J.; Petrunin, I.; Raposo, J.; Tsourdos, A.; Gray, I. Improving Depth Resolution of Ultrasonic Phased Array Imaging to Inspect Aerospace Composite Structures. *Sensors* **2020**, *20*, 559. [CrossRef]

applied sciences

MDPI

Article

Response-Only Parametric Estimation of Structural Systems Using a Modified Stochastic Subspace Identification Technique

Chang-Sheng Lin * and Yi-Xiu Wu

Department of Vehicle Engineering, National Pingtung University of Science and Technology, Pingtung 912301, Taiwan; m10938002@mail.npust.edu.tw
* Correspondence: changsheng@mail.npust.edu.tw

Abstract: The present paper is a study of output-only modal estimation based on the stochastic subspace identification technique (SSI) to avoid the restrictions of well-controlled laboratory conditions when performing experimental modal analysis and aims to develop the appropriate algorithms for ambient modal estimation. The conventional SSI technique, including two types of covariance-driven and data-driven algorithms, is employed for parametric identification of a system subjected to stationary white excitation. By introducing the procedure of solving the system matrix in SSI-COV in conjunction with SSI-DATA, the SSI technique can be efficiently performed without using the original large-dimension data matrix, through the singular value decomposition of the improved projection matrix. In addition, the computational efficiency of the SSI technique is also improved by extracting two predictive-state matrixes with recursive relationship from the same original predictive-state matrix, and then omitting the step of reevaluating the predictive-state matrix at the next-time moment. Numerical simulations and experimental verification illustrate and confirm that the present method can accurately implement modal estimation from stationary response data only.

Keywords: operational modal analysis; ambient modal analysis; stochastic subspace identification; singular value decomposition; stationary white noise

Citation: Lin, C.-S.; Wu, Y.-X. Response-Only Parametric Estimation of Structural Systems Using a Modified Stochastic Subspace Identification Technique. *Appl. Sci.* **2021**, *11*, 11751. https://doi.org/10.3390/app112411751

Academic Editors: Nikos D. Lagaros and Cecilia Surace

Received: 25 September 2021
Accepted: 6 December 2021
Published: 10 December 2021

Publisher's Note: MDPI stays neutral with regard to jurisdictional claims in published maps and institutional affiliations.

Copyright: © 2021 by the authors. Licensee MDPI, Basel, Switzerland. This article is an open access article distributed under the terms and conditions of the Creative Commons Attribution (CC BY) license (https://creativecommons.org/licenses/by/4.0/).

1. Introduction

The dynamic characteristics of a structural system, such as natural frequencies, damping ratios, and mode shapes, can be investigated through numerical and experimental analysis. The response of a structural system is measured with a known excitation in modal testing, which is usually performed under well-controlled laboratory conditions. However, performing experimental modal analysis in real operating conditions may be possible, even for large and complex mechanical systems with real boundary conditions [1,2]. The modal parameters obtained theoretically under the free boundary condition can be calculated by mathematical modeling to obtain the characteristics under arbitrary boundary constraints [3]. However, experimental results obtained under specified boundary conditions cannot be converted to other dynamic characteristics under the constraints of other boundaries. Therefore, it is difficult to perform modal testing under practical boundary conditions. The hammer excitation testing method is generally used to measure the frequency response function of the structural system, and then parametric estimation is performed to understand the dynamic characteristics of the structural system [4].

The system-identification methods described above are generally used to systematically determine or improve a mathematical model for a physical system and are implemented by measuring both observed structural excitation and corresponding response data. However, an obvious difference exists between the operating conditions of realistic structures in practical work and a controlled-environment laboratory in modal testing [5]. Dynamic characteristics cannot fully represent the system mode under real-world operating conditions; thus, it is necessary to study how to perform modal identification of systems in authentic operating environments [6].

Operational modal analysis [7], which is also called "ambient modal analysis", or "output-only modal analysis" [8], is extensively used in modal estimation of large structures under environmental and operational loads [9], such as vehicle suspension systems [10], offshore wind power facilities [11], and stadium structures [12]. Many identification methods have been extensively employed for modal extraction based on ambient response. In 1993, the so-called natural excitation technique (NExT) was proposed and initially used for modal estimation of structures in wind engineering, by assuming that ambient excitation is stationary white noise [13]. It was employed to replace free or impulse response in conventional modal estimation methods in the time domain. Subsequently, if ambient excitation can be expressed as a product model of stationary white noise and an envelope function describing the same variation of time history as excitation amplitude, the corresponding response of a structural system can be converted approximately into free response through the correlation technique [14] or random decrement technique [15]. Modal estimation can then be carried out, using the parametric estimation technique in the time domain. In addition, by introducing the correlation matrix between ambient response data to the procedure of ERA/DC, the ERA/DC can be effectively applied to modal identification of structures subjected to stationary white excitation, even to the practical recorded excitation of an earthquake [16].

In recent years, Stochastic Subspace Identification (SSI), applied with NExT, has been widely employed to modal estimation of structures under ambient vibration [17]. The SSI method is a time-domain modal-estimation method under the assumption of stationary white noise for ambient excitation and can be directly applied to modal estimation from ambient response records only [18]. There is no need for excitation measurement; thus, it is suitable for the analysis of ambient vibration. In addition, among the algorithms for structural health monitoring (SHM) to perform modal identification of structural systems, SSI is a reliable time-domain technique using extended observability matrices [19]. Numerous studies have specifically concentrated on realistic applications of SSI in recent years. The SSI-COV method uses the calculation of correlation function through the output data and then constructs a correlation matrix. The observability matrix can be obtained by using the singular value decomposition (SVD) of the correlation function matrix, and then the modal parameters can be estimated. In 1993, SSI-DATA was proposed, based on the concept of Kalman filter and space-vector projection [18]. Through the projected output matrix obtained by projecting the output vector of the future into the output vector space of the past, we substitute the projected output matrix into the original correlation function matrix. The modal parameters can be estimated from the observability matrix obtained by SVD of the projected matrix [20].

SSI-DATA is relatively complete in the derivation process under the signal length limitation of general response data, but there are some cases where the calculation efficiency is poor. In this study, we introduce correlation function calculations in the SSI-COV system matrix method into the SSI-DATA algorithm. Through the SVD of the improved projection matrix, low computational efficiency due to the large matrix dimension can be avoided. By extracting two predictive-state matrixes with recursive relationships from the same original predictive-state matrix, the efficiency of computation can be improved, and the step of reevaluating the predictive-state matrix at the next-time moment can then be omitted.

2. Stochastic Subspace Identification Method

The analysis of the stochastic subspace identification (SSI) method is based on the framework of the state-space model. To treat the measurement data with the SSI method, this method is derived from the continuous-time domain to discrete time. Because the SSI method can be used to process the output-only system, which is different from the deterministic state space, we consider the input to be a stationary random process that can be expressed as a random, discrete-time, state-space equation.

Since the identification process of the SSI method can be implemented from the output measurement data only, the ambient excitation is assumed to be white noise input,

without considering external force input. Therefore, the external force and the noise can be combined as white noise. To apply the measurement data to the SSI method, we can construct a Hankel matrix $[H]$ composed of the measurement data, from which the relationship between the different measurement channels and different sampling times are as follows:

$$[H]_{2li\times j} = \begin{bmatrix} \underline{y}_0 & \underline{y}_1 & \cdots & \underline{y}_{j-1} \\ \underline{y}_1 & \underline{y}_2 & \cdots & \underline{y}_j \\ \vdots & \vdots & \ddots & \vdots \\ \underline{y}_{i-1} & \underline{y}_i & \cdots & \underline{y}_{i+j-2} \\ \cdots & \cdots & \cdots & \cdots \\ \underline{y}_i & \underline{y}_{i+1} & \cdots & \underline{y}_{i+j-1} \\ \underline{y}_{i+1} & \underline{y}_{i+2} & \cdots & \underline{y}_{i+j+1} \\ \vdots & \vdots & \ddots & \vdots \\ \underline{y}_{2i-1} & \underline{y}_{2i} & \cdots & \underline{y}_{2i+j-2} \end{bmatrix}_{2li\times j} = \begin{bmatrix} [Y_p]_{(li)\times j} \\ \cdots \\ [Y_f]_{(li)\times j} \end{bmatrix} = [\alpha]_{2li\times 2n}[\hat{X}]_{2n\times j} \tag{1}$$

where the upper half of this matrix is called "the past" and denoted $[Y_p]$, and the lower half of the matrix is called "the future" and is denoted $[Y_f]$ [16].

A conditional mean for Gaussian processes can be completely described by its covariance. Since the shifted data matrices are also defined as covariance, the projection can be calculated directly. Note that the state matrix estimated by Kalman filter, and the state-space model can be constructed by the measured output vector used to estimate the predictive-state matrix $[\hat{X}_i]$. The projection matrix $[\Omega]$ can be expressed as a product of the observability matrix $[\alpha]$ and the predictive-state matrix $[\hat{X}_i]$ of the Kalman filter in the following [18]:

$$\begin{aligned} [\Omega] &= E\Big([Y_f][Y_p]^T\Big)\Big(E\Big([Y_p][Y_p]^T\Big)\Big)^{\oplus}[Y_p] \\ &= [\alpha]_{li\times 2n}[\hat{X}_i]_{2n\times j} \end{aligned} \tag{2}$$

where

$$[\alpha]_{li\times 2n} = \begin{bmatrix} [C] \\ [C][A] \\ \cdots \\ [C][A]^{i-1} \end{bmatrix}_{li\times 2n} \tag{3}$$

$$[\hat{X}_i]_{2n\times j} = \begin{bmatrix} \hat{\underline{x}}_i & \hat{\underline{x}}_{i+1} & \cdots & \hat{\underline{x}}_{i+j-1} \end{bmatrix}_{2n\times j} \tag{4}$$

$[C]$ is the output/observation matrix; $\oplus$ is Moore–Penrose pseudoinverse; $[A]$ is the system matrix; $E[\cdot]$ is the expectation operator. In the first line of Equation (2), the first four matrices in the product introduce the covariance between channels at different time delays, and the last matrix in this product defines the conditions. By using the SVD analysis and choosing the effective singular-value number, $[\Omega]$ can be expressed in minimum order realization as:

$$\begin{aligned} [\Omega] = \; & [U][\Delta][V]^T \\ = \; & \begin{pmatrix} [U_1] & [U_2] \end{pmatrix}\begin{pmatrix} [\Delta_1] & 0 \\ 0 & [\Delta_2]\approx 0 \end{pmatrix}\begin{pmatrix} [V_1]^T \\ [V_2]^T \end{pmatrix} \\ \approx \; & [U_1]_{li\times 2n}[\Delta_1]_{2n\times 2n}[V_1]^T{}_{2n\times j} \end{aligned} \tag{5}$$

where $[U]$ and $[V]$ are both unitary matrixes, and $[\Delta]$ is a matrix containing singular values. The dimension of $[\Delta_1]$ can, in general, be employed to estimate the system order or number of poles. However, in practical work, the partial diagonal terms of the singular-value

matrix $[\Delta]$ may be nonzero, produced by noise from the procedure of data acquisition and numerical truncation.

Through the elimination of partial matrix $[\Delta_2]$, consisting of the smaller singular values, a minimum realization is obtained that results in a minimum order system representing the structural system. In Equation (5), we can, therefore, choose the number of effective singular values to obtain the minimum order realization through the SVD analysis of $[\Omega]$. From Equations (2) and (5), with appropriate partitioning of $[\alpha]$ and $[\hat{X}_i]$, the following equations can be written:

$$\begin{array}{l} [\alpha] = [U_1][\Delta_1]^s \\ [\hat{X}_i] = [\Delta_1]^t[V_1]^T \end{array} \tag{6}$$

where $s + t = 1$. Indeed, one possible choice is $[\alpha] = [U_1][\Delta_1]^{1/2}$ and $[\hat{X}_i] = [\Delta_1]^{1/2}[V_1]^T$, which appears to make both $[\alpha]$ and $[\hat{X}_i]$ balanced.

However, poor computational efficiency may occur, caused by relatively large dimensions of $[\Omega]$. In this paper, we construct the data matrix $[\Omega][\Omega]^T$ composed of $[\Omega]$, and perform the SVD analysis of $[\Omega][\Omega]^T$ to determine the order of a structural system to be identified. It can be shown that the eigenvalue of $[\Omega][\Omega]^T$ is the square roots of the eigenvalues of $([\Omega][\Omega]^T)([\Omega][\Omega]^T)$, and that the corresponding eigenvectors of $[\Omega][\Omega]^T$ are the same as those of $([\Omega][\Omega]^T)([\Omega][\Omega]^T)$. The dimension $li \times j$ of $[\Omega]$ can be reduced to the dimension $li \times li$ of $([\Omega][\Omega]^T)([\Omega][\Omega]^T)$, where $j >> li$. Based on the above, the efficiency of modal estimation can be improved, and system order can be determined through the SVD analysis of $([\Omega][\Omega]^T)([\Omega][\Omega]^T)$.

In addition, to further improve the efficiency of the SSI method, we consider extracting the predictive-state matrixes $[\hat{X}_{extract1}]$ and $[\hat{X}_{extract2}]$ with a recursive relationship directly from the original predictive-state matrix $[\hat{X}_i]$, as described next. From Equation (2), the predictive-state matrix $[\hat{X}_i]$ can be obtained from the observation matrix $[\alpha]$ in the following:

$$\begin{array}{l} [\hat{X}_i] = [\alpha]^{\oplus}[\Omega] \\ \quad = \left[\begin{array}{cccccc} \hat{\underline{x}}_i & \hat{\underline{x}}_{i+1} & \cdots & \hat{\underline{x}}_{i+j-3} & \hat{\underline{x}}_{i+j-2} & \hat{\underline{x}}_{i+j-1} \end{array} \right]_{2n \times j} \end{array} \tag{7}$$

From the measured stationary responses at n stations on a structure under test, we define a system matrix $[A]$, such that

$$[A][\hat{X}_{extract1}] = [\hat{X}_{extract2}] \tag{8}$$

where $[\hat{X}_{extract1}]$ is a predictive-state matrix of measured response from $[\hat{X}_i]$, and $[\hat{X}_{extract2}]$ is a predictive-state matrix of time-delayed response from $[\hat{X}_i]$ as follows

$$\begin{array}{l} [\hat{X}_{extract1}] = \left[\hat{\underline{x}}_i \; \hat{\underline{x}}_{i+1} \; \cdots \; \hat{\underline{x}}_{i+j-3} \; \hat{\underline{x}}_{i+j-2} \right]_{2n \times j-1} \\ [\hat{X}_{extract2}] = \left[\hat{\underline{x}}_{i+1} \; \cdots \; \hat{\underline{x}}_{i+j-3} \; \hat{\underline{x}}_{i+j-2} \; \hat{\underline{x}}_{i+j-1} \right]_{2n \times j-1} \end{array} \tag{9}$$

Therefore, following almost the same procedure as used in Equation (7), the system matrix $[A]$ can be obtained through the least-squares method. By extracting the predictive-state matrixes $[\hat{X}_{extract1}]$ and $[\hat{X}_{extract2}]$ with a recursive relationship directly from the original predictive-state matrix $[\hat{X}_i]$, we can then avoid the step of reevaluating the predictive-state matrix at the next-time moment in the conventional SSI method, which can further improve the computational efficiency of the SSI method.

We can further solve the eigenproblem of the system matrix $[A]$ to obtain the dynamic characteristics of the system, and the characteristic equation can be written as:

$$[A][\Psi] = [\Psi][\Lambda] \tag{10}$$

where $[\Psi]$ consists of eigenvectors, i.e., mode shapes, and $[\Lambda]$ contains eigenvalues λ_i. The relationship between discrete-time matrix $[A]$ and continuous-time matrix $[A_S]$ can be expressed as:

$$[A] = e^{[A_S]\Delta t} \in R^{2n \times 2n} \tag{11}$$

Denote the eigenvalues of $[A]$ and $[A_S]$ as λ_i and λ_{si}, respectively. The relationship between λ_i and λ_{si} can then be expressed as

$$\lambda_i = e^{\lambda_{si}\Delta t} \tag{12}$$

Through the eigenvalue analysis associated with the continuous-time system matrix, $[A_S]$, the eigenvalues λ_{si} can be obtained as:

$$\lambda_{si} = -\omega_i \xi_i \pm j\omega_i \sqrt{1 - \xi_i^2} \tag{13}$$

Set the eigenvalues λ_{si} of continuous-time system matrix $[A_S]$

$$\lambda_{si} = a_i + jb_i \tag{14}$$

The natural frequencies ω_i and damping ratios ξ_i of the structural system can be obtained as:

$$\begin{array}{c} \omega_i = \sqrt{a_i^2 + b_i^2} \\ \xi_i = -\frac{a_i}{\sqrt{a_i^2 + b_i^2}} \end{array} \tag{15}$$

Consequently, the parametric estimation of structures can be implemented through the eigenvalue analysis associated with the system matrix, $[A_S]$, once the system matrix $[A_S]$ is obtained through the least-squares estimate from measured response data.

3. Numerical Simulations and Experimental Verification

3.1. Six DOF Chain Model of a Cantilever Beam

To illustrate and confirm the validity of the proposed method in this paper, we first consider a numerical example of a chain model with six degrees of freedom (6-DOF) to simulate a cantilever beam, as shown schematically in Figure 1. The masses m_1, m_2, m_3, m_4, m_5, and m_6 for the 6-DOF chain model are equal to 2, 2, 2, 2, 3, and 4 kg. The stiffnesses k_1, k_2, k_3, k_4, k_5, and k_6 are equal to 1, 1, 1, 1, 2, and 3 N/m, respectively. The damping matrix $[C]$ of the system is in the form of $[C] = 0.1[M] + 0.001[K]\frac{\text{N·s}}{\text{m}}$, which indicates that this structure contains proportional damping because of damping matrix $[C]$, expressed as the linear combination of the mass matrix $[M]$ and stiffness matrix $[K]$. The excitation force is simulated as stationary white noise, which is approximately generated as a zero-mean band-pass noise [21], whose frequency range is from 0 to 50 Hz, and the standard deviation, i.e., power spectrum density, is 0.04 N^2·s/rad. The sampling interval is chosen as $\Delta t = 0.01$ s, and the sampling period, as shown in Figure 2, is $T = N_t \cdot \Delta t = 1310.72$ s, where N_t was chosen as 2^{17}. The cut-off frequency, ω_c is 314.15 rad/s, and the resolution in frequency domain $\Delta\omega$ is 4.79×10^{-3} rad/s. The sampling interval is chosen as 0.01 s, and the sampling period is 150 s. Through Newmark's method, the displacement responses of the system are obtained and then employed for modal estimation through the modified SSI method.

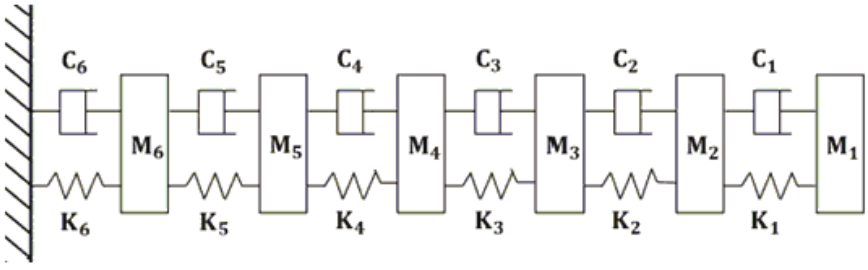

Figure 1. Schematic plot of a 6-DOF chain model of a cantilever beam.

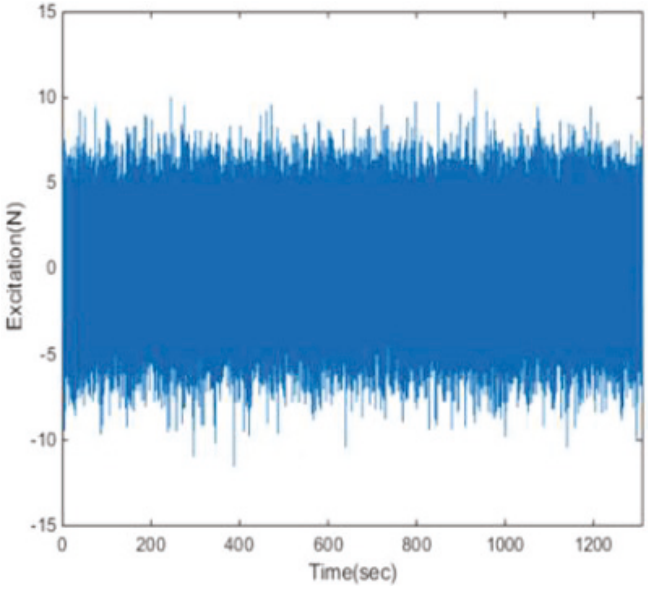

Figure 2. A sample function of stationary white noise in the time domain.

By introducing the procedure of solving the system matrix in SSI-COV, in conjunction with SSI-DATA, we can increase the computational efficiency without using the original large-dimension data matrix, through the singular value decomposition of the improved projection matrix. To make the number of modes evaluated through the SSI algorithm equal to or greater than the number of modes to be identified, the dimensions of the Hankel matrix must be not less than the system order to be identified ($li \geq 2n$). Through the channel expansion technique, we set the number of expansion channels to 20.

In practical engineering analysis, a continuum structure has an infinite number of degrees of freedom and modes; thus, the dimensions of the Hankel matrix depend on the number of modes to be identified. The projection matrix, $[\Omega]$ is obtained by Hankel matrix calculation. The SVD analysis of the projection matrix $[\Omega]$ can then be performed, and the number of singular values is employed to determine the order of system to be identified. In Figures 3 and 4, the distribution of the singular values of $[\Omega][\Omega]^T$ shows a relatively more obvious drop than those of $[\Omega]$ around the singular value number 12 and can be further employed to estimate the system order and the number of modes to be identified. In addition, the SVD analysis of $[\Omega][\Omega]^T$ can be employed to reduce a greater number of calculations, rather than performing the SVD of $[\Omega]$ or system matrix $[A]$. A comparison of the computational efficiency of SVD between $[\Omega]$ and $[\Omega][\Omega]^T$ for different sampling

points is shown in Table 1, in which we clearly see the computation time of SVD of $[\Omega]$ is much longer than that of $[\Omega][\Omega]^T$, especially for $[\Omega]$ with high dimensions. In addition, through the stabilization diagram of different polynomial orders constructed by identified natural frequency, corresponding to eigenvalues from the frequency response function matrix with different polynomial orders, estimation results can then be sorted as either structural or fictitious modes. In addition, the number of structural modes can clearly be seen to be six, as shown in Figure 5.

Table 1. Comparison of computation time of SVD of $[\Omega]$ and $[\Omega][\Omega]^T$ for different sampling points as well as matrix multiplication processing time for $[\Omega][\Omega]^T$.

Sampling Points	Computation Time (s) of SVD		Matrix Multiplication Processing Time for $[\Omega][\Omega]^T$
	$[\Omega]$	$[\Omega][\Omega]^T$	
2^{12}	0.570	0.000574	0.0003616
2^{13}	2.217	0.000760	0.0005376
2^{14}	9.074	0.001219	0.0009967
2^{15}	37.197	0.003244	0.0029074
2^{16}	Out of memory	0.003264	0.0030135
2^{17}	Out of memory	0.006189	0.0059404

Central processing unit (CPU) is Intel® Core™ i7-9700K CPU @ 3.60 GHz. Random-access memory (RAM) is 64.0 GB.

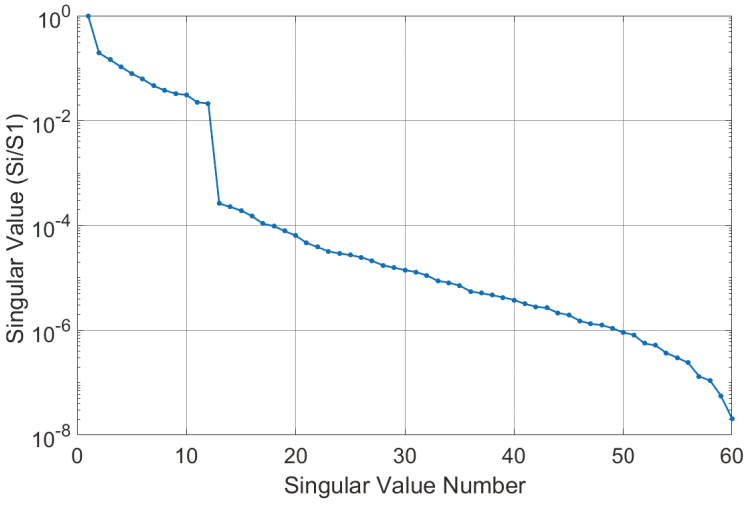

Figure 3. Distribution of the singular values of projection matrix $[\Omega]$ from the stationary responses of a 6-DOF chain model of a cantilever beam.

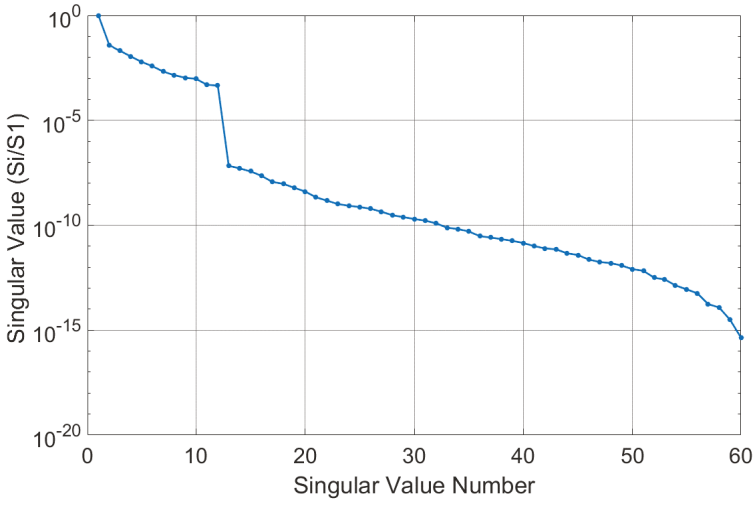

Figure 4. Distribution of the singular values of the data matrix, $[\Omega][\Omega]^T$, constructed by projection matrix, $[\Omega]$, from the stationary responses of a 6-DOF chain model of a cantilever beam.

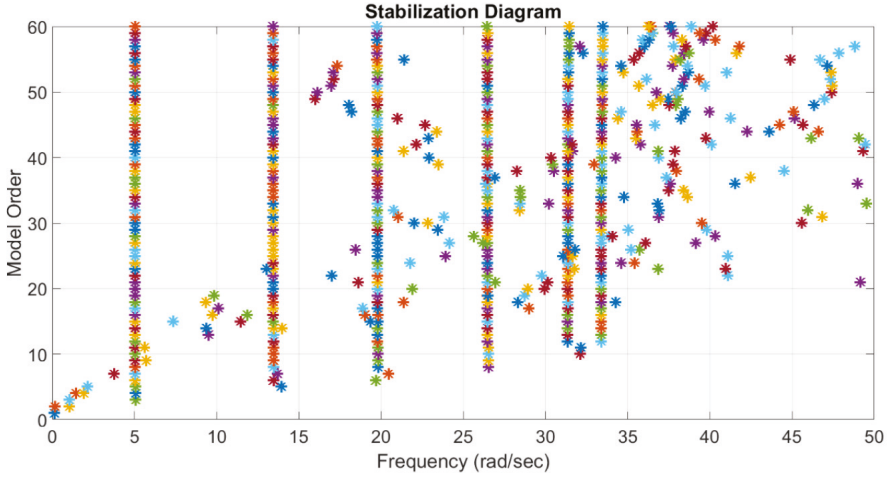

Figure 5. Typical plot of the stabilization diagram of stationary response of first DOF of a 6-DOF chain model of a cantilever beam.

In the stabilization diagram, a clear "location" of modal frequency obviously exists, even though no obvious peaks appear among close modes in the frequency response function because of modal interference. The system matrix, $[A]$, can be obtained from Equations (9)–(11), and the modal parameters can then be estimated through the eigenvalue analysis of system matrix, $[A]$, as summarized in Tables 2 and 3, where we clearly see the well-estimated structural modal parameters through the Modified Stochastic Subspace Identification (MSSI) method of both $[\Omega]$ and $[\Omega][\Omega]^T$. Note that the MSSI method is a combination of the conventional SSI method and SVD analysis. A comparison between the exact and identified mode shapes is shown in Figure 6, and the corresponding Modal Assurance Criterion (MAC) [22] values evaluated are shown in Figure 7, where good agreement is observed.

Table 2. Identification results of 6-DOF chain model through Modified Stochastic Subspace Identification (MSSI) method from projection matrix $[\Omega]$.

Mode	Natural Frequency (rad/s)			Damping Ratio (%)		
	Exact	MSSI	Error (%)	Exact	MSSI	Error (%)
1	5.03	5.04	0.09	1.25	1.38	10.39
2	13.45	13.39	0.41	1.04	1.17	11.73
3	19.80	19.71	0.41	1.24	1.23	0.92
4	26.68	26.56	0.44	1.52	1.47	3.59
5	31.65	31.18	1.48	1.74	1.79	2.78
6	33.72	33.46	0.78	1.84	1.89	3.18

Table 3. Identification results of 6-DOF chain model through Modified Stochastic Subspace Identification (MSSI) method from the data matrix $[\Omega][\Omega]^T$ constructed by projection matrix.

Mode	Natural Frequency (rad/s)			Damping Ratio (%)		
	Exact	MSSI	Error (%)	Exact	MSSI	Error (%)
1	5.03	5.04	0.08	1.25	1.38	8.97
2	13.45	13.39	0.42	1.04	1.17	10.11
3	19.80	19.71	0.42	1.24	1.23	2.47
4	26.68	26.56	0.47	1.52	1.47	4.88
5	31.65	31.18	1.50	1.74	1.79	1.15
6	33.72	33.46	0.78	1.84	1.89	1.19

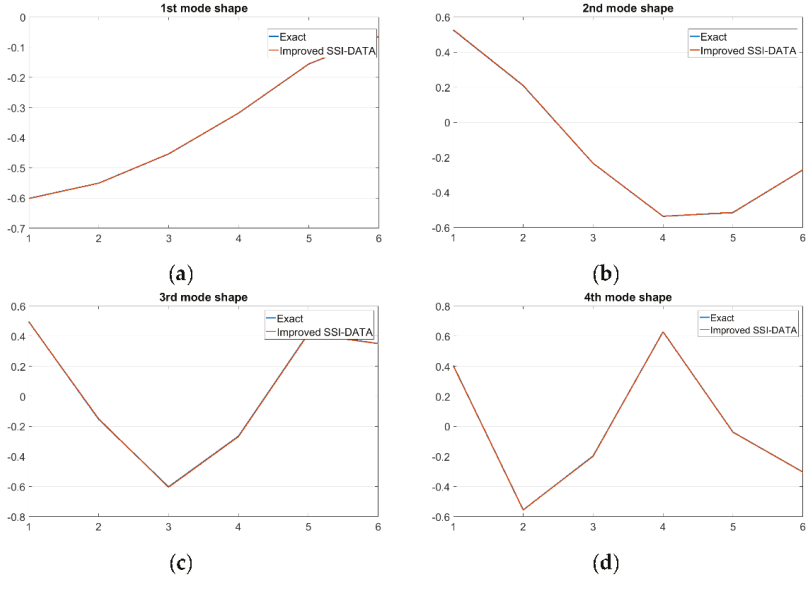

Figure 6. *Cont.*

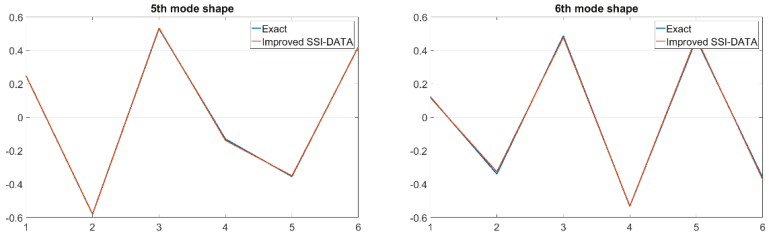

Figure 6. Comparison between the identified mode shapes and the exact mode shapes of a 6-DOF chain model of a cantilever beam subjected to stationary white noise: (**a**) 1st bending mode shape; (**b**) 2nd bending mode shape; (**c**) 3rd bending mode shape; (**d**) 4th bending mode shape; (**e**) 5th bending mode shape; (**f**) 6th bending mode shape.

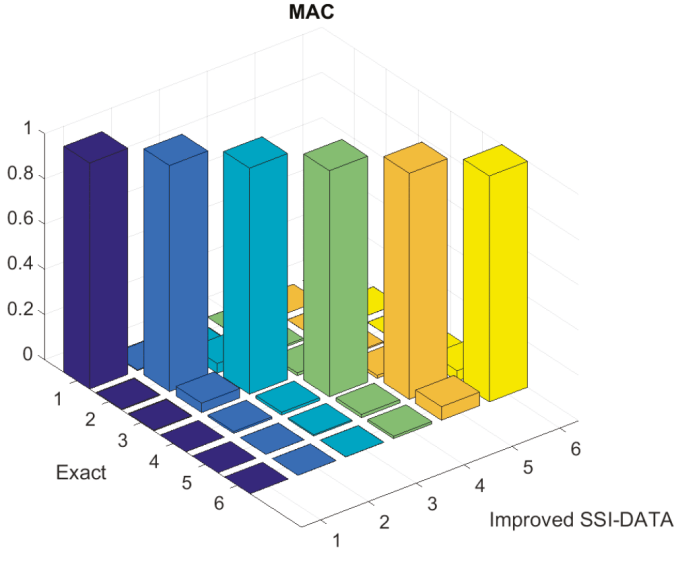

Figure 7. Typical plot of the Modal Assurance Criterion (MAC) for the identified mode shapes and exact mode shapes of a 6-DOF chain model of a cantilever beam.

3.2. Six DOF Railway Vehicle Model with Modal Interference

In the previous examples, only a proportionally damped structure is considered. Actually, the hypothesis of proportional damping, although frequently considered in the literature, is difficult to be found in practice in real mechanical systems [23,24]. To study the feasibility and validity of the proposed method for relatively complex structural systems, we consider a linear 6-DOF railway vehicle model with viscous damping [25], as shown schematically in Figure 8. The mass matrix M, stiffness matrix K, and the damping matrix C of the system are given as follows [26]:

$$M = \begin{bmatrix} 1200 & 0 & 0 & 0 & 0 & 0 \\ 0 & 850 & 0 & 0 & 0 & 0 \\ 0 & 0 & 4125 & 0 & 0 & 0 \\ 0 & 0 & 0 & 125000 & 0 & 0 \\ 0 & 0 & 0 & 0 & 850 & 0 \\ 0 & 0 & 0 & 0 & 0 & 1220 \end{bmatrix} \text{kg}$$

$$K = \begin{bmatrix} k_1+k_2 & -k_2 & 0 & 0 & 0 & 0 \\ -k_2 & k_2+k_3 & -k_3 & -k_3L & 0 & 0 \\ 0 & -k_3 & k_3+k_4 & k_3L-k_4L & -k_4 & 0 \\ 0 & -k_3L & k_3L-k_4L & k_3L^2+k_4L^2 & k_4L & 0 \\ 0 & 0 & -k_4 & k_4L & k_4+k_5 & -k_5 \\ 0 & 0 & 0 & 0 & -k_5 & k_5+k_6 \end{bmatrix} \text{N/m}$$

$$C = \begin{bmatrix} c_1+c_2 & -c_2 & 0 & 0 & 0 & 0 \\ -c_2 & c_2+c_3 & -c_3 & -c_3L & 0 & 0 \\ 0 & -c_3 & c_3+c_4 & c_3L-c_4L & -c_4 & 0 \\ 0 & -c_3L & c_3L-c_4L & c_3L^2+c_4L^2 & c_4L & 0 \\ 0 & 0 & -k_4 & c_4L & c_4+c_5 & -c_5 \\ 0 & 0 & 0 & 0 & -c_5 & c_5+c_6 \end{bmatrix} \text{N·s/m}$$

in which $K_1 = 3 \times 10^7$ N/m, $K_2 = 10^6$ N/m, $K_3 = 6 \times 10^6$ N/m, $K_4 = 6 \times 10^6$ N/m, $K_5 = 10^6$ N/m, $K_6 = 3 \times 10^7$ N/m, L = 8.53 m, $c_1 = 0$, $c_2 = 6 \times 10^3$ N·s/m, $c_3 = 1.8 \times 10^4$ N·s/m, $c_4 = 1.8 \times 10^4$ N·s/m, $c_5 = 6 \times 10^3$ N·s/m, and $c_6 = 0$. This railway structural system has the features of relatively high modal damping levels for third and fourth modes, and a pair of closely spaced fifth and sixth modes. Note that this railway structure has non-proportional damping, because damping matrix, C, cannot be expressed as the linear combination of the mass matrix, M, and stiffness matrix, K. The stationary white noise in the previous numerical example is still used as the excitation force acting the 6th mass of the railway vehicle system. The sampling interval is set as 0.01 s, and the sampling period is 110 s. Then, using Newmark's method, the displacement responses obtained are employed for modal estimation using the modified SSI method proposed in this paper.

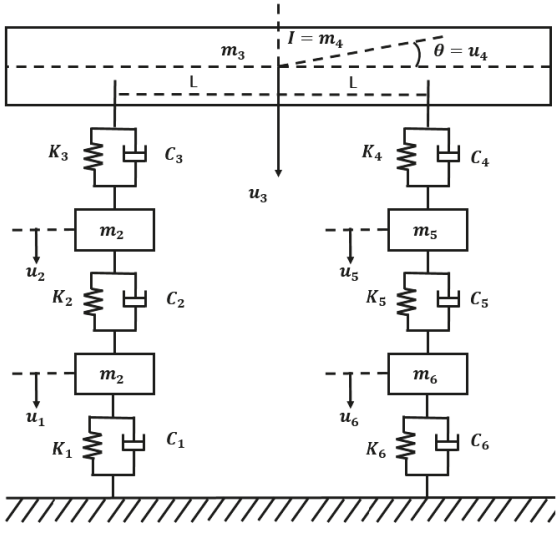

Figure 8. Schematic plot of the railway vehicle model.

It should be noted that the number of modes to be identified serves to determine the dimensions of the Hankel matrix. Using the channel expansion technique, we set the number of expansion channels at 20. The dimensions of the Hankel matrix are not less than the order of the system to be identified, thus satisfying the condition that the number of modes evaluated in the SSI algorithm is not less than the number of modes to be identified. The SVD analysis of the projection matrix, which is obtained from the Hankel matrix calculation, can then be implemented, and the number of singular values is

employed to determine the order of the system to be identified. Around the 12th singular value, an obvious drop showed in the distribution of singular values associated with the data matrix $[\Omega][\Omega]^T$ constructed by projection matrix $[\Omega]$ from stationary response data, as shown in Figure 9. It can be estimated that the order of the system, i.e., the number of modes to be identified, is 12.

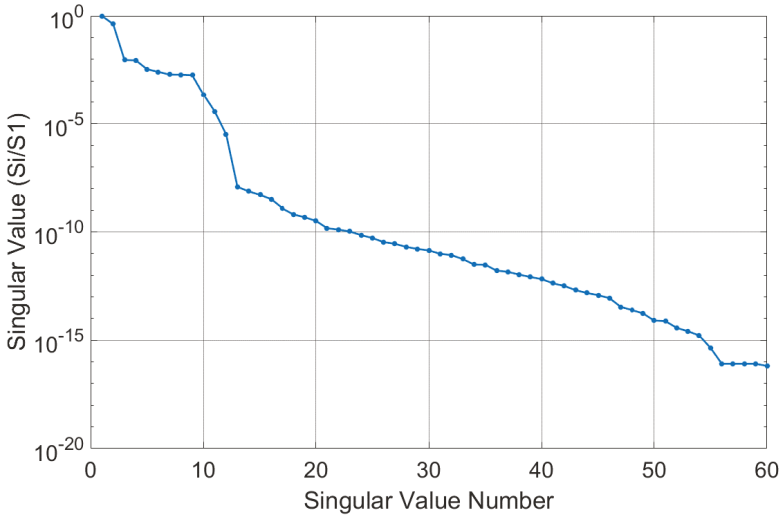

Figure 9. Distribution of the singular values associated with a data matrix, $[\Omega][\Omega]^T$, constructed by projection matrix, $[\Omega]$, from stationary responses of a railway vehicle model..

Compared with the efficiency when performing the SVD of the system matrix $[A]$, computation can be reduced by implementing SVD analysis of data matrix $[\Omega][\Omega]^T$ constructed from the projection matrix $[\Omega]$. As shown in Figure 10, from the stabilization diagram corresponding to different modal orders, it can be observed that the number of structural modes to be identified is six, and serious modal interference can be observed between the last two close modes. The system matrix, $[A]$, can be found using Equations (9)–(11), and the modal parameters can then be determined through Equations (12)–(15). Table 4 presents the well-implemented modal estimation through eigenvalue analysis of the system matrix, $[A]$. A comparison between the exact and identified mode shapes is shown in Figure 11, and the corresponding MAC values evaluated are shown in Figure 12, where good agreement is observed.

Table 4. Identification results of railway vehicle through Modified Stochastic Subspace Identification (MSSI) method.

Mode	Natural Frequency (Hz)			Damping Ratio (%)		
	Exact	MSSI	Error (%)	Exact	MSSI	Error (%)
1	2.79	2.79	0.00	4.89	4.89	0.01
2	3.71	3.71	0.00	6.62	6.62	0.01
3	16.55	16.53	0.09	16.65	16.62	0.17
4	19.27	19.25	0.11	18.78	18.74	0.24
5	25.36	25.30	0.21	1.74	1.74	0.42
6	25.57	25.51	0.21	1.75	1.75	0.43

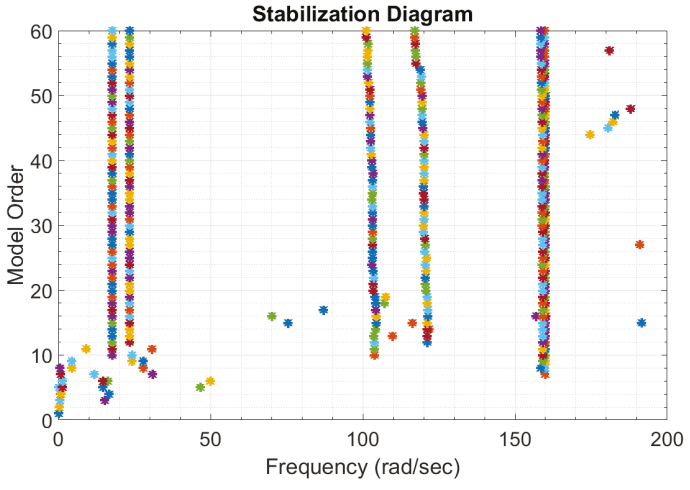

Figure 10. Typical plot of the stabilization diagram of stationary responses of 1st DOF of a 6-DOF chain model of a railway vehicle.

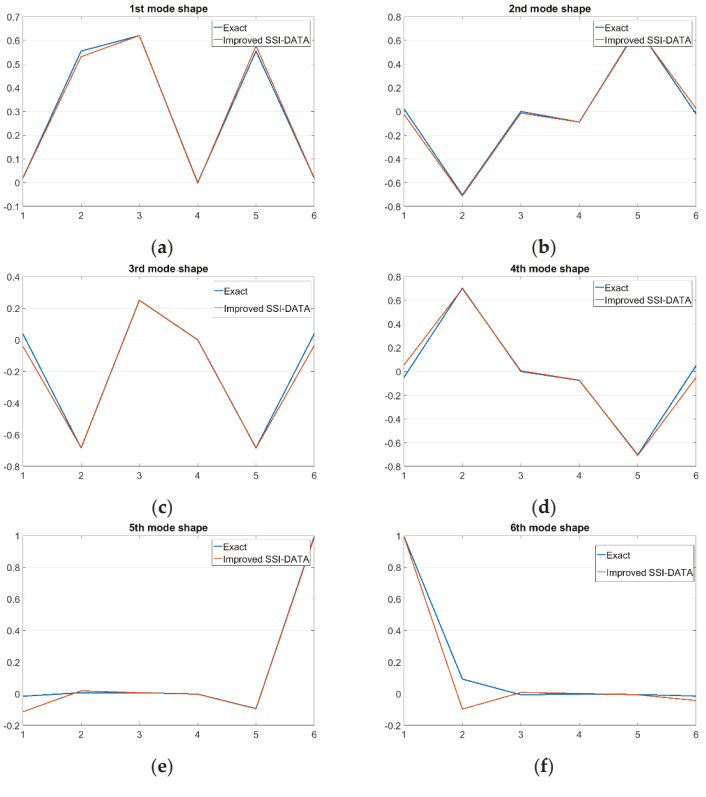

Figure 11. Comparison between the identified mode shapes and the exact mode shapes of 6-DOF chain model of a railway vehicle subjected to stationary white noise: (**a**) 1st mode shape; (**b**) 2nd mode shape; (**c**) 3rd mode shape; (**d**) 4th mode shape; (**e**) 5th mode shape; (**f**) 6th mode shape.

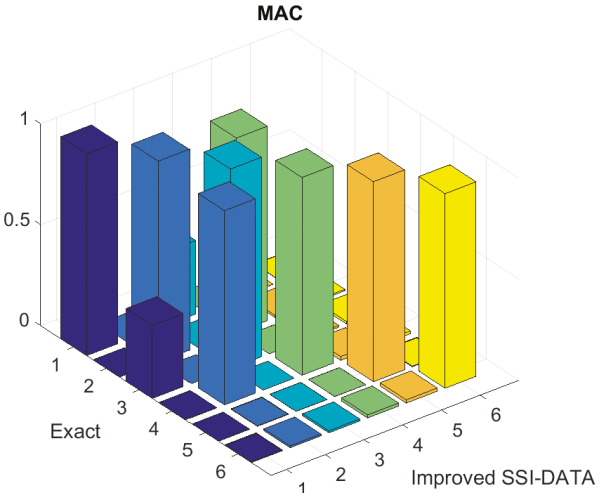

Figure 12. Typical plot of the Modal Assurance Criterion (MAC) for the identified mode shapes and exact mode shapes of 6-DOF chain model of a railway vehicle.

Due to the experimental restrictions of economic cost and structural geometry in the practical measurement of structural response, the number of sensors sited on the structures to record response data is not usually sufficient for the overall degrees of freedom of a structure to be identified. This may cause problems of incomplete measurement of the degrees of freedom of the identified mode-shape vector. To address this issue, we also implement modal estimation from the incomplete modal-information data obtained due to insufficient measurement channels; thus, only response data of the first, third, and fifth DOF of the railway system subjected to ambient excitation in the previous numerical example are employed to implement modal estimation. The modal estimation results are shown in Table 5. The modal parameters estimated by the proposed method and the exact results are in good agreement, because the errors in both natural frequencies and damping ratios are less than 1%. Thus, we confirm the effectiveness of the proposed method under the likely practical conditions of insufficient measurement information.

Table 5. Identification results of railway vehicle through Modified Stochastic Subspace Identification (MSSI) method from incomplete modal-information measurement data.

Mode	Natural Frequency (rad/s) [Ω]			Damping Ratio (%)		
	Exact	MSSI	Error (%)	Exact	MSSI	Error (%)
1	2.79	2.79	0.00	4.89	4.89	0.01
2	3.71	3.71	0.00	6.62	6.62	0.01
3	16.55	16.53	0.09	16.65	16.62	0.16
4	19.27	19.25	0.12	18.78	18.73	0.27
5	25.36	25.30	0.21	1.74	1.74	0.42
6	25.57	25.51	0.21	1.75	1.75	0.42

3.3. Experimental Validation of a Cantilever Beam

To further validate the effectiveness of the method proposed in this paper, an actual beam structure of free boundary is used for the experiment, as shown in Figure 13. Brüel & Kjær RT Pro Photon 7.41 data acquisition system, PCB 208C02 force sensor (with a sensitivity of 112,410 mV/kN, a measurement range of 0.4448 kN, a low frequency response (−5%)

of 0.001 Hz, and an upper frequency limit of 36,000 Hz), and Polytec OFV-5000 Modular Vibrometer (having a frequency range of DC-24 MHz with velocities up to ±10 m/s and displacements from the picometer to meter range) are used for measuring response signal. The simulated nonstationary excitation through Teledyne LeCroy T3AFG40 signal generator is imported into the Modal Shop K20070E01 vibration exciter, and the vibration shaker excites the cantilever beam structure. A typical white noise with an approximately consistent-power spectral density was synchronized with the shaker voltage time history and recorded, as shown in Figure 14, as provided from the waveform source panel in the RT Pro Photon 7.41 data acquisition system. Currently, an OMA-based roving different directions of sensor head of laser doppler vibrometer is performed to measure the actual modal properties of the beam structure by the data acquisition device, including four channels, only twenty measurement positions on the actual aluminum alloy beam were marked, as shown in Figure 15, and the shaker excitation impacts acted as the third location of the beam.

Figure 13. Schematic diagram of the experimental setup.

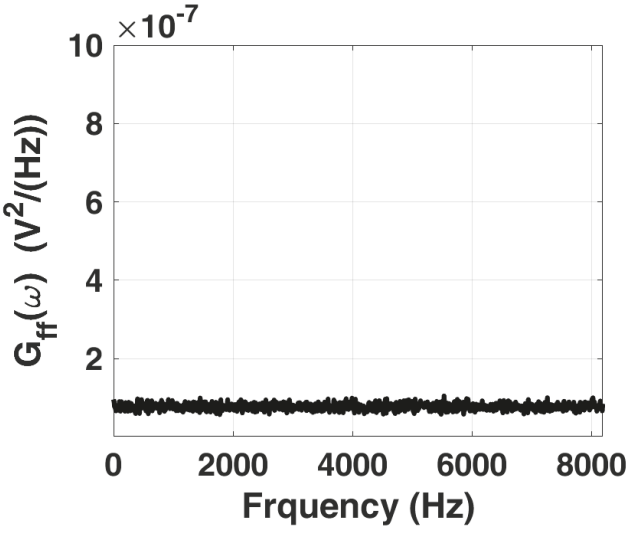

Figure 14. Power spectrum associated with stationary white noise.

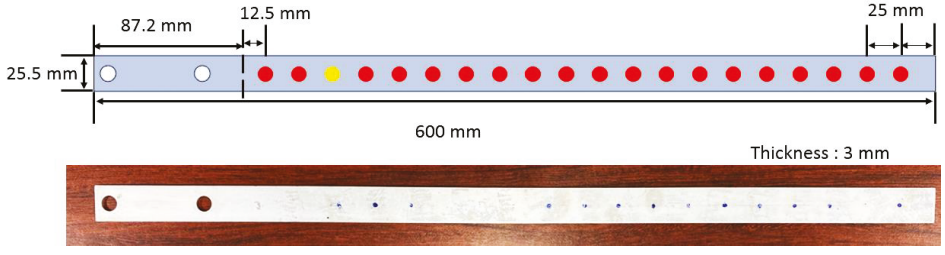

Figure 15. Twenty measurement positions marked on the actual aluminum alloy beam.

The length, width, and height of the beam structure used for this paper are 512.8, 25.5, and 3.0 mm, respectively, the mass is 104.97 g, and the material is 5052-0 aluminum alloy. In addition, the "exact" modal parameters are obtained from the data of auto power spectrum of stationary response and cross power spectrum of stationary excitation and response by using ME'Scope software. Note that "exact" stationary excitation is a built-in stationary white noise generated from Brüel & Kjær RT Pro Photon 7.41 data acquisition system is imported into the Modal Shop K20070E01 electrodynamic shaker to excite the cantilever beam structure. The natural frequencies of the first four modes are about 10.85, 70.32, 176.31, and 290.31 Hz, as listed in Table 6. Finally, the modal parameters obtained are used to compare the identification results of MSSI, as shown in Table 6 and Figure 16. It is observed that the frequency errors are less than 15%, Figure 16 shows the identified mode shapes which are approximately coincident with "exact" mode shapes, and the MAC values are larger than 0.77. This means that the proposed method is effective on modal identification in practical application.

Table 6. Identification results of a practical cantilever beam through Modified Stochastic Subspace Identification (MSSI) method.

Mode	Natural Frequency (rad/s)			MAC
	Exact	MSSI	Error (%)	
1	10.85	10.98	1.22	1.00
2	70.32	70.53	0.30	1.00
3	176.31	159.00	9.82	0.95
4	290.31	246.30	15.16	0.77

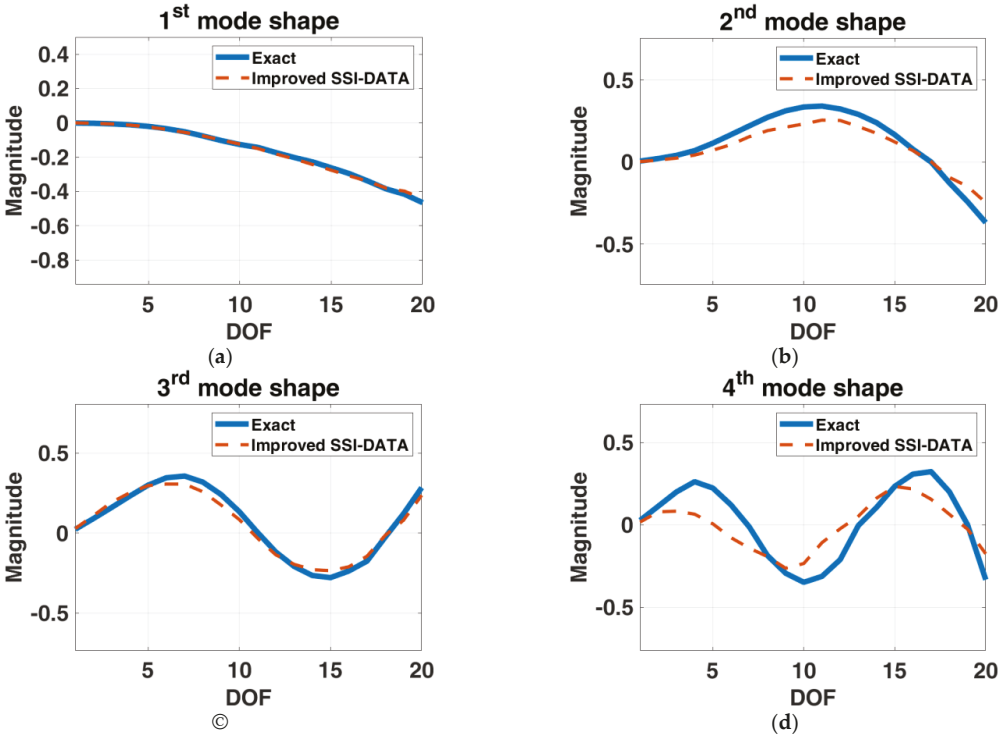

Figure 16. Comparison between the identified mode shapes and the "exact" mode shapes of a practical cantilever beam subjected to stationary white noise: (**a**) 1st mode shape; (**b**) 2nd mode shape; (**c**) 3rd mode shape; (**d**) 4th mode shape.

4. Conclusions

The topic of this paper was a study of ambient modal analysis based on the stochastic subspace identification technique (SSI). The paper aimed to develop the appropriate algorithms for output-only modal analysis to overcome difficulties when performing experimental modal analysis (EMA). As a modification of SSI, we introduced the procedure of solving the system matrix in SSI-COV in conjunction with SSI-DATA, allowing modal estimation to be well implemented. A system matrix can, therefore, be obtained directly from the observability matrix without evaluating the predictive-state matrix, and this will improve the efficiency of computation.

In addition, we extracted predictive-state matrixes with recursive relationships directly from the same original predictive-state matrix, and then omitted the step of reevaluating the predictive-state matrix at the next-time moment to improve the computational efficiency of the SSI method. In addition, through the SVD analysis of a data matrix $[\Omega][\Omega]^T$, evaluated by the projection matrix, $[\Omega]$, the modal estimation can be effectively performed, and the corresponding computational efficiency can be improved.

By solving the system matrix through the observability matrix and constructing a new predictive-state matrix composed from the original measured data matrix, the procedure of modal estimation can be simplified, and the modal parameters can be effectively identified, even for a structural system having closely spaced modes and relatively high damping. Furthermore, the proposed modified SSI algorithm is applicable to the parametric estimation of structures with incomplete modal information obtained from insufficient measurement channels. In addition, the computational efficiency of the SSI method can be improved due to the non-uniqueness of the observability matrix. However, the need for white noise

excitation is still a main limitation to be resolved in the proposed method from ambient response, and many mechanical systems are expected to be excited by significantly different frequency content, in particular, by specific harmonics [27,28]. The actual limitations and the applicability of the proposed method to real mechanical systems could be considered for discussion in future work. Through numerical simulations and experimental verification, we illustrated and validated the effectiveness of the proposed method for modal estimation of structural systems from stationary ambient response data only.

Author Contributions: C.-S.L. conceived of the proposed idea, designed the experiments and verified the data along with Y.-X.W. The draft preparation was originally written by the first and corresponding author C.-S.L. The article was mainly revised by C.-S.L. and reviewed and edited in part by Y.-X.W. All authors have read and agreed to the published version of the manuscript.

Funding: This research was supported by Ministry of Science and Technology of Taiwan under the grant MOST 110-2221-E-020-008-.

Institutional Review Board Statement: Not applicable.

Informed Consent Statement: Not applicable.

Data Availability Statement: Not applicable.

Acknowledgments: This research was supported in part by Ministry of Science and Technology of Taiwan under the grant MOST 110-2221-E-020-008-. The authors would like to thank the anonymous reviewers for their valuable comments and suggestions in revising the paper.

Conflicts of Interest: The authors declare no conflict of interest.

References

1. Martini, A.; Troncossi, M.; Vincenzi, N. Structural and elastodynamic analysis of rotary transfer machines by Finite Element model. *J. Serb. Soc. Comput. Mech.* **2017**, *11*, 1–16. [CrossRef]
2. Manzato, S.; Peeters, B. Wind turbine model validation by full-scale vibration test. In Proceedings of the European Wind Energy Conference (EWEC) 2010, Warsaw, Poland, 20–23 April 2010.
3. Zivanovic, S.; Pavic, A.; Reynolds, P. Modal Testing and FE Model Tuning of a Lively Footbridge Structure. *Eng. Struct.* **2006**, *28*, 857–868. [CrossRef]
4. Ren, W.X.; Peng, X.L.; Lin, Y.Q. Experimental and Analytical Studies on Dynamic Characteristics of a large Span Cables-stayed Bridge. *Eng. Struct.* **2005**, *27*, 535–548. [CrossRef]
5. Orlowitz, E.; Brandt, A. Comparison of experimental and operational modal analysis on a laboratory test plate. *Measurement* **2007**, *102*, 121–130. [CrossRef]
6. Moaveni, B.; Masoumi, Z. Modifying the ERA and fast ERA to improve operational performance for structural system identification. *Mech. Syst. Signal Process.* **2019**, *120*, 664–692. [CrossRef]
7. Brincker, R.; Kirkegaard, P.H. Special issue on Operational Modal Analysis. *Mech. Syst. Signal Process.* **2010**, *24*, 1209–1212. [CrossRef]
8. Reynders, E.; Houbrechts, J.; De Roeck, G. Fully automated (operational) modal analysis. *Mech. Syst. Signal Process.* **2012**, *29*, 228–250. [CrossRef]
9. Yi, W.J.; Zhou, Y.; Kunnath, S.; Xu, B. Identification of localized frame parameters using higher natural modes. *Eng. Struct.* **2008**, *30*, 3082–3094. [CrossRef]
10. Soria, L.; Peeters, B.; Anthonis, J. Operational modal analysis and the performance assessment of vehicle suspension systems. *Shock. Vib.* **2012**, *19*, 1099–1113. [CrossRef]
11. Shirzadeh, R.; Devriendt, C.; Bidakhvidi, M.A.; Guillaume, P. Experimental and computational damping estimation of an offshore wind turbine on a monopile foundation. *J. Wind. Eng. Ind. Aerodyn.* **2013**, *120*, 96–106. [CrossRef]
12. Peeters, B.; Van der Auweraer, H.; Vanhollebeke, F.; Guillaume, P. Operational modal analysis for estimating the dynamic properties of a stadium structure during a football game. *Shock. Vib.* **2007**, *14*, 283–303. [CrossRef]
13. James, G.H.; Carne, T.G.; Lauffer, J.P. *The Natural Excitation Technique for Modal Parameter Extraction from Operating Wind Turbines*; SAND92-1666.UC-261; Sandia National Laboratories: Albuquerque, NM, USA, 1993.
14. Chiang, D.-Y.; Lin, C.-S. Identification of Modal Parameters from Nonstationary Ambient Vibration Data Using Correlation Technique. *AIAA J.* **2008**, *46*, 2752–2759. [CrossRef]
15. Lin, C.-S.; Chiang, D.-Y. Modal identification from nonstationary ambient response data using extended random decrement algorithm. *Comput. Struct.* **2013**, *119*, 104–114. [CrossRef]
16. Chiang, D.-Y.; Lin, C.-S. Identification of modal parameters from ambient vibration data using eigensystem realization algorithm with correlation technique. *J. Mech. Sci. Technol.* **2010**, *24*, 2377–2382. [CrossRef]

17. Liu, F.; Wu, J.; Gu, F.; Ball, A.D. An Introduction of a Robust OMA Method: CoS-SSI and Its Performance Evaluation through the Simulation and a Case Study. *Shock. Vib.* **2019**, *2019*, 1–14. [CrossRef]
18. Van Overschee, P.; De Moor, B. Subspace algorithms for the stochastic identification problem. *Automatica* **1993**, *29*, 649–660. [CrossRef]
19. Shokravi, H.; Shokravi, H.; Bakhary, N.; Koloor, S.S.R.; Petrů, M. Health Monitoring of Civil Infrastructures by Subspace System Identification Method: An Overview. *Appl. Sci.* **2020**, *10*, 2786. [CrossRef]
20. Peeters, B.; De Roeck, G. Reference-based stochastic subspace identification for output-only modal analysis. *Mech. Syst. Signal Process.* **1999**, *13*, 855–878. [CrossRef]
21. Shinozuka, M. Simulation of Multivariate and Multidimensional Random Processes. *J. Acoust. Soc. Am.* **1971**, *49*, 357–368. [CrossRef]
22. Allemang, R.J. The Modal Assurance Criterion—Twenty Years of Use and Abuse. *Sound Vib.* **2003**, *37*, 14–23.
23. Troncossi, M.; Taddia, S.; Rivola, A.; Martini, A. Experimental Characterization of a High-Damping Viscoelastic Material Enclosed in Carbon Fiber Reinforced Polymer Components. *Appl. Sci.* **2020**, *10*, 6193. [CrossRef]
24. Troncossi, M.; Canella, G.; Vincenzi, N. Identification of polymer concrete damping properties. *Proc. Inst. Mech. Eng. Part C J. Mech. Eng. Sci.* **2020**, in press. [CrossRef]
25. Petsounis, K.; Fassois, S. Parametric time-domain methods for the identification of vibrating structures—A critical comparison and assessment. *Mech. Syst. Signal Process.* **2001**, *15*, 1031–1060. [CrossRef]
26. Hu, S.-L.J.; Yang, W.-L.; Liu, F.-S.; Li, H.-J. Fundamental comparison of time-domain experimental modal analysis methods based on high- and first-order matrix models. *J. Sound Vib.* **2014**, *333*, 6869–6884. [CrossRef]
27. Campione, I.; Fragassa, C.; Martini, A. Kinematics optimization of the polishing process of large-sized ceramic slabs. *Int. J. Adv. Manuf. Technol.* **2019**, *103*, 1325–1336. [CrossRef]
28. Zaghbani, I.; Songmene, V. Estimation of machine-tool dynamic parameters during machining operation through operational modal analysis. *Int. J. Mach. Tools Manuf.* **2009**, *49*, 947–957. [CrossRef]

applied sciences

MDPI

Article

An Application of Instantaneous Spectral Entropy for the Condition Monitoring of Wind Turbines

Marco Civera [1,*] and Cecilia Surace [2]

[1] Department of Mechanical and Aerospace Engineering—DIMEAS, Politecnico di Torino, Corso Duca degli Abruzzi 24, 10129 Turin, Italy
[2] Department of Structural, Geotechnical and Building Engineering—DISEG, Politecnico di Torino, Corso Duca degli Abruzzi 24, 10129 Turin, Italy; cecilia.surace@polito.it
* Correspondence: marco.civera@polito.it

Abstract: For economic and environmental reasons, the use of renewable energy sources is a key aspect of the ongoing transition to a sustainable industrialised society. Wind energy represents a major player among these natural, carbon-neutral sources. Nevertheless, wind turbines are often subject to mechanical faults, especially due to ageing. To alleviate Operation and Maintenance costs, Vibration-Based Inspection and Condition Monitoring have been proposed in recent times. This research proposes Instantaneous Spectral Entropy and Continuous Wavelet Transform for anomaly detection and fault diagnosis, departing from gearbox vibration time histories. The approach is validated on experimental data recorded from a turbine suffering bearing failure and total gearbox replacement. From a computational point of view, the proposed algorithm was found to be efficient and therefore even potentially applicable for real-time monitoring.

Keywords: structural health monitoring; condition monitoring; fault detection; rotating machinery; wind turbines; instantaneous entropy; generalised morse wavelet

Citation: Civera, M.; Surace, C. An Application of Instantaneous Spectral Entropy for the Condition Monitoring of Wind Turbines. *Appl. Sci.* **2022**, *12*, 1059. https://doi.org/10.3390/app12031059

Academic Editor: Wei Huang

Received: 16 December 2021
Accepted: 18 January 2022
Published: 20 January 2022

Publisher's Note: MDPI stays neutral with regard to jurisdictional claims in published maps and institutional affiliations.

Copyright: © 2022 by the authors. Licensee MDPI, Basel, Switzerland. This article is an open access article distributed under the terms and conditions of the Creative Commons Attribution (CC BY) license (https://creativecommons.org/licenses/by/4.0/).

1. Introduction

According to the 2020 New Energy Outlook (NEO) released by BloombergNEF, wind and solar energy are expected to grow up to 56% of global electricity demand by 2050, with wind energy retaking the lead from photovoltaic [1]. By way of example, Denmark is intended to achieve 100% non-fossil-based power generation by the same year, mostly thanks to wind power [2].

This represents a unique opportunity for transitioning from classic, polluting fuels to renewable and sustainable resources. In this regard, wind turbines are, nowadays, a well-established technology and cost-efficient, especially when grouped in wind farms (both on- and off-shore). Worldwide, the wind power capacity increased from about 13 Giga Watts in 1999 to >760 GW in 2020 [3]. Furthermore, if compared to other alternatives such as large hydropower plants, solar photovoltaic, or nuclear energy, wind power had the most stable growth in the 2005–2016 period, being less subject to market fluctuations [4].

However, a major issue for the rapidly increasing market of wind power systems is the relatively high probability of mechanical faults in wind turbines' gearboxes. In turn, this generates high Operation and Maintenance (O&M) costs. In detail, it has been estimated that fixed and variable O&M costs account for between 11% and 30% of the Levelized Cost Of Energy (LCOE, €/MWh) for onshore wind farms [5–7]. The costs for offshore installations are much greater, due to the accessibility constraints and the hostile environment (the topic is analysed in-depth in [8]).

Apart from some notable exceptions, like visual inspection (standard or enhanced; see, e.g., [9]), oil analysis [10], or Non-Destructive Testing (NDT) approaches such as Ultrasonic Testing [11], Acoustic Emissions [12], Thermography [13], and X-ray [14], Vibration-Based

Inspection [15] is nowadays widely accepted as the standard for condition-based maintenance, in particular for gearbox condition monitoring. Several signal processing techniques and approaches have been proposed throughout the last 30 years for this specific application; a recent and well-documented review can be found in [16]. In fact, the Structural Health Monitoring (SHM) of the wind turbines' several components has attracted much interest from the researchers' community in the last decade (see, e.g., [17–20]).

The procedure discussed here is based on the instantaneous definition of the Shannon Spectral Entropy (SSE, [21]). That is to say, the Instantaneous Spectral Entropy (ISE) is applied as a time-dependent, damage-sensitive feature for damage event detection. Indeed, Spectral Entropy has been suggested for the assessment of rolling-element bearing performance [22]. In its standard definition, it has been applied to stationary signals for the Structural Health Monitoring of masonry buildings [23,24] and steel pipelines [25,26]. In previous studies, ISE was validated for an aluminium frame structure undergoing structural changes under controlled laboratory conditions [27]. However, to the best of the Authors' knowledge, it has never been investigated for condition monitoring purposes, let alone on experimental data originating from wind turbines under operating conditions.

The remaining of this article is organised as follows. In Section 2, the theory of SSE and ISE is recalled. Section 3 resumes some basic definitions for the Continuous Wavelet Transform (CWT) and the Generalised Morse Wavelet (GMW), which have been utilised here to define the time–frequency (TF) representations needed for the ISE analysis. Section 4 describes the experimental case study. Section 5 reports the results and Section 6 briefly discusses them. The Conclusions end this discussion.

2. The Instantaneous (Shannon) Spectral Entropy

In this research, the Instantaneous Spectral Entropy is proposed as a damage-sensitive index for condition monitoring. Specifically, the Shannon Spectral Entropy is utilised for this aim. The rationale for entropy measurements in SHM is quite straightforward. It derives from the eighth (and last) axiom of Structural Health Monitoring [28], which states that: "*damage increases the complexity of a system*" [29] where the definition of 'complexity' (intentionally left vague by the original authors) can be intended from both a geometrical and signal processing standpoint. In the first case, the damage is intended as a localised inhomogeneity, which can be detected from a certain time instant (the 'damage event') onwards. From the vibrational perspective, this is rather intended as the occurring of additional signal components, previously inexistent in the undamaged baseline. A classic example would be the insertion of super- and sub-harmonics due to the presence of a breathing crack in an otherwise linearly behaving structure [30]. In this sense, the concept of an entropic framework for signal analysis has been recently further detailed in [31].

Noteworthy, the concept of an 'increase' in complexity naturally incorporates the pre-existing conditions, that is to say, randomly distributed manufacturing defects in the structure under investigation and measurement noise in the recordings derived from its analysis [32]. These aspects do not affect the entropy variation when damage is inserted in the system; therefore, this framework fits well in the general context of SHM as an outlier (anomaly) detection problem, i.e., as a deviation from a known baseline [33].

As mentioned earlier, this work deals with the instantaneous definition of entropy, aiming at damage event detection. In this sense, it is necessary to recall that vibration time series can be analysed with different signal processing approaches, depending on the intended purposes. These fall into two main categories:

1. real-time analysis, using a small moving window of recent history over the data stream.
2. retrospective analysis, where the time series data are fully available and analysed a posteriori.

In both cases, instantaneous parameters can be used to perform event detection; this can be then applied to define the instant of damage occurrence (see, e.g., [34]). For the sake of this research, the second case (retrospective analysis) will be considered. This is not uncommon for SHM applications, where signals are sampled periodically (in the case study

of this research, every hour) and then processed. Under these conditions, the rationale is that a mechanical fault should be detected shortly after its appearance, in a near-real-time fashion (i.e., with only some hours or, in the worst case, some days of delay). Truly real-time SHM is more challenging since it strictly requires an uninterrupted, seamless stream of data, plus computationally efficient routines capable of processing the raw data in a short timeframe. This is generally an unnecessary complication, apart from extremely fragile structures or systems, prone to sudden collapse.

In this regard, a notable example comes from the Aerospace Engineering field. In the case of rotorcraft's Health and Usage Monitoring Systems (HUMSs [35]), the real-time condition monitoring of the rotating components is essential due to the rotorcrafts implicit inability to sustain non-propelled flight. This sort of application falls beyond the aims of this study; nevertheless, it will be shown how the proposed approach is suitable for such tasks, thanks to a relatively short execution time.

Another important caveat should be addressed before moving on to the proper mathematical definition of SSE and ISE. That is, it is important to recall that the entropy of the recorded output does not depend solely on the system behaviour. Indeed, it reflects the frequency content of the input as well. For this reason, entropy-based approaches are particularly well-suited for the operational modal analysis of civil structures and infrastructures since the ambient vibrations can be easily approximated to a pure white Gaussian noise [23,24]. However, the concept is still suitable for deterministic driving forces. As long as the input remains constant (or at least similar), any relevant variation in the output entropy can be directly linked to a structural change in the target system. As it will be shown later for the experimental case study, this condition is satisfied for wind turbines operating at similar wind speeds. Furthermore, this input dependence can be easily bypassed by pairing ISE values with wind speed readings and considering only threshold trespassings at a constant wind speed.

2.1. Shannon Spectral Entropy

The general term spectral entropy (SE) refers to any measure of the uniformity of a signal spectral power distribution. The definition of Shannon SE originates from the works of Powell & Percival [21], based on the measure of uncertainty proposed by Shannon in [36]. Specifically, the SSE formula can be considered as the limit form of the generalised Rényi entropy for $\alpha \to 1$ [37]. Specifically, for a given probability distribution in the frequency domain $P(f)$, the SSE can be defined as

$$\mathrm{SSE} = -\sum_{f}^{B} P(f) \log_{10} P(f), \tag{1}$$

where B is the total number of discrete frequencies, i.e., the bins of the distribution. Please note that here, the base 10 logarithm was applied; however, any other base can be used, without major conceptual differences. Equation (1) can be normalised by dividing it by $\log_{10} B$; nevertheless, for the sake of this research, the standard (non-normalised) definition of Equation (1) has been preferred.

For a discretised power spectrum $|H(f)|^2$, where H indicates the Discrete Fourier Transform of a general signal $h(t)$, the probability distribution can be written as

$$P(f) = \frac{|H(f)|^2}{\sum_{f}^{B} |H(f)|^2}. \tag{2}$$

This can be then extended to include the time dependency.

2.2. Instantaneous Spectral Entropy

Similar to Equation (2), it is possible to define the probability distribution at time t as

$$P(f,t) = \frac{|H(f,t)|^2}{\sum_f^B |H(f,t)|^2}, \tag{3}$$

where $H(f,t)$ can be any form of time–frequency (TF) representation of the signal (this aspect will be discussed in more detail in the next section). Then, the Instantaneous (Shannon) Spectral Entropy becomes

$$\mathrm{SSE}(t) = -\sum_f^B P(f,t)\log_{10} P(f,t). \tag{4}$$

Generally speaking, several options are available for the TF analysis of a given signal. For this specific case, the Continuous Wavelet Transform was applied, using a Generalised Morse Wavelet as the mother wavelet.

3. The Continuous Wavelet Transform and Generalised Morse Wavelet

The theory of wavelets and wavelet-based signal processing would be too long to be recalled here; the interested reader is referred to the classic works of Rioul & Vetterli [38], and Daubechies [39] for the basics concepts, and the book of Mallat [40] for a complete discussion. In a few words, the main (but not the only one) feature of any wavelet is its compact support in time. Differently from harmonic functions, which span indefinitely from $t = -\infty$ to $+\infty$, these brief oscillations allow capturing time-varying phenomena [41]. For this reason, orthonormal wavelets have been extensively utilised for signal analysis via Wavelet Transform (WT), especially for SHM applications (see, by way of example, [42]; a review about this topic can be found in [43]). In this regard, several variants of WT exist, depending on the shifting and scaling of the basis function, known as the mother wavelet (these points will be further discussed later). The two main forms are Discrete and Continuous WTs; here in this study, the CWT has been applied.

3.1. Continuous Wavelet Transform

Considering again the signal $h(t)$ defined in the time domain, its CWT can be expressed (according to its most usual definition) as

$$CWT_h(a,b) = \int_{-\infty}^{+\infty} h(t)\psi_{a,b}{}^*(t)dt, \tag{5}$$

i.e., a convolution of the given data sequence (here, the time series) with a resized and time-translated version of the so-called mother wavelet, given as

$$\psi_{a,b}(t) = \frac{1}{\sqrt[2]{a}}\psi\left(\frac{t-b}{a}\right). \tag{6}$$

Therefore, $\psi_{a,b}$ depends on the shift (b) and scale (a) parameters, as well as on the original shape of this mother wavelet, which in turn is an arbitrarily selected localised oscillatory function. Converting the wavelet scale to frequency, the final result is a TF transform of the analysed time series. Please note that the term $\frac{1}{\sqrt[2]{a}}$ in Equation (6) is only needed to ensure equal energy at all time scales.

Importantly, it must be recalled that there is not a unique definition for the mother wavelet ψ. Any time-limited oscillatory function with zero means and that satisfies certain regularity and admissibility conditions [44] can be arbitrarily selected as the mother wavelet. In this sense, a comparative analysis for SHM purposes can be found in [45]. Here for this study, the Generalised Morse Wavelet has been tested.

3.2. Generalised Morse Wavelet

For CWT-based signal processing, analytic wavelets are currently considered the best option for precise TF analysis. These can be seen as complex-valued time/frequency localised filters with vanishing support on negative frequencies [46]. In this regard, the complex (or analytic) Morlet wavelet is arguably the most common option adopted. It has been widely applied for the extraction of instantaneous parameters, e.g., from seismic data [47]. Recently, the Morlet wavelet power spectral entropy has been investigated as well, specifically for bearing fault localisation and severity assessment [48].

However, the complex Morlet wavelet is only approximating analytical for large centre frequency (f_c) values. For small f_c values, it may not meet the admissibility condition and thus potentially lead to a negative frequency [49]. For this reason, the generalised Morse wavelet has been preferred for this application, due to its totally analytic definition and better time resolution.

The GMW was firstly envisioned by Daubechies & Paul [50], and then further detailed and investigated by Lilly & Olhede [46,49]. Its formulation can be expressed in the frequency domain (considering the natural pulsation $\omega = 2\pi f$ for simplicity) as [46]

$$\Psi_{\beta,\gamma}(\omega) = U(\omega)\alpha_{\beta,\gamma}\omega^{\beta}e^{-\gamma\omega}, \tag{7}$$

where $U(\omega)$ is the Heaviside (or unit) step function, $\alpha_{\beta,\gamma}$ is a normalizing constant, and β and γ are the two parameters which govern the specific shape taken by the general formulation of Equation (7). More precisely, these two parameters are known as symmetry (γ) and compactness (β). Furthermore, a third parameter, the time–bandwidth product, can be defined as $P^2 = \beta\gamma$ and is used often (but not here) in lieu of β.

The main feature of the GWT is its adaptability, as it can be dilated or contracted in the time–frequency domain to better suit the signal processing aims.

In detail, $\sqrt[2]{P2}$ is directly proportional to the wavelet support along the time axis. Therefore, for constant γ, increasing β implies a longer time–bandwidth. In turn, this increases the rate of the long-time decay and broadens the central portion of the resulting mother wavelet. For time–frequency analysis, a longer time duration, T, implies more refined frequency resolution, $\Delta f = 1/T$, which is generally useful. This point will be better discussed in the Results (Section 5).

On the other hand, the gamma parameter controls the symmetry of the wavelet in time through the demodulate skewness [49]. Increasing γ for constant β does not affect the time–bandwidth, but broadens the GWT envelope, making it more or less directional. For instance, if $\gamma = 1$, the zeroth-order GWT corresponds to the Cauchy wavelet [51], which is strictly supported in a narrow convex cone in the time–frequency domain.

Different GWT shapes can better serve different purposes. These shapes can be grouped in a piecewise fashion as follows:

1. For constant $\gamma \leq 3$ (negative skewness), the time decay increases as the time–bandwidth (P^2, thus β) increases.
2. For constant $\gamma \geq 3$ (positive skewness), the mother wavelet becomes more symmetric as β increases.

Therefore, for $\gamma = 3$, both the time decay and the wavelet symmetry increase with β, and the resulting mother wavelet narrows in frequency and enlarges in time, with more oscillations under its envelope. This derives from the demodulate skewness of the GWT being null for gamma equal to 3; this results in a global maximum of the time/frequency concentration [46]—that is to say, it maximises the product of the time-domain and frequency-domain standard deviations, known as the Heisenberg's area [40]. Again, all these aspects will be further investigated in a later Section.

4. The Experimental Case Study

The experimental recordings from a wind turbine have been used for the validation of the proposed entropy-based Condition Monitoring strategy. The dataset (described

in detail in [52]) originates from an undisclosed onshore wind farm, located in Northern Sweden and consisting of 18 2.5 MW Nordex N100 wind turbines [53]. The continuous monitoring was performed over 46 consecutive months, acquiring 1.28 s-long time series (16,384 data points for a sampling frequency $f_s = 12,800$) approximately every 12 h.

Specifically, Turbine #5 was considered here, as the only one (out of six installations included in the dataset) that suffered mechanical faults during the monitored timeframe.

The vibration time series of interest were collected from an accelerometer, located and oriented as indicated by the black arrow in Figure 1 (which is based on the original schematics from [52]). This was mounted on the housing of the output shaft bearing of the turbine. The three-stage gearbox was made up of two sequential planetary gear stages, followed by a helical gear stage. The position of the bearing failure is highlighted in red in Figure 1. The damage consisted of an inner raceway failure on one of the four NSK RN2240 cylindrical roller bearings (CRBs) supporting one of the planets in the first planetary gear. From visual inspection after disassembly (refer to [52,53]), the most probable cause was identified as rolling fatigue-induced flaking (according to the NSK definition [54]), with a loss of material and the consequent rough and coarse texture extended over most of the contact surface. This caused the entire gearbox to be replaced after two years of operation.

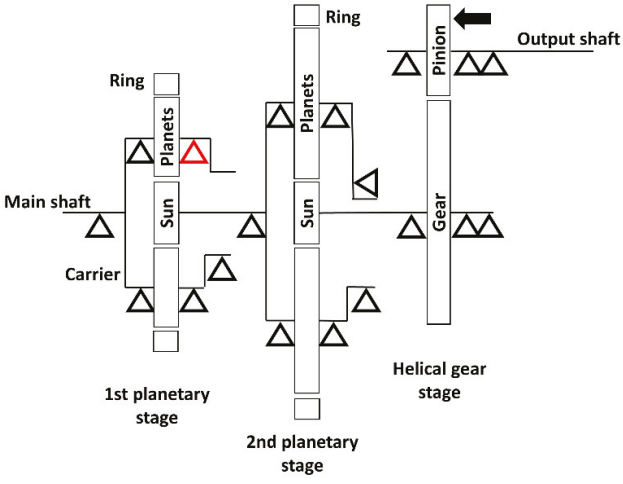

Figure 1. Schematics of the three-stage gearbox, with the damaged bearing highlighted in red and the position and direction of the output channels indicated by the black arrow.

Two signals of interest (portrayed in Figure 2) were defined by concatenating in chronological order some consecutive time histories (THs), recorded from Turbine #5 as described in Table 1 (the period column in Table 1 reports the time since the beginning of the continuous monitoring as year fractions). The concatenating procedure applied here reflects what was performed by Figueiredo et al. [55], to artificially generate a nonstationary experimental benchmark from stationary experimental recordings, emulating time-varying structural conditions with abrupt changes.

For signal #1, three segments were considered. These correspond to one recording (the first one) shortly before replacement and two acquisitions (the remaining two thirds) shortly after. These latter two were chosen since they are consecutive recordings with very similar rotational speeds (i.e., very similar external input; reported as cycles per minute).

Signal #1 was intended to study the effectiveness of the algorithm, presenting a discussion on parameter setting. For Machine Learning purposes, only the first tract was used as training data for the statistical modelling of the normal operating conditions (NOCs). The second and third parts of the signal provided the test points for the damage index.

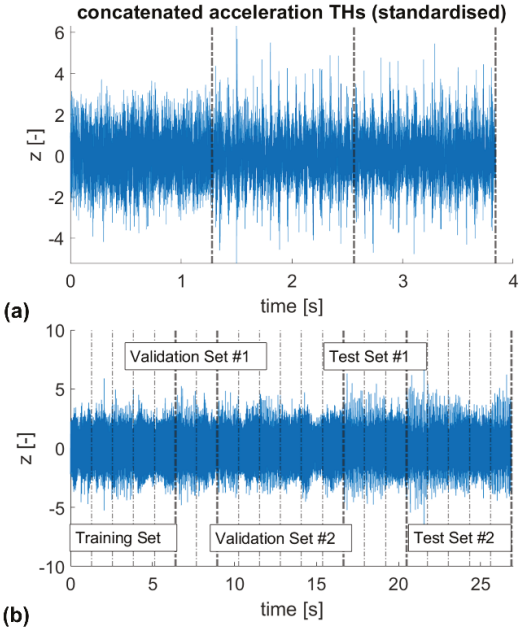

Figure 2. The investigated signals: (**a**) #1, (**b**) #2. Data standardised as $z(t) = (h(t) - \mu(h(t)))/\sigma(h(t))$. In (**a**), the dot-dashed vertical lines represent the three concatenated segments. In (**b**), the thick dot-dashed vertical lines enclose the segments considered for the training set, the two validation sets, and the two test sets, in this order (see Table 1). The single segments are separated by thin vertical lines.

For signal #2, a larger set of acquisitions were included. In this latter case, by considering only the optimised algorithm parameters, the intent was to address the full capabilities of the proposed approach when trained on more than one tract. Thus, signal #2 was evaluated on data with (almost) comparable rotational speeds before and after bearing damage. Specifically, the following segments were used:

1. seven consecutive tracts corresponding to 14 months before fault (the first five elements for training and the last two for validation),
2. the single tract already included in signal #1 plus five other nearby tracts immediately before fault (all included for further validation),
3. three recordings taken immediately after replacement, including the two already considered in signal #1 (all considered for testing),
4. other five segments acquired 7 months later (considered again for further testing).

The second part of Table 1 reports more details about these THs.

For both signal #1 and #2, the data, originally reported in terms of [g], were standardised (subtracting the mean and dividing by the standard deviation, for each recording separately) to remove any potential issue related to the different amplitudes.

Figure 3 reports the Fast Fourier Transforms (FFT) of the five sets included in signal #2. One can notice that the multiple harmonic components of each acquisition do not allow for a simple comparison between the frequency content before and after the gearbox replacement. Thus, the common damage detection strategy based on the analysis of the frequency shift is hardly feasible in these circumstances. The same can be said for signal #1 as well since it comprises a subset of the segments of signal #2. Indeed, the limited reliability of FFT-based signal analysis for these typologies of bearing failure in wind turbine gearboxes was reported as well in [53].

Table 1. The concatenated recordings, as reported in the experimental database [1].

Signal #1				
ID number	Period of recording [years]	Rotational speed [cpm]	Structural conditions	Set
1588	1.9972	785.45	Immediately pre-replacement	Training
1593	2.0040	783.61	Immediately post-replacement	Test
1594	2.0054	783.18	Immediately post-replacement	Test
Signal #2				
ID number	Period of recording [years]	Rotational speed [cpm]	Structural conditions	Set
785	0.7936	777.79	More than one year pre-replacement	Training
786	0.7988	714.90	>1 year pre-replacement	Training
787	0.7989	779.824	>1 year pre-replacement	Training
788	0.8080	708.74	>1 year pre-replacement	Training
789	0.8205	711.63	>1 year pre-replacement	Training
790	0.8208	785.33	>1 year pre-replacement	Validation #1
791	0.8217	774.61	>1 year pre-replacement	Validation #1
1485	1.8480	768.34	Immediately pre-replacement	Validation #2
1486	1.8493	733.26	Immediately pre-replacement	Validation #2
1487	1.8507	772.99	Immediately pre-replacement	Validation #2
1488	1.8521	832.43	Immediately pre-replacement	Validation #2
1489	1.8537	706.29	Immediately pre-replacement	Validation #2
1588 [2]	1.9972	785.45	Immediately pre-replacement	Validation #2
1593 [3]	2.0040	783.61	Immediately post-replacement	Test #1
1594 [3]	2.0054	783.18	Immediately post-replacement	Test #1
1595	2.0076	744.07	Immediately post-replacement	Test #1
2021	2.5995	786.29	More than half a year post-replacement	Test #2
2022	2.6009	777.30	>1/2 year post-replacement	Test #2
2023	2.6023	772.13	>1/2 year post-replacement	Test #2
2024	2.6036	757.19	>1/2 year post-replacement	Test #2
2025	2.6050	836.38	>1/2 year post-replacement	Test #2

[1] http://ltu.diva-portal.org/smash/record.jsf?pid=diva2%3A1244889&dswid=-2411 (accessed on 24 June 2021).
[2] Already included in signal #1 for training. [3] Already included in signal #1 for testing.

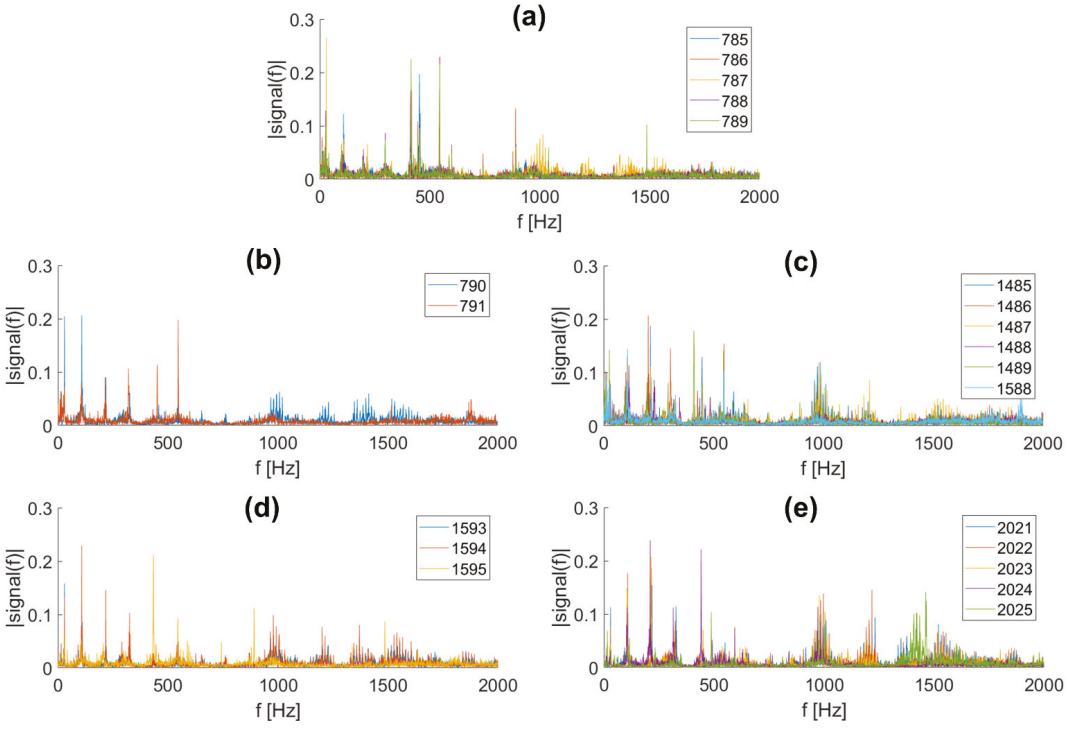

Figure 3. Fast Fourier Transforms (FFTs) of the segments of each set included in signal #2. (**a**): training set; (**b**): validation set #1; (**c**): validation set #2; (**d**): test set #1; (**e**): test set #2.

5. Results

5.1. Signal #1

An example of results is reported in Figure 4. The green line corresponds to the Instantaneous Spectral Entropy, defined at any timestep. The two horizontal dashed lines correspond to the upper and lower bounds of the Gaussian distribution fitted over the ISE values of the training set, that is to say, $\mathrm{ISE}(t) \equiv \mu_b + 2\sigma_b$ and $\mathrm{ISE}(t) \equiv \mu_b - 2\sigma_b$, where μ_b and $2\sigma_b$ correspond, in the same order, to the mean and standard deviation of the baseline tract, which is assumed to be almost stationary.

However, it was verified that these two thresholds were not optimal for anomaly detection. Indeed, as it can be seen, the $\mathrm{ISE}(t)$ value is quite unstable and subject to strong, rapid fluctuations. For this reason, a moving mean (calculated over a sliding window of 10,000 timesteps, i.e., 0.84 s) was preferred as a more stable indicator. This is indicated by the thick black line. The area shaded in grey corresponds to its expected values in 'normal' conditions, defined (similarly as before) as all points in between $\mu_{\mathrm{movmean},b} - 2\sigma_{\mathrm{movmean},b} < \mathrm{ISE}(t) < \mu_{\mathrm{movmean},b} + 2\sigma_{\mathrm{movmean},b}$, i.e., with a 95.45% confidence of belonging to the same population as the training data points. One can see that, for the two test scenarios, the value of the moving average of $\mathrm{ISE}(t)$ generally deviated from the previously stationary conditions, trespassing the lower threshold. This can be used to perform automated and instantaneous fault detection.

The results portrayed in Figure 4 focus on a single value of symmetry ($\gamma = 3$) and varying β. The effects of these two parameters have been thoroughly investigated. The findings will be discussed in the next subsection. However, the two points (1) and (2) highlighted above were encountered for any combination of γ and β. This proves that the $\mathrm{ISE}(t)$, especially when smoothed via a moving average with a properly sized window

length, is, overall, effective and efficient as a time-dependent DSF, thus suitable for damage event detection.

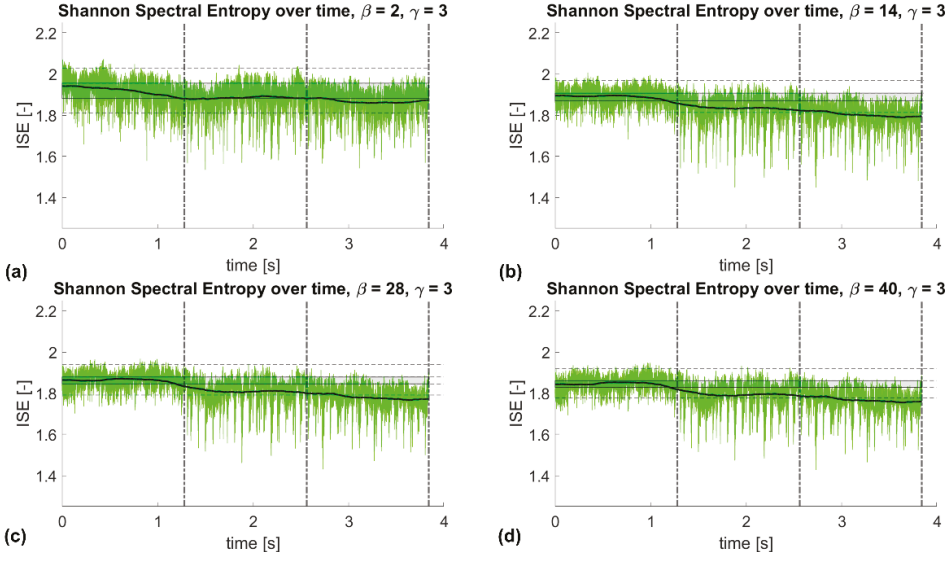

Figure 4. Resulting ISE (signal #1). Values for $\gamma = 3$ and β equal to (**a**) 2, (**b**) 14, (**c**) 28, and (**d**) 40.

5.1.1. Sensitivity Analysis for the GWT Parameters

Since the ISE(t) is a synthetic feature derived from the TF transform of the recorded signal, better time and frequency resolution will return more reliable results. Thus, it is essential to optimise the CWT settings. In the case investigated here, as mentioned in Section 3, the particular shape of the Generalised Morse (mother) Wavelet depends exclusively on the values considered for the doublet of parameters (β, γ). Therefore, to improve the capabilities of the proposed DSF, fine-tuning these two parameters becomes the most critical aspect of the whole procedure. For this reason, a dedicated sensitivity analysis has been performed.

The following cases were considered:

1. Symmetry equal to $\gamma = 1,\ 1.5,\ 2,\ 2.5,\ 3,\ 3.5,$ or 4.
2. β varying from 2 to 40 in steps of 2.

Hence, a total of 140 combinations were analysed. The range of β was defined to not exceed the suggested $\frac{\beta}{\gamma} \leq 40$ ratio [49]. Accordingly, P^2 (as the product of the lowest values of both β and γ) ranges from a minimum of 2 to a maximum of 160.

The aim of this optimisation is dual. For the training dataset, the data should behave as homogeneously as possible, to clearly define a NOCs model. This implies the signal stationarity (that is, constant mean μ and standard deviation σ) and low variability (i.e., low sigma values).

For a constant gamma (in the previous example of Figure 4, $\gamma = 3$) increasing β decreased the absolute value of both $\mu(\text{ISE})$ and $\sigma(\text{ISE})$. This latter point resulted in a narrower interval of confidence. In turn, this increased the sensitivity to damage as the threshold was lowered. The same trend was observed for all the other values of γ investigated here as well.

Regarding the testing part (second and third tracts of the concatenated signal), it is also noticeable how larger β values increased the detectability of the fault condition, making a more marked transition from the "pre" to "post" damage insertion conditions. Again, this finding was verified for all values of $\gamma \in [1, 4]$.

As anticipated, this derives from the detail of the TF representation. Figure 5 shows this point for the examples reported in Figure 4. Please note that to avoid any potential aliasing issue and considering the very high sampling frequency, the TF was truncated at $f_s/4$ (3200 Hz). The instant corresponding to the damage event is marked by the red dashed line.

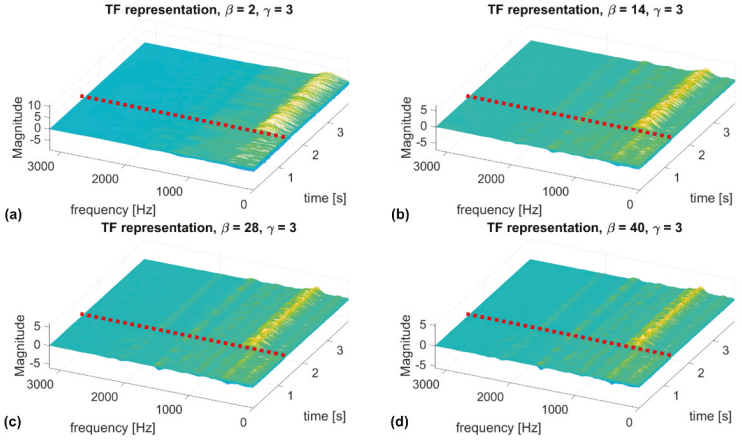

Figure 5. Time–frequency distributions corresponding to the results shown in Figure 4 ($\gamma = 3$ and β equal to (**a**) 2, (**b**) 14, (**c**) 28, and (**d**) 40).

One can see that the TF representation for $\beta = 2$ and $\gamma = 3$ is clearly unreliable. The TF representations become more and more refined over the frequency axis as both (i) the length of the time support and (ii) the number of oscillations under the GWT envelope (and therefore the instantaneous frequency resolution) increase with P^2 (Figure 6). Since $P^2 = \beta\gamma$, this latter effect can be achieved by independently increasing β or γ.

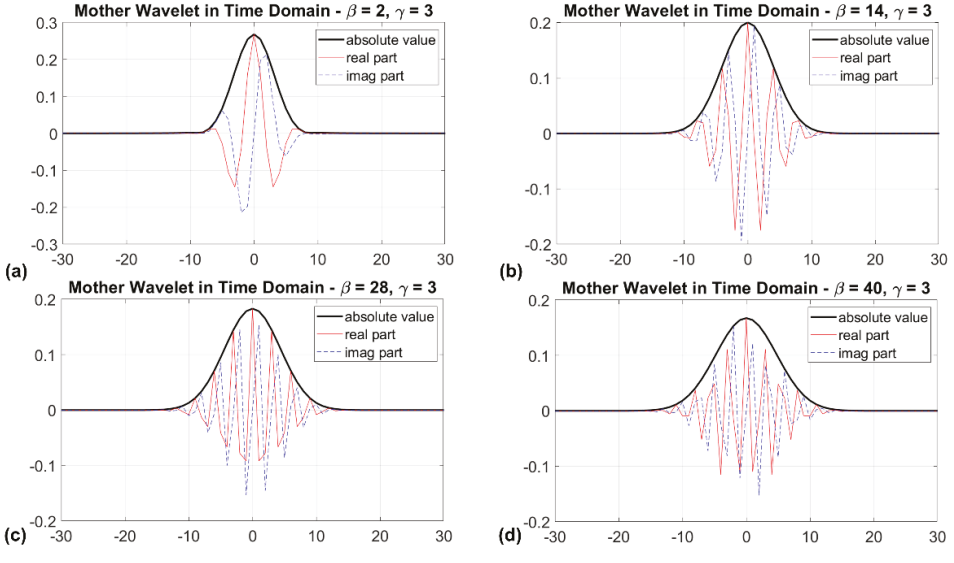

Figure 6. Mother wavelets (in the time domain) corresponding to the results shown in Figure 4 ($\gamma = 3$ and β equal to (**a**) 2, (**b**) 14, (**c**) 28, and (**d**) 40).

On the other hand, the effects of varying γ for constant β can be summarised as follows.

For any value of the symmetry value, lower values of β ($\beta = 2$ in the example of Figure 7) have too coarse a frequency resolution and are thus almost unusable for the intended purposes, as it can be seen from the ISE values barely changing when moving from pre- to post-damage conditions. The corresponding TF representations are reported in Figure 8.

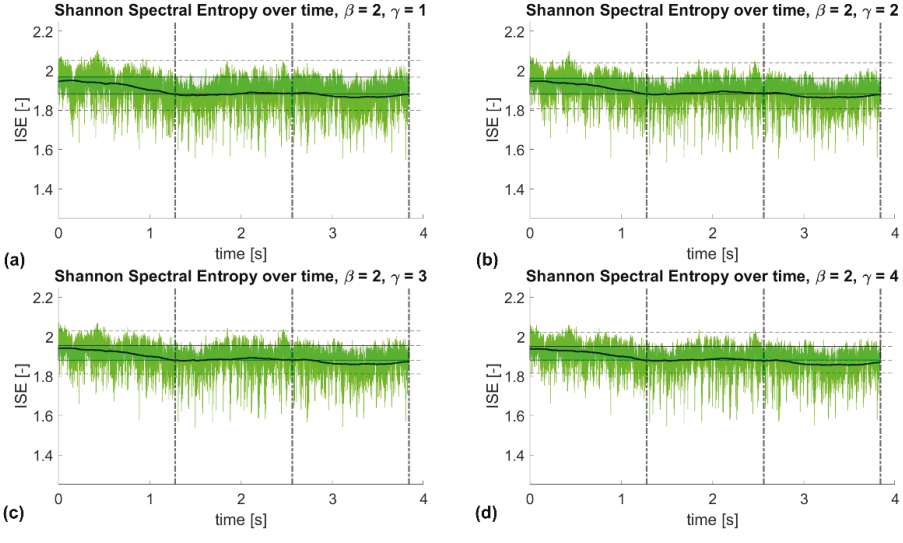

Figure 7. Resulting ISE (signal #1). Values for $\beta = 2$ and γ equal to (**a**) 1, (**b**) 2, (**c**) 3, and (**d**) 4.

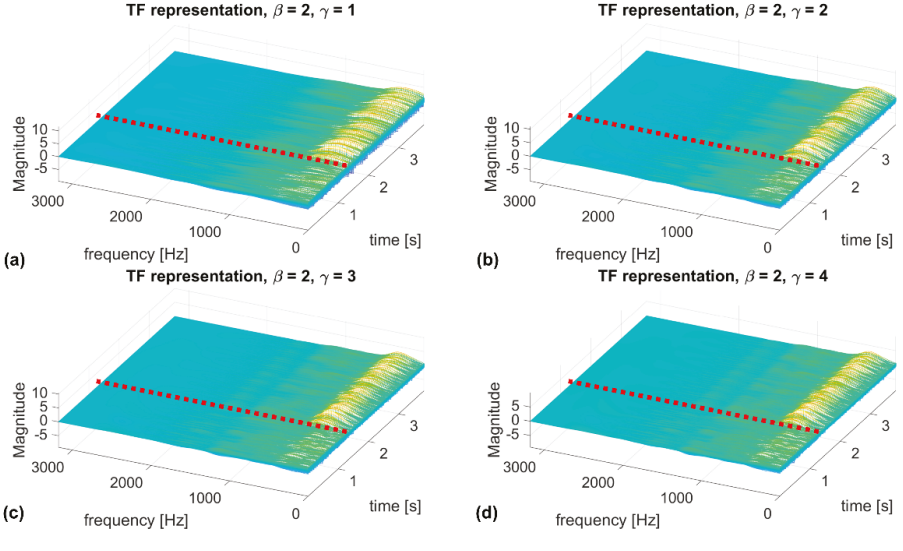

Figure 8. Time–frequency distributions corresponding to the results shown in Figure 7 ($\beta = 2$ and γ equal to (**a**) 1, (**b**) 2, (**c**) 3, and (**d**) 4).

On the other hand, $\beta \geq 4 \div 6$ might return acceptable results, depending on the paired γ values. Generally speaking, $\gamma \leq 2.0 \div 2.5$ returned distorted results, at least for the application investigated here. This is even more noticeable for $\gamma \leq 1.5$, which were found

to be unreliable for any value of β. The results were instead less influenced by β when the symmetry parameter was set as equal or larger than $2.0 \div 3.0$. By way of example, for $\beta = 20$, any gamma larger than 2 returned almost the same ISE(t) time history (see Figure 9; the corresponding TF transforms are reported in Figure 10).

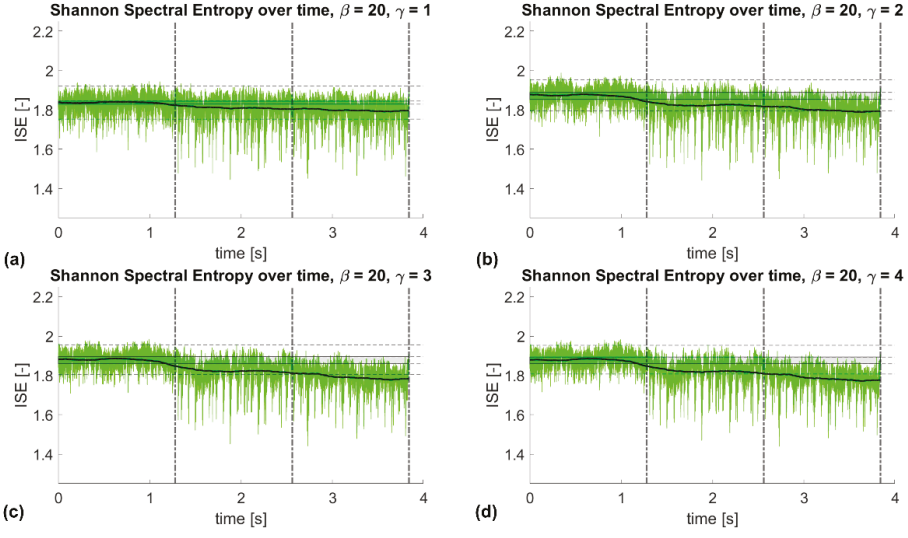

Figure 9. Resulting ISE (signal #1). Values for. $\beta = 20$ and γ equal to (**a**) 1, (**b**) 2, (**c**) 3, and (**d**) 4.

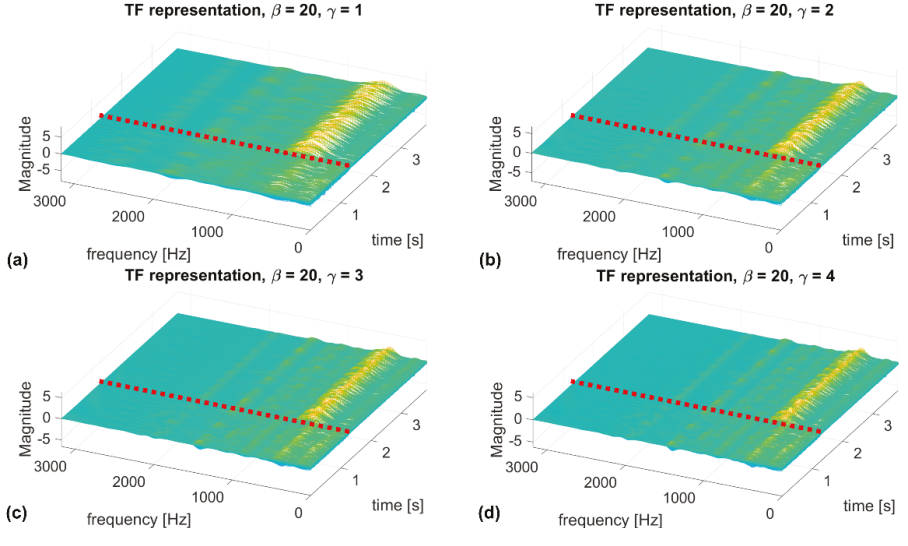

Figure 10. Time–frequency distributions corresponding to the results shown in Figure 9 ($\beta = 20$ and γ equal to (**a**) 1, (**b**) 2, (**c**) 3, and (**d**) 4).

In conclusion, the following points can be highlighted from this sensitivity analysis:

1. Values of $\beta \geq 20$ are all deemed suitable. Increasing β reduces the variability of the results, at least on the specific case study investigated here. Therefore, large values of β are recommended, independently from the selected γ.

2. $\gamma \geq 3$ is suggested to avoid potential issues, even if $2.5 \leq \gamma \leq 3$ were found to be suitable as well for the range of β selected above, at least for this case study.

The suggested range is depicted in Figure 11, considering the mean and standard deviation of the ISE(t) computed over the NOCs. As mentioned previously, it is important to have stationary and low variance over the training dataset. This condition was confirmed for $\beta \geq 20$ and $\gamma \geq 3$. This selected area is also intended to avoid the undesired time-domain sidelobes and frequency-domain asymmetries that arise from very small time–bandwidth and large symmetry values.

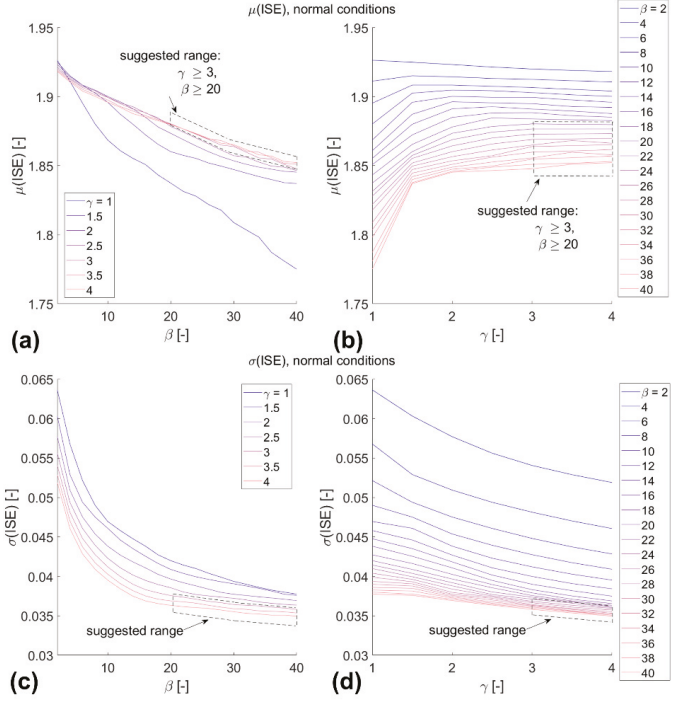

Figure 11. Trends of ISE values for the normal conditions. (**a**): μ(ISE) for varying β; (**b**): μ(ISE) for varying γ; (**c**): σ(ISE) for varying β; (**d**): σ(ISE) for varying γ.

5.1.2. Computational Efficiency

The computational effort required by the feature extraction procedure was further tested. This is essential for online SHM since the whole algorithm (feature extraction and threshold validation) should be performed in real-time, i.e., during the acquisition of an uninterrupted data stream. This is generally performed via a small moving window of recent history. Therefore, the computational time needed should be smaller than the considered time window.

Of the two main steps—TF transform and ISE(t) computation—the first one is the most demanding. Indeed, instantaneous SSE was performed (for the signal length considered here) in less than 0.6 s on average. This test, as well as the following ones, was performed on a laptop equipped with Windows 10 64-bit, Intel Core i7-7700HQ with CPU 2.80 GHz and 16.0 GB RAM, and MatLab R2020b.

The CWT was found to be slightly longer to perform. As it can be seen from Figure 12, the elapsed time is mostly equal for any pair of values in the inspected ranges of the two GWT parameters. Except for ($\gamma = 2$, $\beta = 40$) and ($\gamma = 2.5$, $\beta = 10$), which lasted, respectively, for 5.8 s and 3.5 s, the CWT ran in less than 2.0 s everywhere else. Considering

all cases, the overall mean elapsed time is about 1.08 s (1.02 s excluding the two outliers), with many combinations running in <1 s.

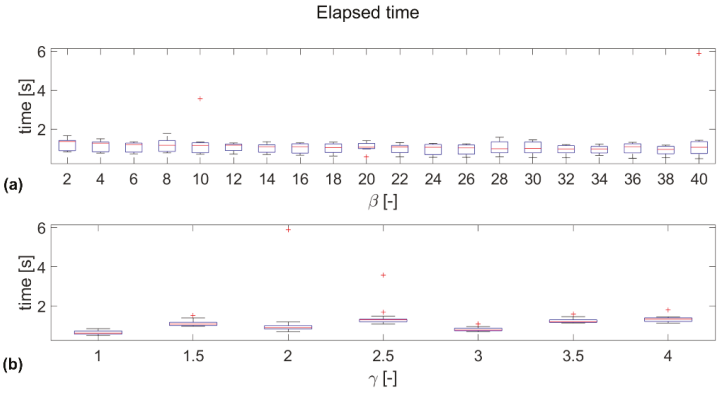

Figure 12. Boxplot of the CWT execution time. (**a**): as a function of β. (**b**): as a function of γ.

5.2. Signal #2

Figure 13 reports the results for the second, longer signal. $\beta = 40$ and $\gamma = 3$ were set for this further study. One can notice that except for some tracts where the rotational speed was slightly higher than the average, the normality model—defined over five consecutive acquisitions—was validated almost everywhere on both the two validation sets (corresponding to, respectively, 14 months and immediately before the gearbox replacement). This indicates that the process has a certain level of robustness for relatively similar rotational speeds. Nevertheless, in some segments (more markedly in tract #1489, belonging to the second validation set, and to a lesser extent in #1487 and #1588, from the same set), three false positives were encountered. This can be explained since in binary classification, fine-tuning the classification algorithm parameters generally induces an increment in both the true positive and the false positive rates.

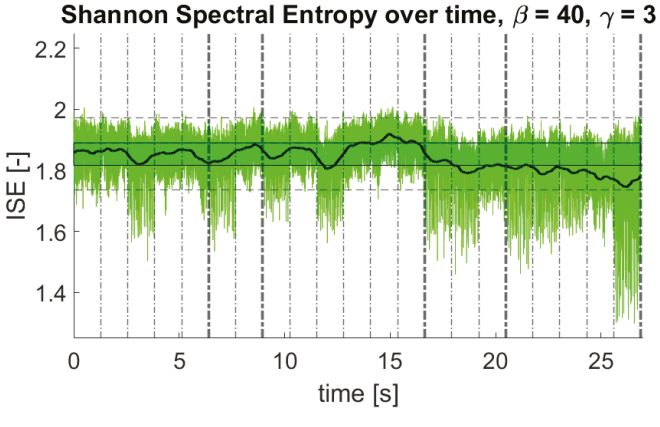

Figure 13. Resulting ISE (signal #2). Values for. $\beta = 40$ and $\gamma = 3$.

Immediately after the gearbox replacement, for a comparable wind speed, the ISE showed a noticeable decrease (as already described in the previous subsection). This behaviour was confirmed in the second test set, i.e., after more than seven months from the gearbox replacement. One can notice how some elements of the training and validation datasets have almost the same rotational speed but different ISE—e.g., tract #1588, the last

one of the second validation set, and #2021, the first one of the second test set, correspond, respectively, to 785.45 and 786.29 cpm. This seems to indicate that the different output is not linked to any input variation but rather to structural changes.

6. Discussion

The experimental results show that the Instantaneous (Shannon) Spectral Entropy can be effectively used as a time-dependent damage index for Pattern Recognition-based SHM. However, one must use care in obtaining a time–frequency distribution which is as refined as possible, especially along the frequency axis. For this reason, a dedicated study was carried out.

High γ and β values return the highest possible time duration and number of oscillations under the GWT envelope, which in turn grants the highest frequency resolution achievable at any instant. This greatly increases the damage detection capabilities of the proposed entropy-based approach. The performance reaches a plateau at a certain point, where the instantaneous power spectrum is refined enough, and further increasing Δf does not significantly improve the final results. In this application, as mentioned previously, this was found at $\beta \cong 20$, $\gamma \cong 3$, which therefore constitute the lower boundaries of the range of suggested settings. If one is interested in further improving the detectability of damage (by further shrinking the confidence interval around the normality model), according to these findings, increasing both β and γ might be helpful. The optimal pair of (γ, β) is, therefore, only limited by possible variations in the computational effort required. However, from the point of view of the computational effort, it was found that there is no relevant difference between different parameters.

However, due to the well-known optimal trade-off between time and frequency resolution (recalled in Section 3.2), it is strongly suggested to test $\gamma = 3$ as a first attempt, independently from the specific dataset, before increasing β. Only if, after reaching $\beta = 40$, the resolution Δf is still insufficient to obtain reliable ISE(t) estimates, the symmetry parameter should be further increased.

7. Conclusions

The Instantaneous Spectral Entropy (ISE) has been discussed as a potential time-dependent damage index. The Shannon Spectral Entropy (SSE) definition was used for this aim. The goal of this research was to perform damage event detection retrospectively on acquired vibration time histories, recorded from a wind turbine gearbox. The Continuous Wavelet Transform (CWT) was applied to define the time–frequency representation needed to extract the ISE. In this regard, a sensitivity analysis has been carried out on the parameters of the Generalised Morse Wavelet (GMW), to investigate their effects on the final results. Some suggestions were made based on the experimental data analysed here. However, further studies will be needed to assess these findings on different datasets, also considering different sampling frequencies and varying the duration of the recorded measurement time series.

The pure ISE was found to be significantly affected by spikes, i.e., very fast, short-termed transients of the instantaneous entropy. For this reason, its moving mean has been preferred as a more stable time-dependent index. The procedure successfully detected the occurrence of bearing faults on experimental data, recorded before and after a bearing failure and concatenated to emulate a time-varying structural condition. The moving mean of ISE returned some isolated false alarms as well; however, only an actual alteration of the machine condition caused a permanent deviation from the baseline.

As an entropy-based approach, the ISE is inherently limited by its dependence on the input force. That is to say, measurements corresponding to highly different wind speeds cannot be directly compared for anomaly detection. Future works will also include the automation of the selection procedure for acquisitions related to similar wind speeds.

Finally, the relatively low computational burden and rapid execution time suggest that the method can be further extended to real-time, online applications. This can be achieved

using a small moving window of recent history over the data stream. These potential applications will be further investigated in future works as well.

Author Contributions: Conceptualization, M.C. and C.S.; methodology, M.C. and C.S.; software, M.C.; validation, M.C.; investigation, M.C.; resources, C.S.; data curation, M.C.; writing—original draft preparation, M.C.; writing—review and editing, C.S.; visualization, M.C.; supervision, C.S.; project administration, C.S. All authors have read and agreed to the published version of the manuscript.

Funding: This research received no external funding.

Institutional Review Board Statement: Not applicable.

Informed Consent Statement: Not applicable.

Data Availability Statement: The experimental data utilised for this research were retrieved from a public dataset, available at http://ltu.diva-portal.org/smash/record.jsf?pid=diva2%3A1244889&dswid=-2411 (accessed on 24 June 2021).

Acknowledgments: The Authors would like to thank S. Martin del Campo Barraza, F. Sandin, and D. Strömbergsson of the Luleå University of Technology for making their experimental data publicly available.

Conflicts of Interest: The authors declare no conflict of interest.

References

1. New Energy Outlook 2020 | BloombergNEF. Available online: https://about.bnef.com/new-energy-outlook/ (accessed on 23 June 2021).
2. Olesen, G.B. *Fast Transition to Renewable Energy with Local Integration of Large-Scale Windpower in Denmark*; Publisher INFORSE: Aarhus, Denmark, 2014; Available online: https://inforse.org/europe/pdfs/Vision_DK_Fast_Transtions_RE_Denmark_article_EN_2014.pdf (accessed on 20 December 2021).
3. Blaabjerg, F.; Ma, K. Future on power electronics for wind turbine systems. *IEEE J. Emerg. Sel. Top. Power Electron.* **2013**, *1*, 139–152. [CrossRef]
4. Aloys, N.; Ariola, M. *Wind in Power: 2016 European Statistics*; WindEurope: Brussels, Belgium, 2017.
5. International Renewable Energy Agency (IRENA). *Renewable Energy Technologies: Cost Analysis Series; Volume 1: Power Sector, Issue 5/5*; IRENA: Abu Dhabi, United Arab Emirates, 2012.
6. European Wind Energy Association (EWEA). *The Economics of Wind Energy*; EWEA: Brussels, Belgium, 2009.
7. Steffen, B.; Beuse, M.; Tautorat, P.; Schmidt, T.S. Experience Curves for Operations and Maintenance Costs of Renewable Energy Technologies. *Joule* **2020**, *4*, 359–375. [CrossRef]
8. Myhr, A.; Bjerkseter, C.; Ågotnes, A.; Nygaard, T.A. Levelised cost of energy for offshore floating wind turbines in a lifecycle perspective. *Renew. Energy* **2014**, *66*, 714–728. [CrossRef]
9. Shihavuddin, A.S.M.; Chen, X.; Fedorov, V.; Christensen, A.N.; Riis, N.A.B.; Branner, K.; Dahl, A.B.; Paulsen, R.R. Wind turbine surface damage detection by deep learning aided drone inspection analysis. *Energies* **2019**, *12*, 676. [CrossRef]
10. Zhu, J.; Yoon, J.M.; He, D.; Bechhoefer, E. Online particle-contaminated lubrication oil condition monitoring and remaining useful life prediction for wind turbines. *Wind Energy* **2015**, *18*, 1131–1149. [CrossRef]
11. Jasiūnienė, E.; Raišutis, R.; Šliteris, R.; Voleišis, A.; Vladišauskas, A.; Mitchard, D.; Amos, M. NDT of wind turbine blades using adapted ultrasonic and radiographic techniques. *Insight Non-Destr. Test. Cond. Monit.* **2009**, *51*, 477–483. [CrossRef]
12. Elforjani, M.; Mba, D. Condition monitoring of slow-speed shafts and bearings with Acoustic emission. *Strain* **2011**, *47*, 350–363. [CrossRef]
13. Rumsey, M.A.; Musial, W. Application of Infrared Thermography Nondestructive Testing during Wind Turbine Blade Tests. *J. Sol. Energy Eng.* **2001**, *123*, 271. [CrossRef]
14. Martin, R.W.; Sabato, A.; Schoenberg, A.; Giles, R.H.; Niezrecki, C. Comparison of nondestructive testing techniques for the inspection of wind turbine blades' spar caps. *Wind Energy* **2018**, *21*, 980–996. [CrossRef]
15. Rytter, A. Vibrational Based Inspection of Civil Engineering Structures. Ph.D. Dissertation, Aalborg Universitet, Aalborg, Denmark, 1993.
16. Salameh, J.P.; Cauet, S.; Etien, E.; Sakout, A.; Rambault, L. Gearbox condition monitoring in wind turbines: A review. *Mech. Syst. Signal Process.* **2018**, *111*, 251–264. [CrossRef]
17. Papatheou, E.; Dervilis, N.; Maguire, A.E.; Antoniadou, I.; Worden, K. A Performance Monitoring Approach for the Novel Lillgrund Offshore Wind Farm. *IEEE Trans. Ind. Electron.* **2015**, *62*, 6636–6644. [CrossRef]
18. Papatheou, E.; Dervilis, N.; Maguire, A.E.; Campos, C.; Antoniadou, I.; Worden, K. Performance monitoring of a wind turbine using extreme function theory. *Renew. Energy* **2017**, *113*, 1490–1502. [CrossRef]

19. Antoniadou, I.; Manson, G.; Dervilis, N.; Barszcz, T.; Staszewski, W.J.; Worden, K. Use of the Teager-Kaiser Energy Operator for Condition Monitoring of a Wind Turbine Gearbox. In Proceedings of the 25th International Conference on Noise and Vibration Engineering (ISMA), Leuven, Belgium, 17–19 September 2012.
20. Ziaja, A.; Antoniadou, I.; Barszcz, T.; Staszewski, W.J.; Worden, K. Fault detection in rolling element bearings using wavelet-based variance analysis and novelty detection. *J. Vib. Control* **2016**, *22*, 396–411. [CrossRef]
21. Powell, G.E.; Percival, I.C. A spectral entropy method for distinguishing regular and irregular motion of Hamiltonian systems. *J. Phys. A Gen. Phys.* **1979**, *12*, 2053–2071. [CrossRef]
22. Pan, Y.N.; Chen, J.; Li, X.L. Spectral entropy: A complementary index for rolling element bearing performance degradation assessment. *Proc. Inst. Mech. Eng. Part C J. Mech. Eng. Sci.* **2009**, *223*, 1223–1231. [CrossRef]
23. Ceravolo, R.; Lenticchia, E.; Miraglia, G. Use of Spectral Entropy for Damage Detection in Masonry Buildings in the Presence of Mild Seismicity. *Proceedings* **2018**, *2*, 432. [CrossRef]
24. Ceravolo, R.; Lenticchia, E.; Miraglia, G. Spectral entropy of acceleration data for damage detection in masonry buildings affected by seismic sequences. *Constr. Build. Mater.* **2019**, *210*, 525–539. [CrossRef]
25. Ceravolo, R.; Civera, M.; Lenticchia, E.; Miraglia, G.; Surace, C. Damage Detection and Localisation in Buried Pipelines using Entropy in Information Theory. In Proceedings of the 1st International Electronic Conference on Applied Sciences, Online, 10–30 November 2020; pp. 30–36.
26. Ceravolo, R.; Civera, M.; Lenticchia, E.; Miraglia, G.; Surace, C. Detection and classification of multiple damages through entropy. *Appl. Sci.* **2021**, *11*, 5773. [CrossRef]
27. Civera, M.; Surace, C. The Instantaneous Spectral Entropy for Real-time, Online Structural Health Monitoring. In Proceedings of the Damage Assessment of Structure (DAMAS), Shanghai, China, 29 October–1 November 2021.
28. Worden, K.; Farrar, C.R.; Manson, G.; Park, G. The fundamental axioms of structural health monitoring. *Proc. R. Soc. A Math. Phys. Eng. Sci.* **2007**, *463*, 1639–1664. [CrossRef]
29. Farrar, C.; Worden, K.; Park, G. *Complexity: A New Axiom for Structural Health Monitoring?* Los Alamos National Lab: Los Alamos, NM, USA, 2010.
30. Pugno, N.; Surace, C.; Ruotolo, R. Evaluation of the Non-linear Dynamic Response to Harmonic Excitation of a Beam with Several Breathing Cracks. *J. Sound Vib.* **2000**, *235*, 749–762. [CrossRef]
31. West, B.M.; Locke, W.R.; Andrews, T.C.; Scheinker, A.; Farrar, C.R. Applying concepts of complexity to structural health monitoring. In *The Conference Proceedings of the Society for Experimental Mechanics Series*; Springer: New York, NY, USA, 2019; Volume 6, pp. 205–215.
32. Civera, M.; Boscato, G.; Zanotti Fragonara, L. Treed gaussian process for manufacturing imperfection identification of pultruded GFRP thin-walled profile. *Compos. Struct.* **2020**, *254*, 112882. [CrossRef]
33. Farrar, C.R.; Worden, K. *Structural Health Monitoring: A Machine Learning Perspective*; John Wiley & Sons Ltd.: Chichester, UK, 2013.
34. Civera, M.; Surace, C. A Comparative Analysis of Signal Decomposition Techniques for Structural Health Monitoring on an Experimental Benchmark. *Sensors* **2021**, *21*, 1825. [CrossRef]
35. Fräser, K.F. *An Overview of Health and Usage Monitoring Systems (HUMS) for Military Helicopters*; Defence Science and Technology Organisation: Melbourne, Australia, 1994.
36. Shannon, C.E. A Mathematical Theory of Communication. *Bell Syst. Technol. J.* **1948**, *27*, 379–423. [CrossRef]
37. Bromiley, P.A.; Thacker, N.A.; Bouhova-Thacker, E. *Shannon Entropy, Renyi Entropy, and Information*; The University of Manchester: Manchester, UK, 2010.
38. Rioul, O.; Vetterli, M. Wavelets and signal processing. *IEEE Signal Process. Mag.* **1991**, *8*, 14–38. [CrossRef]
39. Daubechies, I.; Bates, B.J. *Ten Lectures on Wavelets*; Society for Industrial and Applied Mathematics: Philadelphi, PA, USA, 1992; ISBN 0898712742.
40. Mallat, S. *A Wavelet Tour of Signal Processing*; Elsevier Inc.: San Diego, CA, USA, 2009; ISBN 9780123743701.
41. Sifuzzaman, M.; Islam, M.R.; Ali, M.Z. Application of Wavelet Transform and its Advantages Compared to Fourier Transform. *J. Phys. Sci.* **2009**, *13*, 121–134.
42. Surace, C.; Di Torino, P.; Ruotolo, R. Crack Detection of a Beam Using the Wavelet Transform. In Proceedings of the The International Society For Optical Engineering, Turin, Italy, 10 January 1994.
43. Taha, M.M.R.; Noureldin, A.; Lucero, J.L.; Baca, T.J. Wavelet Transform for Structural Health Monitoring: A Compendium of Uses and Features. *Struct. Health Monit. Int. J.* **2006**, *5*, 267–295. [CrossRef]
44. Poularikas, A.D. *Transforms and Applications Handbook*; CRC Press: Boca Raton, FL, USA, 1996.
45. Silik, A.; Noori, M.; Altabey, W.A.; Ghiasi, R.; Wu, Z. Comparative Analysis of Wavelet Transform for Time-Frequency Analysis and Transient Localization in Structural Health Monitoring. *Struct. Durab. Health Monit.* **2021**, *15*, 1–22. [CrossRef]
46. Lilly, J.M.; Olhede, S.C. Generalized morse wavelets as a superfamily of analytic wavelets. *IEEE Trans. Signal Process.* **2012**, *60*, 6036–6041. [CrossRef]
47. Wang, P.; Gao, J. Extraction of instantaneous frequency from seismic data via the generalized Morse wavelets. *J. Appl. Geophys.* **2013**, *93*, 83–92. [CrossRef]
48. Huang, F.; Chen, D.; Zhou, L. Rotating machine fault diagnosis based on correlation filtering and reconstructed Morlet wavelet power spectral entropy. In Proceedings of the 2020 6th International Conference on Mechanical Engineering and Automation Science, ICMEAS 2020, Moscow, Russia, 29–31 October 2020; pp. 61–65.

49. Lilly, J.M.; Olhede, S.C. Higher-Order Properties of Analytic Wavelets. *IEEE Trans. Signal Process.* **2008**, *57*, 146–160. [CrossRef]
50. Daubechies, I.; Paul, T. Time-frequency localisation operators-a geometric phase space approach: II. The use of dilations. *Inverse Probl.* **1988**, *4*, 661–680. [CrossRef]
51. Olhede, S.C.; Walden, A.T. Generalized Morse Wavelets. *IEEE Trans. Signal Process.* **2002**, *50*, 2661–2670. [CrossRef]
52. Martin-Del-campo, S.; Sandin, F.; Strömbergsson, D. Dictionary learning approach to monitoring of wind turbine drivetrain bearings. *Int. J. Comput. Intell. Syst.* **2021**, *14*, 106–121. [CrossRef]
53. Strömbergsson, D.; Marklund, P.; Berglund, K.; Larsson, P.E. Bearing monitoring in the wind turbine drivetrain: A comparative study of the FFT and wavelet transforms. *Wind Energy* **2020**, *23*, 1381–1393. [CrossRef]
54. NSK Company. *New Bearing Doctor—Maintenance of Bearings*; Publisher NSK Company: Maidenhead, UK, 2009; Available online: https://www.nsk-literature.com/en/new-bearing-doctor-maintenance/offline/download.pdf (accessed on 20 December 2021).
55. Figueiredo, E.; Park, G.; Figueiras, J. *Structural Health Monitoring Algorithm Comparisons Using Standard Data Sets*; Los Alamos National Lab. (LANL): Los Alamos, NM, USA, 2009.

applied sciences

MDPI

Article

Interferometric Satellite Data in Structural Health Monitoring: An Application to the Effects of the Construction of a Subway Line in the Urban Area of Rome

Giulia Delo [1], Marco Civera [2], Erica Lenticchia [2], Gaetano Miraglia [2], Cecilia Surace [2] and Rosario Ceravolo [2,*]

[1] Department of Mechanical and Aerospace Engineering, Politecnico di Torino, 10129 Turin, Italy; giulia.delo@polito.it
[2] Department of Structural, Geotechnical and Building Engineering, Politecnico di Torino, 10129 Turin, Italy; marco.civera@polito.it (M.C.); erica.lenticchia@polito.it (E.L.); gaetano.miraglia@polito.it (G.M.); cecilia.surace@polito.it (C.S.)
* Correspondence: rosario.ceravolo@polito.it

Abstract: In recent years, the use of interferometric satellite data for Structural Health Monitoring has experienced a strong development. The urban environment confirms its fragility to adverse natural events, made even more severe by climate change. Hence, the need to carry out continuous monitoring of structures and artefacts appears increasingly urgent. Furthermore, satellite data could considerably increase the feasibility of traditional Structural Health Monitoring (SHM) approaches. This study aims to explore this remote sensing approach, focusing on the representation techniques that can be adopted to highlight their advantages and provide an interpretation of the results. In particular, the study analyzes records from the urban area of Rome (Italy), subject to the construction of a new subway line. These data are exploited to create a velocity map to highlight the possible subsidence phenomenon induced by excavations. Then, the paper focuses on single buildings or building complexes through the entropy-energy representation. Beyond the different limitations caused by the input data, a correlation is identified between the results of the two representation techniques. Accordingly, the effects of excavation on the urban area are demonstrated, and the methodologies are validated.

Keywords: Structural Health Monitoring; satellite data; remote sensing; SBAS–DInSAR; subsidence; subway excavation

Citation: Delo, G.; Civera, M.; Lenticchia, E.; Miraglia, G.; Surace, C.; Ceravolo, R. Interferometric Satellite Data in Structural Health Monitoring: An Application to the Effects of the Construction of a Subway Line in the Urban Area of Rome. *Appl. Sci.* **2022**, *12*, 1658. https://doi.org/10.3390/app12031658

Academic Editor: Hyung-Sup Jung

Received: 30 December 2021
Accepted: 27 January 2022
Published: 5 February 2022

Publisher's Note: MDPI stays neutral with regard to jurisdictional claims in published maps and institutional affiliations.

Copyright: © 2022 by the authors. Licensee MDPI, Basel, Switzerland. This article is an open access article distributed under the terms and conditions of the Creative Commons Attribution (CC BY) license (https://creativecommons.org/licenses/by/4.0/).

1. Introduction

In recent years, the built environment and entire urban areas have been subjected to many adverse natural phenomena or extreme events, which can often be linked to advancing climate change. It highlighted how buildings, infrastructures and architectural heritage structures are highly fragile and vulnerable. Therefore, there is a growing concern in approaches to examine the built environment and, in particular, the constructions with strategic or historical/architectural value to ensure higher safety and reliability or predict the structural behavior in case of unforeseen events. Thus arises the need for novel Structural Health Monitoring (SHM) techniques and technologies capable of providing continuous datasets, with high efficiency and reduced costs.

Indeed, traditional SHM applications require the use of a high number of sensors (e.g., accelerometers for motion measuring, thermocouples, anemometers, etc.) [1], which can prove costly. Among new SHM technologies, the possibility of using remote sensing techniques [2], especially data gathered by constellations of artificial satellites, is becoming a viable option. Satellites allow observing the earth's surface through the interaction of electromagnetic waves, with objects placed even at a considerable distance from the observer [3]. The main advantages are to guarantee a broad coverage both spatially and temporally, with a low environmental impact.

The potentialities of applying satellite remote sensing for urban applications have been highlighted as long ago as in 1985 by Foster [4]. However, the employment of this remote sensing approach for civil SHM is recent and has been fostered by the increase in data quality and the development of new algorithms for data processing.

The satellite sensors use radar waves, characterized by wavelengths in the range between 1 m and 1 mm. In addition, data can be acquired regardless of the presence of sunlight and can be used even in sub-optimal weather conditions (e.g., in the presence of clouds). Satellites commonly roughly follow polar orbits, with a slight inclination angle to the meridians, and descending and ascending orbits are distinguished depending on the pole toward which the satellite moves. The direction along which there is the emission and reception of the signal is called Line of Sight (LOS) and is the direction along which the sensors gather the images and information about the displacements of points on the earth's surface.

The new SHM approaches exploit the radar images gathered from satellite constellations, adopting Synthetic Aperture Radar (SAR). It is a satellite radar acquisition technique that uses the synthesis of a virtual antenna with a kilometric aperture to improve spatial resolution. This virtual antenna is simulated by acquisitions made on the same area, observed at different times and positions by the same satellite [5].

Among SAR acquisition techniques, the Interferometric SAR (InSAR) is employed to extract displacement information. It allows describing interferograms by comparing the SAR data over a baseline time and evaluating the differences between the measures [6]. A particular kind of InSAR is the Differential Interferometry SAR (DInSAR), in which only the pure displacement components of the differential satellite target phases are depicted from the images acquired by the satellite in the same area at different time instants.

Satellite interferometric data have already been exploited in some early SHM applications for urban areas and to quantify large-scale phenomena, such as land subsidence [7–12]. Recently, the need for efficient real-time monitoring of damage led to the development of new techniques, such as the multi-temporal InSAR (MT-InSAR) [13]. By combining different differential interferograms, MT-InSAR approaches more accurately provide the trends of displacements in the area of interest and their temporal evolution. Therefore, they have been applied to detect anomalies in a single structure [14] and for the assessment of tunnel-induced subsidence and related damage [15]. Despite the advantages afforded by this new approach, there are still many limitations and challenges to overcome [16,17]. They are mainly due to the differences between satellite data and the information required by traditional SHM techniques and obtained from in situ sensors.

Furthermore, new visualization/representation approaches are necessary to give a relevant interpretation of the measures provided by satellite datasets. This issue is of primary importance to realize automatic procedures for the assessment of structures' behavior and for the diagnosis of anomalies, which may be connected to structural damage. The main representation techniques refer to the distribution of direct quantities (i.e., displacements along the LOS, velocities along the LOS). However, it is also possible to create maps or diagrams of indirect measures to enhance data interpretation. It is the case of spectral entropy-energy graphs, which can be used to estimate the average information of the signal and to characterize the behavior of a system.

This study aims to explore and compare the possibilities given by the different methodologies of satellite data representation and to highlight the advantages provided by the evaluation of spectral entropy for the description of whole structural systems. This is accomplished by analyzing the case study of the area of Rome (Italy) subject to excavations for the construction of the T3 section of the subway line C. This work is under construction, which began in 2013, and affects an area rich in architectural heritage.

This paper is organized as follows: Section 2 briefly describes the characteristics of the satellite data employed and the proposed representation approaches; Section 3 concerns the results of the case studies; finally, conclusions are presented in Section 4. The case study initially focuses on representing data at a territorial scale to identify the subsidence

phenomena induced by the excavation of the two tunnels of the underground railways. Then, the entropy-energy diagram is adopted to describe single monumental buildings or building complexes, highlighting the presence of points with outlier signals. However, the data used for this representation refer to a period that is insufficient to detect an actual anomaly in the structural behavior due to the poor frequency content. Consequently, the two types of representation used are compared to verify the results and obtain cross-validation of the methodology. A further comparison is made between the representations in the first and second parts of the analyzed period for a small complex of structures, as well as for the monumental Colosseum structure.

2. Materials and Methods

The analysis conducted employs the ascendant SAR images acquired by the COSMO SkyMed (CSK) satellite constellation in the period from March 2011 to March 2019, the same data employed in the DPC-ReLUIS 2019–2021 project [18]. CSK is an earth observation mission conceived for civil and military purposes, developed by the Italian Space Agency (ASI) [19] in cooperation with the Ministry of Defense. It is based on a constellation of low earth orbit satellites equipped with SAR working in X-band. The differential interferometric SAR information is processed by adopting the Small Baseline Subset algorithm (SBAS–DinSAR) [20,21]; thus, it is possible to obtain the displacements with the accuracy of centimeters and millimeters.

2.1. Satellite Data

It is necessary to underline that the satellite data used are subjected to different levels of preliminary treatments to obtain SAR standard products and higher-level products, such as the interferometric ones [22,23]. Afterward, these are additionally processed according to the SBAS–DinSAR algorithm [20,21]. The processing methods could cause new difficulties in the further treatment of data, e.g., the improper elimination of useful points, or the preservation of non-structural points, increasing the uncertainty of the results [16]. In addition, it has to be considered that the LOS data do not refer to the point on the ground, but to the point measured by the sensor (e.g., the roof of a building). Thus, to exploit them in the assessment of subsidence, the simplifying assumption of having structures undergoing a uniform subsidence phenomenon is introduced. Finally, a further limitation in the use of satellite data is due to the presence of a large dataset, in which points with incorrect measurements due to preliminary processing or insignificant ones (i.e., those that do not fall within the built area) are also included. As mentioned in reference [16], this presence contributes to increasing the analysis' uncertainty, so these measures should be removed. However, this study considers an average, approximate behavior of the urbanized area and not the individual building. Therefore, this issue is neglected. For the evaluation of the case study, SAR images were extrapolated only for the area related to the T3 section of the Line C subway in Rome (Figure 1). This route connects the station of San Giovanni to the Colosseum, with an intermediate station (Amba Aradam/Ipponio). The area has great importance because it includes many structures of architectural and monumental value, such as the Colosseum itself, the Basilica of Santo Stefano Rotondo, the Basilica of Maxentius, the Aurelian Walls, the Colonnades of the Forum of Nerva and the Church of Santa Maria in Domnica. Although construction operations started in 2013, the project required various preparatory works and was subjected to delays. Therefore, tunnel excavation only began in 2018, after the inter-tract shafts realization in 2017 [24] (see Figure 1 for reference). This information is relevant for the identification of the area affected by the subsidence phenomenon induced by the excavations.

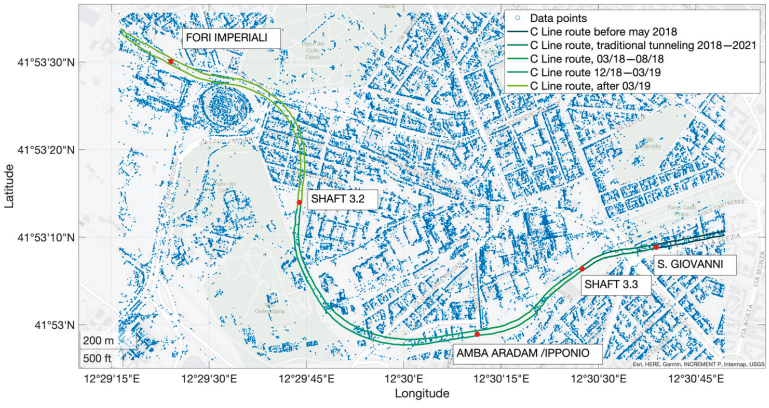

Figure 1. Map showing the T3 section of the Line C subway and the numerosity of points obtained by satellite interferometry over the analyzed urban area of Rome (Italy).

Regarding the soil characteristics, starting from the ground level, the stratigraphic succession shows the first layer of recent deposits, whose thickness reaches values of 13–16 m. It follows a layer of recent alluvial deposits lying on Pleistocene deposits, characterized in the upper portion by clayey silts and silty clays, locally sandy, and in the lower portion by sands and gravels. The water table level is placed at about 8–10 m from ground level. The depth of the tunnels is approximately 30 m between the San Giovanni and Amba Aradam stations, then increasing up to 57 m at shaft 3.2 and subsequently decreasing to 32 m at the Fori Imperiali station.

For each of the measured points, the employed dataset contains the geographic coordinates, the topographic elevation, the velocity and the LOS displacement at each time interval with respect to the initial one. The displacement and velocity values are given along the line of sight of the satellite sensor. Therefore, information on their overall deformation process can only be derived by processing the data obtained from both orbits (ascending and descending). However, a single dataset can still be used to obtain some preliminary information. In the case of subsidence phenomena, it can be assumed that the main direction of deformation is vertical. Thus, it is possible to derive the intensity of the displacement or the velocity along this direction, starting from the projection measured along the LOS of the satellite [18].

Furthermore, from a qualitative point of view, it is possible to observe only the displacements along the LOS, since, according to the assumption made earlier, a negative displacement or velocity (i.e., moving away from the satellite) is representative of a subsidence effect. From these presumptions, an interest in the representations/visualizations of direct quantities along the LOS arises. Furthermore, it is possible to derive valuable information from indirect measures, such as the spectral entropy of the signal.

2.2. Entropy Measures

According to Shannon's definition, which is based on the concepts of information theory (IT), spectral entropy is a measure of uncertainty (or variability) associated with random variables [25]. It describes the information carried by a signal and allows quantifying its complexity. The introduction of this quantity for Structural Health Monitoring purposes arises from the assumption that the complexity of a structural system increases with the development of damage [26]. In the case of perturbations with specific, non-random behavior, there are low values of spectral entropy. On the contrary, a more complex and stochastic behavior leads to higher values of spectral entropy.

Shannon Spectral Entropy (SSE) evaluates the spectral power distribution from the Fourier transform of the signal to represent the dataset behavior in the whole observation

period. Yet, it could be possible to use a spectrogram to estimate the instantaneous entropy and obtain its time series vectors. This study adopts the non-instantaneous spectral entropy, which is evaluated for each point of a system to describe the whole signal. In addition, the values are normalized with respect to the spectral entropy of the corresponding white noise to fit the regression inequalities rules. Given the signal $x(t)$, and the probability distribution P_f in the frequency domain, the normalized Shannon Spectral Entropy is given by

$$H_n = -\frac{\sum_{f=1}^{N} P_f log_2\left[P_f\right]}{log_2 N} \quad (1)$$

where N is the total number of frequencies, and $log_2 N$ is the maximal spectral entropy of white noise. Consequently, this indirect measure can be used to realize maps or diagrams. In the following section, the spectral entropy is plotted on a dispersion diagram as a function of the signal energy. A regression model is adopted to highlight the trend and define the related probability distribution, which is used to impose a threshold for identifying the outliers.

The entropy-energy dispersion and the LOS information are evaluated together, employing scatter plots to assess how the points subjected to subsidence are located on the dispersion. In addition, the representations are evaluated for two subsequent periods, before and after the excavation, comparing their regression parameters to highlight the differences in the results.

3. Results

The present section describes the application of the interferometric satellite data to identify subsidence effects due to the excavation of the T3 section of Line C subway in Rome's urban center. Firstly, the assessment is performed on a territorial scale of observation. Secondly, the entropy-energy representation is adopted to focus on the effects on a single structural system and to detect points with anomalous signals. In the third part, a comparison is discussed and, finally, the approach is applied to the Colosseum case study.

3.1. Territorial Scale Analysis

The subsidence effects induced by the excavation of the two subway tunnels can be observed in the years since 2017. In this period, the construction of the first section began with excavation performed using two TMB excavators. However, the entire route of the T3 section cannot be studied because it had not been finished by March 2019, which is the last time for which data are available. In detail, within this period, the excavations concerned the route from the station of San Giovanni to shaft 3.2, located in an intermediate position between the Amba Aradam/Ipponio station and the Colosseum, as shown in Figure 2. As a result, the area in which the displacements can be analyzed is further reduced.

The dataset contains the displacements along the LOS, which are used to evaluate the average annual velocity along the LOS. Figure 3 reports the velocity (cm/yr) on the map in the period from 2017 to 2019, while Figure 4 refers to the period from 2014 to 2016 and is used for comparison. It is worth observing that, in the period of the excavation (Figure 3), the velocity distribution presents a higher number of points with negative measures when compared to the previous years (Figure 4). These points are shown in yellow or red, and the negative value indicates that they are moving away from the satellite orbit, so they are qualitatively correlated to the subsidence phenomenon. As shown by the presence of negative values in Figure 4, it is not possible to exclude the possibility that subsidence also occurred before the construction of the metro line, for reasons uncorrelated with the excavations. However, it can be noticed how the points with negative velocity values strongly cluster along the subway route in Figure 3. Moreover, the underground work proceeded from the east of the reported area, moving westward; this may explain the larger concentration of these points on the rightmost portion of the figure.

Figure 2. Map showing the T3 section of the Line C subway, the stations, the inter-tract shafts and the interaction with the other subway lines, Rome (Italy), edited from (https://goo.gl/maps/zPUUjveLSWBzj7nC9, accessed on 28 January 2022), [27].

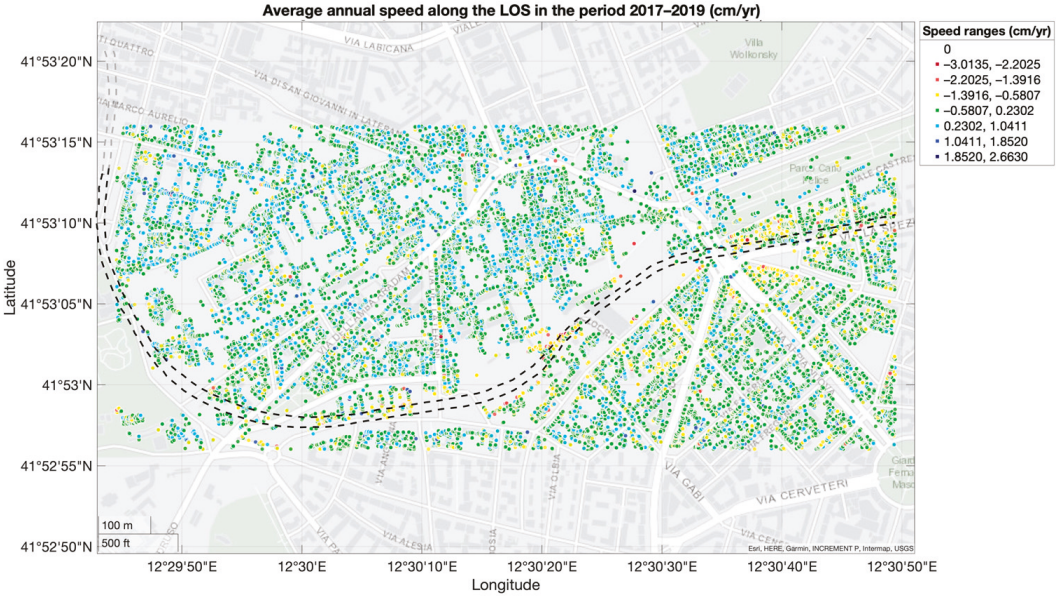

Figure 3. Map showing the dispersion of the average annual velocity along the LOS in the period from 2017 to 2019. The route in black refers to the part already under construction; the route in grey refers to parts not yet built.

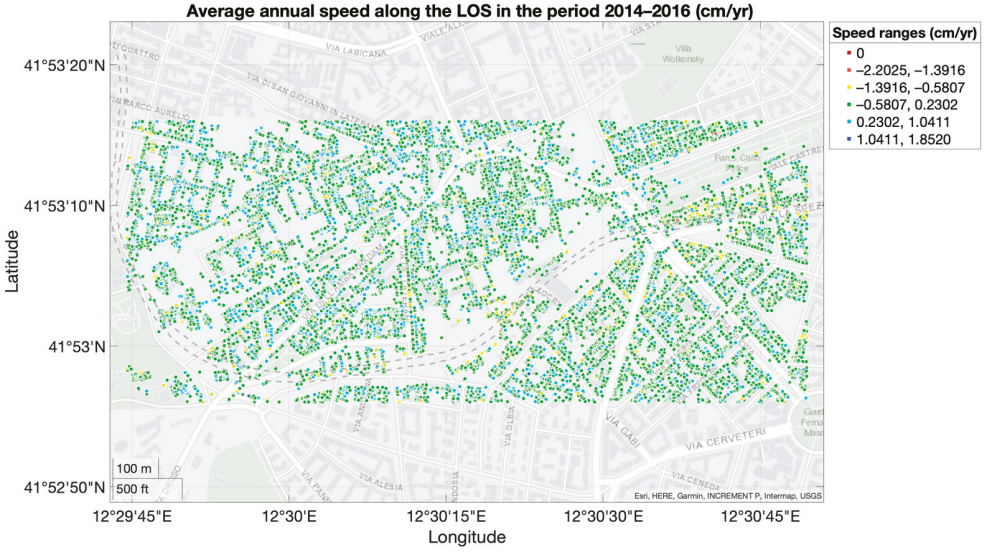

Figure 4. Map showing the dispersion of the average annual velocity along the LOS in the period from 2014 to 2016.

To quantitatively study the subsidence phenomenon in the period from 2017 to 2019, the probability distribution of velocity values is estimated. Assuming a Gaussian distribution, the values have a mean equal to $\mu = 0.0440$ cm/yr and a standard deviation equal to $\sigma = 0.4132$ cm/yr. This distribution allows identifying the negative outliers, points that deviate most from the general behavior of the distribution on the negative branch, in which the velocity is lower than $\mu - 3\sigma$, that is to say, all the points with less than 0.14% probability of belonging to the same statistical distribution. From a physical point of view, these outliers can be interpreted as locations where subsidence is particularly prominent.

As seen in Figure 5, although the points outside this lower threshold are not exclusively distributed along the track, approximately 52% of them are concentrated in the route proximity (route $\pm$ 150 m). These points fall mainly on the route between San Giovanni station and the intermediate station of Amba Aradam/Ipponio, where the depth of the tunnels is about 30 m. On the other hand, in the latter part, the depth increases up to 57 m at shaft 3.2. Moreover, this portion of the track has been subjected to excavations near the end of the period for which data are available, so it was expected to find fewer points outside the threshold. The presence of excavation-induced subsidence was also confirmed in other studies [28,29].

3.2. Entropy-Energy Representation

The representations of mean velocity and entropy-energy data are basically complementary, that is, they provide different information, which are correlated. The entropy of a signal coming from a structural system defines its propensity to follow a deterministic behavior. That is to say, a lower entropy corresponds to a higher deterministic behavior. An output signal can change its characteristics due to: (i) system properties changes, and (ii) variation of input source. The interest here is only to input independent features; thus, what matters is how the entropy changes in relation to its energy value. This allows for discarding input-related variations, which are not of interest for SHM. When the entropy changes its value (in relation to its energy level) this means that the system changes its internal correlation (since entropy is used to estimate system complexity). Importantly, this can also happen if the mean velocities of the points remain constant; however, the

opposite is not true, since an increase in the mean velocity would lead to higher energy and thus lower entropy. Thus, the mean velocity cannot change if the entropy-energy level remains constant.

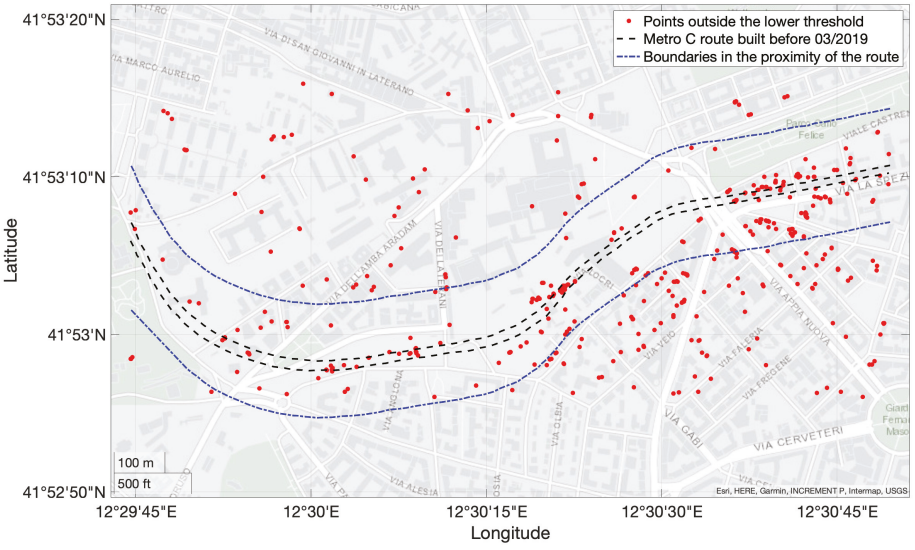

Figure 5. Map showing the points with velocity outside the imposed lower threshold, with respect to the subway route and the proximity boundaries.

Therefore, the energy-entropy representation implicitly carries more information than the mean velocity. The mean velocity is only representative of the displacement trend over time. Instead, any variation in the trend, frequency content, amplitude and phase is reflected in the entropy-energy representation.

An example is when a signal with zero mean increases its amplitude (e.g., due to a loss of stiffness). In this case, the mean velocity, being unchanged, would not allow for any novelty (thus, damage) detection. On the contrary, an increase in amplitude with constant mean velocity would lead to a change in entropy-energy values, and thus to a potential change of the complexity of the system. The mean velocity, however, is still an important datum to monitor because its straightforward physical meaning is connected to the rate of displacement in time (e.g., subsidence or swelling of the soil).

While it is true that entropy-energy representations cannot be adopted for the description of a whole urban area if the systems falling in the area are too different from a structural point of view, in the paper, the entropy-energy representation is used to study individual buildings. From the point scatter regression and probability distribution, it was possible to derive the limit curves (threshold 0.3% and 99.7%, according to the 3-sigma rule) and use them for the identification of outliers, i.e., points at which the signal deviates from the global analytical model and therefore requires further investigation. In order to quantify this deviation, the use of the Mahalanobis distance has been adopted. The points at which the entropy displays a low distance from the mean model can be interpreted as less stochastic (more deterministic). Conversely, if the entropy has a higher distance from the model, it indicates a less deterministic point.

The following results refer to the building complex at the intersection of Via Emanuele Filiberto and Via Castrense (Figure 6), adjacent to San Giovanni's station, in the period from 2017 to 2019. It has been analyzed as, according to the velocity, this area presents a concentration of points that are outside the subsidence threshold shown in Figure 5.

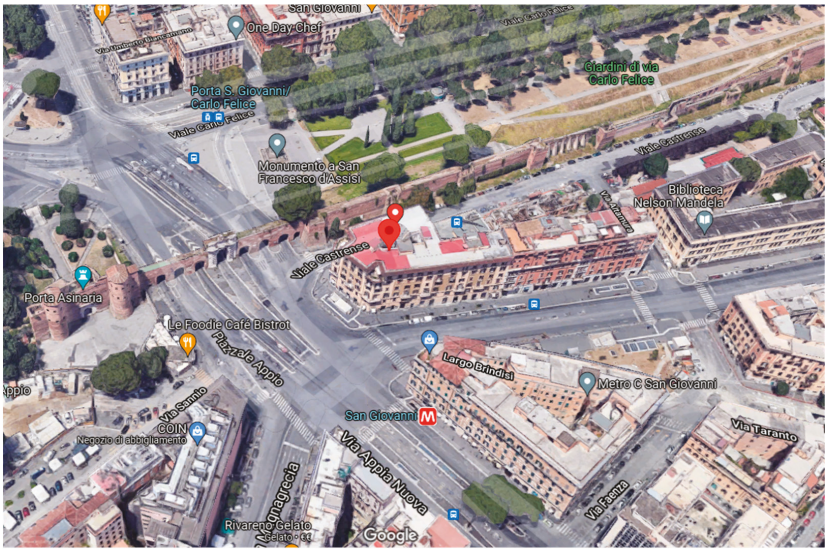

Figure 6. View of the analyzed building on the map, at the intersection of Via Emanuele Filiberto and Via Castrense (https://www.google.it/maps/place/41%C2%B053\T1\textquoteright09.2%22N+12%C2%B030\T1\textquoteright36.6%22E/@41.8835837,12.5093078,320a,35y,39.39t/data=!3m1!1e3!4m5!3m4!1s0x0:0xfe6a6f12a7bebc20!8m2!3d41.885885!4d12.510169, accessed on 25 January 2022).

Figure 7 shows the dispersion of points and the mean model, which has a quadratic trend on a logarithmic scale. It also shows the analytical model's probability distribution function (PDF) and allows the evaluation of the outliers.

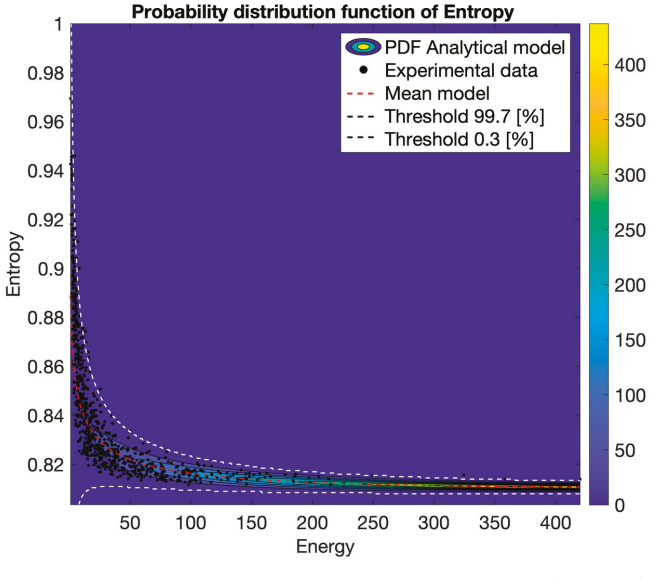

Figure 7. Entropy-energy dispersion and probability distribution function of the analytical model for a building complex near San Giovanni station.

3.3. Comparison of the Two Representations

The two approaches for representing the data shown above allow the localization of points of significant interest for monitoring structures and the subsidence phenomenon. These outcomes cannot be directly interpreted to perform novelty detection due to the limitations of the input data. However, it is possible to compare the results obtained through the two approaches to verify them. In detail, it is investigated how the points with a high-intensity negative velocity are distributed with respect to the values of entropy and energy of the signal. Figure 8a shows that points with higher absolute velocity have lower entropy values, concentrated in the range 0.8–0.82.

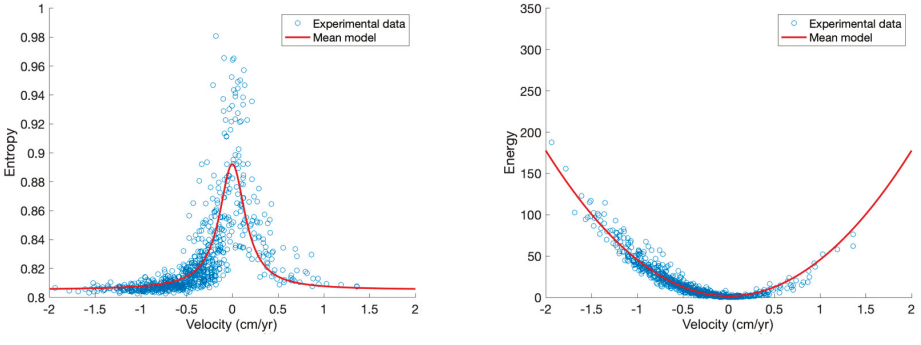

(**a**) (**b**)

Figure 8. Correlation between LOS velocity and entropy-energy dispersion in the period from 2017 to 2019 for a building complex near San Giovanni station: (**a**) Entropy-velocity dispersion; (**b**) Energy-velocity dispersion.

In contrast, points with velocities close to zero exhibit greater entropy. As the velocity increases beyond 0.5 cm/y, a further decrease in entropy is shown. Figure 8b shows how the energy remains low for velocity values close to zero and increases significantly for lower velocity values. These points correspond to locations subject to accentuated subsidence (beyond the $\mu - 3\sigma$ limit). Hence, in the entropy-energy dispersion, they constitute the decreasing branch on the right (Figure 9).

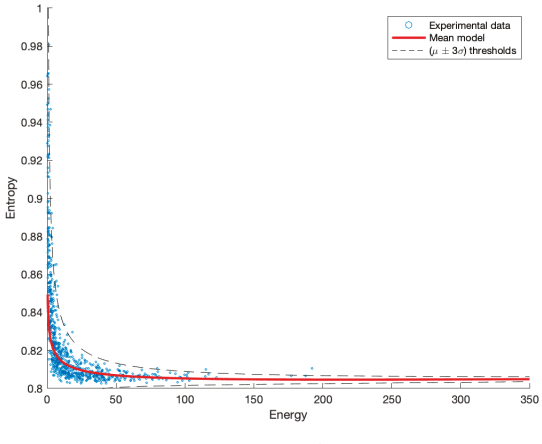

Figure 9. Entropy-energy dispersion for a building complex near San Giovanni station in the period from 2017 to 2019.

It can be observed that the experimental data subject to subsidence (low entropy and high energy) show lower variance with respect to the mean model, hence, lower uncertainty, and could be interpreted as signals related to perturbations that are actually moving those points. These points are represented in blue in Figure 10. The figure also shows in red the points that are defined as outliers of the entropy-energy dispersion, which are above the analytical threshold. Their signals show higher entropy than predicted by the mean model; thus, they are subjected to higher complexity and require further investigation, especially those that coincide with subsidence points.

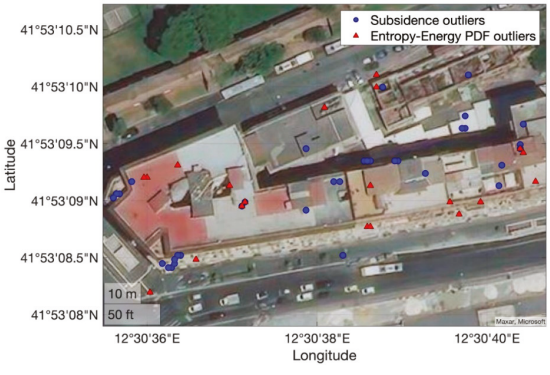

Figure 10. Map showing the experimental data for a building complex near San Giovanni station. The locations where subsidence is most emphasized and the entropy-energy outliers are highlighted.

For greater accuracy of the results, it would be necessary to identify and exclude any spurious points not related to the area of the buildings. In addition, structural type and features, such as the number of stories, should be investigated to reveal any variations due to dissimilarities between the adjacent structures. However, this can be left out as a consequence of the simplifying assumptions adopted in Section 2.

The entropy-energy dispersion can be further discussed by comparing two different periods to study the results before and after tunnel excavation. Given the complete dataset from 2011 to 2019, the following section distinguishes two periods of the same duration: 2011–2015 and 2015–2019. Figure 11 shows the correlation between the entropy-energy dispersion and the LOS velocity in the period from 2011 to 2015. Meanwhile, Figure 12 refers to the period from 2015 to 2019.

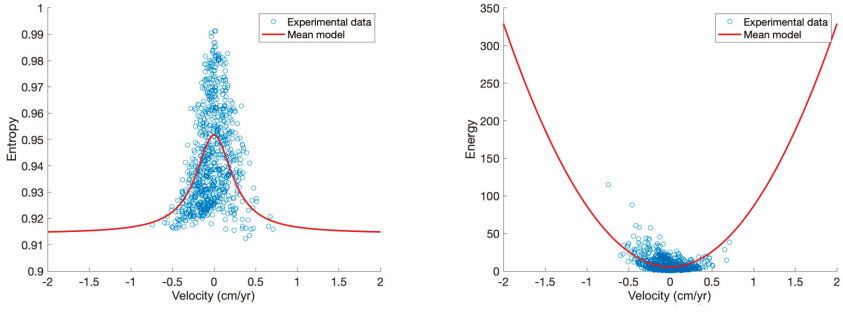

(**a**) (**b**)

Figure 11. Correlation between LOS velocity and entropy-energy dispersion in the period from 2011 to 2015 for a building complex near San Giovanni station: (**a**) Entropy-velocity dispersion; (**b**) Energy-velocity dispersion.

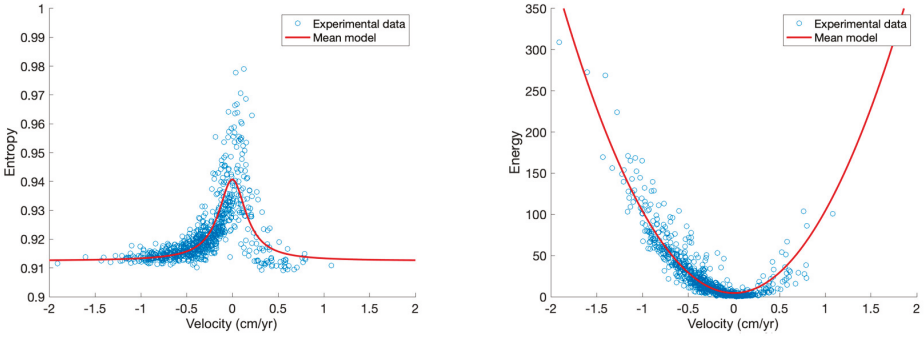

(**a**) (**b**)

Figure 12. Correlation between LOS velocity and entropy-energy dispersion in the period from 2015 to 2019 for a building complex near San Giovanni station: (**a**) Entropy-velocity dispersion; (**b**) Energy-velocity dispersion.

Figure 11a displays a higher level of scattering than Figure 12a. In addition, velocity values in the period 2011–2015 are more evenly dispersed when compared to the following period, and their intensity in the negative portion is lower, therefore significant subsidence is not observed. Consequently, the entropy-energy dispersion in the first period (Figure 13a) has fewer points on the low entropy–high energy branch with respect to Figure 13b, none of which reaches the limit of subsidence previously evaluated.

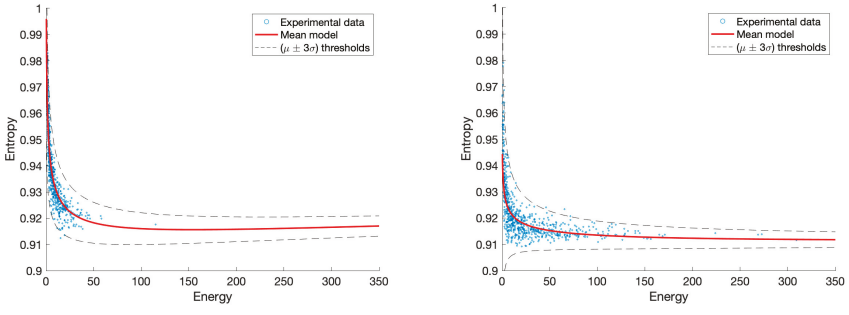

(**a**) (**b**)

Figure 13. Entropy-energy dispersion, mean model and thresholds for a building complex near San Giovanni station: (**a**) period from 2011 to 2015; (**b**) period from 2015 to 2019.

The comparison between the two periods is subsequently carried out by observing the variation in the parameters governing the fitting curves. A rational function of the second degree (Equation (2)) is used to fit the entropy-velocity dispersion (S-v) shown in Figures 11a and 12a, and a nonlinear regression model is used, starting from null initial parameters. Thus, the mean model of the dispersion of the points is obtained. Subsequently, the regression model of the deviations from the mean model is studied, using the same type of equation:

$$S = p_1 \frac{p_2 v^2 + 1}{p_3 v^2 + 1} \tag{2}$$

It can be observed that Equation (2) is symmetrical with respect to the axis ($v = 0$). This condition derives from the intention to study the structural response in the range of

small displacements, for which the structure is deemed to exhibit linear elastic behavior. In addition, it is assumed that the effect of settlements is also linear.

The first parameter of the mean model, which represents the value of the curve for null velocity, is subjected to a slight reduction, which is related to a global decrease in the system entropy in the second period. Instead, the ratio between p_2 and p_3 represents the limit value assumed by the function for high speed (in absolute value), normalized with respect to the p_1 value. In addition, an increase in the values of p_2 and p_3, while maintaining the same ratio, corresponds to a reduction in the amplitude of the curve with respect to the vertical axis, as the inflection points tend to be closer to the axis ($v = 0$). It occurs for the entropy in the second period, as shown by Figure 14a, where the two parameters increase, making the curve narrower with respect to the origin, so it tends toward the horizontal asymptotes more rapidly.

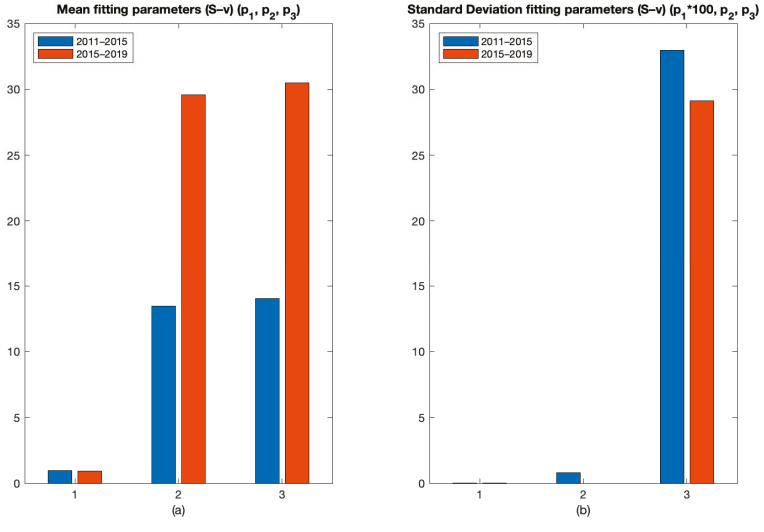

Figure 14. Fitting parameters of the entropy-velocity dispersions in the two periods for a building complex near San Giovanni station: (**a**) parameters of the mean model; (**b**) parameters of the standard deviation model.

For the system's variance (Figure 14b), the three parameters decrease from the first period to the second, reducing variance, especially for high velocity modules. It is worth noting that the parameters fitting guarantees positive variance.

Figure 15 shows the parameters derived from a nonlinear regression model to construct the mean and standard deviation fittings of the energy-velocity $(E\text{-}v)$ dispersion. A second-order polynomial model is used for the evaluation of the mean curve and the standard deviation, as a parabolic shape can easily be identified in the dispersion, especially in Figure 12b. As previously stated, the curves follow the hypothesis of linear elastic behavior; therefore, the vertices of the parabolic curves are fixed on the axis $(v = 0)$.

The two average curves are similar, but higher energy values are reached in the second period at the same velocities. This effect is represented by the increase in the second parameter of the mean curve in Figure 15a.

As shown by the second parameter in Figure 15b, there is a significant reduction in the standard deviation between the first and second periods for higher velocity values in modulus.

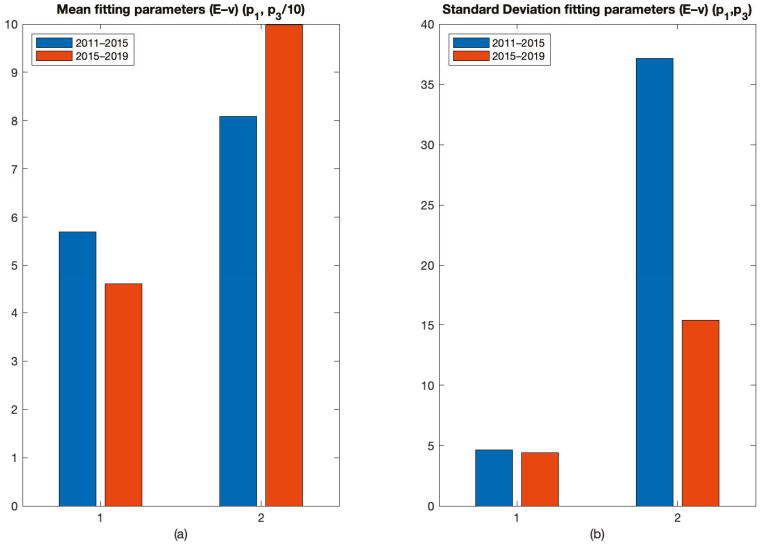

Figure 15. Fitting parameters of the energy-velocity dispersions in the two periods for a building complex near San Giovanni station: (**a**) parameters of the mean model; (**b**) parameters of the standard deviation model.

Figure 16 represents the parameters used to construct the mean and standard deviation model of the entropy-energy $(S\text{-}E)$ dispersion. These parameters are evaluated using a nonlinear constrained minimization, where p_1 must be positive. A second-order polynomial model is used for the mean curve on a logarithmic scale, as given by

$$S = exp\left(p_1 \ln E^2 + p_2 \ln E + p_3\right) \tag{3}$$

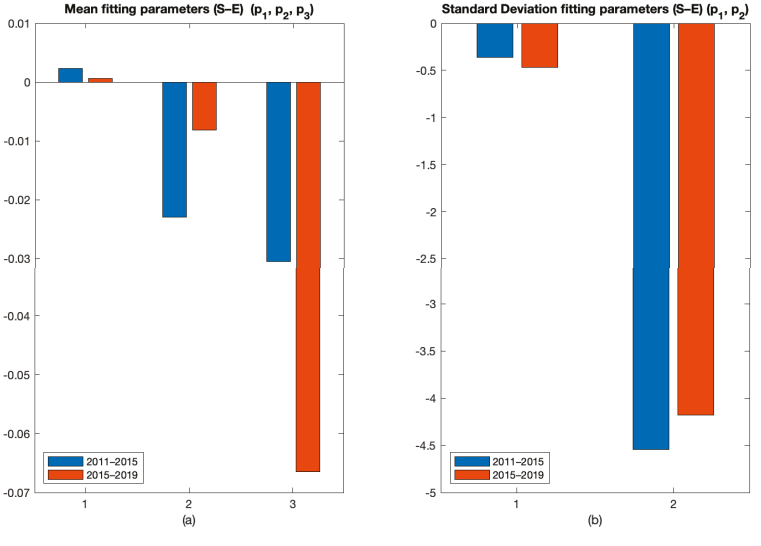

Figure 16. Fitting parameters of the entropy-energy dispersions in the two periods for a building complex near San Giovanni station: (**a**) parameters of the mean model; (**b**) parameters of the standard deviation model.

The value of p_3 represents the limit of the entropy, on the logarithmic scale, for an energy value that tends toward zero, so S tends toward $exp(p_3)$. The sign of p_1 expresses the concavity of the quadratic curve, while the ratio $-p_2/2p_1$ expresses its minimum. As mentioned above, a positive value of p_1 is enforced, in accordance with the physical meaning of the interpolated data. The decrease in the third parameter leads to a downward curve shift toward lower entropy values from the first period to the second. The module of the second parameter also decreases, leading to an increase in the curve slope on the logarithmic scale. Instead, the increase in the first parameter reduces the model's curvature; therefore, the entropy decreases faster with the energy increase.

The curve tends to lower and shift toward higher energy values. The effect given by the first and third parameters is to obtain an approximately constant stretch at low entropy. A first-order polynomial curve models the standard deviation adopting the least-squares method. The parameters are shown in Figure 16b. The first parameter increases in modulus, representing a more rapid reduction in variance with increasing energy. In addition, the effect of the second parameter is added, causing an upward shift. Thus, for low energy values, a similar standard deviation is obtained in the two periods, whereas for lower entropy values, a lower deviation is obtained. The points result closer to the mean model.

Hence, in the second period (the one affected by excavations) there is an evident variation of the dispersions, underlined through the analysis of the fitting parameters. Moreover, the three dispersions analyzed display a reduction of the signal deviation from the mean model, which can be interpreted as lower uncertainty in the measures.

3.4. The Colosseum Case Study

The velocity-entropy-energy approach is also adopted to analyze another case study, i.e., the Colosseum, chosen for its importance in the area, considering its artistic, historical and cultural significance.

The period for which the data are available (2011–2019) does not include the excavation operations on the tunnel in the proximity of this structure, which are more recent. Nevertheless, it is possible to evaluate the application of the entropy-energy approach to a monumental structure with distinctive features to identify the outliers. In addition, since the area has not yet been subjected to excavation, it is possible to compare the dispersions in the two periods identified above to verify that no significant variations have occurred. It allows validating the correlation between the parameters' variation and the effects of excavation on the building studied in previous sections.

The first analysis concerns the entropy-energy distribution for the available period, shown in Figure 17. Defining the average model and the thresholds related to the standard deviation makes it possible to identify the outliers. It is observed that these points fall mainly on the high values of entropy and low energy. The localization of these points on the Colosseum, reported in Figure 18, highlights that they are distributed mainly on the base and in a cluster on the west end of the structure. Therefore, although further investigation is required, the presence of these outliers could be due to a differential behavior of the west end with respect to the whole system.

Analogously to the previous case study, the velocity, entropy and energy dispersions in the first and second half of the reference period are studied to highlight possible changes (Figures 19–21). In addition, the parameters for the mean trends and standard deviation curves, respectively, are reported (Figures 22–24).

The entropy-velocity $(S\text{-}v)$ scatter in Figures 19a and 20a shows a slight decrease in entropy for velocities with high modulus, represented by the change in the first parameter of the mean curve (Figure 22a). The energy-velocity $(E\text{-}v)$ dispersion in Figures 19b and 20b shows minimal changes in the average behavior, as shown by the parameters in Figure 23, though, in the second period, there are points showing higher velocity modules in the negative, as well as the positive section.

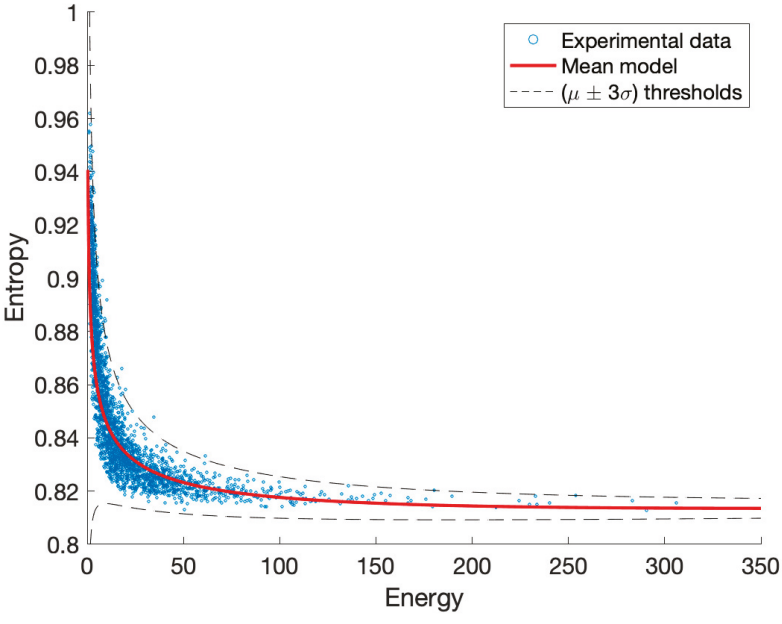

Figure 17. Entropy-energy dispersion and mean model for the Colosseum, from 2011 to 2019.

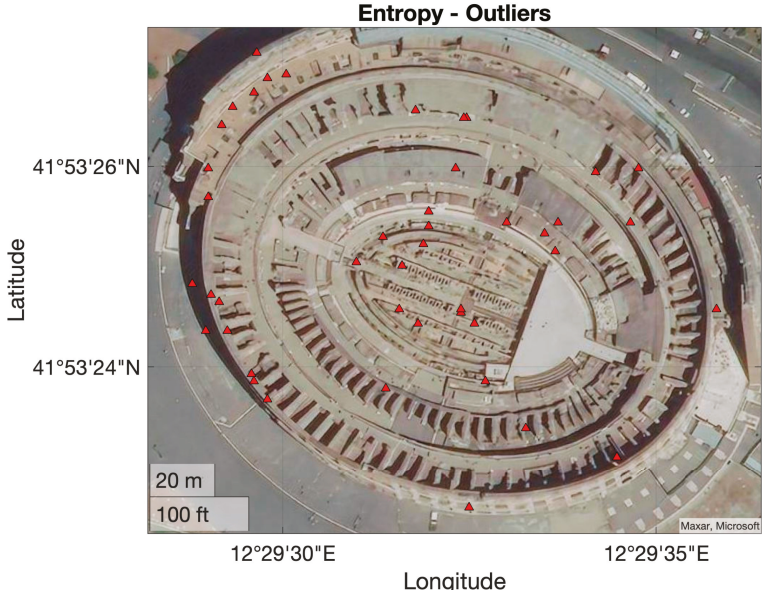

Figure 18. Map showing the outliers evaluated from the entropy-energy PDF for the Colosseum.

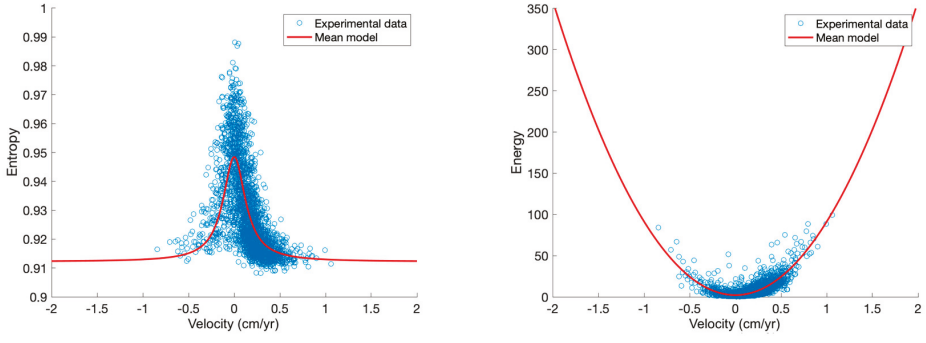

(**a**) (**b**)

Figure 19. Correlation between LOS velocity and entropy-energy dispersion for the Colosseum in the period from 2011 to 2015: (**a**) Entropy-velocity dispersion; (**b**) Energy-velocity dispersion.

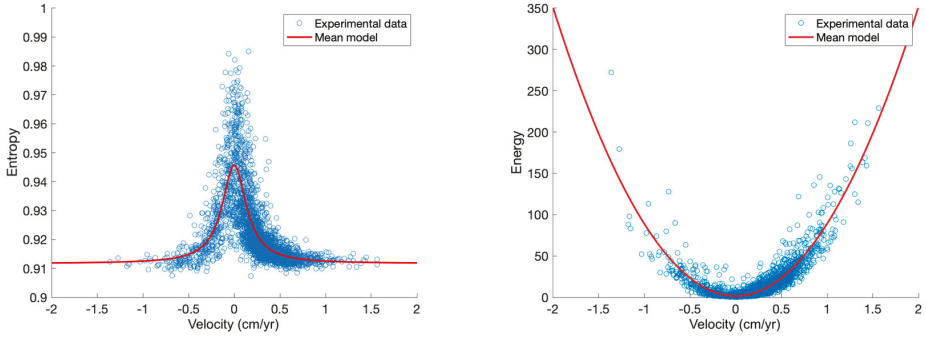

(**a**) (**b**)

Figure 20. Correlation between LOS velocity and entropy-energy dispersion for the Colosseum in the period from 2015 to 2019: (**a**) Entropy-velocity dispersion; (**b**) Energy-velocity dispersion.

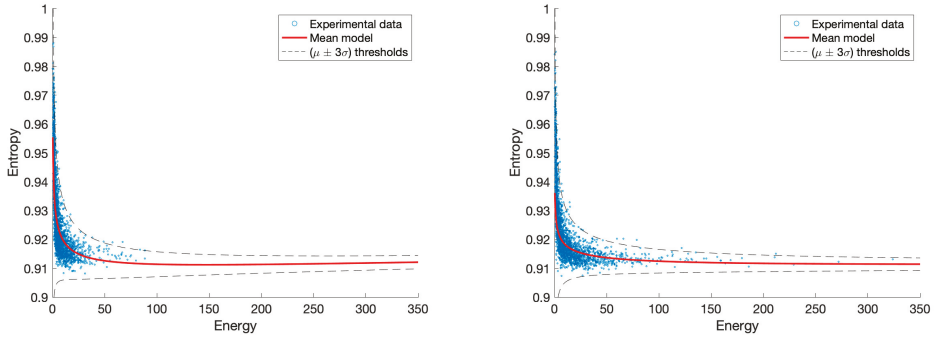

(**a**) (**b**)

Figure 21. Entropy-energy dispersion, mean model and thresholds for the Colosseum: (**a**) period from 2011 to 2015; (**b**) period from 2015 to 2019.

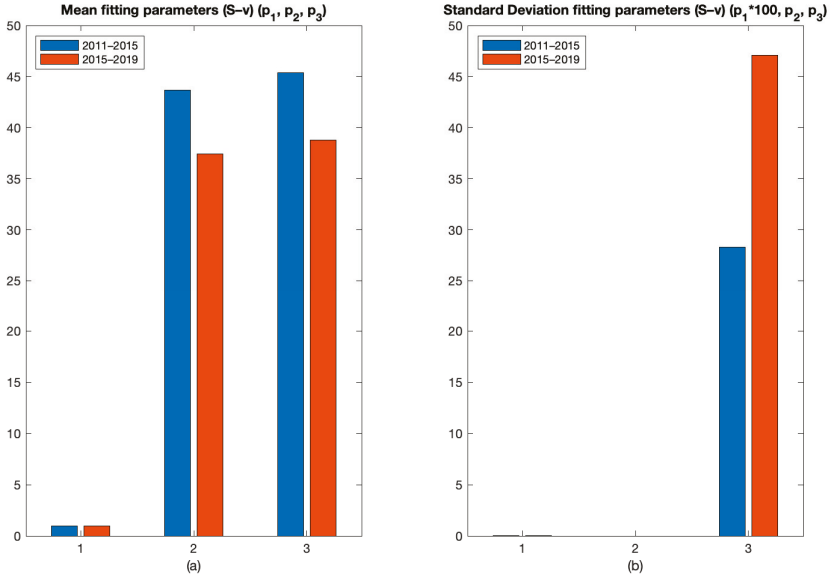

Figure 22. Fitting parameters of the entropy-velocity dispersions in the two periods for the Colosseum: (**a**) parameters of the mean model; (**b**) parameters of the standard deviation model.

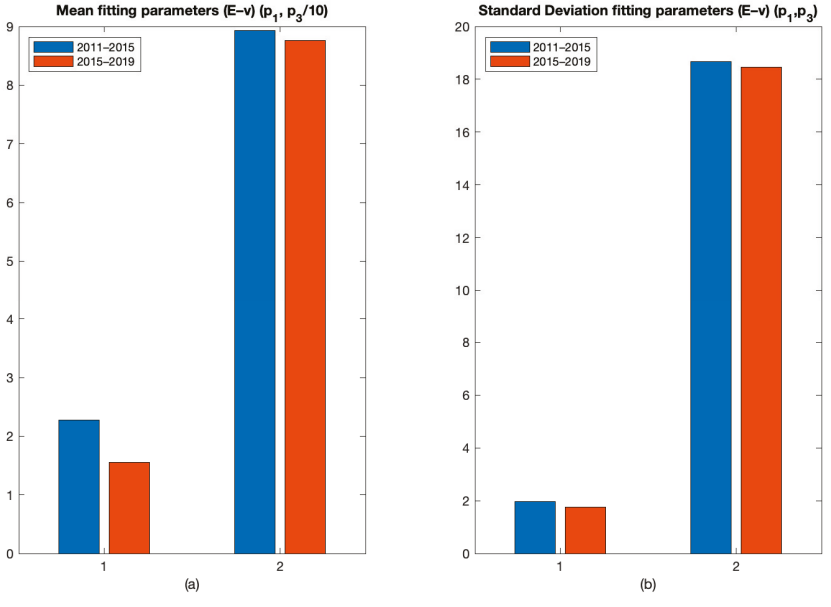

Figure 23. Fitting parameters of the energy-velocity dispersions in the two periods for the Colosseum: (**a**) parameters of the mean model; (**b**) parameters of the standard deviation model.

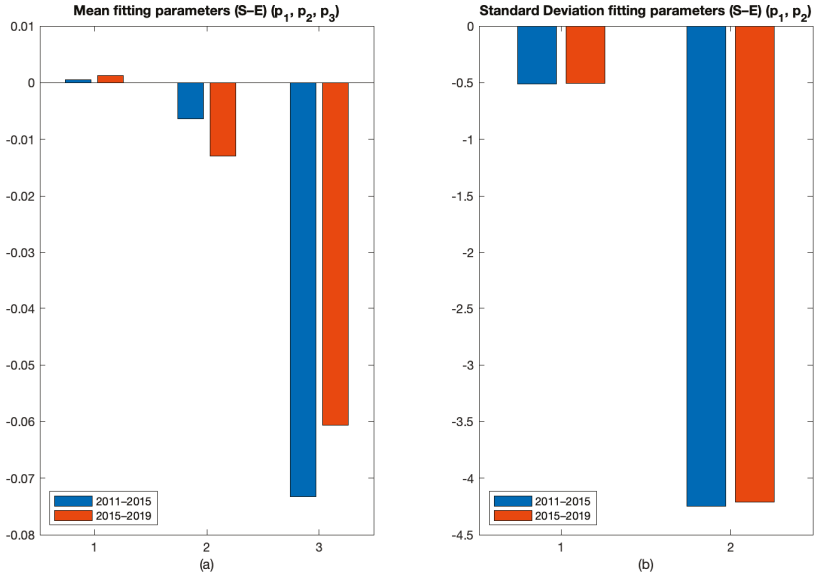

Figure 24. Fitting parameters of the entropy-energy dispersions in the two periods for the Colosseum: (**a**) parameters of the mean model; (**b**) parameters of the standard deviation model.

Finally, the entropy-energy $(S\text{-}E)$ dispersions in Figure 21 exhibit similar characteristics, highlighted by the parameters in Figure 24. It can be observed that there is no significant change in the standard deviation of the points from the mean models. Moreover, as expected, the overall variation in the mean models is lower than in the previous case study. It should be noted that the Colosseum is only analyzed on an anthropogenic basis. Therefore, it would be appropriate to extend the analysis to also consider other aspects because of its complex hydrogeological configuration, which could lead to further data perturbations.

4. Conclusions

Recent developments in the acquisition of satellite interferometric data allow their integration to more traditional methods for Structural Health Monitoring purposes, providing additional insights that are often not available from in situ sensors and ensuring high spatial and temporal coverage. However, there are still some challenges related to their application because of the differences in the data gathered compared to the traditional on-site data.

The new kind of data requires the development of optimal representation techniques that may be used to identify anomalous behavior necessary to provide an interpretation and carry out damage identification. Therefore, this paper explores different approaches; the first one is the representation of direct quantities, such as the velocity along the LOS of the satellite, which allows the identification of slow territorial-scale phenomena, such as subsidence. A second representation concerns the indirect quantities of entropy and energy, which allows modeling the behavior of a system (e.g., single building, building complex, monumental structure).

These approaches are used to identify the effects of subsidence induced by the excavation of a new subway line in the urban area of Rome. In detail, the first representation highlights the presence of subsidence in the track's proximity. The second one studies the effects on a smaller observation scale and identifies the outliers. The entropy-energy representation is compared to the LOS velocity to validate the results. It is observed that the points subjected to subsidence are distributed on a low-entropy and high-energy branch

and are mainly characterized by low uncertainty, which can be interpreted as the signal of an actual movement.

In addition, the paper compares results obtained from two periods, before and after the start of excavation, studying parameter changes in the curve-fitting process. It highlights an evident variation in the signal response, especially in the variance parameters, indicating the presence of effects induced by tunnel construction.

The same procedure, applied to the Colosseum case study, does not show significant changes in the behavior of this monument, which was an expected result, given that its area had not been subjected to tunnel excavation during the analysis period. Furthermore, the ability of the entropy-energy representation to be applied to monumental structures is demonstrated, identifying the presence of outliers, i.e., points that should be further investigated, as they could also be related to anomalous structural and non-structural processes. Further studies are required to provide an objective interpretation of the outliers from the structural point of view. Nevertheless, future developments and the continuous increase in the quality of satellite data may allow the practical application of such information for SHM, leading to a low-cost, automated process for the study of large urban areas.

Author Contributions: Conceptualization, G.D., M.C., E.L., G.M., C.S. and R.C.; methodology, G.D., M.C., E.L., G.M., C.S. and R.C.; software, G.D., M.C., E.L., G.M., C.S. and R.C.; validation, G.D., M.C., E.L., G.M., C.S. and R.C.; formal analysis, G.D., M.C., E.L., G.M., C.S. and R.C.; investigation, G.D., M.C., E.L., G.M., C.S. and R.C.; resources, G.D., M.C., E.L., G.M., C.S. and R.C.; data curation, G.D., M.C., E.L., G.M., C.S. and R.C.; writing—original draft preparation, G.D.; writing—review and editing, G.D., M.C., E.L., G.M., C.S. and R.C.; visualization, G.D., M.C., E.L., G.M., C.S. and R.C.; supervision, M.C., E.L., G.M., C.S. and R.C.; project administration, M.C., E.L., G.M., C.S. and R.C.; funding acquisition, R.C. All authors have read and agreed to the published version of the manuscript.

Funding: This research was funded by "Progetto DPC-ReLUIS 2019–2021—WP 6 Monitoraggio e dati satellitari" (https://www.reluis.it/it/progetti-dpc-reluis/dpc-reluis-2019-2021.html, accessed on 25 January 2022).

Institutional Review Board Statement: Not applicable.

Informed Consent Statement: Not applicable.

Data Availability Statement: Data available from the authors upon reasonable request.

Acknowledgments: The authors want to acknowledge the "Progetto DPC-ReLUIS 2019–2021—WP 6 Monitoraggio e dati satellitari" for the provided experimental data.

Conflicts of Interest: The authors declare no conflict of interest.

References

1. Farrar, C.R.; Worden, K. *Structural Health Monitoring: A Machine Learning Perspective*; John Wiley & Sons: Chichester, UK, 2012; ISBN 1-118-44321-7.
2. Gili, P.; Civera, M.; Roy, R.; Surace, C. An unmanned lighter-than-air platform for large scale land monitoring. *Remote Sens.* **2021**, *13*, 2523. [CrossRef]
3. Campbell, J.B.; Wynne, R.H. *Introduction to Remote Sensing*; Guilford Press: New York, NY, USA, 2011; ISBN 1-60918-177-8.
4. Forster, B. An examination of some problems and solutions in monitoring urban areas from satellite platforms. *Int. J. Remote Sens.* **1985**, *6*, 139–151. [CrossRef]
5. Curlander, J.C.; McDonough, R.N. *Synthetic Aperture Radar*; Wiley: New York, NY, USA, 1991; Volume 11.
6. Rodriguez, E.; Martin, J. Theory and design of interferometric synthetic aperture radars. *IEE Proc. F Radar Signal Process.* **1992**, *139*, 147–159. [CrossRef]
7. Bonano, M.; Manunta, M.; Pepe, A.; Paglia, L.; Lanari, R. From previous C-band to new X-band SAR systems: Assessment of the DInSAR mapping improvement for deformation time-series retrieval in urban areas. *IEEE Trans. Geosci. Remote Sens.* **2013**, *51*, 1973–1984. [CrossRef]
8. Cigna, F.; Lasaponara, R.; Masini, N.; Milillo, P.; Tapete, D. Persistent scatterer interferometry processing of COSMO-SkyMed StripMap HIMAGE Time series to depict deformation of the historic centre of Rome, Italy. *Remote Sens.* **2014**, *6*, 12593–12618. [CrossRef]

9. Zhu, M.; Wan, X.; Fei, B.; Qiao, Z.; Ge, C.; Minati, F.; Vecchioli, F.; Li, J.; Costantini, M. Detection of building and infrastructure instabilities by automatic spatiotemporal analysis of satellite SAR interferometry measurements. *Remote Sens.* **2018**, *10*, 1816. [CrossRef]
10. Arangio, S.; Calò, F.; Di Mauro, M.; Bonano, M.; Marsella, M.; Manunta, M. An application of the SBAS-DInSAR technique for the assessment of structural damage in the city of Rome. *Struct. Infrastruct. Eng.* **2014**, *10*, 1469–1483. [CrossRef]
11. Bozzano, F.; Esposito, C.; Mazzanti, P.; Patti, M.; Scancella, S. Imaging multi-age construction settlement behaviour by advanced SAR interferometry. *Remote Sens.* **2018**, *10*, 1137. [CrossRef]
12. Macchiarulo, V.; Milillo, P.; Blenkinsopp, C.; Reale, C.; Giardina, G. InSAR monitoring of regional infrastructure networks. In Proceedings of the 2021 IEEE International Geoscience and Remote Sensing Symposium IGARSS, Brussels, Belgium, 11–16 July 2021; pp. 6233–6236.
13. Di Carlo, F.; Miano, A.; Giannetti, I.; Mele, A.; Bonano, M.; Lanari, R.; Meda, A.; Prota, A. On the integration of multi-temporal synthetic aperture radar interferometry products and historical surveys data for buildings structural monitoring. *J. Civ. Struct. Health Monit.* **2021**, *11*, 1429–1447. [CrossRef]
14. Tang, P.; Chen, F.; Zhu, X.; Zhou, W. Monitoring cultural heritage sites with advanced multi-temporal InSAR technique: The case study of the summer palace. *Remote Sens.* **2016**, *8*, 432. [CrossRef]
15. Milillo, P.; Giardina, G.; DeJong, M.J.; Perissin, D.; Milillo, G. Multi-temporal InSAR structural damage assessment: The London crossrail case study. *Remote Sens.* **2018**, *10*, 287. [CrossRef]
16. Lenticchia, E.; Miraglia, G.; Ceravolo, R. Exploring problems and prospective of satellite interferometric data for the seismic structural health monitoring of existing buildings and architectural heritage. In Proceedings of the 10th International Conference on Structural Health Monitoring of Intelligent Infrastructure, SHMII 10, Porto, Portugal, 30 June–2 July 2021.
17. Talledo, D.A.; Miano, A.; Bonano, M.; Di Carlo, F.; Lanari, R.; Manunta, M.; Meda, A.; Mele, A.; Prota, A.; Saetta, A. Satellite radar interferometry: Potential and limitations for structural assessment and monitoring. *J. Build. Eng.* **2021**, *46*, 103756. [CrossRef]
18. ReLUIS. Pubblicata la Prima Versione delle Linee Guida per l'Utilizzo dei Dati Interferometrici Satellitari Ai Fini dell'interpretazione del Comportamento Strutturale delle Costruzioni. Available online: https://www.reluis.it (accessed on 15 November 2021).
19. Agenzia Spaziale Italiana (ASI). Home Page. Available online: https://www.asi.it (accessed on 15 November 2021).
20. Lanari, R.; Mora, O.; Manunta, M.; Mallorquí, J.J.; Berardino, P.; Sansosti, E. A small-baseline approach for investigating deformations on full-resolution differential SAR interferograms. *IEEE Trans. Geosci. Remote Sens.* **2004**, *42*, 1377–1386. [CrossRef]
21. Ferretti, A.; Guarnieri, A.M.; Prati, C.; Rocca, F. *InSAR Principles: Guidelines for SAR Interferometry Processing and Interpretation*; ESA Pubblications ESTEC: Noordwijk, The Netherlands, 2007.
22. Tapete, D.; Cigna, F. COSMO-SkyMed SAR for detection and monitoring of archaeological and cultural heritage sites. *Remote Sens.* **2019**, *11*, 1326. [CrossRef]
23. Italian Space Agency. ASI COSMO-SkyMed Mission and Products Description. In *Doc. N°ASI-CSM-PMG-NT-001, 8 July 2019, Issue 3*; Italian Space Agency: Rome, Italy, 2019.
24. Metro C, S.P.A. Metro C—Il GC Che Sta Realizzando la Linea C. Available online: https://metrocspa.it (accessed on 15 November 2021).
25. Shannon, C.E. A mathematical theory of communication. *Bell Syst. Tech. J.* **1948**, *27*, 379–423. [CrossRef]
26. Farrar, C.; Park, G.; Worden, K. *Complexity: A New Axiom for Structural Health Monitoring?* Los Alamos National Laboratory: Los Alamos, NM, USA, 2010.
27. Metro C, S.P.A. Metro C: Un VIaggio Nella Storia. La Stazione Amba Aradam/Ipponio. Available online: https://metrocspa.it/blog/metro-c-un-viaggio-nella-storia-la-stazione-amba-aradam-ipponio/ (accessed on 29 December 2021).
28. Miliziano, S.; de Lillis, A. Predicted and Observed settlements induced by the mechanized tunnel excavation of metro line c near S. Giovanni station in Rome. *Tunn. Undergr. Space Technol.* **2019**, *86*, 236–246. [CrossRef]
29. D'Aranno, P.J.; Gizzi, F.; Marsella, M.; Scifoni, S.; Scutti, M.; Sonnessa, A.; Bonano, M.; Manunta, M. Understanding the effects of tunneling on buildings by analyzing dinsar data: The case of the new subway in Rome, Italy. In Proceedings of the 1st IMEKO TC4 International Workshop on Metrology for Geotechnics, MetroGeotechnics, Benevento, Italy, 17–18 March 2016.

applied sciences

MDPI

Article

Modal Identification of Structures with Interacting Diaphragms

Rosario Ceravolo [1,2,*], Erica Lenticchia [1,2], Gaetano Miraglia [1,2], Valerio Oliva [1] and Linda Scussolini [1]

[1] Department of Structural, Geotechnical and Building Engineering-DISEG, Politecnico di Torino, Corso Duca degli Abruzzi 24, 10129 Turin, Italy; erica.lenticchia@polito.it (E.L.); gaetano.miraglia@polito.it (G.M.); valerio.oliva@polito.it (V.O.); linda.scussolini@polito.it (L.S.)
[2] Responsible Risk Resilience Interdepartmental Center (R3C), Politecnico di Torino, Corso Duca degli Abruzzi 24, 10129 Turin, Italy
* Correspondence: rosario.ceravolo@polito.it

Abstract: System identification proves in general to be very efficient in the extraction of modal parameters of a structure under ambient vibrations. However, great difficulties can arise in the case of structures composed of many connected bodies, whose mutual interaction may lead to a multitude of coupled modes. In the present work, a methodology to approach the identification of interconnected diaphragmatic structures, exploiting a simplified analytical model, is proposed. Specifically, a parametric analysis has been carried out on a numerical basis on the simplified model, i.e., a multiple spring–mass model. The results were then exploited to aid the identification of a significant case study, represented by the Pavilion V, designed by Riccardo Morandi as a hypogeum hall of the Turin Exhibition Center. The structure is indeed composed of three blocks separated by expansion joints, whose characteristics are unknown. As the main result, light was shed on the contribution of the stiffness of the joints to the global dynamic behavior of structures composed of interacting diaphragms, and, in particular, on the effectiveness of the joints of Pavilion V.

Keywords: system identification; simplified analytical models; interacting diaphragms; expansion joints; structural health monitoring; operational modal analysis; Riccardo Morandi; Pavilion V

Citation: Ceravolo, R.; Lenticchia, E.; Miraglia, G.; Oliva, V.; Scussolini, L. Modal Identification of Structures with Interacting Diaphragms. *Appl. Sci.* **2022**, *12*, 4030. https://doi.org/10.3390/app12084030

Academic Editor: Raffaele Zinno

Received: 25 March 2022
Accepted: 14 April 2022
Published: 15 April 2022

Publisher's Note: MDPI stays neutral with regard to jurisdictional claims in published maps and institutional affiliations.

Copyright: © 2022 by the authors. Licensee MDPI, Basel, Switzerland. This article is an open access article distributed under the terms and conditions of the Creative Commons Attribution (CC BY) license (https://creativecommons.org/licenses/by/4.0/).

1. Introduction

The study of the dynamic response of structures under ambient vibrations is fundamental in many engineering fields, including, but not limited to, Structural Health Monitoring (SHM). Even in the range of small linear deformations, such as are observed under ambient excitation, understanding the dynamic behavior of a system might be challenging, especially when testing rigid and massive structures. To make things more difficult, there are then the interactions with the surrounding environment, the uncertainty in geometry, materials characteristics, details, and above all the difficulty in defining the constraints, which often call for simplified models to drive the modal identification process.

In its broadest sense, system identification can be defined as the field of study where models are fitted into measured data [1]. In civil engineering, output-only modal identification techniques allow to significantly extend the range of structures where modal analysis can be applied [2], overcoming the difficulty deriving from producing and measuring proper excitations in large-sized structures. Practically, ambient vibration testing is used in all contexts in which only the dynamic response can be measured, while excitation (e.g., wind, traffic, environmental noise, etc.) is known only in a probabilistic sense or is even unknown [3,4]. Like in any other kind of experimental modal analysis, the measured data come from the record of the sensors at different locations of the structure [3]. A comprehensive amount of literature on the comparison of output-only modal techniques can be found in [4–8].

Throughout the years, output-only dynamic identification relied primarily on the time-domain approach, which declines in many robust and accurate algorithms [7]. Since the

theoretical part overcomes the goal of this paper, references can be found in [9–13]. Time-domain techniques, in particular, are demonstrated to be very effective in the detection of closely spaced modes, easy to optimize, and automate [13]. It should be also pointed out that, in the presence of strong non-stationary components, a possible option is recurring in time–frequency representations and algorithms [14].

The main results deriving from linear identification techniques are the modal parameters of the structure, as they result from diagrams of stabilization to the varying of the order of the system used in the identification. The discrimination of authentic modal components from spurious ones is achieved with the use of modal assurance criteria, and sometimes exploiting clustering techniques, which consist in dividing different data from a data set into property-based groups. However, the detection and classification of the authentic modal parameters from the numerical solutions to the inverse problem are not exempt from criticalities.

The main critical aspect certainly lies in the well-known limitations of experimental modal analysis procedures in massive or otherwise rigid structures. Indeed, identification algorithms have been successfully applied to structures presenting a diaphragmatic behavior, for instance on multi-span concrete bridges, e.g., see [10,13,15,16]. However, the sensitivity of the identification process to the external or mutual constraints of these diaphragms has never been investigated.

The second criticality concerns the choice of the model used in the identification process. In structures with complex, sometimes non-linear, interactions, a choice could be to adopt black-box models [17,18]. In spite of many successful applications of such an approach, the solution of the inverse problem strongly depends on the choice of the parameters of the black-box model [19]. Thus, an alternative approach consists of the improvement of analytical models using test data [20], possibly recurring to surrogate models to increase the computational efficiency of the whole process [21]. In fact, this tool not only allows to overcome the problem of the high number of modes resulting from the identification but also to identify and differentiate local modes from global ones, especially regarding tight couplings between vertical and horizontal modes. In the case of bridges [22], the local damage can be detected often at very high modes, better identified by a surrogate model. Similar results can be obtained on specific schemes by using model reduction techniques, as far as applicable.

The main purpose of the present work is to propose a methodology to approach interconnected diaphragmatic structures (interacting at their joints, at the external constraints, and the surrounding environment, e.g., embankment), and the identification of their modal parameters, aided by parametric analyses on simplified/reduced analytical models.

To accomplish the scope stated above, the case study of the Pavilion V of Turin Exhibition Center is analyzed. This hypogeum pavilion, designed in 1959 by Riccardo Morandi, represents a fascinating case study of a structure composed of three macro blocks separated by two joints. The fundamental static scheme of the structure is a version of Morandi's balanced beam. The diaphragmatic and massive behavior of the roofing system, with post-tensioned concrete ribs, the uncertainties related to the soil-structure interaction, and the effectiveness of the joints are just a few elements that contribute to the high complexity of the building's dynamics.

The paper is organized as follows. In Section 2, the dynamic equation for rigid diaphragms interacting at linear elastic joints is developed. The methodology is then applied in Section 3 on a numerical benchmark to demonstrate the effective contribution of the joints to the dynamic behavior of the structure. As a result, the effects of the variation of the stiffness of the springs governing the interaction are investigated, and, consequently, a discrimination between the global and the local modes is provided. In Section 4, the case study of Pavilion V is first introduced and then the description of the experimental setups of a test campaign carried out in 2019 is reported. The modal identification of the structure is then finally carried out by exploiting a simplified analytical model and the

modal parameters are extracted in Section 5. The outcomes of an analysis to investigate the effectiveness of the joints are reported in Section 6. Conclusions are drawn in Section 7.

2. Dynamic Equilibrium Equation for Structures with Interacting Diaphragms

For simplicity, diaphragms are assumed to have only three degrees of freedom, namely two in-plane translations, along x- and y-directions, and the rotation around the z-direction.

Referring to the i-th diaphragm, one can define m_i as the mass, $J_{0,i}$ as the polar moment of inertia and $m_i^{x\gamma}$ and $m_i^{y\gamma}$as static moments, $\overline{k}_i^x$ and $\overline{k}_i^y$ as, respectively, the translational stiffnesses in the x-direction and in the y-direction, $\overline{k}_i^\gamma$ as the torsional stiffness, $\overline{k}_i^{x\gamma}$and $\overline{k}_i^{y\gamma}$ mixed stiffness terms that regulate the coupling between the translational and rotational degree of freedom, and u_i, v_i and γ_i as the displacements in the x-direction, in the y-direction, and the rotation, respectively.

In free undamped vibration conditions, the dynamic equilibrium of the i-th diaphragm, if connected only to the ground, writes:

$$\begin{bmatrix} m_i & 0 & m_i^{x\gamma} \\ 0 & m_i & m_i^{y\gamma} \\ m_i^{x\gamma} & m_i^{y\gamma} & J_{0,i} \end{bmatrix} \begin{Bmatrix} \ddot{u}_i \\ \ddot{v}_i \\ \ddot{\gamma}_i \end{Bmatrix} + \begin{bmatrix} \overline{k}_i^x & 0 & \overline{k}_i^{x\gamma} \\ 0 & \overline{k}_i^y & \overline{k}_i^{y\gamma} \\ \overline{k}_i^{x\gamma} & \overline{k}_i^{y\gamma} & \overline{k}_i^\gamma \end{bmatrix} \begin{Bmatrix} u_i \\ v_i \\ \gamma_i \end{Bmatrix} = \begin{Bmatrix} 0 \\ 0 \\ 0 \end{Bmatrix} \tag{1}$$

Now assume that the generic i-th diaphragm is part of a system of n interacting diaphragms. The interaction is assumed to be chain-like, i.e., only between adjacent diaphragms, and it is described by means of linear springs.

In analogy with Equation (1), it is possible to define the mass matrices of the system $\mathbf{M_{xx}}$ and $\mathbf{M_{yy}}$, the matrix of polar moments of inertia $\mathbf{M_{\gamma\gamma}}$ and the matrices of the static moments $\mathbf{M_{x\gamma}}$ and $\mathbf{M_{y\gamma}}$, as well as the stiffness matrices along the three directions $\mathbf{K_{xx}}$, $\mathbf{K_{yy}}$ and $\mathbf{K_{\gamma\gamma}}$, and the mixed terms stiffness matrices $\mathbf{K_{x\gamma}}$ and $\mathbf{K_{y\gamma}}$, so that the equilibrium equation in compact form writes in terms of $3n \times 3n$ matrices:

$$\begin{bmatrix} \mathbf{M_{xx}} & 0 & \mathbf{M_{x\gamma}} \\ 0 & \mathbf{M_{yy}} & \mathbf{M_{y\gamma}} \\ \mathbf{M_{x\gamma}} & \mathbf{M_{y\gamma}} & \mathbf{M_{\gamma\gamma}} \end{bmatrix} \begin{Bmatrix} \ddot{\mathbf{u}} \\ \ddot{\mathbf{v}} \\ \ddot{\boldsymbol{\gamma}} \end{Bmatrix} + \begin{bmatrix} \mathbf{K_{xx}} & 0 & \mathbf{K_{x\gamma}} \\ 0 & \mathbf{K_{yy}} & \mathbf{K_{y\gamma}} \\ \mathbf{K_{x\gamma}} & \mathbf{K_{y\gamma}} & \mathbf{K_{\gamma\gamma}} \end{bmatrix} \begin{Bmatrix} \mathbf{u} \\ \mathbf{v} \\ \boldsymbol{\gamma} \end{Bmatrix} = \begin{Bmatrix} 0 \\ 0 \\ 0 \end{Bmatrix} \tag{2}$$

Defining then the translational stiffness of the springs connecting the i-th diaphragm with two adjacent diaphragms in the x-direction as k_i^x and k_{i+1}^x, the stiffness matrix along the x-direction $\mathbf{K_{xx}}$ writes:

$$\mathbf{K_{xx}} = \begin{bmatrix} k_1^x + k_2^x + \overline{k}_1^x & -k_2^x & \dots & \dots & 0 \\ \dots & \dots & \dots & \dots & \dots \\ \dots & -k_i^x & k_i^x + k_{i+1}^x + \overline{k}_i^x & -k_{i+1}^x & \dots \\ \dots & \dots & \dots & \dots & \dots \\ 0 & \dots & \dots & -k_n^x & k_n^x + \overline{k}_n^x \end{bmatrix} \tag{3}$$

Similarly to Equation (3), also the stiffness matrix along the y-direction, $\mathbf{K_{yy}}$, and rotation γ, $\mathbf{K_{\gamma\gamma}}$, can be formulated.

The interaction between the i-th diaphragm and the adjacent ones by means of linear springs is described in Figure 1.

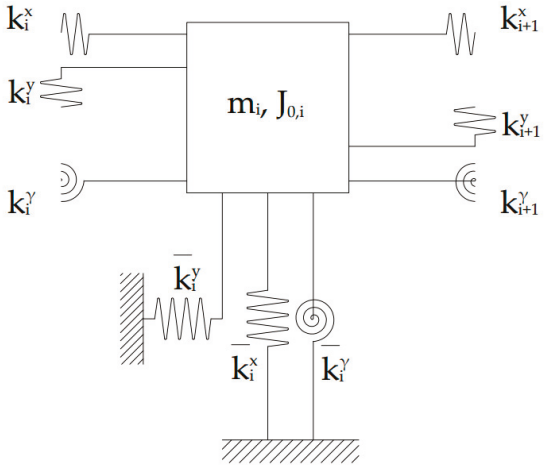

Figure 1. Lumped mass model of the interacting *i*-th diaphragm.

3. Numerical Benchmark: System with Three Interacting Diaphragms

The lumped mass model of three adjacent interacting diaphragms represented in Figure 2 is now considered. The system, presenting a diaphragmatic behavior with a chain-like interaction, is composed of three masses m_1, m_2 and m_3, and their respective polar moments of inertia $J_{0,1}$, $J_{0,2}$ and $J_{0,3}$.

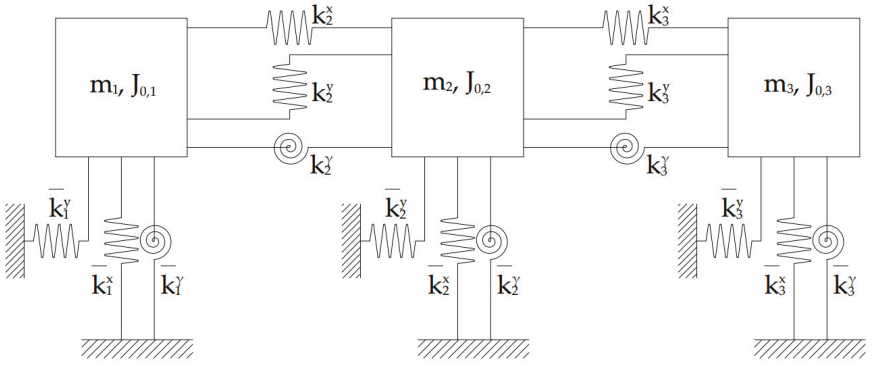

Figure 2. Lumped mass model of three adjacent interactive diaphragms.

The values of the translational stiffnesses along the x-direction, $\bar{k}_1^x$, $\bar{k}_2^x$ and $\bar{k}_3^x$, the translational stiffnesses along the y-direction, $\bar{k}_1^y$, $\bar{k}_2^y$ and $\bar{k}_3^y$, the torsional stiffnesses $\bar{k}_1^\gamma$, $\bar{k}_2^\gamma$ and $\bar{k}_3^\gamma$ around γ, were chosen to represent typical values of square concrete diaphragms of 50 m on each side. The mixed terms of stiffnesses $\bar{k}_1^{x\gamma}$, $\bar{k}_2^{x\gamma}$, $\bar{k}_3^{x\gamma}$ and $\bar{k}_1^{y\gamma}$, $\bar{k}_2^{y\gamma}$, $\bar{k}_3^{y\gamma}$, and the static moments S_1^x, S_2^x, S_3^x and S_1^y, S_2^y, S_3^y have been calculated accordingly. The numerical values of masses, polar moments of inertia, static moments, and stiffnesses are reported in Table 1.

Table 1. Numerical values of parameters.

Parameter	Numerical Value	Unit
$m_1 = m_2 = m_3$	4.2×10^6	kg
$J_{0,1}$	1.0×10^{10}	N·m^2
$J_{0,2}$	3.2×10^{10}	N·m^2
$J_{0,3}$	7.5×10^{10}	N·m^2
$m_1^{y\gamma}$	1.1×10^8	kg·m
$m_2^{y\gamma}$	3.2×10^8	kg·m
$m_3^{y\gamma}$	5.4×10^8	kg·m
$m_1^{x\gamma} = m_2^{x\gamma} = m_3^{x\gamma}$	-1.5×10^8	kg·m
$\overline{k}_1^x = \overline{k}_2^x = \overline{k}_3^x$	8.7×10^8	N/m
$\overline{k}_1^y = \overline{k}_2^y = \overline{k}_3^y$	3.4×10^8	N/m
$\overline{k}_1^\gamma$	2.2×10^{12}	N/m
$\overline{k}_2^\gamma$	3.9×10^{12}	N/m
$\overline{k}_3^\gamma$	7.4×10^{12}	N/m
$\overline{k}_1^{x\gamma} = \overline{k}_2^{x\gamma} = \overline{k}_3^{x\gamma}$	-3.0×10^{10}	N·m/m
$\overline{k}_1^{y\gamma}$	8.6×10^9	N·m/m
$\overline{k}_2^{y\gamma}$	2.6×10^{10}	N·m/m
$\overline{k}_3^{y\gamma}$	4.3×10^{10}	N·m/m
$k_2^x = k_3^x$	8.7×10^8	N/m
$k_2^y = k_3^y$	3.4×10^8	N/m
$k_2^\gamma = k_3^\gamma$	2.2×10^{12}	N/m

The stiffnesses describing the interaction k_2^x, k_2^y, k_2^γ, and k_3^x, k_3^y, k_3^γ are set as a fraction (factor varying between 0 and 2), defined as k_{var}, of the values reported in Table 1, which corresponds to the continuity of the spring. The eigenvalue problem of the above-mentioned system has been then solved to extract the modal parameters, i.e., natural frequencies and mode shapes of the system.

Parametric simulations were conducted to study the relative variation of the modal frequencies of the system with respect to k_{var}. A simultaneous uniform variation of k_2^x, k_2^y, k_2^γ, and k_3^x, k_3^y, k_3^γ has been considered. To this aim, the modal frequencies of the system, generally called f_r (with r varying from 1 to 9), were normalized with respect to the fundamental frequency.

Figures 3–5 represent the variation of the 9 modes and of the 9 natural frequencies of the system with respect to k_{var}. To have a better visualization, the representation is divided into groups of 3 modes each: Figure 3 represents the modes from 1 to 3, Figure 4 from 4 to 6, and Figure 5 from 7 to 9. It is worth noting that the y-axis scales of Figures 3–5 are different.

Considerations can be made concerning the modal parameters of the system. In general, an increasing linear trend can be observed in the case of the natural frequencies. Figure 3 shows that the curve corresponding to the first natural frequency f_1 is almost flat, while a clear variation of f_r can be observed for the curves corresponding to the second and the third ones (f_2 and f_3). A similar trend is observed for the other two groups reported in Figures 4 and 5. Therefore, it can be said that increasing values of the stiffness characterizing the interaction clearly affect the higher modal frequencies of each group more. Comparing the three figures, it is noticeable that in the case of the groups of frequencies f_1, f_2, f_3 and f_4, f_5, f_6, for values of k_{var} equal to 0, the numerical value of the frequencies is almost the same. The same behavior is not found for the group of frequencies f_7, f_8 and f_9, where the numerical value of f_9 is almost double the numerical values of f_7 and f_8.

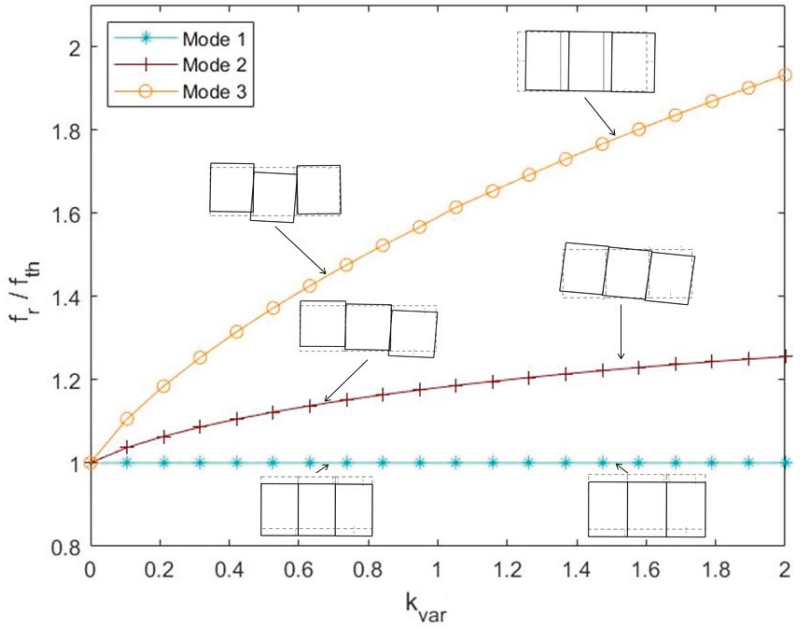

Figure 3. Variation of the modes and of the natural frequencies of the system from 1 to 3 as a function of k_{var}.

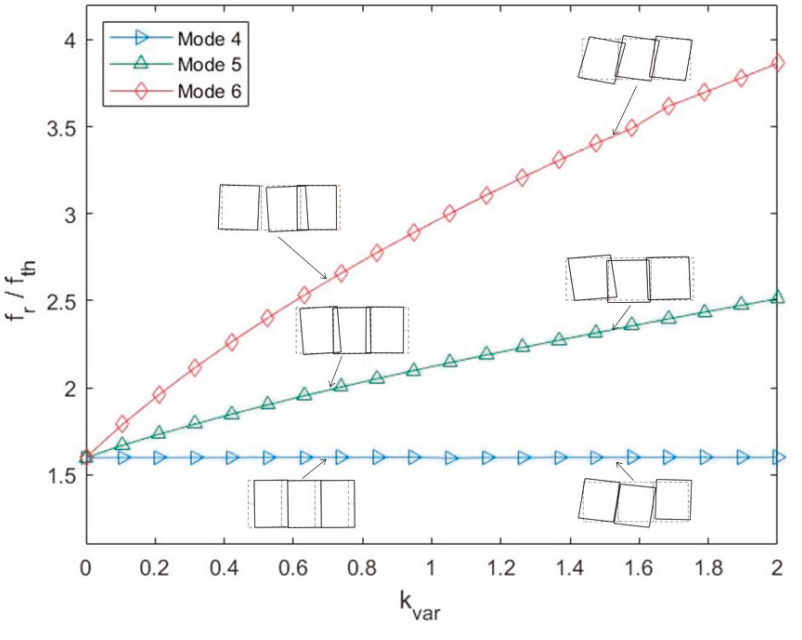

Figure 4. Variation of the modes and of the natural frequencies of the system from 4 to 6 as a function of k_{var}.

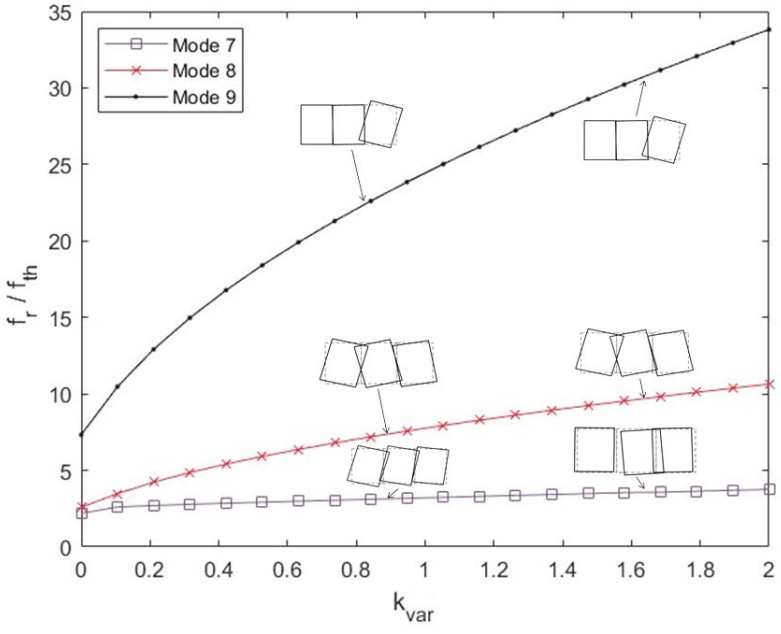

Figure 5. Variation of the modes and of the natural frequencies of the system from 7 to 9 as a function of k_{var}.

Concerning the mode shapes, when k_{var} is equal to 0 the diaphragms are uncoupled and show the same three modes. The first mode corresponds to a translational mode along the transversal direction (y-direction) of the system, while the second mode corresponds to a rotational one. While the first mode does not change as a function of k_{var}, in the case of the second mode, the stiffening effect of the springs characterizing the interaction can be clearly observed: indeed, if the presence of the interaction is clearly visible for values of k_{var} equal to 0.8, in the case of higher values of k_{var} the three masses tend to rotate as one single mass, showing therefore a monolithic behavior (see Figure 3).

If the frequency curves present a crossing, the modes undergo the so-called re-ordering phenomenon, consisting of a change of order of the modes of the system. In the case of this numerical benchmark, a re-ordering can be observed in two cases, as reported in Figure 6.

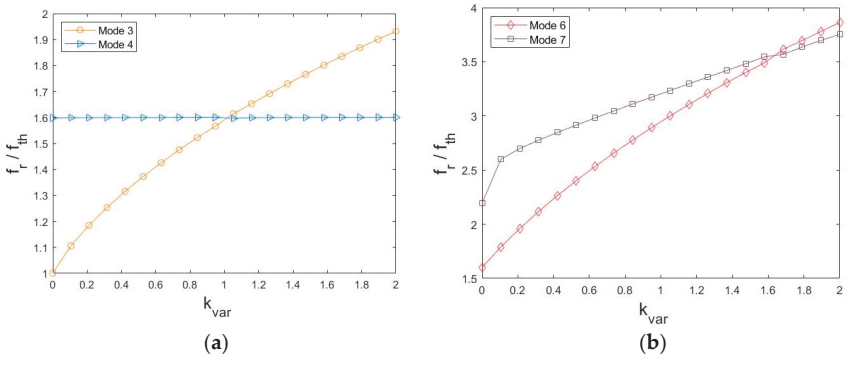

(**a**) (**b**)

Figure 6. Re-ordering of modes: (**a**) modes 3 and 4; (**b**) modes 6 and 7.

A first re-ordering of modes can be observed in correspondence with the third and fourth natural frequencies f_3 and f_4 of the system for increasing values of k_{var} (Figure 6a): indeed, in the case of the third one, a translational mode along the longitudinal direction (x-direction) is observed for high values of k_{var}, instead of a mixed torsional-bending one, observed at low values of k_{var} (the mode shapes can be found in Figures 3 and 4). A similar situation (Figure 6b) can be observed for the sixth and seventh mode (the mode shapes can be found in Figures 4 and 5).

Consequently, it can be said that for very high values of k_{var}, i.e., when the three masses behave as one single mass, the first three modes result to be the global modes of the system, corresponding to the translations in the directions x and y and to the rotation. On the other hand, the modes from 4 to 9 can be defined as local modes of the system.

The application of the reported dynamic equation on a numerical benchmark highlights the influence of the interaction between adjacent diaphragms on the dynamic behavior of the system.

4. The Case Study of Morandi's Hypogeum Pavilion in Turin

Having numerically analyzed the interaction between adjacent diaphragms, which plays a key role in the comprehension of the dynamic behavior of a system, the dynamic model developed in Section 2 can be now exploited in the identification of the modal parameters of a significant case study, represented by Morandi's Pavilion V of the Turin Exhibition Center. First, a description of the pavilion including some historical background is provided. Then, the experimental setups of a vast dynamic test campaign carried out in 2019 are introduced and described.

4.1. Description of the Pavilion

The Pavilion V, also known as the hypogeum pavilion, was built by Riccardo Morandi in the years 1958–1959 as part of the Turin Exhibition Center. The project was commissioned by *Società Torino Esposizioni*, almost entirely owned by FIAT motor company, and it was conceived as an extension of the existing Nervi's halls, mainly aimed at hosting the annual Automobile Show, also considering the upcoming celebrations for the 100th anniversary of Italy's unification [23].

The pavilion was not only an occasion for Morandi to show his structural art but also an opportunity to exploit the long years of experimentation on prestressed reinforced concrete. The scheme adopted by Morandi for Pavilion V is the so-called balanced beam scheme, widely used by the designer between the 1950s and 1960s, for example in the construction of bridges and overpasses [24]. In particular, Morandi used a version of the balanced beam with subtended tie rods as the main resistant element.

The pavilion is composed of a single large hall with a width of 69 m and a length of 151 m positioned 8 m below the middle level of the surrounding streets. A general view of the pavilion is reported in Figure 7.

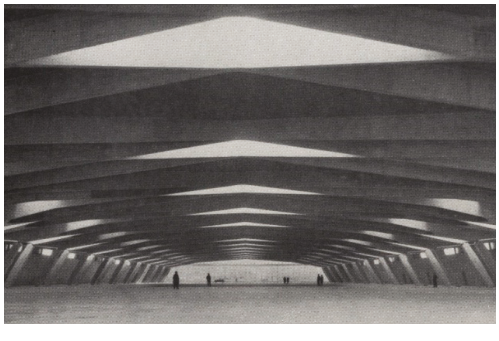

Figure 7. Interior view of Morandi's Pavilion V.

The structure is composed of three blocks linked by two expansion joints, crossing the roof and the external walls. The division of the underground structure into three blocks is clearly observable in Figure 8.

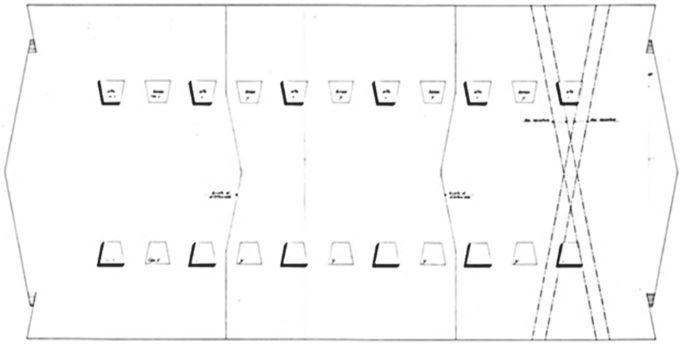

Figure 8. Scheme of the plan of Morandi's Pavilion V showing the division into three blocks linked by joints.

A system of intertwining thin beams in prestressed reinforced concrete composes the roof slab, defining the pavilion's space. The roof is composed of hollow core concrete and supported by 3.2 m spaced main ribs in prestressed concrete, resting on the pairs of inclined intermediate struts and anchored to the perimeter walls by small strut beams 1 m tall, 50 cm wide, and of variable section. Inside the small rods, the vertical prestressing cables are placed, with the aim to reduce the moment stress arising in the span of the ribs. The bending stresses in the roof and in the crossed ribs are reduced by the inclination of the struts. The balance constraint is produced by the perimeter walls that contain the ground, as well as support the roofing system. The thin ribs would be singularly unstable, but their intertwining makes the structure mostly rigid and robust. One of the intersections is in correspondence with the inclined struts, creating a dovetail geometry [25], as shown in Figure 9.

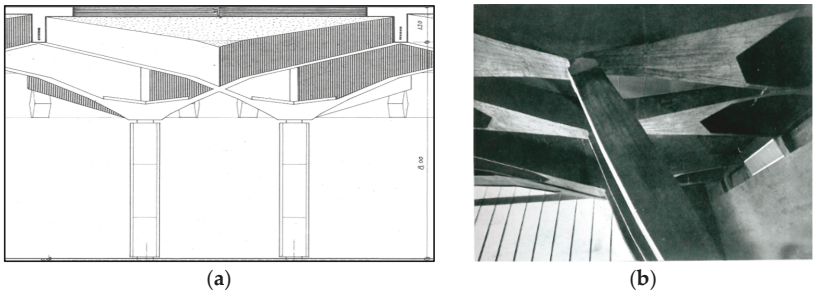

(**a**) (**b**)

Figure 9. Intersection of the thin ribs creating a dovetail geometry: (**a**) general section; (**b**) detail of the restraints of the shorter strut beams.

4.2. Dynamic Test Campaign

A vast test campaign was conducted in February 2019, as reported in [25]. Indeed, non-invasive tests represent an efficient tool to investigate dynamic properties not only for modern civil structures [26] but also for heritage buildings [27]. Among other tests, dynamic acquisitions were carried out employing 20 monoaxial piezoelectric accelerometers, positioned on the ribs and struts. In greater detail, the acquisition system was composed of 20 PCB piezoelectric monoaxial capacitive accelerometers with a sensitivity of 1 V/g,

a measurement range between 0 and 3 g, and a resolution of 30µg, whose mass is 17.5 g. The accelerometers were connected via coaxial cables to an acquirer that amplifies the signals, then the signals are sent to a laptop on which the acquisition software was installed. With the intention of favoring modal decoupling, the design of two setups was carried out, based on a preliminary FE model. The first setup allowed to acquire information mainly on the horizontal direction. In fact, the structure exhibits horizontal components of the three diaphragmatic blocks, possibly interacting at their joints, and fixed at the vertical members (longer and shorter strut beams), that define the translational and rotational stiffnesses. The boundary conditions are very clear, in which they reflect the balanced beam conceived by Morandi (see the restraints in Figure 9). A second setup focused instead on the vertical dynamic behavior, which is not accounted for by the model described in Section 2.

Among the 20 accelerometers used, 8 were positioned in the x-direction, 10 in the y-direction, and 2 in the vertical direction. Only the sensors measuring horizontal components are reported in Figure 10 with red arrows.

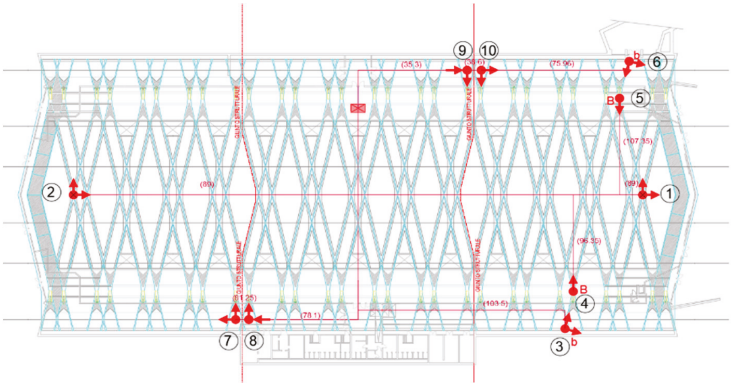

Figure 10. Sensors on the x-y plane in Setup 1. The numbers 1–10 in figure refer to identifiers of different sensors position.

The positioning of sensors was designed to study both the global and the local behavior of the structure. In particular, accelerometers 1 and 2 were positioned on the main ribs composing the roof, while accelerometers 4 and 5 were positioned on the large struts. Accelerometers 3 and 6 were positioned on the small struts.

Accelerometers with positions 7, 8, 9, and 10 were placed in correspondence with the joints linking the blocks, to investigate how the interaction affects the dynamic horizontal behavior of the three distinct bodies.

Only ambient excitation signals were used, with acquisitions length between 18 and 98 min and two different sampling frequencies (128 Hz and 256 Hz).

5. Dynamic Identification

5.1. System Identification Procedure

In the case of Pavilion V, the system identification was carried out with algorithm 3 of [28], belonging to the Stochastic Subspace Identification (SSI) family. The aim of this procedure was to understand the horizontal dynamic behavior of the structures, potentially ascribed to dynamic interactions at the joints.

The identification process resulted in the typical stabilization and clustering diagrams [29]. The assumed weighting scheme was that of the classical Canonical Variate Analysis (CVA, SSI-CVA). For the clustering analysis, the Agglomerative Hierarchical cluster method described in [29] has been adopted. The *average* criterion was then used to identify the cluster reference points, focusing on a bandwidth of the spectrum limited in the 0.5–25 Hz range, in accordance with the preliminary data cleansing.

The data were sampled at 256 Hz, in accordance with typical values used for civil structures. The retained signals (horizontal) were detrended and filtered with a band-pass Butterworth filter between 0.5 and 25 Hz with order 5. The signal length is about 64 min; thus, identification sessions were performed on both the entire signal and 8 sessions of 8 min each.

The measured acceleration responses and their Power Spectral Density (PSD) estimate are reported in Figure 11.

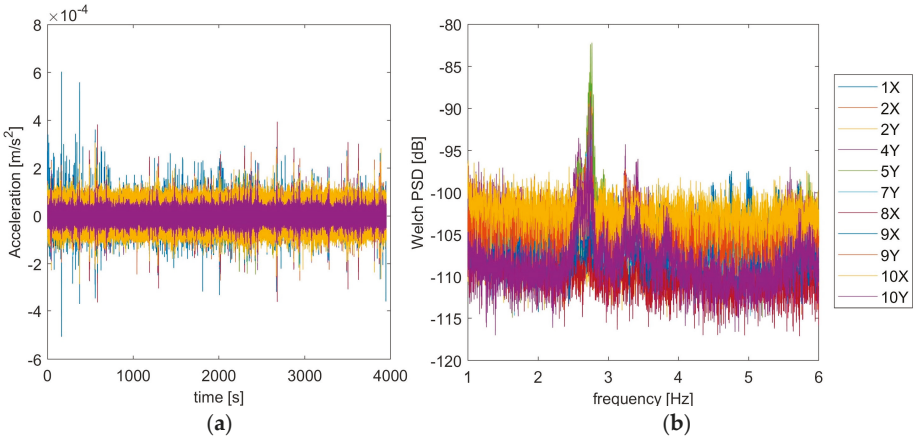

Figure 11. Measured acceleration responses: (**a**) time−domain; (**b**) frequency−domain.

5.2. Identified Modes

The most recurrent experimental mode was seen to be the one at 2.57 Hz. By way of example, the stabilization and clustering diagrams of the identification of a sub-signal are reported in Figure 12.

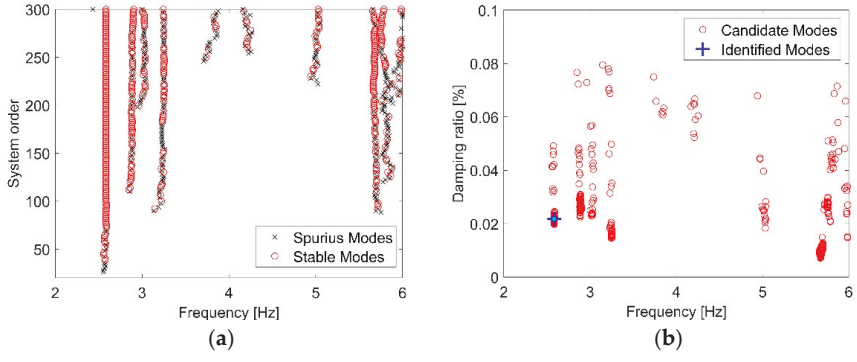

Figure 12. Stabilization (**a**) and clustering (**b**) diagram of the identification performed on the sixth sub−signal of setup 1 of the entire Pavilion V, with evidence of the mode at 2.57 Hz.

The main identified modes are reported in Table 2 in terms of natural frequency and damping ratio. From Figure 12, it can be observed that several clusters are likely to indicate authentic modes. For instance, additional modes are detectable at 3.24 Hz and 5.67 Hz. However, it is worth pointing out that the results presented in this work descend from the assumption that the three blocks belong to the same dynamic system, and a safe attribution, in the presence of a limited number of sensors, will require an accurate mechanical FE

model to be calibrated. Due to the redundancy of the measured degrees of freedom with respect to the ones of the diaphragmatic model, the representation of the modal shapes would require an optimization problem to be solved, as reported in Section 6 for the first horizontal mode.

Table 2. Identified modes of the entire pavilion.

Description	Mode Id.	Natural Frequency (Hz)	Damping Ratio (%)
Horizontal (with roof bending) mode	1	2.57	2.11
Mainly vertical mode	2	2.73	0.91

6. Interpretation of the Results and Discussion

For a hypogeum pavilion, vertical modes are relatively more amplified than horizontal ones, especially in the presence of important slab spans. Consequently, the identification of horizontal modes can be affected by unfavorable levels of signal-to-noise ratio (SNR), with respect to the vertical ones. This resulted from a comparison between the normalized spectral entropy of vertical and horizontal channels data, which indicates how close is a spectrum to the Gaussian noise condition. For further details about the relation between entropy and SNR, one can refer to [30,31]. Furthermore, in Morandi's pavilion, the roofing system is connected at the extrados by non-structural materials, including waterproofing layers. In particular, while the expansion joints between the blocks measure about 0.04 m, the blocks are connected by a thin concrete screed (approximately 0.05 m tick) to create continuity on the walking surface. It was precisely the uncertainty described above that prompted the authors to aid the identifications with the analytical model reported in Section 2.

As said before, since the model admits only diaphragmatic degrees of freedom, to compare the experimental results with the model prediction, the horizontal components of the first horizontal mode (identified at 2.57 Hz) have been estimated with the least squares method, also to reduce spillover effects. If $\boldsymbol{\Theta}_{id}$ denotes the identified eigenvector matrix, the equivalent diaphragmatic body mode components of the eigenvectors can be estimated with a linear transformation matrix $\mathbf{D}$ as $\boldsymbol{\Theta}_{D,id} = \mathbf{D}\,\boldsymbol{\Theta}_{id}$, where $\boldsymbol{\Theta}_{D,id}$ contains the diaphragmatic components, i.e., the two horizontal translations and the rotation about the vertical axis of each block, and $\mathbf{D}$ is the linear transformation matrix. In accordance with the theoretical model of Section 2, Figure 13 limits the representation to the horizontal components of the examined mode (undeformed configuration in dashed lines, with sensor positions).

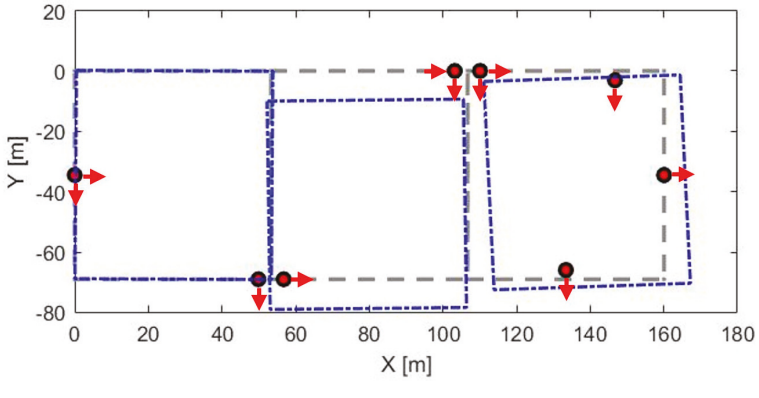

Figure 13. Identified mode shape #1 at 2.57 Hz (horizontal components).

From a preliminary analysis of the first mode, the blocks are not appreciably affected by mutual interaction, this being indicative of the full effectiveness of the joints. In other words, the three blocks are likely to behave as fairly separated dynamic systems. This observation can be extended also to joints with relatively low nominal stiffnesses (see Figures 3–5). On the other hand, this uncoupled behavior is reflected in Figure 13.

To shed light on the effectiveness of the joints, a numerical analysis was carried out on the nominal values of the model stiffnesses of the joints. The multiplier of the three stiffness components of each joint was varied between 0 and 1. In particular, with reference to Figure 10, two multipliers have been defined as $k_{var,left}$ and $k_{var,right}$, respectively. The Modal Assurance Criterion (MAC) [32] between the identified mode shape and the predicted ones was then calculated for each combination of the two multipliers. Defining m as the double of the number of modes, the objective function $J\left(k_{var,left}, k_{var,right}\right)$ writes [33,34]:

$$J\left(k_{var,left}, k_{var,right}\right) = \sum_{j=1}^{m/2} \alpha_w \left| \frac{f_j^{id} - f_j}{f_j^{id}} \right| + \beta_w \left| \frac{1 - \sqrt{MAC_j}}{1} \right| \tag{4}$$

where, for each j-th combination of the two multipliers, α_w and β_w are the weights of the residuals in frequency and mode shapes, respectively, f_j^{id} is the j-th identified natural frequency, f_j is the j-th predicted natural frequency, and MAC_j is the j-th MAC between the identified mode shape and the j-th predicted mode shape.

Figure 14 reports the resulting plot of the objective function, with the assumption to consider only the first vibration mode.

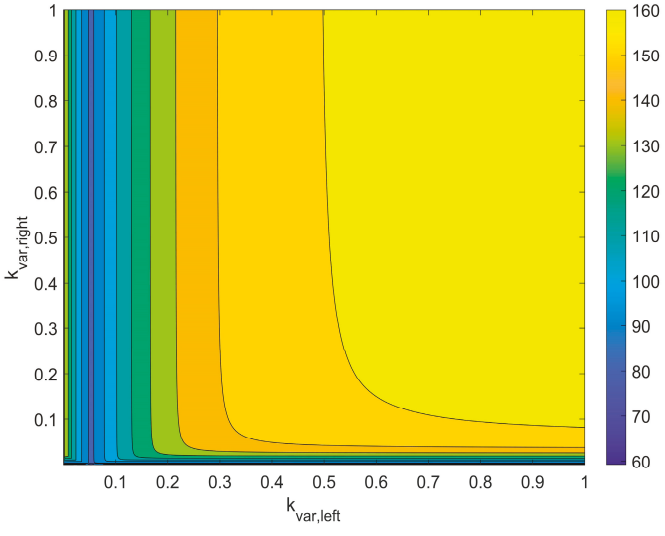

Figure 14. Objective function for a variation of $k_{var,left}$ and $k_{var,right}$ in the range between 0 and 1.

It can be observed from Figure 14 that the objective function tends to decrease dramatically for very low values of $k_{var,left}$ and $k_{var,right}$, corresponding to full effectiveness of all the joints. A local minimum is also visible, which is associated with the frequency residual only. Therefore, a further investigation has been conducted for the values of $k_{var,left}$ and $k_{var,right}$ varying between 0 and 1×10^{-3}. The results obtained for very low values of the joint stiffnesses are reported in Figure 15, showing that the absolute minimum happens when the joints are fully effective.

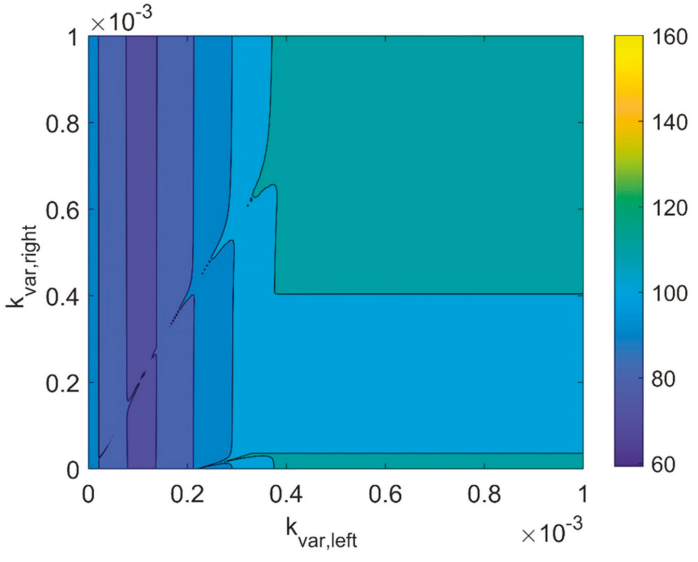

Figure 15. Objective function for a variation of $k_{var,left}$ and $k_{var,right}$ in the range between 0 and 1×10^{-3}.

The above-described analyses also highlighted a high sensitivity of the joint stiffnesses for values of $k_{var,left}$ and $k_{var,right}$ close to zero.

7. Conclusions

The dynamics of many civil engineering structures, e.g., multi-span bridges and buildings with interacting bodies, are influenced by the presence of joints, this introducing complexity in the modal response. In particular, uncertainties related to the possible degradation of materials as well as in boundary conditions make it difficult to infer the modal parameters. Consequently, modal identification, even if conducted in the linear field, can become a difficult task, calling for simplified models to unravel different components and aid the mode attribution process.

Morandi's Pavilion V of the Turin Exhibition Center is an example of a building with interacting bodies, thus reflecting all the previously stated criticalities. A further problem of this structure is related to its underground configuration, which results in low SNR unfavorably affecting the operational modal analysis.

From the results of this work, the following general conclusions can be drawn:

- Not only the presence of joints does result in modal complexity, but also in very high sensitivity of the stiffness parameters, especially when the joints are fully effective.
- This complexity also affects the design of the experimental setups, which often are not able to capture the whole-body dynamics.

Possible development of the analysis will contemplate the identification of the three blocks as independent bodies with the consequent updating of a high-fidelity numerical model. It is worth noting that the results reported in this paper are valid in operational conditions. This means that, in the presence of a strong excitation (e.g., an earthquake), the stiffness of the joints could be activated in the non-linear field, giving rise to even more complex behavior.

Author Contributions: Conceptualization, R.C., L.S., V.O., E.L. and G.M.; methodology, R.C., L.S., V.O., E.L. and G.M.; software, L.S. and G.M.; validation, R.C., L.S., E.L., V.O. and G.M.; formal analysis, L.S. and G.M.; investigation, R.C., L.S., V.O., E.L. and G.M.; resources, R.C., L.S., V.O., E.L.

and G.M.; data curation, R.C., L.S., V.O., E.L. and G.M.; writing—original draft preparation, L.S. and V.O.; writing—review and editing, R.C., E.L. and G.M.; visualization, R.C., L.S., V.O., E.L. and G.M.; supervision, R.C., E.L., and G.M.; project administration, R.C.; funding acquisition, R.C. and E.L. All authors have read and agreed to the published version of the manuscript.

Funding: This research received no external funding.

Institutional Review Board Statement: Not applicable.

Informed Consent Statement: Not applicable.

Data Availability Statement: Not applicable.

Conflicts of Interest: The authors declare no conflict of interest.

References

1. Reynders, E. System identification methods for (operational) modal analysis: Review and comparison. *Arch. Comput. Methods Eng.* **2012**, *19*, 51–124. [CrossRef]
2. Brincker, R.; Ventura, C.; Andersen, P. Why output-only modal testing is a desirable tool for a wide range of practical applications. In Proceedings of the International Modal Analysis Conference (IMAC) XXI, Kissimmee, FL, USA, 3–6 February 2003; Volume 265.
3. Ren, W.-X.; Zong, Z.-H. Output-only modal parameter identification of civil engineering structures. *Struct. Eng. Mech.* **2004**, *17*, 429–444. [CrossRef]
4. Ceravolo, R.; Abbiati, G. Time domain identification of structures: Comparative analysis of output-only methods. *J. Eng. Mech.* **2013**, *139*, 537–544. [CrossRef]
5. Andersen, P.; Brincker, R.; Peeters, B.; De Roeck, G.; Hermans, L.; Krämer, C. Comparison of system identification methods using ambient bridge test data. In Proceedings of the 17th International Modal Analysis Conference (IMAC), Kissimmee, FL, USA, 8–11 February 1999; pp. 1035–1041.
6. Peeters, B. System Identification and Damage Detection in Civil Engeneering. Ph.D. Thesis, Katholieke Universiteit Leuven, Leuven, Belgium, 2000.
7. Peeters, B.; De Roeck, G. Stochastic system identification for operational modal analysis: A review. *J. Dyn. Syst. Meas. Control* **2001**, *123*, 659–667. [CrossRef]
8. Reynders, E.; Pintelon, R.; De Roeck, G. Uncertainty bounds on modal parameters obtained from stochastic subspace identification. *Mech. Syst. Signal Process.* **2008**, *22*, 948–969. [CrossRef]
9. Van Overschee, P.; De Moor, B.L. *Subspace Identification for Linear Systems: Theory—Implementation—Applications*; Springer Science & Business Media: Berlin/Heidelberg, Germany, 2012.
10. Peeters, B.; De Roeck, G. Reference-based stochastic subspace identification for output-only modal analysis. *Mech. Syst. Signal Process.* **1999**, *13*, 855–878. [CrossRef]
11. Brincker, R.; Andersen, P. Understanding stochastic subspace identification. In Proceedings of the Conference and Exposition on Structural Dynamics IMAC-XXIV, St. Louis, MO, USA, 30 January–2 February 2006.
12. Kim, J.; Lynch, J.P. Subspace system identification of support-excited structures—Part I: Theory and black-box system identification. *Earthq. Eng. Struct. Dyn.* **2012**, *41*, 2235–2251. [CrossRef]
13. Ubertini, F.; Gentile, C.; Materazzi, A.L. Automated modal identification in operational conditions and its application to bridges. *Eng. Struct.* **2013**, *46*, 264–278. [CrossRef]
14. Bonato, P.; Ceravolo, R.; De Stefano, A.; Molinari, F. Cross-time frequency techniques for the identification of masonry buildings. *Mech. Syst. Signal Process.* **2000**, *14*, 91–109. [CrossRef]
15. Peeters, B.; De Roeck, G.; Pollet, T.; Schueremans, L. Stochastic subspace techniques applied to parameter identification of civil engineering structures. *New Adv. Modal Synth. Large Struct.* **1997**, 145–156.
16. Londono, N.A.; Desjardins, S.L.; Lau, D.T. Use of stochastic subspace identification methods for post-disaster condition assessment of highway bridges. In Proceedings of the 13th World Conference on Earthquake Engineering, Vancouver, BC, Canada, 1–6 August 2004.
17. Ljung, L. Black-box models from input-output measurements. In Proceedings of the (IMTC 2001) 18th IEEE Instrumentation and Measurement Technology Conference, Rediscovering Measurement in the Age of Informatics (Cat. No. 01CH 37188), Budapest, Hungary, 21–23 May 2001; Volume 1, pp. 138–146.
18. Sjöberg, J.; Zhang, Q.; Ljung, L.; Benveniste, A.; Delyon, B.; Glorennec, P.-Y.; Hjalmarsson, H.; Juditsky, A. Nonlinear black-box modeling in system identification: A unified overview. *Automatica* **1995**, *31*, 1691–1724. [CrossRef]
19. Alvin, K.F.; Robertson, A.N.; Reich, G.W.; Park, K.C. Structural system identification: From reality to models. *Comput. Struct.* **2003**, *81*, 1149–1176. [CrossRef]
20. Berman, A.; Nagy, E.J. Improvement of a large analytical model using test data. *AIAA J.* **1983**, *21*, 1168–1173. [CrossRef]
21. Sobester, A.; Forrester, A.; Keane, A. *Engineering Design via Surrogate Modelling: A Practical Guide*; John Wiley & Sons: Hoboken, NJ, USA, 2008.

22. Qin, S.; Zhang, Y.; Zhou, Y.-L.; Kang, J. Dynamic model updating for bridge structures using the kriging model and PSO algorithm ensemble with higher vibration modes. *Sensors* **2018**, *18*, 1879. [CrossRef]
23. Bruno, E. Riccardo Morandi per il Vpadiglione di Torino Esposizioni. In *La Concezione Strutturale: Architettura e Ingegneria in Italia Negli Anni 50 e 60*; P. Desideri, A., Magistris, C., Olmo, M., Pogacnik, S., Sorace, S., Eds.; Umberto Allemandi & C.: Torino, Italy, 2013; pp. 229–238.
24. Levi, F.; Chiorino, M.A. Concrete in Italy. A review of a century of concrete progress in Italy, Part 1: Technique and architecture. *Concr. Int.* **2004**, *26*, 55–61.
25. Earthquake Engineering & Dynamics Laboratory. *Relazione Sulle Prove di Caratterizzazione Dinamica del Padiglione Morandi di Torino Esposizioni*; Earthquake Engineering & Dynamics Laboratory: Torino, Italy, 2019.
26. Pierdicca, A.; Clementi, F.; Fortunati, A.; Lenci, S. Tracking modal parameters evolution of a school building during retrofitting works. *Bull. Earthq. Eng.* **2019**, *17*, 1029–1052. [CrossRef]
27. Giordano, E.; Marcheggiani, L.; Formisano, A.; Clementi, F. Application of a Non-Invasive Technique for the Preservation of a Fortified Masonry Tower. *Infrastructures* **2022**, *7*, 30. [CrossRef]
28. Van Overschee, P.; Moor, B. De Stochastic identification. In *Subspace Identification for Linear Systems*; Springer: Berlin/Heidelberg, Germany, 1996; pp. 57–93.
29. Pecorelli, M.L.; Ceravolo, R.; Epicoco, R. An Automatic Modal Identification Procedure for the Permanent Dynamic Monitoring of the Sanctuary of Vicoforte. *Int. J. Archit. Herit.* **2018**, *14*, 630–644. [CrossRef]
30. Freiman, A.; Pinchas, M. A maximum entropy inspired model for the convolutional noise PDF. *Digit. Signal Process.* **2015**, *39*, 35–49. [CrossRef]
31. Beenamol, M.; Prabavathy, S.; Mohanalin, J. Wavelet based seismic signal de-noising using Shannon and Tsallis entropy. *Comput. Math. Appl.* **2012**, *64*, 3580–3593. [CrossRef]
32. Allemang, R.J. The modal assurance criterion—Twenty years of use and abuse. *Sound Vib.* **2003**, *37*, 14–23.
33. Merce, R.N.; Doz, G.N.; de Brito, J.L.V.; Macdonald, J.; Friswell, M.I. Finite element model updating of a suspension bridge using ansys software. In Proceedings of the Inverse Problems, Design and Optimization Symposium, Miami, FL, USA, 16–18 April 2007.
34. Moller, P.W.; Friberg, O. Updating large finite element models in structural dynamics. *AIAA J.* **1998**, *36*, 1861–1868. [CrossRef]

applied sciences

MDPI

Article

Determining the Severity of Open and Closed Cracks Using the Strain Energy Loss and the Hill-Climbing Method

Cristian Tufisi [1], Catalin V. Rusu [2], Nicoleta Gillich [1], Marius Vasile Pop [3], Codruta Oana Hamat [1], Christian Sacarea [2] and Gilbert-Rainer Gillich [1,3,*]

[1] Department of Engineering Sciences, Babes-Bolyai University, P-ta Traian Vuia 1-4, 320085 Resita, Romania; cristian.tufisi@ubbcluj.ro (C.T.); nicoleta.gillich@ubbcluj.ro (N.G.); codruta.hamat@ubbcluj.ro (C.O.H.)
[2] Department of Computer Science, Institute of German Studies, Babeș-Bolyai University, Str. M. Kogălniceanu 1, 400084 Cluj-Napoca, Romania; vasile.rusu@ubbcluj.ro (C.V.R.); christian.sacarea@ubbcluj.ro (C.S.)
[3] Doctoral School of Engineering, Babeș-Bolyai University, P-ta Traian Vuia 1-4, 320085 Resita, Romania; marius.pop1@ubbcluj.ro
* Correspondence: gilbert.gillich@ubbcluj.ro

Abstract: Evaluating the integrity of structures is an important issue in engineering applications. The use of vibration-based techniques has become a common approach to assessing cracks, which are the most frequently occurring damage in structures. When involving an inverse method, it is necessary to know the influence of the position and the geometry of the crack on the modal parameter changes. The geometry of the crack, both in size and shape, defines the damage severity (DS). In this study, we present a method (DS-SHC) used for estimating the DS for closed and open transverse cracks in beam-like structures using the intact and damaged beam deflections under its weight and a Stochastic Hill Climbing (SHC) algorithm. After describing the procedure of applying DS-SHC, we calculate for a prismatic cantilever beam the severities for different crack types and depths. The results are tested by comparing the DS obtained with DS-SHC with those acquired from dynamic tests made using professional simulation software. We obtained a good fit between the severities determined in these two ways. Subsequently, we performed laboratory experiments and found that the severities obtained with the DS-SHC method can accurately predict the frequency changes due to the crack. Hence, these severities are a valuable tool for damage detection.

Keywords: crack severity; strain energy loss; beam deflection; frequency shift; hill-climbing method

Citation: Tufisi, C.; Rusu, C.V.; Gillich, N.; Pop, M.V.; Hamat, C.O.; Sacarea, C.; Gillich, G.-R. Determining the Severity of Open and Closed Cracks Using the Strain Energy Loss and the Hill-Climbing Method. *Appl. Sci.* **2022**, *12*, 7231. https://doi.org/10.3390/app12147231

Academic Editor: Cecilia Surace

Received: 23 June 2022
Accepted: 14 July 2022
Published: 18 July 2022

Publisher's Note: MDPI stays neutral with regard to jurisdictional claims in published maps and institutional affiliations.

Copyright: © 2022 by the authors. Licensee MDPI, Basel, Switzerland. This article is an open access article distributed under the terms and conditions of the Creative Commons Attribution (CC BY) license (https://creativecommons.org/licenses/by/4.0/).

1. Introduction

Numerous damage detection methods have been developed in recent decades. These are usually applied to check sensitive structures or structures involving high risk in operation. Depending on the principle of the non-destructive testing method applied, there are two main categories: local methods and global methods [1]. Local methods require approximate knowledge of the position of the damage and can only be applied to accessible areas. The advantage of these methods is the high accuracy in characterizing the type and size of the defect. However, in most cases the position of the structural damage is unknown before the control is performed. For this reason, global control is essential to observe the occurrence or propagation of damage and thus to characterize the state of integrity of structures, especially complex or large ones. Global damage detection methods use information regarding the vibration of the structure [2,3]. The essence of damage detection based on changes in the dynamic behavior of the structure is the deterministic relationship between physical and modal parameters [4]. More specifically, the presence of defects causes changes in the modal parameters of the structure, and these changes are used to diagnose, locate, and estimate the severity of the damage [5].

The simplest case of structural damage is the transverse crack in an isotropic and homogeneous structure. For this type of damage, non-destructive testing aims to identify its position and estimate its depth. The position of the crack can be unequivocally related to the change of a modal parameter, namely the modal curvature [6]. The case of the crack depth is different, as it cannot be directly related to a modal parameter. However, there is an indirect link between the depth of the crack and the natural frequency of the structure, and both parameters mentioned above are related to the damage severity.

Deterministic damage detection methods fall into two categories: the finite element approach and the continuous approach. In most damage detection cases that use the finite element method, the structure is divided into identical elements that extend over the entire cross-section of the structure. All elements have the mechanical and physical characteristics of the intact structure, except one or a few elements where there is a defect. The defective element, simulating the crack, commonly has a reduced Young's modulus. In most of the studies, the number of finite elements in the model is taken between 4 and 30, and the reduction of the elastic modulus of an element is in the range of 20% to 50%, see, for example, [7–11]. This approach requires centering the crack on an element and, therefore, the precision of assessing damage is determined by the distribution of the elements along the beam [10]. However, the biggest problem with using this method is the lack of a definite relationship between the severity of the damage and the depth of the crack, because the relationship depends on the size of the elements used for discretization [12]. When examining the methods proposed in the literature, we observed that the dependency between the reduction in the size of the crack and the stiffness is rarely considered. In general, the authors limit the study to finding the element in the beam with the lower Young modulus value [13]. When damage detection is applied to trusses, finding the member with the lower Young modulus is usually the target.

Another approach to modeling damage is to divide the structure into two segments that are linked by a rotational massless spring. This equivalent spring introduces four more unknowns in the system, which are determined from the continuity conditions [14]. The correlation between the crack depth determining the local compliance and the equivalent spring stiffness is found using fracture mechanics results [15]. There are many mathematical relations to express the compliance functions relative to the crack depth available in the literature, see for instance [16–19]. Involving this approach, damage detection consists of fitting the position and the stiffness for one finite element to obtain by calculus similar natural frequencies to those obtained for the damaged beam by experiments [20]. Analyzing a multitude of compliance functions, we found significant differences between the results achieved for certain crack depths, resulting in a negative influence on the accuracy of the damage assessment methods based on this approach.

Recent research focuses on detecting damage by involving artificial intelligence (AI). Examples of current methods aiming to detect damage in beams can be found in [21–23], while in [24–26] are exemplified methods applicable to complex structures. These approaches are based on the analysis of the vibration signal parameters in the time domain (acceleration, damping), or in the frequency domain (mode shapes and curvatures, frequencies). The training data are obtained from simulation or measurements, thus initially it involves a limited number of damage cases. If for a given structure it is possible to determine the relationship between the damage parameters and the vibration signal parameters, it is possible to generate a multitude of damage cases [27] including the case of imperfect clamping. In this way, the training process can be improved, and the AI algorithms provide more accurate prediction results.

In prior research, we determined a mathematical relation to finding the severity of closed or open cracks [28]. The data used to calculate the severity are the deflections at the free end of a cantilever beam for the healthy and damaged case, respectively. Because the severity is an intrinsic parameter of the damage, it is the same for beams with any boundary conditions. Thus, it is sufficient to determine the severity just for the cantilever beam. For the reasons presented in the next section, determining the deflection of the damaged beam

implies regression analysis followed by extrapolation. Thus, the results are influenced by the nature of the regression curve used and may vary accordingly.

In this paper, we propose a mathematical relation to calculate the effect of a crack located anywhere on the beam on its deflection. This relation is used to find the damage severity from static tests made with cracks having a random position on the beam. Instead of regression analysis, we use Stochastic Hill Climbing (SHC) as an optimization method. To the best of our knowledge, there is no research to determine the severity of the defect using AI. Using this procedure to find the damage severity we avoid obtaining results that depend on the analysis strategy, thus these are very accurate.

The paper is structured as follows: the expression of the cracked beam deflection is deduced in Section 2, then we present the procedure to determine the damage severity (Section 3) and the achieved results for several beams and crack dimensions (Section 4), while in Section 5 we test the capacity of estimating frequency changes due to damage by involving the achieved damage severities. Finally, we present the conclusions of the research in Section 6.

2. The Expression of the Cracked Beam Deflection

This section presents a method for determining the deflection at the free end of a cantilever beam with a crack. The challenge faced when attempting to evaluate damages is that the effect of the crack, both on the deflection as well as on the natural frequencies, is different when it is placed in different positions along the beam. However, the crack has the biggest effect when it is in the beam slice in which the mechanical stresses are highest, i.e., where the bending moment reaches its maximum value. In the case of the cantilever beam, this location is the fixed end. In prior research [29], we have determined a method for assessing the severity of transverse cracks, considering the deflection of a cantilever beam in the intact state and when it is altered by a breathing crack of known depth a that is located at the fixed end. This mathematical relation is:

$$\gamma(a) = \frac{\sqrt{\delta(a,0)} - \sqrt{\delta_u}}{\sqrt{\delta(a,0)}} \tag{1}$$

In Equation (1) we denoted: $\gamma(a)$ the severity of a crack with depth a located at the fixed end; $\delta(a,0)$ the deflection at the free end of the cantilever beam having a crack with depth a at the fixed end (index 0 stays for location x = 0 mm); δ_u the deflection of the intact beam at the free end.

It is easy to determine the deflection at the free end for the beam with a constant cross-section subjected to dead mass, as:

$$\delta_u = \frac{\rho A g L^4}{8EI} \tag{2}$$

Here, ρ is the volumetric mass density, A is the cross-sectional area, g is the gravity, E is Young's modulus and I is the second moment of inertia. This deflection is also easy to be obtained from a finite element analysis (FEA).

Regarding the deflection of a beam affected by cracks, there are no analytical relations for calculating the deflection. Thus, it becomes difficult to determine the severity of cracks. Problems also occur when involving FEA. For a crack positioned at the fixed end, the stresses and deformations of the beam can manifest only on one side of the crack, unlike the case where the crack is located elsewhere along the beam. Thus, the rotation in the cracked region is smaller than that achieved for a crack located in the neighborhood. This has as a consequence a smaller deflection than expected at the free end. The phenomenon is explained in detail in [30]. A suggestive representation of transverse displacements for a cantilever beam's extreme segment fixed at the left end, for two crack positions, is given in Figure 1.

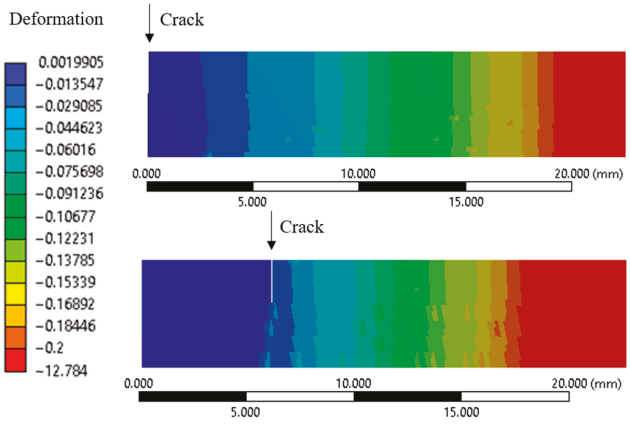

Figure 1. Comparison of the transverse deflections for the cantilever beam segment clamped at the left end for two damage locations.

From the color scheme, one can observe in the above figure that, when the crack is positioned exactly at the fixed end (upper image), the deflection in the transverse direction is bigger at the slice located at 6 mm than the deflection of the beam with a crack located on that slice (bottom image). Subsequently, going toward the free end, the deflections increase faster for the beam with the crack located at 6 mm. Without a doubt, at the free end, this latter beam will achieve a bigger deflection.

A supplementary proof can be made with the results presented in Table 1. Here, we present the deflection under dead mass for a steel cantilever beam of length $L = 1$ m and cross-section $A = 0.02 \times 0.005$ m^2. The simulations were performed using ANSYS, for the crack positions and depths presented in Table 1. The chosen material is *Structural Steel* and the mesh is made using hexahedral elements of a maximum 1 mm edge size, thus obtaining a mesh of ~30,000 elements.

Table 1. Deflection at the free end for a cantilever beam affected by a transverse crack located at a distance x from the fixed end.

Crack Position [m]	δ_x (a) [mm] for a = 0.4 mm	δ_x (a) [mm] for a = 1 mm	δ_x (a) [mm] for a = 2 mm
x = 800	23.046	23.047	23.052
x = 600	23.048	23.057	23.097
x = 400	23.052	23.083	23.219
x = 200	23.059	23.134	23.455
x = 20	23.072	23.207	23.798
x = 0	23.061	23.124	23.401

From Table 1, it is easy to observe that the deflection caused by a crack located at the fixed end is smaller than that when the crack is located at x = 20 mm and even x = 200 mm for all analyzed crack depths.

Taking into account the above, we can conclude that the severity to be considered when calculating the natural frequencies of the defective beams is the one estimated to be obtained at x = 0 on the curve constructed using the deflections determined for different positions of the defect. This theoretical deflection corresponds to that resulting from the deformation on both sides of the crack, which is impossible to obtain directly from FEA. Note that this severity does not apply when the crack is very close to the fixed end; here it indicates a bigger damage severity than it is in the real case.

Let us now introduce the pseudo-severity $\gamma_i(a,x)$, which reflects the effect of the severity weighted with the effect of the crack position. In fact, it reflects a decrease in the beam's ability to store energy due to damage. This decrease, associated with the fact that energy distribution is in concordance with the modal curvature, permitted us to derive a function to calculate the natural frequency of a beam with a crack $f_{i-D}(a,x)$. The obtained mathematical relation is [31]

$$f_{i-D}(a,x) = f_{i-U}\left\{1 - \gamma(a)\left[\overline{\Phi_i}''(x)\right]^2\right\} \tag{3}$$

which makes use of the natural frequency of the intact beam f_{i-U}, the damage severity $\gamma(a)$, and the normalized mode shape curvature $\overline{\Phi_i}''(x)$. This relationship was successfully used to assess cracks [32], which proves its reliability.

From the right term in the parentheses of Equation (3), we can deduce the pseudo-severity as being

$$\gamma_i(a,x) = \frac{\sqrt{\delta_i(a,x)} - \sqrt{\delta_u}}{\sqrt{\delta_i(a,x)}} = \frac{\sqrt{\delta(a,0)} - \sqrt{\delta_u}}{\sqrt{\delta(a,0)}}\left[\overline{\Phi_i}''(x)\right]^2 = \gamma(a)\left[\overline{\Phi_i}''(x)\right]^2 \tag{4}$$

In Equation (4) we denoted the deflection of the beam with a crack of depth a that is located at the distance x from the fixed end as $\delta_i(a,x)$. One can observe that, dissimilar to the severity, the pseudo-severity severity depends on the vibration mode number i.

From Equation (4), we can deduce the mathematical relation for the deflection $\delta_1(a,x)$ of the cantilever beam under dead mass, when it has a crack located at the distance x from the free end, by performing the following steps:

$$\sqrt{\delta_1(a,x)}\sqrt{\delta(a,0)} - \sqrt{\delta_u}\sqrt{\delta(a,0)} = \sqrt{\delta_1(a,x)}\left(\sqrt{\delta_0} - \sqrt{\delta_u}\right)\left[\overline{\Phi_1}''(x)\right]^2 \tag{5}$$

$$\sqrt{\delta_1(a,x)}\left(\sqrt{\delta(a,0)} - \left(\sqrt{\delta(a,0)} - \sqrt{\delta_u}\right)\left[\overline{\Phi_1}''(x)\right]^2\right) = \sqrt{\delta_u}\sqrt{\delta(a,0)} \tag{6}$$

$$\sqrt{\delta_1(a,x)} = \frac{\sqrt{\delta_u}\sqrt{\delta(a,0)}}{\sqrt{\delta(a,0)} - \left(\sqrt{\delta(a,0)} - \sqrt{\delta_u}\right)\left[\overline{\Phi_1}''(x)\right]^2} \tag{7}$$

$$\delta_1(a,x) = \frac{\delta_u\delta(a,0)}{\left(\sqrt{\delta(a,0)} - \left(\sqrt{\delta(a,0)} - \sqrt{\delta_u}\right)\left[\overline{\Phi_1}''(x)\right]^2\right)^2} \tag{8}$$

If the crack is located at the fixed end, thus $\overline{\Phi_1}''(0) = 1$, the deflection of the free beam end is $\delta_1(a,0)$. On the other hand, if the crack is located at the free end, thus $\overline{\Phi_1}''(L) = 0$, the deflection of the free beam end is δ_u. This mathematical relation can be used to calculate the deflection at the free end of a cantilever beam with a crack. In this paper, we use the function given in Equation (8) to find the theoretical deflection $\delta_1(a,0)$ by an optimization algorithm.

3. Using the SHC to Estimate the Deflection When the Crack Is Located at the Fixed End

Stochastic Hill Climbing (SHC) is an optimization algorithm, which starts from a solution and expands it through incremental searches within a local area of the search space, using an objective function, until an optimum is found. This essentially makes it an ideal candidate in unimodal optimization problems, or after the application of a global optimization algorithm. Other similar types of algorithms, which aim to approximate a 'good-enough' solution instead of searching for a global best, exist. These include genetic algorithms, simulated annealing, random recursive search, and Tabu search. Most of these are applicable for a broad range of problems because they: (i) generally require little or no a priori knowledge, and (ii) can easily find an optimum solution by following local gradients using the objective function.

The SHC algorithm as used in this study considers as input three points $P_k(a, x_k)$ with $k = 1 \ldots 3$. These points are the deflections of the beam at the free end when the crack is located at distances x_1, x_2 and x_3, found involving the FEA. In addition, we indicate the deflection of the intact beam derived by the means of FEA, which is P_u. The output consists of one point, which is the deflection of the beam at the free end $\delta(a, 0)$ achieved when the crack is located at the fixed end. The steps performed when running the algorithm are:

1. Generate an initial point.
2. Evaluate the initial point.
3. Take a step s.
4. Evaluate candidate point.
5. Check if we should keep the new point.

The objective function used to evaluate a candidate solution is given by

$$c(s) = \sqrt{\sum_{i=1}^{n} \left(\delta_1^*(a, x_k) - P_k(a, x_k)\right)^2} \tag{9}$$

In Equation (9), the points P_k are the deflections found from the finite element analysis and $\delta_1(a, x_k)$ are the deflections calculated, for the locations x_1, x_2 and x_3, with the mathematical relation

$$\delta_1^*(a, x_k) = \frac{\widehat{\delta}(a, 0)\delta_u}{\left(\sqrt{\widehat{\delta}(a, 0)} - \left(\sqrt{\widehat{\delta}(a, 0)} - \sqrt{\delta_u}\right)\left[\overline{\Phi_1}''(x_k)\right]^2\right)^2} \tag{10}$$

Here, $\widehat{\delta}(a, 0) = s \cdot \delta_u$. The search process starts with considering $s = 1$, and its value is subsequently increased until $c(s)$ achieves the lowest value possible. We exemplify here the case of a crack with a depth of 1 mm. Figure 2 shows the objective function evaluation for each improvement during the hill-climbing search. During the optimization process, we initially get big changes, and toward the end of the search, these changes become very small. After about 50 iterations the algorithm manages to converge on the optima.

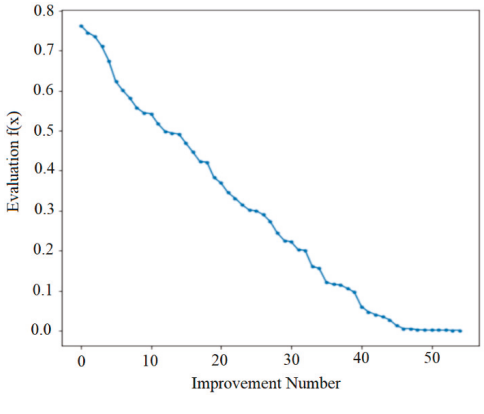

Figure 2. Objective function evaluation for each improvement during the Hill Climbing Search.

We have implemented our SHC algorithm in Python and created a basic user interface that allows us to easily estimate the deflections. Figure 3 shows the main window of the PySHC application.

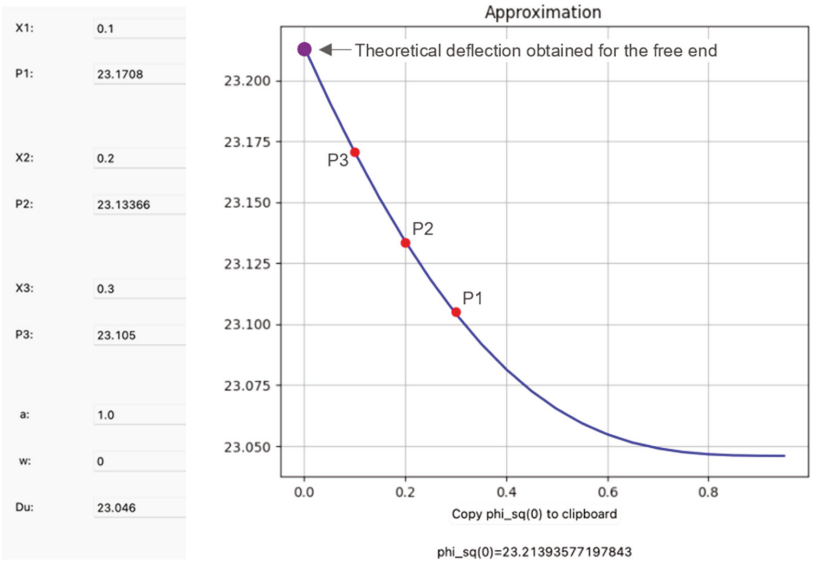

Figure 3. The main window of the PySHC application.

In the developed Python application, it is necessary to input the damage depth a, the coordinates x_k/L, and the associated deflections $P_k(a, x_k)$ for the damaged beam P_u. After the input values are introduced, the algorithm determines the theoretical deflection obtained for the free end, when the crack is located at the fixed end. It is recommended that the chosen points are not too close.

If the crack is an open one, as shown in Figure 4, in addition to the crack depth it is necessary to indicate the crack width w. This value is set to 0 by default in the application, indicating a closed crack. The input value for w should not exceed 5 mm, otherwise another damaged beam model is applicable [33,34].

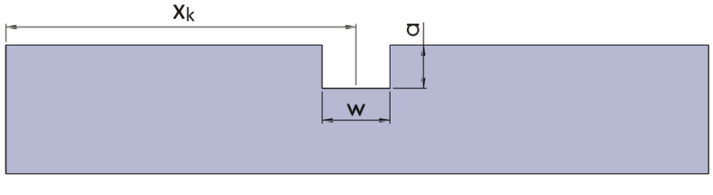

Figure 4. The geometry of the open crack.

4. Severity Curves Derived from the Calculated Damage Deflections

To determine the deflection caused by a crack that is located at the fixed end, using the described SHC algorithm, we have conducted FEM static simulations considering multiple damage scenarios. The beam considered in this study is like that presented in Section 2, thus it has the following dimensions: the length L = 1000 mm, the width B = 20 mm, and the thickness H = 5 mm. We also used the same material (*Structural steel*) and applied an identical simulation strategy.

The simulated transverse cracks are located at distances x_1 = 100 mm, x_2 = 200 mm, and x_3 = 300 mm from the fixed end. The crack depth starts from a = 0.2 mm and increases iteratively with a step Δa = 0.2 mm until the depth of 2 mm is achieved. The applied load was the dead weight, which produces a deflection in the transverse (vertical) direction. For each crack depth, we obtain from the FEM simulations three deflections for the beam's

free end, which are $P_1(a,100)$, $P_2(a,200)$ and $P_3(a,300)$. Using PySHC, we determine the theoretical deflection at the free end. The input data for the considered damage scenarios and the obtained deflection values are presented in Table 2 for the closed crack and in Tables 3–5 for open cracks with different widths.

Table 2. Deflection at the free end for a cantilever beam with a crack that has the width w = 0 mm.

Damage Scenario	a [mm]	$P_1(a,100)$ [mm]	$P_1(a,200)$ [mm]	$P_1(a,300)$ [mm]	$\delta(a,0)$ [mm]
1	0.2	23.05051	23.04915	23.04807	23.05203
2	0.4	23.06576	23.05987	23.05525	23.07250
3	0.6	23.09069	23.07740	23.06701	23.10592
4	0.8	23.12546	23.10178	23.08331	23.15287
5	1	23.17079	23.13365	23.10461	23.21369
6	1.2	23.22881	23.17437	23.13201	23.29203
7	1.4	23.30028	23.22457	23.16553	23.38859
8	1.6	23.38823	23.28624	23.20691	23.50768
9	1.8	23.49632	23.36178	23.25774	23.65446
10	2	23.62840	23.45544	23.32010	23.83521

Table 3. Deflection at the free end for a cantilever beam with a crack that has the width w = 0.5 mm.

Damage Scenario	a [mm]	$P_1(a,100)$ [mm]	$P_1(a,200)$ [mm]	$P_1(a,300)$ [mm]	$\delta(a,0)$ [mm]
11	0.2	23.05194	23.04741	23.04642	23.05161
12	0.4	23.07330	23.06490	23.05782	23.08210
13	0.6	23.10278	23.08532	23.07122	23.12135
14	0.8	23.14164	23.11220	23.08964	23.17352
15	1	23.19285	23.14674	23.11277	23.24136
16	1.2	23.25361	23.19128	23.14087	23.32423
17	1.4	23.32764	23.24303	23.17532	23.42406
18	1.6	23.42321	23.30889	23.22357	23.55420
19	1.8	23.54339	23.39505	23.27568	23.71710
20	2	23.68598	23.494056	23.34586	23.91250

Table 4. Deflection at the free end for a cantilever beam with a crack that has the width w = 1 mm.

Damage Scenario	a [mm]	$P_1(a,100)$ [mm]	$P_1(a,200)$ [mm]	$P_1(a,300)$ [mm]	$\delta(a,0)$ [mm]
21	0.2	23.05194	23.04966	23.04784	23.05331
22	0.4	23.08282	23.07153	23.06199	23.09481
23	0.6	23.11673	23.09484	23.07764	23.13992
24	0.8	23.16138	23.12612	23.09826	23.19984
25	1	23.21792	23.16637	23.12452	23.27626
26	1.2	23.28805	23.21417	23.15746	23.37020
27	1.4	23.37186	23.27379	23.19689	23.48408
28	1.6	23.47622	23.34780	23.24623	23.62638
29	1.8	23.60532	23.44105	23.30606	23.80360
30	2	23.77482	23.55553	23.38395	24.03240

Table 5. Deflection at the free end for a cantilever beam with a crack that has the width w = 2 mm.

Damage Scenario	a [mm]	$P_1(a,100)$ [mm]	$P_1(a,200)$ [mm]	$P_1(a,300)$ [mm]	$\delta(a,0)$ [mm]
31	0.2	23.05984	23.05340	23.05021	23.06241
32	0.4	23.10104	23.08376	23.06999	23.11881
33	0.6	23.14577	23.11485	23.09062	23.17848
34	0.8	23.20197	23.15414	23.05194	23.25396
35	1	23.27400	23.20445	23.14956	23.35081
36	1.2	23.36256	23.26645	23.19063	23.47044
37	1.4	23.47207	23.34311	23.24154	23.61869
38	1.6	23.60779	23.43813	23.30477	23.80337
39	1.8	23.77636	23.55631	23.38347	24.03397
40	2	23.98833	23.70488	23.48253	24.32582

The main purpose of determining the theoretical deflections is to calculate the damage severities, which have a direct application in Structural Health Monitoring (SHM). We calculate the crack severities with Equation (1), the data utilized being $\delta(a,0)$ for the damaged beam and $\delta_u = 23.046$ mm for the intact beam. The results obtained for the closed cracks are represented graphically in Figure 5.

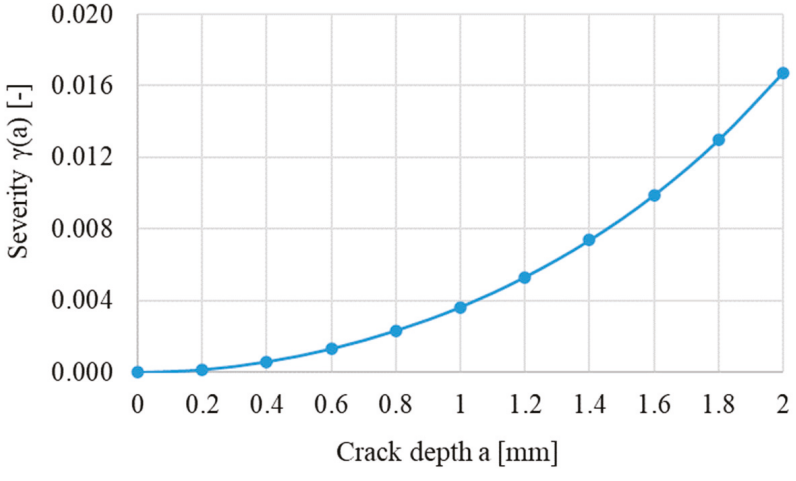

Figure 5. Severity evolution versus crack depth for the closed crack scenario.

Furthermore, we determine the severity values for open cracks, considering the results presented in Tables 3–5. The severities calculated accordingly are depicted in Figure 6, along with the severities for the closed cracks for comparison. One can observe that an increase in the damage width has as a result an increase in the severity. However, the curves have the same shape.

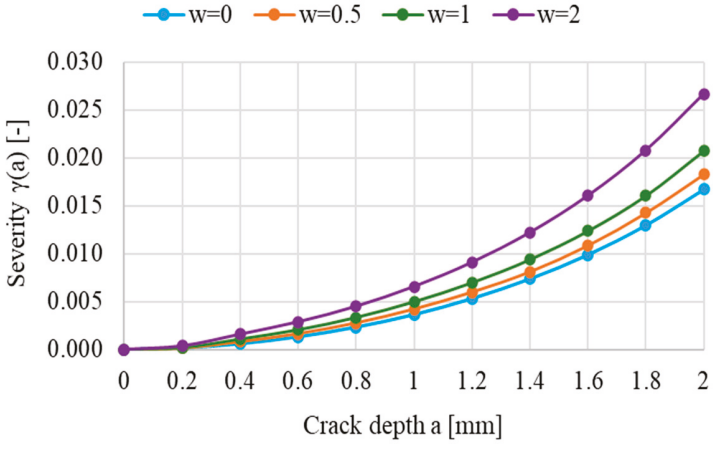

Figure 6. Severity evolution with the crack depth for closed and open cracks.

5. Testing the Capacity of the Derived Severities to Accurately Predict Frequency Changes Due to Damage

In this section, we test the accuracy of the developed SHC algorithm and implicitly the analytical relation to calculate the deflection of beams with cracks. To this aim, we perform FEM simulation and laboratory experiments. Because the frequency changes are small, and even big errors can be overseen, we also compare the relative frequency shifts (RFS). The RFSs are frequency changes normalized by the natural frequencies of the intact beam and are calculated using the following mathematical relation [35]:

$$\Delta \overline{f}_{i-D}(a,x) = \frac{f_{i-U} - f_{i-D}(a,x)}{f_{i-U}} = \gamma(a)\left[\overline{\phi}_i''(x)\right]^2 \tag{11}$$

By normalization, the changes become more easily comparable, and a better assessment of the method's reliability is possible. Moreover, these RFSs are used in damage detection, so it is important to evaluate if analytically deduced RFSs can be used to construct reliable databases that contain the structural response for a multitude of damage scenarios.

We can extract the severity from Equation (11), resulting in

$$\gamma(a) = \frac{1}{\left[\overline{\phi}_i''(x)\right]^2} \frac{f_{i-U} - f_{i-D}(a,x)}{f_{i-U}} \tag{12}$$

Testing is made by comparing the severity obtained from static tests with the RFS obtained from dynamic tests made in the laboratory. From the static tests, made through FEM simulations, we obtain the deflections and calculate the severity with Equation (1). From the dynamic tests, made involving the FEM or laboratory experiments, we obtain the frequencies of the beam in the intact and damaged state. In addition, we can calculate the normalized modal curvature $\overline{\phi}_i''(x)$, and eventually the right term in Equation (12), which has also the meaning of the severity. Now, by comparing the two results, we can conclude if these fit and if the prediction of frequency changes can be reliably made with Equation (3). In this mathematical relation, we consider the measured frequency of the intact real beam and the severity deduced from the deflections of the beam under its own weight.

5.1. Tests Performed with FEA

Damage detection using modal parameters requires accurate algorithms to detect the slightest frequency changes in structures. For determining the accuracy of the described method used for detecting transverse cracks, we have performed FEM modal simulations

using the ANSYS software for the same cantilever beam described in Section 2. The beam is successively affected by closed and open transverse cracks with different depths and located in different slices of the beam.

As a first example, we present in Figure 7 the natural frequencies obtained from simulation and with Equation (3) for the beam with a transverse crack that has the parameters: x = 604 mm, a = 1 mm, and w = 0 mm. When using the analytical approach, we calculate the frequencies with Equation (3) in which we consider the measured frequency of the intact beam and the severity deduced from the deflections achieved by static analysis.

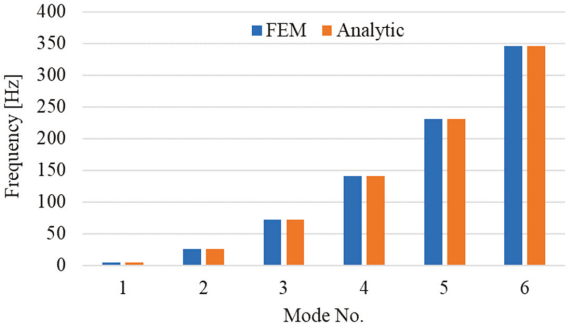

Figure 7. Comparison of the natural frequencies obtained for the cantilever beam with a transverse closed crack that has the parameters x = 604 mm and a = 1 mm.

At a first look, the frequencies in Figure 7 fit, but it is difficult to evaluate the accuracy of the method. However, one can observe that the differences between the natural frequencies obtained involving the analytical method and the FEM results are small.

To trace a relevant conclusion, we represent in Figure 8 the difference between the predicted frequencies and those obtained from simulation. Before being represented, the differences are normalized, according to the mathematical relation

$$\varepsilon = \frac{f_{i-D}(FEM) - f_{i-D}(a,x)}{f_{i-U}} \tag{13}$$

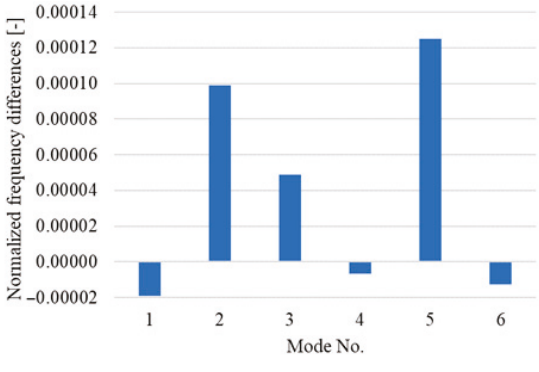

Figure 8. The normalized differences between the natural frequencies determined analytically and using FEM for the cantilever beam with a transverse closed crack that has the parameters x = 604 mm and a = 1 mm.

One can observe that absolute normalized differences are extremely small, between −0.000019 and +0.000125. Because the frequency differences are normalized, the error does

not increase with the mode number. By calculating the normalized differences for more damage scenarios, we found out that the errors are comparable or smaller. This proves that the results obtained with the DS-SHC method are reliable.

A second example considers also closed cracks, thus $w = 0$ mm. The damage scenarios are defined in ANSYS, for three crack depths $a = 0.2$, 1, and 1.6 mm. For each crack depth, the position of the crack is $x = 125$ mm and $x = 489$ mm, respectively. After we defined the damage scenarios, we determined the severity $\gamma(a)_{FEM}$ using relation 12 for the first six weak-axis vibration modes. Relative to the crack's main dimensions, a, x, and w, the damage scenarios are noted as $C(a,x,w)$. The severity values $\gamma(a)_{FEM}$ are compared, in Figure 9, with the calculated ones $\gamma(a)$.

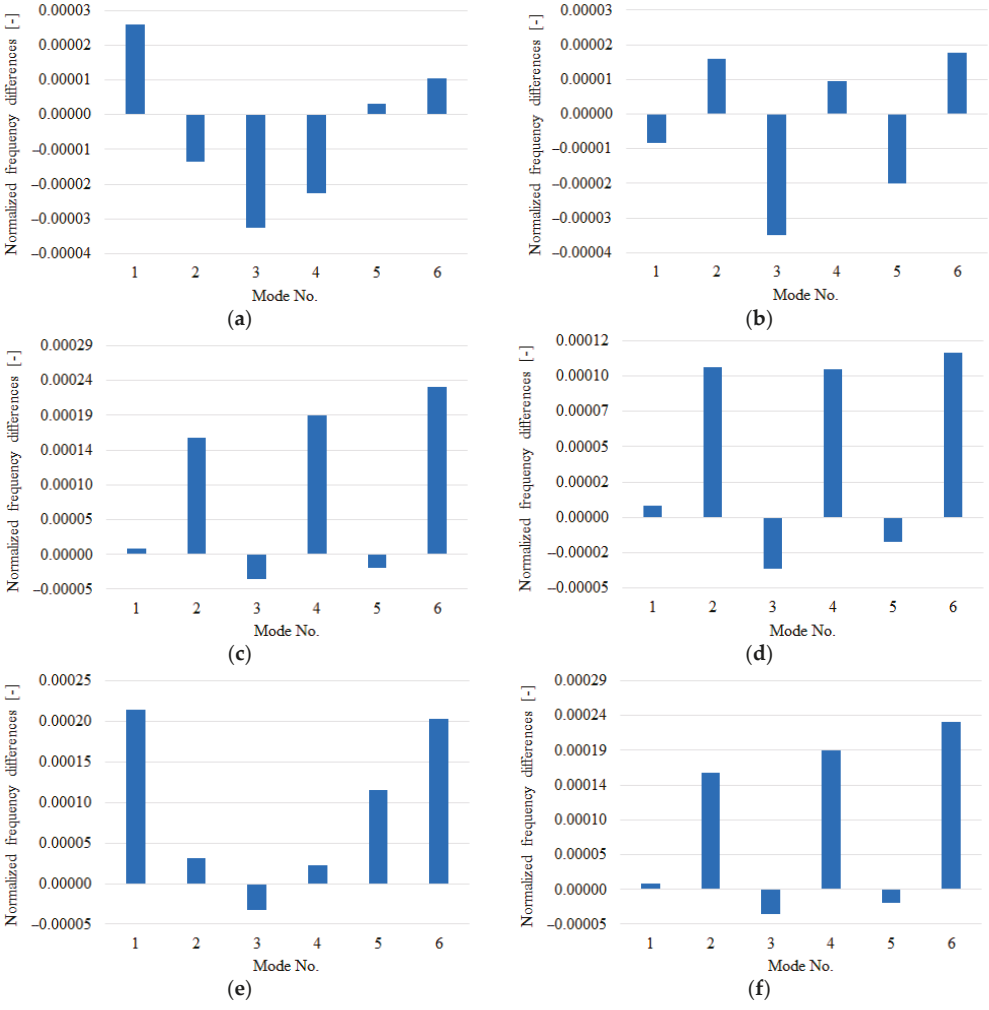

Figure 9. The normalized differences obtained between the natural frequencies determined analytically and by means of FEM for the cantilever beam with a transverse crack: (**a**) Damage scenario C(0.2, 125, 0); (**b**) Damage scenario C(0.2, 489, 0); (**c**) Damage scenario C(1, 125, 0); (**d**) Damage scenario C(1, 489, 0); (**e**) Damage scenario C(1.6, 125, 0); (**f**) Damage scenario C(1.6, 489, 0).

A third example considers open cracks. We performed FEM simulations for defined damage scenarios that involve cracks with widths w of 0.5, 1, and 2 mm. The results for all damage scenarios are presented in [36].

For a part of the open damage scenarios, noted as $C(a,x,w)$, the normalized differences calculated between the natural frequencies determined analytically and employing FEM are presented in Figure 10.

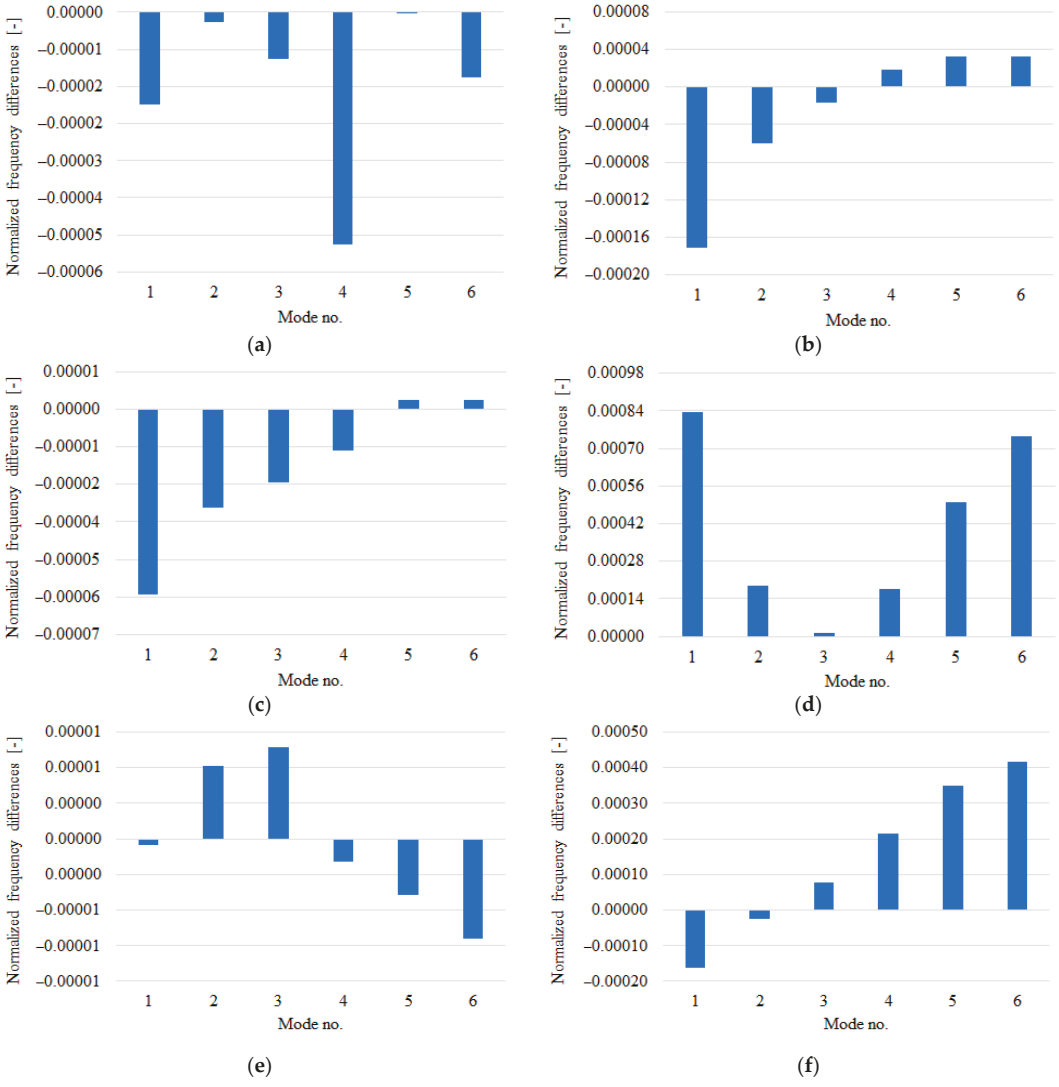

Figure 10. The normalized differences obtained between the natural frequencies determined analytically and using FEM for the cantilever beam with an open transverse crack: (**a**) Damage scenario C(0.2, 125, 0.5); (**b**) Damage scenario C(1, 125, 0.5); (**c**) Damage scenario C(0.2, 125, 1); (**d**) Damage scenario C(1, 125, 1); (**e**) Damage scenario C(0.2, 125, 2); (**f**) Damage scenario C(1, 125, 2).

5.2. Tests Performed Involving Laboratory Experiments

To prove the accuracy of the developed algorithm, we also conducted laboratory studies on steel cantilever beams affected by transverse cracks of known location, depth, and width. The tests consist of measuring the natural frequencies in the intact and damaged state. Because the accuracy of RFS calculated with Equation (11) is relevant for damage detection, in this section we compare these RFS with those obtained from measurements. The laboratory setup consists of a rigid structure including a vise in which the beam is fastened, an excitation device, and the data acquisition system. The experimental setup is presented in Figure 11 and described in detail in [27].

Figure 11. Experimental setup.

The excitation system involves a speaker and amplifier which are controlled using AudioDope software. The beam is excited at specific frequencies, and the vibration response is acquired. To acquire the signals, we use a data acquisition system consisting of a Kistler 8772 accelerometer which transmits the signal through the analog-to-digital conversion module NI9234 to the compact chassis NIcDAQ-9175. This module is connected to a second laptop, on which the LabVIEW software is installed. The acceleration signal is acquired and is subsequently processed to extract the natural frequencies with high accuracy using the procedure described in [37,38]. The Python code implementing the procedure is available in [39].

The experimental study was carried out on four S355 JR steel cantilever beams of dimensions $1 \times 0.05 \times 0.005$ m, at first in an intact state and later in a damaged state, by generating transverse cracks of width $w = 2$ mm by saw cutting. One end of the beams is fixed in a vise (see Figure 12).

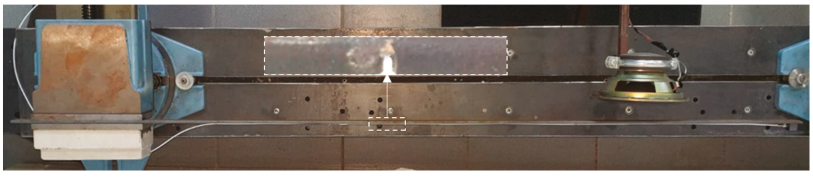

Figure 12. Test specimen with generated transverse crack mounted on the experimental stand.

At least five natural frequency readings were made for each test and the arithmetic mean was considered. For each reading, the first six natural frequencies of the beam were extracted, and the obtained values are listed and compared with the natural frequencies

obtained from FEM in Table 6. From the compared values the small differences can be observed.

Table 6. Obtained natural frequencies for the undamaged test beams.

Beam nr.	Measured Natural Frequencies [Hz]					
	Mode 1	**Mode 2**	**Mode 3**	**Mode 4**	**Mode 5**	**Mode 6**
Beam 1	4.060	25.439	71.426	139.902	231.038	344.750
Beam 2	4.052	25.448	71.213	139.342	230.295	343.254
Beam 3	4.011	25.237	71.102	138.575	229.421	342.904
Beam 4	4.044	25.482	71.287	139.420	228.528	344.177

A transverse open crack was generated on each beam analyzed above, thus resulting, for a single beam, six natural frequency values corresponding to the six transverse vibration modes.

We present in Table 7 the crack dimensions for each damage scenario and the measured natural frequencies. In this table, we also included the severities for the four cracks, derived using the method described in the current research.

Table 7. Obtained natural frequencies for the damaged beams.

Damage Scenario	a [mm]	x [mm]	w [mm]	$\gamma(a)$ [-]	Measured Natural Frequencies [Hz]					
					Mode 1	**Mode 2**	**Mode 3**	**Mode 4**	**Mode 5**	**Mode 6**
Beam 1	0.8	310	2	0.004503233	4.054	25.425	71.286	139.832	230.933	343.984
Beam 2	1.2	587	2	0.009104778	4.051	25.356	71.071	139.131	229.403	343.204
Beam 3	1.2	395	2	0.009104778	4.003	25.166	71.002	138.496	228.555	342.860
Beam 4	2	795	2	0.026682373	4.044	25.431	70.553	137.544	226.899	343.963

We calculate now the RFSs with the frequencies taken from Tables 6 and 7, which are found from experiments. To this aim we use Equation (11). We also calculate the RFSs analytically (see Section 2). In this case, the input data consists of the deflections obtained from FE simulations; these permit calculation of the severity with Equation (1). With the calculated severity we find the frequency drop with Equation (3) and, finally, the RFSs with Equation (11). The comparison between the RFSs obtained with experimental results and those calculated is presented in Figure 13.

From the diagrams represented in this figure, it can be observed that there is a good fit between the compared values. Note that once the severity curves are known and plotted as in Figure 6, the severity can be easily determined for any damage depth. Thus, the FE simulations are no longer required when the procedure is applied.

By using the method described in the current paper, by employing Equation (11), we have generated training data for developing a damage detection neural network similar to the one presented in [13]. The training data consist of the RFS values for the six transverse vibration modes. After the network was trained, we successfully determined the position and depth of the cracks for the four experimental cases by considering the RFS values. The errors obtained are presented in Table 8.

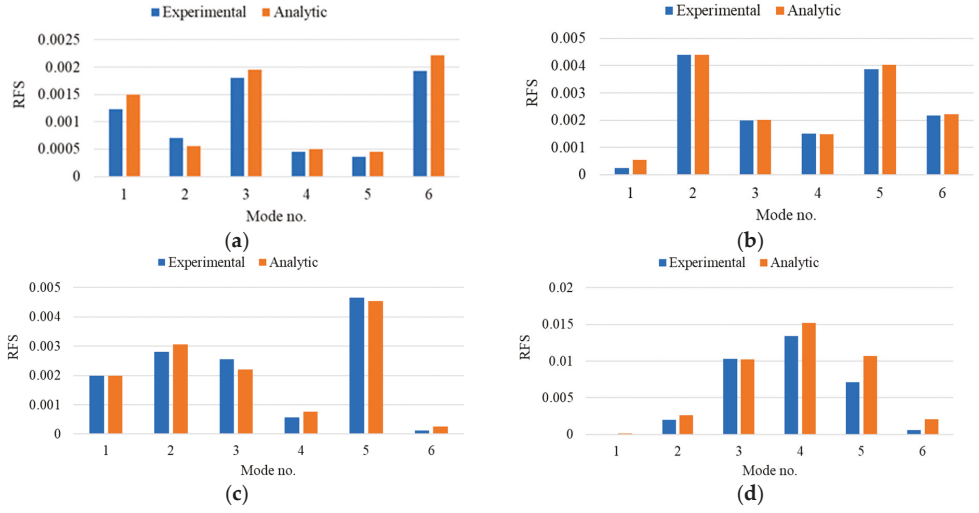

Figure 13. Compared RFS values between the experimental measurements and analytical determined ones. (**a**) Damage scenario C(0.8, 310, 2); (**b**) Damage scenario C(1.2, 587, 2); (**c**) Damage scenario C(1.2, 395, 2); (**d**) Damage scenario C(2, 795, 2).

Table 8. Predicted locations and depths of the damage.

Damage Scenario	x [mm]	a [mm]	w [mm]	ANN Predicted Values			
				x [mm]	ε_x [%]	a [mm]	ε_a [mm]
Beam 1	310	0.8	2	321.07	1.107	1.06	0.26
Beam 2	587	1.2	2	598.01	1.101	1.49	0.29
Beam 3	395	1.2	2	394.41	−0.059	1.38	0.18
Beam 4	795	2	2	791.09	−0.391	1.94	−0.06

The results prove the accuracy of the applied method for determining the position and severity of transverse cracks.

6. Conclusions

The paper presents the DS-SHC method, which can determine the severity of a crack involving just four static tests, one for the intact beam and three for the beam affected by a defect for which the positions are changed successively. From the tests performed for the defective beam, deflection is determined at the free end of a cantilever. Subsequently, using the SHC algorithm, the theoretical deflection that occurs when the crack is at the fixed end is determined. The matching of the three points is carried out on the function proposed in this paper, which expresses the deflection with the crack position. This theoretical deflection is different from the deflection achieved when the crack is at the fixed end because of constructive reasons. Finally, the severity is calculated from the capability of the beam with a crack to store energy, which is reflected by the increase of deflection at the free end.

To prove the reliability of the DS-SHC method, we compared the frequencies of the damaged beam calculated with the severity derived by employing the theoretical deflection with the frequencies obtained for the damaged beam using the FEM. The normalized differences between these frequencies are extremely low, less than ± 0.001, which proves the reliability of the DS-SHC method. Moreover, we demonstrated here that the theoretical deflection for the damaged beam has to be considered when calculating the damage severity.

An additional check was made to find out whether the prediction of the frequency changes made with the severity calculated based on the theoretical deflection permits assessing the damage. In the laboratory experiments we conducted, we were able to localize the damage with high accuracy, the errors being less than 1.1%. The damage depth was also found with high accuracy; the difference between the depth of the generated damage and the prediction is smaller than 0.3 mm.

In the next studies, we will focus on finding whether the severity derived for the cantilever beam can be used for beams with other boundary conditions, and how accurate the severities for structures with other shapes of the cross-section can be determined.

Author Contributions: Conceptualization, G.-R.G.; methodology, N.G.; software, C.V.R., C.S., and C.T.; validation, G.-R.G. and C.V.R.; formal analysis M.V.P.; investigation N.G. and C.T.; writing—original draft preparation, M.V.P. and C.O.H.; writing—review and editing, G.-R.G.; visualization, M.V.P.; supervision, G.-R.G. All authors have read and agreed to the published version of the manuscript.

Funding: This research received financial support through the project "Entrepreneurship for innovation through doctoral and postdoctoral research": POCU/380/6/13/123866, a project co-financed by the European Social Fund through the Operational Program Human Capital 2014–2020.

Institutional Review Board Statement: Not applicable.

Informed Consent Statement: Not applicable.

Data Availability Statement: The data presented in this study are openly available on the Mendeley platform at https://doi.org/10.17632/g6tc23z48p.1 (accessed on 13 July 2022) and https://doi.org/10.17632/t8bscbsv5d.1 (accessed on 13 July 2022).

Conflicts of Interest: The authors declare no conflict of interest.

References

1. Housner, G.W.; Bergman, L.A.; Caughey, T.K.; Chassiakos, A.G.; Claus, R.O.; Masri, S.F.; Skelton, R.E.; Soong, T.T.; Spencer, B.F.; Yao, J.T.P. Structural Control: Past, Present, and Future. *J. Eng. Mech.* **1997**, *123*, 897–971. [CrossRef]
2. Doebling, S.W.; Farrar, C.R.; Prime, M.B. A Summary Review of Vibration-Based Damage Identification Methods. *Shock Vib. Dig.* **1988**, *30*, 91–105. [CrossRef]
3. Fan, W.; Qiao, P. Vibration-based Damage Identification Methods: A Review and Comparative Study. *Struct. Health Monit.* **2011**, *10*, 83–111. [CrossRef]
4. Yang, Y.; Zhang, Y.; Tan, X. Review on Vibration-Based Structural Health Monitoring Techniques and Technical Codes. *Symmetry* **2021**, *13*, 1998. [CrossRef]
5. Gillich, G.-R.; Praisach, Z.I.; Wahab, M.A.; Vasile, O. Localization of Transversal Cracks in Sandwich Beams and Evaluation of Their Severity. *Shock Vib.* **2014**, *2014*, 607125. [CrossRef]
6. Onchis, D. Observing damaged beams through their time–frequency extended signatures. *Signal Process.* **2014**, *96*, 16–20. [CrossRef]
7. Grandić, I.; Grandić, D. Estimation of damage severity using sparse static measurement. *J. Civ. Eng. Manag.* **2017**, *23*, 213–221. [CrossRef]
8. Li, X.-L.; Serra, R.; Olivier, J. Performance of Fitness Functions Based on Natural Frequencies in Defect Detection Using the Standard PSO-FEM Approach. *Shock Vib.* **2021**, *2021*, 8863107. [CrossRef]
9. Lee, Y.-S.; Chung, M.-J. A study on crack detection using eigenfrequency test data. *Comput. Struct.* **2000**, *77*, 327–342. [CrossRef]
10. Friswell, M.I. Damage Identification using Inverse Methods, Dynamic Methods for Damage Detection in Structures. In *Dynamic Methods for Damage Detection in Structures*; CISM International Centre for Mechanical Sciences, Morassi, A., Vestroni, F., Eds.; Springer: Vienna, Austria, 2008; Volume 499, pp. 13–66. [CrossRef]
11. Long, H.; Liu, Y.; Huang, C.; Wu, W.; Li, Z. Modelling a Cracked Beam Structure Using the Finite Element Displacement Method. *Shock Vib.* **2019**, *2019*, 7302057. [CrossRef]
12. Friswell, M.I. Damage identification using inverse methods. *Philos. Trans. R. Soc. A* **2007**, *365*, 393–410. [CrossRef] [PubMed]
13. Gillich, G.-R.; Maia, N.M.M.; Wahab, M.A.; Tufisi, C.; Korka, Z.-I.; Gillich, N.; Pop, M.V. Damage Detection on a Beam with Multiple Cracks: A Simplified Method Based on Relative Frequency Shifts. *Sensors* **2021**, *21*, 5215. [CrossRef] [PubMed]
14. Dimarogonas, A.D. *Dynamic Response of Cracked Rotors*; Internal Report; General Electric Co.: Schenectady, NY, USA, 1970.
15. Chondros, T.G. Dynamic Response of Cracked Beams. Master's Thesis, University of Patras, Patras, Greece, 1977.
16. Liebowitz, H.; Claus, W.D.S., Jr. Failure of notched columns. *Eng. Fract. Mech.* **1968**, *1*, 379–383. [CrossRef]
17. Ostachowicz, W.; Krawczuk, M. Analysis of the effect of cracks on the natural frequencies of a cantilever beam. *J. Sound Vib.* **1991**, *150*, 191–201. [CrossRef]

18. Chondros, T.J.; Dimarogonas, A.D.; Yao, J. A continuous cracked beam vibration theory. *J. Sound Vib.* **1998**, *215*, 17–34. [CrossRef]
19. Bilello, C. Theoretical and Experimental Investigation on Damaged Beams under Moving Systems. Ph.D. Thesis, Università degli Studi di Palermo, Palermo, Italy, 2001.
20. Gomes, G.F.; Mendez, Y.A.D.; da Silva Lopes Alexandrino, P.; da Cunha, S.S.; Ancelotti, A.C. A Review of Vibration Based Inverse Methods for Damage Detection and Identification in Mechanical Structures Using Optimization Algorithms and ANN. *Arch. Comput. Methods Eng.* **2019**, *26*, 883–897. [CrossRef]
21. Senthilkumar, M.; Reddy, S.M.; Sreekanth, T.G. Dynamic Study and Detection of Edge Crack in Composite Laminates Using Vibration Parameters. *Trans. Indian Inst. Met.* **2021**, *75*, 361–370. [CrossRef]
22. Zhou, Y.-L.; Wahab, M.A. Damage detection using vibration data and dynamic transmissibility ensemble with auto-associative neural network. *Mechanics* **2017**, *23*, 688–695. [CrossRef]
23. Li, M.; Jia, D.; Wu, Z.; Qiu, S.; He, W. Structural damage identification using strain mode differences by the iFEM based on the convolutional neural network (CNN). *Mech. Syst. Signal Process.* **2022**, *165*, 108289. [CrossRef]
24. Zhou, Q.; Ning, Y.; Zhou, Q.; Luo, L.; Lei, J. Structural damage detection method based on random forests and data fusion. *Struct. Health Monit.* **2013**, *12*, 48–58. [CrossRef]
25. Tran-Ngoc, H.; Khatir, S.; De Roeck, G.; Bui-Tien, T.; Wahab, M.A. An efficient artificial neural network for damage detection in bridges and beam-like structures by improving training parameters using cuckoo search algorithm. *Eng. Struct.* **2019**, *199*, 109637. [CrossRef]
26. Kim, B.; Kim, C.; Ha, S.-H. Multiple Damage Detection of an Offshore Helideck through the Two-Step Artificial Neural Network Based on the Limited Mode Shape Data. *Sensors* **2021**, *21*, 7357. [CrossRef] [PubMed]
27. Gillich, N.; Tufisi, C.; Sacarea, C.; Rusu, C.V.; Gillich, G.-R.; Praisach, Z.-I.; Ardeljan, M. Beam Damage Assessment Using Natural Frequency Shift and Machine Learning. *Sensors* **2022**, *22*, 1118. [CrossRef] [PubMed]
28. Gillich, N.; Tufisi, C.; Vasile, O.; Gillich, G.R. Statistical Method for Damage Severity and Frequency Drop Estimation for a Cracked Beam using Static Test Data. *Rom. J. Acoust. Vib.* **2019**, *16*, 47–51.
29. Gillich, G.R.; Tufoi, M.; Korka, Z.I.; Stanciu, E.; Petrica, A. The relations between deflection, stored energy and natural frequencies, with application in damage detection. *Rom. J. Acoust. Vib.* **2016**, *13*, 87–93.
30. Negru, I.; Praisach, Z.I.; Gillich, G.R.; Vasile, O. About the Neutral Axis Distortion due to Cracks and its Influence upon the Beams Natural Frequencies. *Rom. J. Acoust. Vib.* **2012**, *12*, 35–38.
31. Gillich, G.-R.; Praisach, Z.-I. Modal identification and damage detection in beam-like structures using the power spectrum and time-frequency analysis. *Signal Process.* **2014**, *96*, 29–44. [CrossRef]
32. Dahak, M.; Touat, N.; Kharoubi, M. Damage detection in beam through change in measured frequency and undamaged curvature mode shape. *Inverse Probl. Sci. Eng.* **2019**, *27*, 89–114. [CrossRef]
33. Tufisi, C.; Gillich, G.R.; Hamat, C.O.; Gillich, N.; Praisach, Z.I. Numerical study of the stiffness degradation caused by branched cracks and its influence on the natural frequency drop. *Rom. J. Acoust. Vib.* **2018**, *15*, 53–57.
34. Gillich, G.-R.; Praisach, Z.I.; Iancu, V.; Furdui, H.; Negru, I. Natural Frequency Changes due to Severe Corrosion in Metallic Structures. *Stroj. Vestn.-J. Mech. E.* **2015**, *61*, 721–730. [CrossRef]
35. Gillich, G.-R.; Furdui, H.; Wahab, M.A.; Korka, Z.-I. A robust damage detection method based on multi-modal analysis in variable temperature conditions. *Mech. Syst. Signal Process.* **2019**, *115*, 361–379. [CrossRef]
36. Tufisi, C. Stochastic Hill Climbing for Damage Detection; Version 1; Mendeley Data. Available online: https://data.mendeley.com/datasets/t8bscbsv5d/1 (accessed on 13 July 2022).
37. Cornel, M.I.; Gillich, G.R.; Maia, N.M.M. A method for an accurate estimation of natural frequencies using swept-sine acoustic excitation. *Mech. Syst. Signal Process.* **2019**, *116*, 693–709. [CrossRef]
38. Nedelcu, D.; Gillich, G.-R. A structural health monitoring Python code to detect small changes in frequencies. *Mech. Syst. Signal Process.* **2021**, *147*, 107087. [CrossRef]
39. Gillich, G.R.; Nedelcu, D. Data for: PyFEST—A Python Code for Accurate Frequency Estimation; Version 1; Mendeley Data. Available online: https://data.mendeley.com/datasets/g6tc23z48p/1 (accessed on 13 July 2022). [CrossRef]

applied sciences

MDPI

Review

Scour Detection with Monitoring Methods and Machine Learning Algorithms—A Critical Review

Sinem Tola [1], Joaquim Tinoco [1,*], José C. Matos [1] and Eugene Obrien [2]

[1] Department of Civil Engineering, University of Minho, ISISE, 4800-058 Guimarães, Portugal
[2] School of Civil Engineering, University College Dublin, D04 V1W8 Dublin, Ireland
* Correspondence: jtinoco@civil.uminho.pt; Tel.: +351-253510200

Abstract: Foundation scour is a widespread reason for the collapse of bridges worldwide. However, assessing bridges is a complex task, which requires a comprehensive understanding of the phenomenon. This literature review first presents recent scour detection techniques and approaches. Direct and indirect monitoring and machine learning algorithm-based studies are investigated in detail in the following sections. The approaches, models, characteristics of data, and other input properties are outlined. The outcomes are given with their advantages and limitations. Finally, assessments are provided at the synthesis of the research.

Keywords: bridge scour; scour detection; scour monitoring; machine learning algorithms

Citation: Tola, S.; Tinoco, J.; Matos, J.C.; Obrien, E. Scour Detection with Monitoring Methods and Machine Learning Algorithms—A Critical Review. *Appl. Sci.* **2023**, *13*, 1661. https://doi.org/10.3390/app13031661

Academic Editor: Cecilia Surace

Received: 5 December 2022
Revised: 20 January 2023
Accepted: 23 January 2023
Published: 28 January 2023

Copyright: © 2023 by the authors. Licensee MDPI, Basel, Switzerland. This article is an open access article distributed under the terms and conditions of the Creative Commons Attribution (CC BY) license (https://creativecommons.org/licenses/by/4.0/).

1. Introduction and Background—Scour Identification Approaches

Scour is one of the most common causes of bridge collapse. Bridge collapses cause large numbers of fatalities and financial losses. Therefore, the vulnerability of bridges to scour should be assessed and adequate actions should be taken. Piers, abutments, foundations, and piles at risk of scour could be protected from scour by taking countermeasures (with backfills, sheet piles, sacrificial piles, etc.) and repairing damaged elements (using ripraps, splitter plates, etc.) before global damage occurs. However, even after the bridges are properly protected against scour, it is important to continue monitoring the scouring condition. For several reasons, scour detection is a complex task; diving inspections to identify scouring are relatively dangerous. Underwater conditions complicate the implementation and maintenance of scour depth measurement devices. Moreover, hydraulic scour models are dependent on various parameters and there are still unsolved modeling issues caused by scaling and sediment gradation [1]. Traditional empirical scour formulas do not result in very accurate predictions of scour depths. To overcome this complex task to detect and locate scour, various methods have been developed. This review paper mainly focuses on a detailed assessment of scour monitoring and machine learning (ML)-based scour identification methods with relevant recent studies. However, an introduction with brief explanations of other scour detection approaches is provided as well. This section includes underwater inspections, empirical formulas, hydraulic and representative scour modeling, experimental studies, and probabilistic scour detection methods.

To begin with, empirical studies are one of the former scour detection and scour depth estimation methods [2–5]. These former studies were based on extracting scour length formulas using laboratory experimental results or field measurements. The relationship between flow velocity and duration, depth of charge, bed material properties, sediment movement, and substructure geometric properties on maximum local scour depth of piers and abutments or stresses in the riverbed were aimed to be quantified. Some of the scour formulas used are 65-1, 65-2 (Chinese), Melville-Sheppard, MBW, Hydraulic Engineering Circular No. 18 (HEC-18), Dey and Barbhuiya [6], and Muzammil [7].

Underwater inspections could be classified as eye inspections and equipment-based ones. In the eye inspection, the divers go through a difficult and dangerous search and a

detailed examination report is prepared. During underwater inspections, the human eye might fail to detect scour. Ground-penetrating radars, water-penetrating radars, SONAR, and some specific laser systems are examples of equipment-based underwater examinations. Penetrating radars in boats of floating units emit electromagnetic waves and receive echoes from the soil. In one of the latest studies in this field, the researchers mapped the bathymetric profile (water depths and sediment thicknesses) of a river bed in North Ireland and managed to detect scour holes around upstream piers using a water-penetrating radar [8]. On the other hand, another study aimed to quantify scour depths in a river in Switzerland with a gravel bed and find the relationship between the subsurface and the structure of the riverbed using a ground-penetrating radar [9]. The researchers detected a four-meter-deep scour hole that could not be detected by bathymetric (water-based) surveys. Moreover, SONAR is another technology for collecting underwater images and therefore can help detect scour holes. A recent and successful study managed to locate and measure scour depths by combining SONAR data and a deep convolutional network [10]. Furthermore, it was revealed that although it performs worse in high turbidity, green laser technology was able to detect scour around bridge piers in an economic and safe way [11].

The scour development process and how it is affected by the flow, bed material characteristics, and geometry of the scoured elements have been investigated by hydraulic model-based studies. [2] is a sample study examining the non-cohesive sediment's movement in sloping and [12] is another study where the fundamentals of the scour development process and mathematical modeling of flows around bridge piers/piles, below pipelines, and other structures such as groins, breakwaters, and seawalls were examined. According to a former study [13] the basic idea behind scour development was believed to be the horseshoe vortex system [14]. Later, the whole turbulence scheme was shown to be the most important eroding flow process; horseshoe vortex is only an element of this scheme and the whole pattern also consists of downflow and acceleration of the discharge around the sides of the pier [10]. Experimental studies have been used to test the effects of different layouts, shapes of piers, and flow parameters on scour [3,4,15,16]. Scour in clear water and accumulations around hexagonal arrays of emergent circular cylinders for various solid portions and an orientation of cylinders that resulted in less scour than an individual large pile was proposed [15]. Another study measured the complex turbulent discharge for different fluid velocities, Reynold shear stresses, and the density of the horseshoe vortex [4]. There were also studies on perpendicular wall abutments [5] investigating how channel width, shape, sediment dimensions, flow depths, and abutment lengths affect pier and abutment scour.

Furthermore, there have been studies that simulate scour instead of building a hydraulic model that directly represents it. To identify scour, mode shape ratio, apparent profile, Eigen frequencies, and decentralized modal analysis methods were adopted by various studies, namely [17], [18], and [19]. These studies did not aim to obtain scour depth but rather to detect its presence by identifying changes in the dynamic properties of the structure as an index that reveals the existence of scour. Alternatively, to evaluate the performance of scour-critical bridges, a soil–pile–structure interaction analysis was performed [20]. Some researchers have validated their approaches with experiments, [21–23] and therefore gathered more trusted results. Many studies with scour indexes were explained in detail in Section 2.1.1 with their approaches, model features, and outcomes.

Finally, there are probabilistic approaches that overcome the uncertainties of deterministic approaches summarized above. Uncertainties of scour identification problems include insufficiencies of visual inspections, assumptions, and estimations of parameters (geometric properties, hydraulic parameters, etc.). Since the accuracy of the deterministic models is highly dependent on the input, these might lead to over or underestimation of scour. Probabilistic scour models investigate the probability of structural failure under scour [24–28]. The limit state function is defined as the residual resistance of the structure after load effects are compensated; where load, resistance, and therefore limit state function are dependent on random variables [28]. To solve the probabilistic failure problem, there

are different types of reliability methods, for example risk-based, numerical, approximation, and semi-probabilistic designs [28]. Changing environmental conditions such as climate change effects might invalidate initial assumptions and cause unexpected rainfall regimes, floods, and therefore scour issues. The effects of such uncertainty, i.e., gradual change of flow properties was investigated by [24] and probabilistic scour failure analysis was performed. The researchers statistically analyzed the maximum annual flow of a UK river and aimed to predict local pier scour with Monte Carlo simulation. Simultaneous gradual increments of flow variability and the mean of the flow resulted in the greatest scour depth predictions. Another study investigated scour around a complex bridge pier and adopted a reliability analysis with an optimization method with a semi-probabilistic design [25]. Using this method, these researchers developed a safety factor to reach the desired safety level of the foundation design. Additionally, their sensitivity analysis revealed that pier width and correction factor were the most effective variables on the reliability of bridge pier against scour. A very remarkable uncertainty is caused by the memory effects, i.e., the accumulated scouring effects throughout the long service life of bridges [26]. Using a Markovian approach, scour depth changes aimed to be observed and scour depth domain was decomposed into multiple discrete states for various flood events. The research showed that after the first years of prediction, in time, the probabilistic scour depth distribution evolved and reached a stationary value [26]. The probabilistic local scour analysis of a bridge pier in a clay and sand mixture sediment was performed in five different reliability methods [27]. These simulation-based methods were line sampling, subset simulation, importance sampling, Monte Carlo simulation, and directional simulation. The most accurate results were obtained through subset simulation.

2. Conventional Monitoring-Based and Machine Learning-Based Methods to Identify Scour

Both machine learning and conventional monitoring approaches are based on measured or simulated data. However, the way of processing the input data creates the main difference between these two approaches. Conventional methods require the creation of models, whereas machine learning methods eliminate the need of knowing the relationship between input and output [29]. Even though it is possible to generate simulated signals, field (full-scale) measurements provide more realistic information. Hence, many different types of sensors have been developed to collect signals. Sensors used for signal monitoring were classified under three main categories: kinematic, ambient, and mechanical property collectors [30]. Kinematic properties are accelerations, velocities, and displacements; ambient properties include features such as temperature, wind, and soil permeability; while mechanical properties are strain, stress, and shear/bending/torsional deformations. Accelerometers, strain gauges, and displacement gauges are the most widely-used monitoring sensors. Narrowing down to sensors to monitor scour was explained under the two following main clusters [31]: the ones using devices that measure the depth and those utilizing changes in the dynamic properties of the structure. They listed depth monitoring devices as follows:

1. Single-use devices;
2. Pulse or radar devices;
3. Fiber Bragg grating sensors;
4. Buried or data-driven equipment;
5. Sound wave appliances;
6. Electrical conductivity devices.

They noted that accelerometers and tiltmeters were some of the sensors that use changes in the dynamic properties of the bridge. Bridge scour monitoring devices were visualized in Figure 1 [32]. With developing technology, monitoring devices have improved and alternative systems have been generated. A Scour Monitoring Decision Framework was developed, which was based on software [33]. This framework assisted the Minnesota Department of Transportation engineers to determine the most adequate fixed scour mon-

itoring equipment for the specific bridge they were working on. It decreased potential issues related to the sensor chosen by the user and supplied warnings on the occasion of abnormal scour activity in the field. One of the recent experimental monitoring studies investigated the consequences of scour for bridge frequencies [34]. The outcomes of the theoretical model corresponded with the laboratory outcomes. The numerical background of another study was used to decide the location of the sensors and the limitations of the railway bridge monitoring [35].

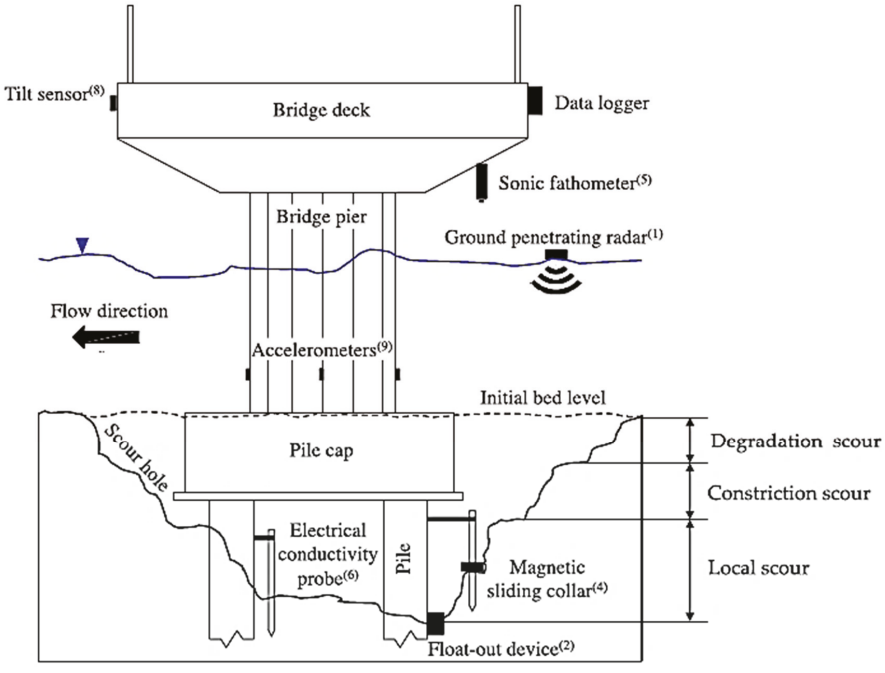

Figure 1. Scour monitoring devices - copied from [32].

Data collection systems include several other elements rather than sensor technology. The main elements when instrumenting a data acquisition scheme were listed as [36]:

1. Sensors;
2. Sensor data collection topologies;
3. Wireless connection;
4. Power supply;
5. Synchronizing the data obtained from a set of sensors;
6. Environmental effects and data;
7. Collection and processing systems.

The data collection system has to be adequately implemented according to the structure and service conditions. For large-scale bridges, locating, implementing, and maintaining sensors should be well planned since some parts of the structure could be inaccessible, such as the deck bottom of the suspension bridges. Although indirect monitoring techniques do not interrupt service conditions, for direct monitoring systems, service conditions are important factors to be considered. There can be time restrictions during the day or parts of the structure that cannot be closed to service for data acquisition. After obtaining data through sensors, wireless connections are used to transfer signals. Wireless sensing units were leveled up when combined with low-cost mobile devices and these units are still being developed for better software and hardware [37].

The following sections explain the methods, properties, and main outcomes of conventional monitoring-based and machine learning-based studies. For conventional monitoring-based studies, the databases searched were Google Scholar and Scopus and a total of 168 studies were screened. After applying the exclusion criteria, 22 studies remained. For machine learning-based studies, the databases searched were Web of Science and Scopus. A total of 38 elements were screened. Applying the exclusion criteria, this resulted in 14 studies.

The eligibility criteria applied were:

- Academic papers published in the recent years;
- Written in English;
- Aiming to detect bridge scour, not other types of damage;
- Scour detection methods were monitoring or ML-based.

2.1. Methods, Properties, and Main Outcomes of Studies

2.1.1. Cluster 1—Conventional Monitoring-Based Approaches to Detect Scour

Table 1 provides the type of monitoring, numerical approach, and dynamic structural property addressed, and the presence of experimental/field data in the studies. Descriptions of direct and direct monitoring systems, technical information about the sensors, and analysis methods used in the studies in Table 1 are explained in this section.

Scour monitoring could be classified under direct and indirect methods [38]. In direct monitoring, structural parts of the bridge are equipped with sensors. The sensors are fixed while in indirect monitoring, the vehicle passing over the structure is instrumented with measurement devices, i.e., sensors are moving. Indirect or so-called drive-by monitoring utilizes the responses of the sensors on the vehicles to extrapolate the condition of the bridge [38]. These responses (measurements) could be accelerations, displacements, or speed. There are some challenges of direct monitoring as well as its major advantages of ensuring improvement in public safety early risk detection and minimizing downtime [39]. There are some disadvantages. Direct monitoring is not suitable for all applications, the whole scheme is costly, and there are some undesired implications such as high maintenance costs. This was where indirect monitoring became more advantageous since it was found to be more economical, independent from the features of the structural system to be assessed, and provided maintenance-friendly measurements. The indirect monitoring technique is also known as drive-by monitoring and enables scour identification without any traffic interruptions to the railway or highway operations on the bridge. In direct monitoring, signals are obtained from structure form input data, while signals of single run or multiple vehicle batches are products of indirect monitoring. To extract the dynamic properties of the bridge, data were processed with numerical approaches. Utilizing displacements of a beam which were found from a vehicle–bridge interaction finite element model was aimed to calculate the distribution of the flexural rigidities throughout the length retrospectively [40]. They also sought to estimate the damage level of the bridge. For detecting damage, it is also possible to eliminate the dependence on reference signals from a healthy bridge. Another study focused on monitoring analyzed the difference between right and left accelerations of the train (i.e., roll component) which occurred in the presence of deformation, to prove the imbalance in the bridge behavior [41].

Table 1. List of monitoring-based scour detection studies.

Monitoring Type	Study Reference	Numerical Method and Sensor Technology	Presence of Experimental Cases /Field Tests
Direct	[42]	Mode Shape Ratio	None
	[43]	Vibration energy harvesting device	Yes
	[44]	Hilbert Huang Transform	Yes
	[45]	Fiber Optic Sensors	Yes
	[46]	Eigen frequency	None
	[47] [17]	Frequency Domain Decomposition	None
	[23]	Decentralized modal analysis	Yes
	[48] [49] [50]	Frequency analysis of piezoelectric rod sensors	Yes
	[51]	Unmanned Aerial Vehicle using smart rocks	Yes
	[31] [52]	Smart probes instrumented with electromagnetic sensors	Yes
	[53]	Micro energy harvesters	None
	[54]	Horizontally-displaced mode shapes and changes in dynamic flexibility	Yes
	[55]	Unmanned Aerial Vehicle-based smart rock	Yes
Indirect	[56] [37] [57]	Wavelet transformation	None
	[18]	Eigen frequency	None
	[19]	Closed-form mode shape derivation	Yes

The studies listed in Table 1 use numerous sensors. Accelerometers were located at the mid-spans and piers of the bridges. Signals from the superstructure of the bridge were collected using velocity sensors to reveal the dynamic features of scour [55]. Their experimental setup consisted of inclinometers, a camera, a level transmitter, and a wireless transmitter as well. As the flow continued, the velocity sensors sensed vibrations and the inclinometer showed the angle of tilt during scour. Besides accelerometers and velocity sensors, piezoelectric rods, electromagnetic sensors, micro-electro-mechanical systems (MEMS), vibrational power generators, optic sensors (image tracking), and permittivity change of the soil were utilized for the detection of scour. When the water flowed, the buried piezoelectric rods were subjected to hydrodynamic effects resulting in vibrations that created voltage in the rods [48]. A frequency domain analysis of the voltage–time history of the rod will result in the length. As sediment moves away, the length of the rod increases and this is felt through the change in the frequency. The difference between the initial and instantaneous length will give scour depth. Moreover, unconstrained distributed fiber optic sensors are one of the recent technologies used for investigating scour. In the research of [45], fibers deform freely under water flow. Deformation changes are detected by ultra-weak fiber Bragg grating which is written in the optical fiber. Since temperature changes at pier at an elevation of around 10 meters below water are slow and small, the central wavelength of the fiber is only affected by the altered strains, i.e., deformations of the fiber. Differences in central wavelength changes give scour length. Some innovative researchers used innovative technology, i.e., smart rocks for scour monitoring. [51,55]. Based on the theory of the magnetic field, developed algorithms were able to find the locations of the rocks, which were rolled down into scour holes. The proposed system for

scour monitoring of other studies [31,52] had a probe with an integrated electromagnetic sensor that identifies different dielectric permittivity values of the soil that surround the foundation of the bridge. Using the frequency of the oscillators implemented in the sensors, measuring the capacitance which only changes with the dialectic property of the soil around them was proven possible [33]. The monitoring system of [53] on the other hand, consisted of MEMS harvesters to detect pier scour, which gathered energy from environmental energy sources to produce electricity. Further expiation of the authors about these micro energy harvesters revealed that depending on the frequency change induced by the oscillation of the electrode, having the rent as output was possible and the frequency was detected via a small wireless apparatus.

There are many various transformation methods to decompose signals gathered from different sensors. Fourier transform is one of the most common signals processing methods in a frequency domain analysis. Fourier integrals containing the Fourier transform represent non-periodic (arbitrarily changing) excitations [58]. Direct Fourier transform equals the o multiplication of the Fourier transform and complex frequency response function. To obtain a response in the time domain, inverse Fourier transform is applied. Fourier transform is best applied to stationary and transient signals since it results in average frequency [59]. Hilbert spectrum is also an amplitude in the frequency–time domain; however, it is used for processing non-stationary signals as well. [50]. [60] indicates one of the most significant features of the Hilbert transform—it could detect frequency response nonlinear effects. Since applying the Hilbert transform to the frequency response of a linear structure regenerates the original frequency response, any distortion could be an indicator of non-linearity. The Frequency Domain Decomposition method [61] identifies very close and repeated modes. [47] stated that the approach also makes the extrapolation of dynamic parameters possible with no information about excitation in the beginning. After calculating the continuous wavelet transform matrix from raw data, singular values and singular vectors are the products of the singular value decomposition used to find damping ratios, frequencies, and mode shapes [62]. Wavelet transformations were defined as visual tools to assess signals more easily and the computation of these transformations is a prerequisite when a signal will be modified selectively or its pattern will be sought [63]. A wavelet function has zero mean, changes with a dimensionless time parameter, and is located in both time and frequency domains, while the convolution of discrete sequence with the translated and scaled status of the wavelet transformation was defined as continuous wavelet transformation [64]. The selection of the wavelet transformation is important. A decentralized modal analysis is engaging the sectors of mode shapes which are computed at distinct sensor locations [65–67]. The sensors were accelerometers in the research of [23] and mode shape amplitudes were computed using Frequency Domain Decomposition explained above. Eigenvalue analysis is performed to obtain mode shapes, amplitudes, and frequencies of the system. [58] noted that since this method includes a large computational volume in a large number of degrees of freedom systems, efficient algorithms were generated in time. Solutions for the eigenvalue problem were categorized under vector iteration, transformation, and polynomial iteration methods.

All the studies listed in Table 1 have numerical models except for [49]. There were a lot of studies focused on using accelerations of the bridge to identify scour. They adopted different frequency analysis methods to interpret acceleration signals to obtain mode shapes or frequencies and finally set a scour index to identify scoured cases. In [42], the Mode Shape Ratio was applied to acceleration signals and utilized as an indicator of scour. Acceleration signals of two points on the bridge were used to gather amplitudes of mode shapes. Mode shape ratio was the ratio of these amplitudes. Energy harvesting devices were used in [43], which produce electricity from piezoelectric material's strain changes. These were used to identify scour-based frequency shifts of the bridge. [46] and [18] investigated the influence of scour at different points on eigen frequencies. To obtain mode shapes from acceleration signals of the structure, [47] and [17] used the Frequency Domain Decomposition method. Without information on the input motion, it was possible to

evaluate the dynamic parameters in this method. Decentralized modal analysis enabled [23] to derive the modal amplitudes of sensors at different locations. To detect bridge pile scour, [54] utilized the change of the shape of horizontally-displaced modes and flexibility deformations of a frame-type bridge. Continuous wavelet transformation of a signal was utilized to process acceleration signals in the research of [56], [57], and [37]. By comparing responses to the features of a base wavelet, this method could detect transient changes in frequency signals [68]. To process acceleration signals, [19] proposed a closed-form model derivation. Based on instantaneous amplitudes calculated for a target bridge frequency, mode-shape squares were obtained and a damage index was computed.

Direct Monitoring-Based Studies

This section includes main properties and outcomes only direct monitoring-based studies listed in Table 1. In Table 2, devices, sensing mechanisms, the methods of sensor signal processing, and the target property of the direct monitoring studies. Additionally, scour validation tests, and experiments on real bridges are tabulated here. The assessments, outcomes of the studies, performance, and efficiencies are provided at the end of this section.

Table 2. Properties of devices used in direct monitoring studies.

Study Ref.	Device Type	Sensing Mechanism	Signal Processing Method	The Target Property of Signal Processing	Scour Validation Tests	Laboratory or Field Tests	Target Property
[45]	Unconstrained distributed fiber optic sensors	Ultra-weak fiber Bragg grating	Empirical formula	Central wavelengths	Detecting different signals of set of fibers embedded in sand and other fibers freely in water	Standard deviation value higher than zero for several minutes	Scour depth and location
[44]	Velocity sensors, inclinometer, wireless transmitter, and camera	2 Velocity sensors	Hilbert transform and empirical mode decomp.	Individual instant frequencies	Single-pier laboratory scour test	Caisson-type and pile-group foundation scour tests	Rigid body motion
[48]	Rod sensor	Piezoelectric Polymer Film	Wavelet packet transform and Hilbert transform	Instant the natural frequency of the rod	Flume test	Test with different pier cross-sections	Scour depth
[49]		Piezoelectric Polymer Film	Fast fourier transform	Instant natural frequency of the rod	Clamped to a laboratory bench Planted in sand Implemented in the sand	None	
[50]					Flume test	Tested on 1 pier	
[51]	1 Direction-Unknown and 1 Direction-Known smart rocks	Ambient magnetic field	Theory of magnetic field	Distribution of the magnetic field induced by smart rocks	Field validation tests	Tests on the upstream side of a pier	Localize the position or track the move of the smart rock
[52]	E.magnetic sensors	Changes in the dielectric permittivity of the soil	The reflection feature of e.magnetic waves	The porosity of the soil	'Static' scour simulations Real-time open channel flume tests	Not provided	Scour depth variation
[55]	Unmanned Aerial Vehicle -based smart rock positioning system	3-axis magnetometer and global positioning system on Unmanned Aerial Vehicle	Algorithm to locate smart rocks using measured magnetic intensities	Magnetometer measuring magnetic fields before and after the smart rock has been deployed	Not provided	I-44W Roubidoux Creek Bridge Pier	Depth of scour, i.e., vertical move of the rock

The research listed in Table 2 mainly focused on the monitoring device they used. [49], [50], [48], [44], and [45] aimed to measure scour depth with the sensors they used. [52] monitored sediment deposition processes. On the other hand, [44] searched for the rigid body motions of the piles and piers, using velocity sensors. [51] and [55] tried to locate and track the movement of smart rocks they deployed along the scour hole. Vertical displacement of the rock into the hole revealed the depth of scour. Direction known and unknown smart

rocks induced the distribution of the electromagnetic field and their locations were detected through an unmanned aerial vehicle, equipped with a locating algorithm. [45] preferred a spiral shape since this geometry brings the sensing points of the fiber optic sensor closer and to obtain a higher spatial resolution. Adjusting the number of rings around the piers changes the scour monitoring range along the length. Fibers are supported by the pier only in two points so that they can freely deform and so central wavelength differences can be obtained clearly.

Studies that are not tabulated in Table 2 are those having a finite element model to represent the bridge and piers. [43], [47], [17] [46], [31], [53], and [54] represented the bridge superstructure (deck and beams) with Euler-Bernoulli beams. Springs were assumed for the piers and the foundations beneath them. Different spring stiffnesses corresponded to different stages of scour. In their studies, [23] and [42] also included vehicles in their finite element models, i.e., vehicle–bridge interaction models. Vehicles were modeled as rigid masses and were connected with springs and dampers. [31], [43], [54], and [23] also verified their numerical approaches with experiments.

The scour indicators in the research of [43], [42] and [14], and [53] were the frequency shifts of the bridge. While [63] used differences in the first mode shape amplitudes at pier locations, [17] and [54] chose mode shape changes. [54] specifically focused on horizontally-displaced mode shapes of a frame-type bridge. [23] set fitting curves to the mode shapes and used root mean square (RMS) differences between healthy and damaged mode shapes to indicate scour. [48], [49], and [50] detected scour through changes in the fundamental frequencies of the polymer rods. [52] used the increasing permittivity of the soil to identify scour; as scour developed, the sensors' permittivity suddenly increased. Higher apparent permittivity was related to the reduced soil density of the re-deposited sediment around the sensor.

The outcomes of the direct monitoring studies were summarized here. [43] numerically proved that the frequencies decreased due to a reduction in foundation stiffness in two piers (mimicking 24.5% and 44.9% scour cases). In their experimental setup, cantilever-based piezoelectric energy harvesting devices were used and three scour scenarios were adopted. One device attached to the pier was successfully the detecting frequency shift in that pier. When the device was attached to a healthy pier, it could detect the scour of another damaged pier. For a better performance of the method, they suggested performing an initial modal analysis of the bridge with accelerometers since this way it would be possible to monitor obtained modal frequencies in the frequency domain of the device's voltage. In the research of [17], the normalized mode shape of a two-span integral-type concrete bridge changed by around 50%, with a 20% frequency difference for scour depth of 5 m. They noted that their approach might alleviate the known frequency-associated problems because the method is based on using the same sensors as the ones used for gathering the frequency. According to [46], abutments and piers had local vibration modes and the corresponding frequencies were only sensitive to scour related with the adjacent element. In their experiment, sensors were represented by virtual node points and located on two abutments and one pier. The method successfully identified the local frequencies and the location of the scour. However, they indicated that experimental validation through a field study was needed. [42] generated research for a two-span integral-type bridge. For 5 m of scour depth, due to central pier scour, the mode shape ratios of two points on the pier and deck changed by around 50% over the center of the foundation. The loading sensitivity to vehicle bridge interaction responses, random errors of ambient loading were main limitations of the study. Moreover, applying the developed approach to abutment by using the first mode was not possible. The approach was extended to a three-span bridge but a steady trend could not be obtained. In another study of the author, [46] noted that as the scour got more severe, the mean-normalized mode shape values at piers decrease. For example, pier 1 changed from 0.62 to 0.35 when 30% scour was simulated at pier 3. The experimental setup of the study had accelerometers located at two of the piers and the midspan of the bridge model, and 24.5% and 44.9% scour were observed. Compared

with the healthy case, mean-normalized mode shape increased at the scoured pier while it decreased in the other piers. Their work eliminated the need for knowledge of vehicle excitation forces, material, and geometrical information of the bridge. However, when multiple piers had scour at the same time, the approach was not successful. Another numerical study by [31] showed that the permittivity and porosity of the soil increased when scour was present. The sensors were installed along four-meter-long scour probes in the experimental setup. One probe was for measuring the total scour at one pier while the other one was measuring constriction scour at the middle of the channel. A length of 30 cm scour was measured by the probe in the middle of the channel after a peak flood. When the empirical scour formulas and the experimental scour depth were compared, overestimation of formulas was revealed. Additionally, if the scour hole was not uniform or located at a very specific point, they suggested that sensor response and the effects of suspended sediments on the values of dielectric permittivity should be examined in a laboratory. In the research of [53], a 30% reduction in the values of the first three natural frequencies was observed compared to the scoured case. The renewable energy sources of the monitoring devices (wind, heat, electromagnetic field, and light) were a virtue of this study. However, the approach was only validated for particular structural types.

Furthermore, [54] showed that vertical mode shapes were not sensitive to scour, and increasing pile heights resulted in a decrease in flexural stiffness and horizontally-displaced mode frequencies for four scour cases relative to the healthy case. The experimental model had 11 uniformly distributed unidirectional Integrated Electronics Piezoelectric accelerometers. The authors concluded that in theory, the modal curvature changes and bending deflections could be used to detect scour because of their low sensitivity to the irregularity of the obtained mode shapes. However, the method was not reliable enough to locate the scour in practice. [23] found that 25% and 45% of scour decreased the stiffness of the foundation at the central and the right-side piers and reduced mode amplitudes locally and globally. Additionally, the average change in the central pier was 7.2% and 16.8%, respectively. They used seven re-deployable accelerometers: four at the midspan and three at the piers in their laboratory test setup. They found reductions in the mode amplitudes at pier locations and an increase in the amplitudes of non-scoured piers. As foundation stiffness decreased, the difference in the root means square between healthy and scoured modes increased linearly. Their study did not require previous information about the structural behavior and used only two sensors that were sequentially moved along a bridge to detect mode shapes. However, the study was limited to one-dimensional models and simplified experiments. [45] managed to locate and measure scour by adopting the UWFBG technique that was able to sense changes in the wavelength of 0.05–0.06 nm. This change is related to strain changes of the fibers using an empirical formula. The effects of water buoyancy and loosening sand on signals were easily excluded. A value of 0.002 for the standard deviation indicated scour and the accuracy was $\pm$ 2.5 cm. Instability index developed by [44] was able to rapidly evaluate bridge safety conditions. A caisson-type experiment with 10 sensors was performed. These sensors were located at the center of every deck panel and the cap beam of a pier, as well as 14 velocity sensors for the pile group. Pier 1 was always in a state of instability. Before the pile started to incline too much, the instability index changed significantly relative to its original state. Their study could be used as an early warning system but was limited to the specific types of foundations tested, i.e., caissons.

Moreover, [48] and [49] calculated scour height, i.e., the exposed length of the rod calculated via a time history analysis in the frequency domain voltage induced by the hydrodynamic effect. Sensors were tested in the sand surrounding each pier, in a laboratory. They observed that as exposed length increased, natural frequencies diminished. The measurements could last throughout the scour duration, and the sensors had a low cost. To improve the accuracy, [48] emphasized the need for full-scale tests and [49] pointed out the requirements for more realistic simulations in a flume. Later research by [50] compared measured and observed scour depths and showed that the sensor results were

accurate. At the same time, they revealed difficulties in the implementation of sensors in real-life applications, and the debris effect could be a challenge for the proposed system. Magnetic field-based algorithms were developed for locating and tracking smart rocks moving around scour holes by [51] and [55]. [51] conducted two smart rocks—one direction-unknown and one direction-known at a bridge pier (upstream). Tracing the vertical displacements of the smart rock and monitoring the process of the peak scour depth was possible. Compared to former studies, higher accuracy, validation that considered a geomagnetic field, and calibration tests were supplied. Nevertheless, the measurement error was enhanced because of the instability of the direction-known rock during the field test. The reason was due to the effects of changing ambient magnetic field, caused by environmental factors. Picking the measurement points and stations (to locate the smart rock) close to the pier was suggested to diminish errors because the location had an intense magnetic field due to steel reinforcement. In the study of [55], real-time monitoring was performed for more accurate results. Before implementing the smart rock, magnetic field and coordinates were measured by an Unmanned Aerial Vehicle. The Unmanned Aerial Vehicle could detect the location with an error of less than 36 cm (verified by total station measurements). In the study of [52], different permittivity values corresponded to pre- and post-scour conditions. To test the application, six instrumented probes were installed in the bed segment and fixed on the flume floor. As scour developed, sensors' permittivity increased. The higher apparent permittivity is believed to be related to the reduced soil density of the re-deposited sediment around the sensor. It was an economical, realistic, and real-time monitoring method, but was not efficient in saline water.

Overall, a lot of direct monitoring-based scour detection studies were focused on developing monitoring systems such as smart rocks, piezoelectric rod sensors, image-recognizing micro cameras, or smart probes instrumented with electromagnetic sensors. Sensor-based studies were advantageous since they provide direct information on scour depth. Some researchers compared their results with empirical scour formulas and showed that the formulas overestimated scour, which made the proposed sensors more economical solutions. Despite being more economical alternatives to traditional monitoring devices, a couple of issues narrowed down the application fields of newly developed sensors. The implementation of the developed sensors was problematic; some devices could not be used after a major flood or regular maintenance was required. This might prevent the device from being an economical solution in the long-term. Durability problems might be overcome by improving the mechanical properties of the materials used to build the sensor. Another issue was that some devices were proven not to be effective in taking accurate measurements. The studies using the latest technology like unmanned aerial vehicles equipped with three-axis high-resolution GPS units were promising. However, the location errors need to be reduced. Developed sensors should be tested in the field to provide more robust information about their outcomes.

Indirect Monitoring-Based Studies

This section includes only indirect-monitoring-based studies listed in Table 1. Vehicle/bridge dynamic interaction models were used to test the drive-by or indirect monitoring concept. Vehicles were generally modeled as half or quarter cars, representing one or two axles of a vehicle. The quarter car was particularly unrealistic but its simplicity had value in that it kept the focus on the bridge structure and did not require assumptions on axle spacing and other vehicle properties. It should be noted that the half-car was also simplistic but did serve to introduce some inter-axle effects that have a significant influence.

The studies addressed in the scope of this section processed the acceleration signals due to multiple train passes. [56] used a dynamic model that considered vehicle bridge interactions; a quarter car model of the train and two simple supported bridges with a shared pier. Zero mean base wavelet was chosen as "Mexican Hat" and a set of wavelets were derived from this base by modifying it with position and scale parameters. Coefficients are results of continuous wavelet transformation and these relate the analyzing wavelet

with the specific region in the signal—they give signs of specific frequencies that are valid in the signal for a given time point. The existence of scour was proven by finding the difference in wavelet coefficients between healthy and scoured cases. The dynamic model of [19] consisted of a simple vehicle and a simple supported Euler-Bernoulli beam representing the bridge. Acceleration of the vehicle was obtained using equations of motion and Hilbert transform was applied to accelerations to find bridge mode shapes that were already known to be sensitive to the damping of the structure. [19] investigated the effect of damping on the mode shape and degree and rearranged the formula that calculates mode shape squares using the amplitude of the Hilbert transform. The difference between scoured and healthy cases' mode shapes was the scour indicator. The researchers also verified their algorithm numerically with two laboratory experiments. [37] and [57] also used wavelet coefficients. The dynamic model of [37] first analyzed the vehicle and then computed beam local and global mass and stiffness matrices using finite element method. The forces were distributed to the degree of freedoms using shape functions which considered the location of the vehicle that changed every time step. The chosen base was Morlet wavelet. Scoured case was simulated in the model by reducing the stiffness of the bridge pier. For each of the 10, 20, and 30% of scour cases, 200 vehicle runs were generated in the dynamic model. Continuous wavelet transformation was applied to accelerations of both healthy and scoured cases and the differences of the coefficients indicated scour. [18] generated a vehicle–bridge–soil interaction model. The horizontal accelerations due to passing vehicle were recorded from the top of the pier. They extracted mode shapes out of acceleration measurements through an Eigen value analysis of a highway bridge. Three different levels of soil stiffness were considered to represent dense, medium-dense, and loose sand. For all types of soil, lateral frequencies were calculated for zero and 10-m scour.

The results of the study by [63] showed that bogie accelerations decreased due to a 30% scour case. Identifying a scoured pier was possible by using the difference between the wavelet coefficients of the scoured case and the healthy case. Vehicle properties such as mass and speed were considered stable. [37] detected and located scour by showing the difference between the wavelet coefficients of the scoured case and the healthy case. Vehicle signals were generated by an external numerical party. Batches of 20, 50, 100, and 200 vehicle crossings were tested for comprehending the reaction of the method. However, in a low number of batches, false-positive scour indications were seen to increase. [57] measured instant accelerations at every support and the mean value was obtained and converted into the frequency–spatial domain using 1000 vehicle passages, and operating deflection shapes were evaluated for 25 and 45% scour cases. [19] extracted mode shapes from drive-by data, using the Hilbert transform. In their experimental setup, one of eight accelerometers was located on the vehicle and seven were fixed to the bridge to gather modal parameters. Foundation scour was able to be identified only for the fifth bridge mode shape. They noted that high vehicle speed decreased the accuracy of the mode shape. Near the damage location, the damage index reached a maximum value. Nevertheless, an edge effect limited the ability to find the exact location with this approach. The effects of operational and environmental parameters were not in their scope. Finally, taking the arithmetical average of multiple runs was suggested. [18] investigated the response of lateral acceleration at the top level of a pier and a 40% frequency change was obtained due to scour. The results were only validated for the two-axle truck case.

Overall, all the studies successfully detected scour by processing acceleration signals from batches of vehicle passes. Since the results of continuous wavelet transformation were in both spatial and frequency domains, locating scour and having detailed structural modal information was possible. Both wavelet transformation and operating deflection shapes methods were proven to be more reliable in locating the scour than modal analyses. It should be highlighted that when working with the continuous wavelet transformation, a low number of vehicles per batch leads to an increase in the false-positive scour indications. Generally, these types of research required fewer sensors, had a lower power requirement compared to direct monitoring, and did not require underwater inspections. These features

make this type of monitoring more economical than the direct type. The possibility of monitoring the bridge under regular service conditions without special monitoring devices and causing no service interruptions were additional advantages. All these properties suggest that indirect monitoring is a highly promising approach for scour investigations of bridges. Having more field tests will help verify studies with real-life applications. Studies can be expanded by considering variable vehicle properties such as speed and mass, different types of vehicles, and sensitivities to environmental conditions, and performing more detailed numerical analyses.

2.1.2. Cluster 2—Machine Learning-Based Research

This section briefly introduces commonly used machine learning algorithms. The introduction is followed by detailed information about the research noted in Table 3; characteristics of the input data used for training or validating, main and assisting algorithms used, and the scour property sought. Studies were mainly focused on estimation of the scour depth around the piers using machine learning algorithms. The characteristics of black-box models and their prediction capabilities enabled machine learning algorithms very handy tools for scour –damage formed by various parameters which require detailed investigations. Introducing the basics of some of the commonly-used machine learning algorithms and the optimization algorithms for hyperparameter selection might ease understanding the studies given in this section.

Before training the main algorithm, the majority of the machine learning algorithms specify a group of hyperparameters, whose determination could remarkably affect the efficiency of the resultant model [69]. Optimization algorithms are also used for assisting the search for the value of a parameter that is involved in two different predictions/calculations for the same structure or for searching the optimal hidden neuron number. Gradient-based and heuristic methods are two main structural optimization techniques [70]; in gradient-based ones, the direction of the search, i.e., the gradient, has to be described before seeking the best solution. However, gradient-based approaches might get stuck the in local optimum before they access the global optimum, execute insufficient in coping with the structures with nonlinear, hidden, and impermanent constraints, and a few of them include detailed optimization constraints [71,72]. Therefore, for overcoming such limitations in complex problems, heuristic methods were introduced. By solving actual problems of life simply, quickly, and in an applicable and efficient way, the utilization, requirement, and prestige of heuristic techniques have quickly boosted [70]. Some of the well-known heuristic optimization methods applied to civil engineering problems are the genetic algorithm, ant colony algorithm, particle swarm optimization, and simulated annealing [73]. First, because of being simple and easy to work with and having minimum requirements, genetic algorithms have been preferred extensively to solve numerous problems by imitating basic rules of evolution and natural genetic science [74]. These algorithms can solve the problem quickly and are handy for extensive problems, nevertheless there is no guarantee for the best solution in the end of the analysis [75]. Secondly, art colony algorithms are the most frequently utilized to solve NP-hard problems: for these kinds of problems, well-known algorithms assuring to detect an optimal result contain worst case scenario case convolution [76]. Art colony algorithms are used to optimize construction time and cost [77], task scheduling [78], and design problems [79]. Furthermore, in particle swarm optimization, the current location of every particle is updated by a vector of velocity, according to the social attitudes of individuals; when the swarm readjusts itself to the ambient by reappearing in the advantageous areas that were explored before [80].

An artificial neural network includes a couple of units of neurons (or layers, joints), one to three inexplicit (hidden) neuron layers, and a last unit of resultant neurons [81]. These algorithms do not need to go through lots of statistical training; however, they have some limitations such as a high volume of network training calculation, and the necessity of a preprocess for independent variables or predictor [82]. Still, they can help reduce the uncertainties of the problem. They eliminate the need for a clear description of the

physical links between bridge scour and numerous affects and they provide better results than empirical formulations owing to small errors and correlation coefficients [22]. Back propagation neural network is defined as a method that regularly modifies the weights of the connections of the network to make the difference between the absolute output vector and requested output vector minimum [83]. It is a monitor-learning technique which uses gradient descent and multivariate linear regression for recognition of change with the weight of connection in the network [84]. In many studies that adopted back propagation neural network, the accuracy levels of empirical scour formulas were increased [85]. Multivariate linear regression seeks for the relationship between the variable to be analyzed and its independent variables, and applied for prediction purposes [86]. Trial-error method [87] and beetle antennae search [87,88] are generally preferred when the hyperparameters of back propagation neural network models are tuned. Support Vector Machines by Vladimir Vapnik navigate input vectors from primary feature space to a feature space which is multi-dimensional via a Kernel function [89]. Support Vector Machines were derived from statistical learning theory and are considerably new and encourage learning to sort functions to recognize the pattern or to operate an evaluation for a function within a regression problem [90]. Variations of cross-validation such as Leave One Out and k-Fold, Xi-Alpha bound, generalized comparative Generalized Kullback–Liebler Distance, approximate span bound, and Radius-margin bounds are some of the successful performance measures to pick hyperparameters of a Support Vector Machine model; except for Vapnik Chervonenkis (VC) bound, which failed to provide and efficiently estimate the parameters [91]. Support Vector Machines can deal with various feature spaces and can categorize the data with no structure or semi-structure (i.e., image and texts) very well; nevertheless, they require high computation of complicated data, are bad at processing noisy input, and comprehending the resulting model, the effect, and weights of the variables is not easy [82]. Compared with the conventional algorithms based on gradient, extreme learning machines learn more quickly and eliminate some challenges of stating a criterion to stop, rate of learning, duration of learning, and local minima [88]. Their fundamental benefit is reducing the volume of calculation, which is particularly related to working with the templates within a high dimensional space [89]. Differential evolution algorithms [92], statistical learning theory [93], and particle swarm optimization [94] are proven to be effective in optimizing hyperparameters of the extreme learning machines. Gradient tree boosting aims to find a link which is capable of navigating the input to output to minimize the difference between the loss function for the pre-defined and anticipated value [95]. Although the process is time-consuming, Bayesian hyperparameter optimization is a method to set the parameters of a gradient tree boosting model and grid search; while GPU acceleration provided more speed in the selection process [96]. Another algorithm providing successful applications for scour estimation [97,98] is group method of data handling, a procedure which organizes itself through models created step-by-step, based on their performance assessment on a group of multi-input–single-output data couples [99]. Grid search is one of the most common methods to set parameters of group method of data handling models. [100–102]. Finally, ANFIS is a composite neuro-fuzzy system [103] and is the combination of neural networks and fuzzy logic methods; internal parameters are learnt off-line, such as neural network does and acts fuzzy logic system when it is operated [104]. Grasshopper optimization algorithm [105] and cultural algorithm [106] are utilized to set parameters of ANFIS models.

Table 3. Properties of Machine Learning studies—Cluster 2.

Study Reference	Quantity of Data	Training/Validation Percentages	Base Algorithm	Assisting Approach/Algorithm	Compared Algorithms/Existing Formulas	Most Significant Parameters Considered	Target
[107]	Not provided	Not provided	Convolutional Neural Network	Not provided	Empirical Formulas: - 65-1, 65-2 of China - Melville-Sheppard -MBW - HEC-18	Velocity of flow Depth of water Diameter of the sediment Pier width	Local scour depths around piers
[108]	11 sets of field and laboratory data (scour depth measurement-bathymetric data measured with point laser sensors)		Multiple linear regression method	The cost function for determination of the accuracy of the model			
[109]	99 examples of relative scour depths of a 0.7 m deep flume		Kstar model with five hybrid algorithms: - Weighted Instance Handler Wrapper-Kstar	Pearson correlation coefficient (to pick the most relevant input parameters)	Empirical equations of Dey and Barbhuiya, [6] and Muzammil [7].	Relative Flow Depth Excess Abutment Froude number Relative Sediment Size Relative Submergence	Relative scour depth around abutments
[110]	122 laboratory datasets of scour depths. An experiment in a sand bed flume and measured with a vertical point gauge.	70% Training 30% Validation	Reduced Error Pruning Tree base classifier	- Mean Absolute Error - Root Mean Squared Error - R (Correlation Coefficient) - Taylor diagram (For fitting and performance optimization)	- Artificial Neural Networks - Support Vector Machine - M5P - Reduced Error Pruning Tree algorithms and 2 empirical formulas of the Florida Department of Transportation and Hydraulic Engineering Circular No. 18 (HEC-18).	Pile cap width Thickness Column width	Local scour depth at complex piers
[111]	476 field pier scour depth measurements for 4 different geometric shapes of piers.	80% Training 20% Testing	- The Extreme Learning Machines regression method - The self-adaptive version of Differential Evolution	- Root Mean Squared Error - Mean Absolute Relative Error - Support Vector Machine - Artificial Neural Networks	Not provided	Pier dimensions Sediment mean diameter	Scour depth around piers
[112]	321 experimental datasets of flumes, scour depths measured with a point gauge	75% Training 25% Testing	Extreme Learning Machines	Different sets of input combinations were used to find the most effective variables.	- Support Vector Machine - Artificial Neural Networks	Critical and avarage flow velocity Flow depth Median diameter of particles Pile diameter Number of piles normal to the flow Distance between adjacent piles in line with the flow	Scour depth around piers
[113]	476 field pier scour depth measurements	80% Training 20% Testing	Extreme Learning Machines	Dimensional analysis to detect effective dimensionless parameters	Existing regression based models Richardson & Davis [114] Johnson [115] Shen [116] Laursen and Toch [13]	Ratio of pier width to flow depth Ratio of pier length to flow depth	
[117]	104 sets of experiments to measure scour depths with an electronic total station device	Not provided	- Gradient Tree Boosting - Group Method of Data Handling technique.	Coefficient of Determination as to the performance index	Support Vector Machine ANFIS Particle Swarm Optimization-Based Support Vector Machine.	For clear water scour: Sediment size and quantity Velocity Flow time	The scour depth of circular, rectangular round-nosed, and sharp-nosed piers

Table 3. *Cont.*

Study Reference	Quantity of Data	Training/Validation Percentages	Base Algorithm	Assisting Approach/Algorithm	Compared Algorithms/Existing Formulas	Most Significant Parameters Considered	Target
[118]	237 pier scour depth measurement datasets taken with echo sounder	Not provided	Evolutionary Radial Basis Function Neural Network model = Radial Basis Function Neural Network and Artificial Bee Colony	Not provided	Genetic Programming Back-propagation neural network Regression Tree Support Vector Machine - HEC18 -Mississippi's method Van Wilson [119] Laursen and Toch [13] Froehlich [120]	Pier shape factor Pier width Skew of the pier to approach the flow Velocity of the flow Depth of flow Grain Size of The Bed Material (d_{50}) Gradation of bed material	Scour depth
[121]	170 data samples of clear-water scour depths	Not provided	Support Vector Regression-based model	Filter and wrapper feature selection strategies (for performance improvement)	HEC18 Richardson & Davis [114] Melville & Coleman [122] Ataie-Ashtiani [123]	Under three groups: Pier geometry Flow property Material characteristic of the riverbed	Local scour around complex piers
[124]	403 sets of upstream and 61 sets of field downstream scour depth measurements	80% Training 20% Validation	Nondominated Sorting Genetic Algorithm	Support Vector Machine for increasing the pool of field data	HEC18 Froehlich [120] Gene expression programming model	Pier width Approaching flow depth Median grain size, Sediment gradation coefficient Gradation of bed material	Critical scour depth
[85]	232 field data	66% Training 34% Testing	Deep Neural Network	Back-Propagation Neural Network	Froehlich Equation [120] Froehlich Design HEC-18 HEC-18/Mueller Equation (1996) Back-Propagation Neural Network	- Not provided	Local scour around bridge piers
[125]	175 experimental datasets for scour depth	Not provided	Sequential quadratic programming optimization Least Square Support Vector Machine	Sequential quadratic programming to seek the optimal coefficients	- HEC18 - Melville and Coleman [122] - Ataie-Ashtiani [123]	Flow direction Pile-cap width Covering soil height Pier length Critical velocity of sediment movement Flow velocity Median grain size Flow depth River bed material Standard deviation	Scour depth of a Bridge with a complex pier

One of the most important features of the studies is the characteristics of the data such as the quality, source, and properties. Details of the input data of the studies in Table 3 were noted here. [107] only noted that the training data source was both field and laboratory measurements without providing further details. They also indicated that the verification data belonged to Hangzhou Bay Bridge in China. The input data for the model training and validation of [108] was scour depth measurements of bridge piers. Data were gathered from the two following sources: the field data were collected from three bridges in China—Mingchu, Silo, and Houfeng bridges; while the second source was laboratory experiments—two sets of laboratory tests were obtained from J. Sterling Jones Water Conservancy Laboratory of Turner-Fairbank Highway Research Center and the Colorado State University. Additional laboratory tests were also used from related studies. In the end, they obtained a total of 12 sets of measurements. Four sets of parameters were used for training the model. These parameters (data labels) included flow velocity, water depth, sediment size, and pier width. Relative scour depth data that [109] used was obtained from flume experiments. At the technology institute of India, 295 runs were performed in the hydraulic laboratory for three different abutment shapes. The dimensions of the flume were 20m (longitudinal), 0.7m (depth), and 0.9m (width). [110] obtained experimental local scour depth measurements of complex piers from National Hydraulic

Research Institute of Malaysia and Sharif University of Technology in Iran. The laboratory models scaled existing bridges of Malesia. The tests were performed under clean water conditions on various complex piers with different geometric parameters such as plan dimensions of the pier and the piles, water depth, distance of the pile to the edge of the pile cap, flow direction, the distance between piles, and pile cap elevation [126]. Experimental setups were such adjusted that the effects of flow depth, sediment size, and contraction on piers were eliminated. Data sources of [111] were from field measurements of 14 distinct bridges in Canada, Pakistan, and India. Four different data labels were available—sharp, round, cylindrical, and square-shaped bridge piers' scour depth measurements. There were also sub-labels of this scour depth data—narrow, wide, and intermediate-sized piers' measurements. Finally, the sub-labels were grouped under five dimensionless categories of scour depth to flow depth ratio, Froude number, median diameter to flow depth ratio, pier length to flow depth ratio, standard deviation of bed size grain diameter, and pier diameter to flow depth ratio. Later in another study, [112] collected the input data from three different studies. Two of the studies performed the experiments in a four-meter-long flume and controlled the mean sediment size (0.98 mm) and pipe diameters (0.016m). The measurements were taken for various pile plan layouts (1:2, 4:1 etc.). The third study of data resource used a smaller sediment size (0.80 mm) and pipe diameters (0.06m and 0.041m) but a longer flume (46m). In another study, [109] used the same data as they used in 2017 [113].

Moreover, the data set of [117] included both scour conditions of clear-water and live-bed. The effect of the independent parameters flow depth, velocity of approach, duration of flow, median sediment size was investigated on predicting scour. There were also four different data labels of sharp-nosed, round-nosed, rectangular, and circular piers' scour depth measurements. [118] adopted field scour depth measurements gathered from 79 sites in 17 states of USA for prediction of equilibrium scour depth. They excluded scour in group-type bridges and cohesive bed material, moderate, and substantial debris effects. The parameters considered were the width and the shape factor of the pier, skew of the pier to approach flow, size of the grain in the bed, gradation of bed material, and depth and velocity of the flow. [121] used laboratory data which includes four datasets from the Hydrotech Research Institute of National Taiwan University. Complex pier foundation scour measurements were taken in a sand bed. Parameters considered were soil-covering height, median grain size, standard deviation of river bed material, radio of the mean velocity of the sediment to the critical velocity, flow depth, pier width which is perpendicular to the flow direction, the width of the pile cap, and pile cap-pier face to face distance. [124] combined two sets of field data—from bridge scour data management system (BSDMS) and FHWA documentation by USGS. Departing from the information of different direction of vortices (and therefore scour developments) in upstream and downstream, their first data label was location. Velocity and flow depth of approach, median grain size, gradation of sediment, and scour depth were other data labels. To improve the overall quality of the input, data with missing location or other properties listed above were excluded. [85] picked 232 upstream scour length measurements from another study [127] that collected scour observations in 79 different rivers several states of USA. Data included skew of the pier to approach flow, pier shape factor, pier dimensions, flow velocity and depth, grain size, and gradation of bed material. Only raw data were used to obtain a better performance. In testing the dataset, root mean square values of both neural networks in the scope of the research were compared to obtain the ideal values for various parameters defined by user.

In terms of the accuracy level of predictions made, [107] and [108] stated that their predictions are in good agreement with the measurements, with only one dataset outside the 50% error line. They stated that their approach was more effective in terms of accuracy when compared to empirical formulas such as M/S, MBW, HEC-18, 65-1, and 65-2. According to their sensitivity analysis, [108] stated that the most effective parameter in predicting scour was pier width. They also suggested an increase in the quantity of training data

to predict scour depths more accurately. [109] investigated scour occurrence for different shapes of the abutment. They noted that, for all shapes of the abutment, the most effective parameter was the Excess Abutment Froude number (Fe). Moreover, for vertical-wall-shaped abutments, the most effective parameter combination contained Excess Abutment Froude number, relative sediment size (d_{50}/l, where "d_{50}" is the sediment size and "l" is the dimension of the abutment which is perpendicular to the flow), and relative flow depth (h/l). Finally, for semicircular and 45° wing shape abutments, the combination of Excess Abutment Froude number and relative sediment size was the most effective parameter combination in scour prediction. The weighted instance handler wrapper-Kstar for vertical-wall abutments, random committee-Kstar for semicircular walls, and 45° wing wall were the best algorithms among five novel hybrid algorithms studied. Their algorithms outperformed the empirical formulas of Dey and Barbhuiya [6] and Muzzammil [7]. The hybrid approach of [107], based on a random subspace meta classifier, resulted in the pile cap level being the most sensitive factor in the prediction of complex piers' local scour depths. The reduced error pruning tree base classifier resulted in similar root mean square errors to artificial neural networks, support vector machines, and M5P. The predictions obtained through reduced error pruning tree and other machine learning algorithms were significantly better than the scour depths computed with the empirical models of FDOT and HEC-18. Both [109] and [110] were able to increase the prediction power of standalone algorithms with the hybrid algorithms they proposed. [111] proposed a self-adaptive evolutionary extreme learning machine to predict scour around bridge piers. They indicated that the ratio of the median diameter of particle size to flow depth, the ratio of pier length to flow depth, and the ratio of pier width to flow depth were the most effective parameters. Self-adaptive evolutionary extreme learning machines outperformed artificial neural networks and support vector machines. In 2018, [112] proposed 25 models to predict scour around coastal and hydraulic pile groups. The extreme learning machine model generated had the most optimal input parameter combination and provided better results than the artificial neural networks and support vector machines considered. They also identified that pier diameter affected the predictions the most. Later in 2019, it was shown that extreme learning machines were one of the most effective heuristic optimization algorithms for non-linear systems [113]. The sensitivity analysis included 31 models with different input combinations [113]. Their approach outperformed the empirical equations of Richardson and Davis [114], Johnson [115], Shen [116], and Laursen and Toch [13]. They recommended that the proposed methodology be improved by utilizing other artificial intelligence methods such as gene expression programming, and the group method of data handling.

Furthermore, [117] generated a model based on gradient tree boosting to predict scour depth around piers with different geometries: rectangular, circular, sharp-nosed, and round-nosed. In conclusion, gradient tree boosting was more accurate and effective than the group method of data handling for all shapes. It was noted that the model worked best with the rectangular form. [118] proposed a model using an evolutionary radial basis function neural network and it outperformed not only empirical HEC-18, Mississippi's, Laursen and Toch's (1956), and Froehlich's methods, but also other algorithms being compared (back-propagation neural network, genetic programming, M5 regression tree, and support vector machine). They suggested future studies consider the efficiency, duration required for computation, stability of artificial intelligence methods, and techniques in between complements. In their research based on support vector regression, [121] obtained better predictions when support vector regressions are used together with algorithms for selecting features. The variable neighborhood search algorithm had the best performance when compared with sequential forward selection and sequential backward selection for parameter selection. The proposed method also made more accurate scour depth predictions compared to HEC18, Melville and Coleman [122], and Ataie-Ashtiani [123]. They recommended a future study of the support vector regression and other Kernel Functions together. Nondominated sorting genetic algorithm-based method of [124] outperformed

both hydraulic engineering circular no. 18 and Froehlich equations and gene expression programming. The authors highlighted that their approach was as simple as empirical formulas. They noted that the failure rates should be decreased. They also suggested modifying the function and picking field data and other independent parameter combinations more explicitly. [85] found out that ignoring randomly selected neurons (dropout layers) on deep neural networks could not level up accuracy level significantly. When the prediction values were compared with the measurements, it was seen that both deep neural networks and back-propagation neural networks performed equally well in predicting the scour depth. Additionally, predictions of deep neural networks outperformed four empirical formulas listed in Table 3; root mean square errors were 2-4 times better. [125] proposed an algorithm of sequential quadratic programming optimization and managed to increase the accuracy of the existing formulas of HEC18, Melville and Coleman [122], and Ataie-Ashtiani [123] up to 2–4 times.

Overall, the majority of the data used in the studies reviewed under the machine learning-based cluster were used for training (to feed machine learning algorithms) and the rest was kept for validation. Selecting the training data correctly by pre-processing before applying the algorithm-based models helped the models approach accurate predictions more quickly. The studies provided root mean squared error, mean square error, coefficient of determination (R2), or cumulative sums of orthogonal distance indexes to compare their approaches with frequently used machine learning algorithms and/or empirical scour formulas. The main objective was to generate a new model which provides more robust scour depths than empirical scour formulas and/or some frequently used machine learning algorithms. These models adopt one or more (hybrid) algorithms and heuristic parameter selection algorithms for better predictions and computation time. [74] stated that the usage, demand, and reliability of heuristic techniques have quickly boosted their use because these solve actual problems of life simply, quickly, efficiently, and in an applicable way. Of the studies summarized here in this review, it can be seen that those with sensitivity analysis, i.e., following an optimization method for hyperparameter selection, resulted in faster and more accurate predictions of scour depth. Particle swarm optimization and artificial bee colony were two of the methods used in the studies presented here. With such optimization methods, it was easier to identify the most effective parameter or combination of parameters influencing the prediction. One should highlight that this parameter was not fixed: studies resulted in different conclusions about "the most effective parameter" because their training data, i.e., input was different from each other. Since all the studies claimed to make better predictions than empirical formulas, a comparison in terms of outperforming frequently used, (i.e., reference) algorithms can be meaningful. Specifically, the researchers adopting extreme learning machines, gradient tree boosting, radial basis function neural networks, and reduced error pruning tree algorithms, were successful in performing better than reference algorithms such as artificial neural networks and support vector machines.

2.2. Synthesis of the Results

This review consists of the detail investigation of 36 studies, represented in two clusters (one cluster contains both direct and indirect conventional monitoring-based studies) which were effective in detecting scour damage either by processing vehicle signals, signals directly gathered from the bridge, or estimating scour depth using machine learning algorithms. The synthesis of their results was provided below.

2.2.1. Cluster 1—Synthesis of Conventional Monitoring-Based Studies to Detect Scour

First, sensors used for direct monitoring have been improved with developing technology. The device types were not only limited to inclinometers and velocity sensors, but also micro cameras, wireless transmitters, fiber-optic sensors, and even Unmanned Aerial Vehicle-deployed smart rocks. Studies with alternative sensing mechanism sensors in this review processed the signals gathered via bed-level image recognition, instantaneous

frequencies, distribution of magnetic field, and porosity of the soil. Although these types of devices provided direct information, and real-time monitoring of scour and eliminated the need for underwater inspections, monitoring also involved some challenges. These were implementation difficulties and maintenance requirements that might be overcome through the better design of the devices. Additionally, debris and saline water were challenges in some cases. Direct monitoring-based studies which use traditional sensors such as accelerometers and global positioning system devices were able to detect the presence of scour through changes in frequency and mode shape. These occurred due to the decrement in the foundation stiffness, as a consequence of scour. Direct monitoring-based studies were advantageous since they did not require knowledge of vehicle forces, or detailed geometrical and mechanical information about the bridge. Alternatively, energy harvesting devices are being increasingly utilized as monitoring sensors. They can detect frequency changes and produce energy out of this vibration at the same time. They have clear advantages over regular accelerometers in terms of the source of the energy. However, there were limitations of loading sensitivities and possible errors in the presence of multiple scoured piers.

Second, it was possible to identify and locate different percentages of scour by processing the vehicle signals. In these studies, (i.e., indirect monitoring-based research) signals due to multiple vehicle passages were processed to obtain mode shapes or frequencies, or scour was indicated by the differences between operating deflection shapes or continuous wavelet transform coefficients between healthy and scoured cases. Mode shape ratio methods were used in many studies and were able to detect scour successfully. Very significant changes in the mode shape ratios were observed for the scoured stages. Yet, the sensitivities due to vehicle load and random errors due to the variability of the ambient loading are issues that needed to be resolved. Specifically, the mean normalized mode shape method of [63] was successful in detecting scour at a single pier. However, it was not an efficient solution when multiple piers were scoured at the same time. Investigating multiple scours of bridge piers through numerical methods could be a future study. Furthermore, frequency domain decomposition was a frequently applied method to process acceleration signals and can be applied to gather modal properties and frequencies of the bridge. Hilbert Huang transform was another signal analysis method proven to be efficient in decomposing acceleration signals to mode functions. However, due to the very short duration of the data segment, there is insufficient data. Scour detection based on mode shape methods appeared to be more robust. Some of the leading advantages of these indirect monitoring are the need for fewer sensors, eliminating the need for special monitoring devices, underwater examinations, and the occasional challenges of placing sensors. Furthermore, the service conditions of the infrastructure were not interrupted and the instrumenting vehicle was a more economical option than direct monitoring. On the other hand, the most common limitations were changing vehicle parameters (such as mass and speed) and the need for large numbers of vehicle runs.

It was highly recommended for all studies with numerical models and algorithms developed needed to be applied in full-scale bridge tests to be deemed fully effective. Another improvement for the studies could be upgrading the mathematical models to two- or three-dimensional ones. Both applying more field tests and replicating mathematical models could address the limitations of the studies to specific types of structures. The future studies then can be better and more clearly defined.

2.2.2. Cluster 2—Synthesis of Machine Learning-Based Studies

Machine Learning-based studies reviewed in the scope of this study aimed to find local or total scour around bridge piers or abutments. The models of the studies were trained with laboratory or field data. The newly proposed algorithms include convolutional neural network, multiple linear regression method, K-Star model, reduced error pruning tree base classifier, extreme learning machines, gradient tree boosting, group method of data handling, ERBNN model, support vector regression-based model, non-dominated sorting

genetic algorithm, Gaussian processes regression, relevance vector machines, deep neural network, and LS-support vector machine. The studies either compared their approach with other algorithms or with existing empirical formulas. The most frequently used reference algorithms for comparison with the newly proposed algorithms were artificial neural networks, support vector machine, gradient tree boosting, group method of data handling, and extreme learning machines. Most of the time, the proposed algorithms outperformed these well-known ones, which is the main target of designing new models. The reference empirical formulas were 65-1, 65-2, Melville-Sheppard, MBW, HEC-18, Laursen & Toch [13], and Froehlich [120], Mississippi's method Van Wilson [119], and Ataie-Ashtiani [123]. All the proposed algorithms performed better in predicting scour than the traditional equations mentioned above. The proposed models either improved the empirical formulas' accuracy levels (one study) or developed a model adapting one algorithm (four studies) or hybrid models (nine studies) for a more successful prediction of scour depth around the piers.

Some of the challenges faced were the need to decrease the duration of computation, picking the field data, and the combination of independent parameters more explicitly. It was usually stated in the discussions that more training data would improve the accuracy levels of the studies in future work. Another work to improve the accuracy level could be the contributions of different algorithms to the hybrid models. Improving the accuracy of the scour height estimations will result in more economical solutions by preventing overdesigns.

Author Contributions: Conceptualization, S.T., J.T. and E.O.; methodology, S.T.; software, not applied; validation, S.T., J.T., E.O. and J.C.M.; formal analysis, S.T.; investigation, S.T.; resources, S.T.; writing—original draft preparation, S.T.; writing—review and editing, E.O. and J.T.; visualization, S.T., supervision, J.T. and E.O.; project administration, not applied; funding acquisition, J.T., J.C.M. and E.O. All authors have read and agreed to the published version of the manuscript.

Funding: This research was funded by FCT (Portuguese national funding agency for science, research, and technology)/MCTES through national funds (PIDDAC) under the R&D Unit Institute for Sustainability and Innovation in Structural Engineering (ISISE), under reference UIDB/04029/2020 and trough the doctoral Grant 2021.06162.BD. This work has also been partly financed within the European Horizon 2020 Joint Technology Initiative Shift2Rail through contract no. 101012456 (IN2TRACK3).

Conflicts of Interest: The authors declare no conflict of interest.

References

1. Zhao, M. A Review on Recent Development of Numerical Modelling of Local Scour around Hydraulic and Marine Structures. *J. Mar. Sci. Eng.* **2022**, *10*, 1139. [CrossRef]
2. Bihs, H.; Olsen, N.R.B. Numerical modeling of abutment scour with the focus on the incipient motion on sloping beds. *J. Hydraul. Eng.* **2011**, *137*, 1287–1292. [CrossRef]
3. Nordila, A.; Ali, T.; Faisal, A.; Badrunnisa, Y. Local scour at wide bridge Piers. *Int. J. Eng. Res. Technol. (IJERT)* **2014**, *3*, 742–754.
4. Guan, D.; Chiew, Y.M.; Wei, M.; Hsieh, S.C. Characterization of horseshoe vortex in a developing scour hole at a cylindrical bridge pier. *Int. J. Sediment Res.* **2019**, *34*, 118–124. [CrossRef]
5. Oliveto, G.; Hager, W.H. Temporal evolution of clear-water pier and abutment scour. *J. Hydraul. Eng.* **2002**, *128*, 811–820. [CrossRef]
6. Dey, S.; Barbhuiya, A.K. Time variation of scour at abutments. *J. Hydraul. Eng.* **2005**, *131*, 11–23. [CrossRef]
7. Muzzammil, M. ANFIS approach to the scour depth prediction at a bridge abutment. *J. Hydroinform.* **2010**, *12*, 474–485. [CrossRef]
8. Campbell, K.E.; Ruffell, A.; Pringle, J.; Hughes, D.; Taylor, S.; Devlin, B. Bridge Foundation River Scour and Infill Characterisation Using Water-Penetrating Radar. *Remote Sens.* **2021**, *13*, 2542. [CrossRef]
9. Huber, E.; Anders, B.; Huggenberger, P. Quantifying scour depth in a straightened gravel-bed river with ground-penetrating radar. In Proceedings of the 17th International Conference on Ground Penetrating Radar (GPR) IEEE, Rapperswil, Switzerland, 18–21 June 2018; pp. 1–4.
10. Hou, S.; Jiao, D.; Dong, B.; Wang, H.; Wu, G. Underwater inspection of bridge substructures using sonar and deep convolutional network. *Adv. Eng. Inform.* **2022**, *52*, 101545. [CrossRef]
11. Raju, R.D.; Nagarajan, S.; Arockiasamy, M.; Castillo, S. Feasibility of Using Green Laser in Monitoring Local Scour around Bridge Pier. *Geomatics* **2022**, *2*, 355–369. [CrossRef]
12. Mutlu Sumer, B. Mathematical modeling of scour: A review. *J. Hydraul. Res.* **2007**, *45*, 723–735. [CrossRef]
13. Laursen, E.M.; Toch, A. *Scour around Bridge Piers and Abutments*; Ames, I.A., Ed.; Iowa Highway Research Board: Iowa City, IA, USA, 1956; Volume 4.

14. Kirkil, G.; Constantinescu, G.; Ettema, R. Detached eddy simulation investigation of turbulence at a circular pier with scour hole. *J. Hydraul. Eng.* **2009**, *135*, 888–901. [CrossRef]
15. Yagci, O.; Yildirim, I.; Celik, M.F.; Kitsikoudis, V.; Duran, Z.; Kirca, V.O. Clearwater scour around a finite array of cylinders. *Appl. Ocean Res.* **2017**, *68*, 114–129. [CrossRef]
16. Oben-Nyarko, K.; Ettema, R. Pier and abutment scour interaction. *J. Hydraul. Eng.* **2011**, *137*, 1598–1605. [CrossRef]
17. Malekjafarian, A.; Prendergast, L.J.; OBrien, E.J. Detecting bridge scour using mode shapes derived from time-domain data. In Proceedings of the Civil Engineering Research in Ireland 2018 (CERI2018) Conference, Dublin, Ireland, 29–30 August 2018.
18. Prendergast, L.J.; Hester, D.; Gavin, K. Determining the presence of scour around bridge foundations using vehicle-induced vibrations. *J. Bridge Eng.* **2016**, *21*, 04016065. [CrossRef]
19. Tan, C.; Zhao, H.; OBrien, E.J.; Uddin, N.; Fitzgerald, P.C.; McGetrick, P.J.; Kim, C.W. Extracting mode shapes from drive-by measurements to detect global and local damage in bridges. *Struct. Infrastruct. Eng.* **2020**, *17*, 1–8,11,13. [CrossRef]
20. Klinga, J.V.; Alipour, A. Assessment of structural integrity of bridges under extreme scour conditions. *Eng. Structures* **2015**, *82*, 55–71. [CrossRef]
21. Prendergast, L.J.; Gavin, K.; O'Sullivan, J.J. Non-intrusive bridge scour analysis technique using laboratory test apparatus. In Proceedings of the Bridge and Concrete Research in Ireland, Dublin, Ireland, 6–7 September 2012.
22. Ahmad, N.; Bihs, H.; Kamath, A.; Arntsen, Ø.A. Three-dimensional CFD modeling of wave scour around a side-by-side and triangular arrangement of piles with REEF3D. *Procedia Eng.* **2015**, *116*, 683–690. [CrossRef]
23. Khan, M.A.; McCrum, D.P.; Prendergast, L.J.; OBrien, E.J.; Fitzgerald, P.C.; Kim, C.W. Laboratory investigation of a bridge scour monitoring method using decentralized modal analysis. *Struct. Health Monit.* **2021**, *20*, 3327–3341. [CrossRef]
24. Kallias, A.N.; Imam, B. Probabilistic assessment of local scour in bridge piers under changing environmental conditions. *Struct. Infrastruct. Eng.* **2016**, *12*, 1228–1241. [CrossRef]
25. Muzzammil, M.; Alam, J.; Kumar, K.; Khalid, M. Reliability Analysis of a Complex Pier Against Local Scour. *J. Inst. Eng. Ser. A* **2022**, *103*, 1237–1245. [CrossRef]
26. Tubaldi, E.; Macorini, L.; Izzuddin, B.A.; Manes, C.; Laio, F. A framework for probabilistic assessment of clear-water scour around bridge piers. *Struct. Saf.* **2017**, *69*, 11–22. [CrossRef]
27. Jafari-Asl, J.; Ben Seghier, M.; Ohadi, S.; Dong, Y.; Plevris, V. A comparative study on the efficiency of reliability methods for the probabilistic analysis of local scour at a bridge pier in clay-sand-mixed sediments. *Modelling* **2021**, *2*, 63–77. [CrossRef]
28. Jonkman, S.N.; Steenbergen, R.D.J.M.; Morales-Napoles, O.; Vrouwenvelder, A.C.W.M.; Vrijling, J.K. *Probabilistic Design: Risk and Reliability Analysis in Civil Engineering*; Collegedictaat CIE4130; TU Delft, Department Hydraulic Engineering: Delft, The Netherlands, 2015; p. 103. Available online: http://resolver.tudelft.nl/uuid:e53b8dca-a0db-4433-b9f9-e190a507f99f (accessed on 22 January 2023).
29. Ley, C.; Martin, R.K.; Pareek, A.; Groll, A.; Seil, R.; Tischer, T. Machine learning and conventional statistics: Making sense of the differences. Knee Surgery, Sports Traumatology. *Arthroscopy* **2022**, *30*, 1–5.
30. Gattulli, V.; Lepidi, M.; Potenza, F. Dynamic testing and health monitoring of historic and modern civil structures in Italy. *Struct. Monit. Maint.* **2016**, *3*, 71–90. [CrossRef]
31. Prendergast, L.J.; Gavin, K. A review of bridge scour monitoring techniques. *J. Rock Mech. Geotech. Eng.* **2014**, *6*, 138–149. [CrossRef]
32. Maroni, A.; Tubaldi, E.; Ferguson, N.; Tarantino, A.; McDonald, H.; Zonta, D. Electromagnetic sensors for underwater scour monitoring. *Sensors* **2020**, *20*, 4096. [CrossRef] [PubMed]
33. Marr, J. *Bridge Scour Monitoring Technologies: Development of Evaluation and Selection Protocols for Application on River Bridges in Minnesota*; (No. MN/RC 2010-14); Minnesota. Dept. of Transportation, Research Services Section: Saint Paul, MN, USA, 2010.
34. Boujia, N.; Schmidt, F.; Chevalier, C.; Siegert, D.; Pham Van Bang, D. Using rocking frequencies of bridge piers for scour monitoring. *Struct. Eng. Int.* **2021**, *31*, 286–294. [CrossRef]
35. Purnomo, D.A.; Aspar, W.A.N.; Barasa, W.; Harjono, S.M.; Sukamdo, P.; Fiantika, T. Initial Implementation of Structural Health Monitoring System of a Railway Bridge. In *IOP Conference Series: Materials Science and Engineering*; IOP Publishing: Bristol, UK, 2021; Volume 1200, No. 1, p. 012019.
36. Van der Auweraer, H.; Peeters, B. Sensors and systems for structural health monitoring. *J. Struct. Control* **2003**, *10*, 117–125. [CrossRef]
37. Lynch, J.P. An overview of wireless structural health monitoring for civil structures. *Philos. Trans. R. Soc. A Math. Phys. Eng. Sci.* **2007**, *365*, 345–372. [CrossRef]
38. Fitzgerald, P.C.; Malekjafarian, A.; Cantero, D.; OBrien, E.J.; Prendergast, L.J. Drive-by scour monitoring of railway bridges using a wavelet-based approach. *Eng. Struct.* **2019**, *191*, 1–11. [CrossRef]
39. Chandrasekaran, S. Structural Health Monitoring. In *Structural Health Monitoring with Application to Offshore Structures*; Indian Institute of Technology Madras: Toh Tuck Link, Singapore, 2019; pp. 24–26. [CrossRef]
40. Martinez, D.; Malekjafarian, A.; OBrien, E. Bridge flexural rigidity calculation using measured drive-by deflections. *J. Civ. Struct. Health Monit.* **2020**, *10*, 833–844. [CrossRef]
41. Bernardini, L.; Carnevale, M.; Somaschini, C.; Matsuoka, K.; Collina, A. A Numerical Investigation of New Algorithms for The Drive-by Method in Railway Bridge Monitoring. In Proceedings of the EURODYN 2020, XI. International Conference on Structural Dynamics, Athens, Greece, 23–26 November 2020; pp. 1033–1043.

42. Malekjafarian, A.; Prendergast, L.J.; OBrien, E. Use of mode shape ratios for pier scour monitoring in two-span integral bridges under changing environmental conditions. *Can. J. Civ. Eng.* **2020**, *47*, 962–973. [CrossRef]
43. Fitzgerald, P.C.; Malekjafarian, A.; Bhowmik, B.; Prendergast, L.J.; Cahill, P.; Kim, C.W.; OBrien, E.J. Scour damage detection and structural health monitoring of a laboratory-scaled bridge using a vibration energy harvesting device. *Sensors* **2019**, *19*, 2572. [CrossRef] [PubMed]
44. Lin, T.K.; Chang, Y.S. Development of a real-time scour monitoring system for bridge safety evaluation. *Mech. Syst. Signal Process.* **2017**, *82*, 503–518. [CrossRef]
45. Liu, W.; Zhou, W.; Li, H. Bridge scour estimation using unconstrained distributed fiber optic sensors. *J. Civ. Struct. Health Monit.* **2022**, *12*, 775–784. [CrossRef]
46. Prendergast, L.J.; Gavin, K.; Hester, D. Isolating the location of scour-induced stiffness loss in bridges using local modal behavior. *J. Civ. Struct. Health Monit.* **2017**, *7*, 483–503. [CrossRef]
47. Malekjafarian, A.; Kim, C.W.; OBrien, E.J.; Prendergast, L.J.; Fitzgerald, P.C.; Nakajima, S. Experimental Demonstration of a Mode Shape-Based Scour-Monitoring Method for Multispan Bridges with Shallow Foundations. *J. Bridge Eng.* **2020**, *25*, 04020050. [CrossRef]
48. Funderburk, M.L.; Huang, S.K.; Loh, C.H.; Loh, K.J. Densely distributed and real-time scour hole monitoring using piezoelectric rod sensors. *Adv. Struct. Eng.* **2019**, *22*, 3395–3411. [CrossRef]
49. Azhari, F.; Tom, C.; Benassini, J.; Loh, K.J.; Bombardelli, F.A. Design and characterization of a piezoelectric sensor for monitoring scour hole evolution. *Sens. Smart Struct. Technol. Civ. Mech. Aerosp. Syst.* **2014**, *9061*, 301–309.
50. Azhari, F.; Loh, K.J. Laboratory validation of buried piezoelectric scour sensing rods. *Struct. Control Health Monit.* **2017**, *24*, e1969. [CrossRef]
51. Chen, Y.; Tang, F.; Li, Z.; Chen, G.; Tang, Y. Bridge scour monitoring using smart rocks based on magnetic field interference. *Smart Mater. Struct.* **2018**, *27*, 085012. [CrossRef]
52. Michalis, P.; Tarantino, A.; Tachtatzis, C.; Judd, M.D. Wireless monitoring of scour and re-deposited sediment evolution at bridge foundations based on soil electromagnetic properties. *Smart Mater. Struct.* **2015**, *24*, 125029. [CrossRef]
53. Hashimoto, K.; Shiotani, T.; Mitsuya, H.; Chang, K.C. MEMS Vibrational Power Generator for Bridge Slab and Pier Health Monitoring. *Appl. Sci.* **2020**, *10*, 8258. [CrossRef]
54. Elsaid, A.; Seracino, R. Rapid assessment of foundation scour using the dynamic features of the bridge superstructure. *Constr. Build. Mater.* **2014**, *50*, 42–49. [CrossRef]
55. Zhang, H.; Li, Z.; Reven, A.; Scharfenberg, B.; Chen, G.; Ou, J. UAV-Based Smart Rock Positioning for Determination of Bridge Scour Depth. In Proceedings of the 9th International Conference on Structural Health Monitoring of Intelligent Infrastructure (SHMII-9), St. Louis, MO, USA, 4–7 August 2019.
56. OBrien, E.J.; Malekjafarian, A.; Fitzgerald, P.C. Bridge Scour Detection using Vehicle Acceleration Measurements. In Proceedings of the Civil Engineering Research in Ireland 2018 Conference (CERI 2018), Dublin, Ireland, 29–30 August 2018.
57. OBrien, E.J.; McCrum, D.P.; Khan, M.A.; Prendergast, L.J. Wavelet-based operating deflection shapes for locating scour-related stiffness losses in multi-span bridges. *Struct. Infrastruct. Eng.* **2021**, *19*, 238–253. [CrossRef]
58. Chopra, A.K. *Dynamics of Structures*, 4th ed.; Prentice-Hall International Series; Civil Engineering and Engineering Mechanics: Delhi, India, 2007; pp. 428–441, 883–904.
59. Cerna, M.; Harvey, A.F. The Fundamentals of FFT-Based Signal Analysis and Measurement. In *Application Note 041*; National Instruments: Austin, TX, USA, 2000.
60. Feldman, M. Hilbert transform in vibration analysis. *Mech. Syst. Signal Process.* **2011**, *25*, 735–802. [CrossRef]
61. Brincker, R.; Zhang, L.; Andersen, P. Modal identification of output-only systems using frequency domain decomposition. *Smart Mater. Struct.* **2001**, *10*, 441. [CrossRef]
62. Le, T.P.; Paultre, P. Modal identification based on the time–frequency domain decomposition of unknown-input dynamic tests. *Int. J. Mech. Sci.* **2013**, *71*, 41–50. [CrossRef]
63. Grossmann, A.; Kronland-Martinet, R.; Morlet, J. Reading and understanding continuous wavelet transforms. In *Wavelets*; Springer: Berlin/Heidelberg, Germany, 1990; pp. 2–20.
64. Torrence, C.; Compo, G.P. A practical guide to wavelet analysis. *Bull. Am. Meteorol. Soc.* **1998**, *79*, 61–78. [CrossRef]
65. Gao, Y. *Structural Health Monitoring Strategies for Smart Sensor Networks, Microform Edition*; University of Illinois at Urbana-Champaig: Champaign, IL, USA, 2005.
66. Nagayama, T.; Spencer Jr, B.F.; Rice, J.A. Autonomous decentralized structural health monitoring using smart sensors. *Struct. Control Health Monit Off. J. Int. Assoc. Struct. Control Monit. Eur. Assoc. Control Struct.* **2009**, *16*, 842–859. [CrossRef]
67. Sim, S.H.; Spencer, B.F., Jr.; Zhang, M.; Xie, H. Automated decentralized modal analysis using smart sensors. *Struct. Control Health Monit.* **2010**, *17*, 872–894. [CrossRef]
68. Teolis, A.; Benedetto, J.J. *Computational Signal Processing with Wavelets*; Springer: Boston, MA, USA, 1998.
69. Claesen, M.; De Moor, B. Hyperparameter Search in Machine Learning. *arXiv* **2015**, arXiv:1502.02127.
70. Zanakis, S.H.; Evans, J.R. Heuristic "optimization": Why, when, and how to use it. *Interfaces* **1981**, *11*, 84–91. [CrossRef]
71. Aldwaik, M.; Adeli, H. Advances in optimization of highrise building structures. *Struct. Multidiscip. Optim.* **2014**, *50*, 899–919. [CrossRef]
72. Topping, B.H.V. Shape optimization of skeletal structures: A review. *J. Struct. Eng.* **1998**, *109*, 1933–1951. [CrossRef]

73. Cong, S.; Jia, Y.; Deng, K. Particle Swarm and Ant Colony Algorithms and Their Applications in Chinese Traveling Salesman Problem. In *New Achievements in Evolutionary Computation*; Korosec, P., Ed.; IntechOpen: Rijeka, Croatia, 2010; pp. 298–302.
74. Sivanandam, S.N.; Deepa, S.N. Genetic algorithm optimization problems. In *An Introduction to Genetic Algorithms*; Springer: Berlin/Heidelberg, Germany, 2008; pp. 165–209.
75. Hare, W.; Nutini, J.; Tesfamariam, S. A survey of non-gradient optimization methods in structural engineering. *Adv. Eng. Softw.* **2013**, *59*, 19–28. [CrossRef]
76. Dorigo, M.; Birattari, M.; Stutzle, T. Ant colony optimization. *IEEE Comput. Intell. Mag.* **2006**, *1*, 28–39. [CrossRef]
77. Ng, S.T.; Zhang, Y. Optimizing construction time and cost using an ant colony optimization approach. *J. Constr. Eng. Manag.* **2008**, *134*, 721–728. [CrossRef]
78. Christodoulou, S. Ant colony optimization in construction scheduling. In Proceedings of the International Conference on Computing in Civil Engineering, Cancun, Mexico, 12–15 July 2005; pp. 1–11.
79. Kaveh, A.; Talatahari, S. An improved ant colony optimization for constrained engineering design problems. *Eng. Comput.* **2010**, *27*, 155–182. [CrossRef]
80. Venter, G.; Sobieszczanski-Sobieski, J. Particle swarm optimization. *AIAA J.* **2003**, *41*, 1583–1589. [CrossRef]
81. Wang, S.C. Artificial neural network. In *Interdisciplinary Computing in Java Programming*; Springer: Boston, MA, USA, 2003; pp. 81–100.
82. Uddin, S.; Khan, A.; Hossain, M.E.; Moni, M.A. Comparing different supervised machine learning algorithms for disease prediction. *BMC Med. Inform. Decis. Mak.* **2019**, *19*, 1–16. [CrossRef] [PubMed]
83. Rumelhart, D.E.; Hinton, G.E.; Williams, R.J. Learning representations by back-propagating errors. *Nature* **1986**, *323*, 533–536. [CrossRef]
84. Li, J.; Cheng, J.H.; Shi, J.Y.; Huang, F. Brief introduction of back propagation (BP) neural network algorithm and its improvement. In *Advances in Computer Science and Information Engineering*; Springer: Berlin/Heidelberg, Germany, 2012; pp. 553–558.
85. Pal, M. Deep neural network-based pier scour modeling. *ISH J. Hydraul. Eng.* **2019**, *28*, 80–85. [CrossRef]
86. Maulud, D.; Abdulazeez, A.M. A review on linear regression comprehensive in machine learning. *J. Appl. Sci. Technol. Trends* **2020**, *1*, 140–147. [CrossRef]
87. Sun, Y.; Zhang, J.; Li, G.; Wang, Y.; Sun, J.; Jiang, C. Optimized neural network using beetle antennae search for predicting the unconfined compressive strength of jet grouting coalcretes. *Int. J. Numer. Anal. Methods Géoméch.* **2019**, *43*, 801–813. [CrossRef]
88. Sun, J.; Wang, J.; Zhu, Z.; He, R.; Peng, C.; Zhang, C.; Huang, J.; Wang, Y.; Wang, X. Mechanical Performance Prediction for Sustainable High-Strength Concrete Using Bio-Inspired Neural Network. *Buildings* **2022**, *12*, 65. [CrossRef]
89. Charfi, I.; Miteran, J.; Dubois, J.; Atri, M.; Tourki, R. Definition and performance evaluation of a robust SVM based fall detection solution. In Proceedings of the 2012 Eighth International Conference on Signal Image Technology and Internet-Based Systems IEEE, Sorrento, Italy, 25–29 November 2012; pp. 218–224.
90. Ukil, A. Support vector machine. In *Intelligent Systems and Signal Processing in Power Engineering*; Springer: Berlin/Heidelberg, Germany, 2007; pp. 161–226.
91. Duan, K.; Keerthi, S.S.; Poo, A.N. Evaluation of simple performance measures for tuning SVM hyperparameters. *Neurocomputing* **2003**, *51*, 41–59. [CrossRef]
92. Dong, S.; Yang, J. On computing the hyperparameter of extreme learning machines: Algorithm and application to computational PDEs, and comparison with classical and high-order finite elements. *J. Comput. Phys.* **2021**, *463*, 111290. [CrossRef]
93. Oneto, L.; Bisio, F.; Cambria, E.; Anguita, D. Slt-based elm for big social data analysis. *Cogn. Comput.* **2017**, *9*, 259–274. [CrossRef]
94. Bao, X.; Li, Y.; Li, J.; Shi, R.; Ding, X. Prediction of train arrival delay using hybrid ELM-PSO approach. *J. Adv. Transp.* **2021**, *2021*, 7763126. [CrossRef]
95. Truong, V.H.; Vu, Q.V.; Thai, H.T.; Ha, M.H. A robust method for safety evaluation of steel trusses using Gradient Tree Boosting algorithm. *Adv. Eng. Softw.* **2020**, *147*, 102825. [CrossRef]
96. Anghel, A.; Papandreou, N.; Parnell, T.; De Palma, A.; Pozidis, H. Benchmarking and optimization of gradient boosting decision tree algorithms. *arXiv* **2018**, arXiv:1809.04559.
97. Ghodsi, H.; Khanjani, M.J. Application of improved GMDH models to predict local scour depth at complex bridge piers. *Civil Eng. J.* **2020**, *6*, 69–84. [CrossRef]
98. Najafzadeh, M.; Azamathulla, H.M. Neuro-fuzzy GMDH to predict the scour pile groups due to waves. *J. Comput. Civ. Eng.* **2015**, *29*, 04014068. [CrossRef]
99. Madandoust, R.; Bungey, J.H.; Ghavidel, R. Prediction of the concrete compressive strength by means of core testing using GMDH-type neural network and ANFIS models. *Comput. Mater. Sci.* **2012**, *51*, 261–272. [CrossRef]
100. Xu, L.; Wang, X.; Bai, L.; Xiao, J.; Liu, Q.; Chen, E.; Jiang, X.; Luo, B. Probabilistic SVM classifier ensemble selection based on GMDH-type neural network. *Pattern Recognit.* **2020**, *106*, 107373. [CrossRef]
101. Stefenon, S.F.; Ribeiro, M.H.D.M.; Nied, A.; Mariani, V.C.; dos Santos Coelho, L.; da Rocha, D.F.M.; Grebogi, R.B.; de Barros Ruano, A.E. Wavelet group method of data handling for fault prediction in electrical power insulators. *Int. J. Electrical Power Energy Syst.* **2020**, *123*, 106269. [CrossRef]
102. Samsudin, R.; Saad, P.; Shabri, A. River flow time series using least squares support vector machines. *Hydrol. Earth Syst. Sci.* **2011**, *15*, 1835–1852. [CrossRef]

103. Martinek, R.; Zidek, J. The real implementation of ANFIS channel equalizer on the system of software-defined radio. *IETE J. Res.* **2014**, *60*, 183–193. [CrossRef]
104. Vieira, J.; Dias, F.M.; Mota, A. Neuro-fuzzy systems: A survey. In Proceedings of the 5th WSEAS NNA International Conference on Neural Networks and Applications, Udine, Italia, 25–27 March 2004; pp. 1–6.
105. Han, M.; Zhao, Y. Dynamic control model of BOF steelmaking process based on ANFIS and robust relevance vector machine. *Expert Syst. Appl.* **2011**, *38*, 14786–14798. [CrossRef]
106. Fattahi, H.; Hasanipanah, M. An integrated approach of ANFIS-grasshopper optimization algorithm to approximate flyrock distance in mine blasting. *Eng. Comput.* **2021**, *38*, 2619–2631. [CrossRef]
107. Zhang, J.; Zhao, H. A Prediction Model for Local Scour Depth around Piers Based on CNN. In Proceedings of the 2020 International Conference on Information Science, Parallel and Distributed Systems (ISPDS) IEEE, Xi'an, China, 14–16 August 2020; pp. 318–320.
108. Dong, H.; Chen, F.; Zhou, H.; Guo, C.; Sun, Z. A Prediction Model for Local Scour Depth around Piers Based on Machine Learning. In *IOP Conference Series: Earth and Environmental Science*; IOP Publishing: Bristol, UK, 2020; Volume 525, No. 1, p. 012080.
109. Khosravi, K.; Khozani, Z.S.; Mao, L. A comparison between advanced hybrid machine learning algorithms and empirical equations applied to abutment scour depth prediction. *J. Hydrol.* **2021**, *596*, 126100. [CrossRef]
110. Tien Bui, D.; Shirzadi, A.; Amini, A.; Shahabi, H.; Al-Ansari, N.; Hamidi, S.; Singh, S.K.; Thai Pham, B.; Ahmad, B.B.; Ghazvinei, P.T. A Hybrid Intelligence Approach to Enhance the Prediction Accuracy of Local Scour Depth at Complex Bridge Piers. *Sustainability* **2020**, *12*, 1063.
111. Ebtehaj, I.; Sattar, A.M.; Bonakdari, H.; Zaji, A.H. Prediction of scour depth around bridge piers using self-adaptive extreme learning machine. *J. Hydroinform.* **2017**, *19*, 207–224. [CrossRef]
112. Ebtehaj, I.; Bonakdari, H.; Moradi, F.; Gharabaghi, B.; Khozani, Z.S. An integrated framework of Extreme Learning Machines for predicting scour at pile groups in clearwater conditions. *Coast. Eng.* **2018**, *135*, 1–15. [CrossRef]
113. Ebtehaj, I.; Bonakdari, H.; Zaji, A.H.; Sharafi, H. Sensitivity analysis of parameters affecting scour depth around bridge piers based on the non-tuned, rapid extreme learning machine method. *Neural Comput. Appl.* **2019**, *31*, 9145–9156.
114. Richardson, E.V.; Davis, S.R. *Evaluating Scour at Bridges*; (No. FHWA-NHI-01-001); The United States. Federal Highway Administration, Office of Bridge Technology: Lakewood, CO, USA, 2001.
115. Johnson, P.A. Reliability-based pier scour engineering. *J. Hydraul. Eng.* **1992**, *118*, 1344–1358. [CrossRef]
116. Shen, H.W.; Schneider, V.R.; Karaki, S. Local scour around bridge piers. *J. Hydraul. Div.* **1969**, *95*, 1919–1940. [CrossRef]
117. Sreedhara, B.M.; Patil, A.P.; Pushparaj, J.; Kuntoji, G.; Naganna, S.R. Application of gradient tree boosting regressor for the prediction of scour depth around bridge piers. *J. Hydroinform.* **2021**, *23*, 849–863. [CrossRef]
118. Cheng, M.Y.; Cao, M.T.; Wu, Y.W. Predicting equilibrium scour depth at bridge piers using evolutionary radial basis function neural network. *J. Comput. Civ. Eng.* **2015**, *29*, 04014070.
119. Van Wilson, K. *Scour at Selected Bridge Sites in Mississippi*; US Department of the Interior: Washington DC, USA; US Geological Survey: Denver, CO, USA, 1995; Volume 94, No. 4241.
120. Froehlich, D.C. Analysis of onsite measurements of scour at piers. In *Hydraulic Engineering: Proceedings of the 1988 National Conference on Hydraulic Engineering*; American Society of Civil Engineers: New York, NY, USA, 1988; pp. 534–539.
121. Hoang, N.D.; Liao, K.W.; Tran, X.L. Estimation of scour depth at bridges with complex pier foundations using support vector regression integrated with feature selection. *J. Civ. Struct. Health Monit.* **2018**, *8*, 431–442.
122. Melville, B.W.; Coleman, S.E. *Bridge Scour*; Water Resources Publication: Littleton, CO, USA, 2000.
123. Ataie-Ashtiani, B.; Baratian-Ghorghi, Z.; Beheshti, A.A. Experimental investigation of clear-water local scour of compound piers. *J. Hydraul. Eng.* **2010**, *136*, 343–351. [CrossRef]
124. Kim, I.; Fard, M.Y.; Chattopadhyay, A. Investigation of a bridge pier scour prediction model for safe design and inspection. *J. Bridge Eng.* **2015**, *20*, 04014088. [CrossRef]
125. Liao, K.W.; Muto, Y.; Lin, J.Y. Scour depth evaluation of a bridge with a complex pier foundation. *KSCE J. Civ. Eng.* **2018**, *22*, 2241–2255.
126. Amini, A.; Mohammad, T.A. Local scour prediction around piers with complex geometry. *Mar. Georesources Geotechnol.* **2017**, *35*, 857–864. [CrossRef]
127. Mueller, D.S.; Wagner, C.R. *Field Observations and Evaluations of Streambed Scour at Bridges*; (No. FHWA-RD-03-052); United States, Federal Highway Administration, Office of Research, Development, and Technology: Richmond, VA, USA, 2005.

Disclaimer/Publisher's Note: The statements, opinions and data contained in all publications are solely those of the individual author(s) and contributor(s) and not of MDPI and/or the editor(s). MDPI and/or the editor(s) disclaim responsibility for any injury to people or property resulting from any ideas, methods, instructions or products referred to in the content.

MDPI
St. Alban-Anlage 66
4052 Basel
Switzerland
Tel. +41 61 683 77 34
Fax +41 61 302 89 18
www.mdpi.com

Applied Sciences Editorial Office
E-mail: applsci@mdpi.com
www.mdpi.com/journal/applsci

MDPI
St. Alban-Anlage 66
4052 Basel
Switzerland

Tel: +41 61 683 77 34

www.mdpi.com

ISBN 978-3-0365-7543-8